

CHEMIA

**STUDIA
UNIVERSITATIS BABEȘ-BOLYAI
CHEMIA**

1/2017

EDITORIAL BOARD OF STUDIA UNIVERSITATIS BABEȘ-BOLYAI CHEMIA

ONORARY EDITOR:

IONEL HAIDUC - Member of the Romanian Academy

EDITOR-IN-CHIEF:

LUMINIȚA SILAGHI-DUMITRESCU

EXECUTIVE EDITOR:

CASTELIA CRISTEA

EDITORIAL BOARD:

PAUL ȘERBAN AGACHI, Babeș-Bolyai University, Cluj-Napoca, Romania

LIVAIN BREAU, UQAM University of Quebec, Montreal, Canada

HANS JOACHIM BREUNIG, Institute of Inorganic and Physical Chemistry,
University of Bremen, Bremen, Germany

MIRCEA DIUDEA, Babeș-Bolyai University, Cluj-Napoca, Romania

JEAN ESCUDIE, HFA, Paul Sabatier University, Toulouse, France

ION GROSU, Babeș-Bolyai University, Cluj-Napoca, Romania

EVAMARIE HEY-HAWKINS, University of Leipzig, Leipzig, Germany

FLORIN DAN IRIMIE, Babeș-Bolyai University, Cluj-Napoca, Romania

FERENC KILAR, University of Pecs, Pecs, Hungary

BRUCE KING, University of Georgia, Athens, Georgia, USA

ANTONIO LAGUNA, Department of Inorganic Chemistry, ICMA, University of
Zaragoza, Zaragoza, Spain

JURGEN LIEBSCHER, Humboldt University, Berlin, Germany

KIERAN MOLLOY, University of Bath, Bath, UK

IONEL CĂȚĂLIN POPESCU, Babeș-Bolyai University, Cluj-Napoca, Romania

CRISTIAN SILVESTRU, Babeș-Bolyai University, Cluj-Napoca, Romania

<http://chem.ubbcluj.ro/~studiachemia/>; studiachemia@chem.ubbcluj.ro

http://www.studia.ubbcluj.ro/serii/chemia/index_en.html

YEAR
MONTH
ISSUE

Volume 62 (LXII) 2017
MARCH
1

STUDIA UNIVERSITATIS BABEȘ-BOLYAI CHEMIA

1

STUDIA UBB EDITORIAL OFFICE: B.P. Hasdeu no. 51, 400371 Cluj-Napoca, Romania,
Phone + 40 264 405352

CUPRINS – CONTENT – SOMMAIRE – INHALT

ADINA GHIRIȘAN, SIMION DRĂGAN, VASILE MICLĂUȘ, Freeze-Drying Kinetics Approach of Soluble Coffee. Mass Transfer Parameters Estimation.....	7
DANA-MARIA SABOU AND ALEXANDRA ANA CSAVDĂRI, Combined Kinetic Response of two Substrates with Similar Reactive Patterns ..	19
GULZIYA A. SEILKHANOVA, AINUR N. IMANGALIYEVA, DINA N. AKBAYEVA, ZHANNA ZH. KENZHALINA, Modified Raw Materials: Synthesis, Characterization and Application for Cd ²⁺ Ions Removal.....	35
ADRIAN EUGEN CIOABLĂ, ALEKSANDAR DJURIC, GABRIELA-ALINA DUMITREL, DANIEL CHIRILĂ, VASILE PODE, Biogas Production Using Waste Waters – Influence of Process Parameters for Test RIG at Laboratory Scale	51
BOGDAN CULIC, CRISTINA GASPARIK C, MIHAI VARVARA, CARINA CULIC, CRISTIAN DRAGOS, LAURA SILAGHI-DUMITRESCU, DIANA DUDEA, Evaluation of Bleaching on a CAD/CAM Hybrid Ceramic Material	61
RAMONA I. CHELCEA, DUMITRIȚA MOLDOVAN, DAN E. DEMCO, EUGEN CULEA, RADU FECHETE, <i>In Vitro</i> Degradation and Phase Composition of Cosmetic Emulsions	73

DANIELA-RODICA MITREA, SIMONA CLICHICI, ADRIANA FILIP, DIANA OLTEANU, IOANA BÂLDEA, REMUS MOLDOVAN, NICOLETA DECEA, OANA-ALINA HOTEIUC, Resveratrol and Loratadine Effects on Oxidative Stress Induced by Experimental Inflammation	89
ADRIANA MUNTEAN, IRINA SMICAL, ZOLTÁN TÖRÖK, Validation of an Alternative Method for Total Nitrogen Analysis in Water Samples	101
ADRIAN PATRUT, SÉBASTIEN GARNAUD, OUMAR KA, ROXANA T. PATRUT, TOMAS DIAGNE, DANIEL A. LOWY, EDIT FORIZS, JENŐ BODIS, KARL F. VON REDEN, African Baobabs with a Very Large Number of Stems and False Stems: Radiocarbon Investigation of the Baobab of Warang.....	111
ALEXANDRU BANARU, ALEXANDER KOCHNEV, The Minimal Set of Intermolecular Interactions in the Structures of Substituted Prolines..	121
MAHDIEH AZARI, ALI IRANMANESH, MIRCEA V. DIUDEA, Vertex-Eccentricity Descriptors in Dendrimers.....	129
ESMAT MOHAMMADINASAB, Modeling Boiling Points of Alkane Derivatives.....	143
PAUL ATYIM, NELI KINGA OLAH, GYÖNGYI OSSER, CLAUDIA CRINA TOMA, CLAUDIU MORGOVAN, ELISABETA ATYIM, Practical Investigation of Gels Containing Aristolochia (<i>Aristolochia Clematitis</i>) Extract	153
KHURAM SHAHZAD AHMAD, Investigating the Impact of Soils' Physicochemical Composition on Chlorsulfuron Pedospheric Sorption	165
SZABOLCS FOGARASI, MELINDA NAGY, FLORICA IMRE-LUCACI, ARPAD IMRE-LUCACI, Identification of Mass Transfer Parameters for Rock Salt Dissolution in a Plug Flow System.....	175
SÁNDOR NAGY, PETRA KOZMA, PÉTER KISSZÉKELYI, DÓRA BEZZEGH, PÉTER HUSZTHY, JÓZSEF KUPAI, Synthesis of Three New Bifunctional Glucose-Thiourea Organocatalysts and Their Application in Asymmetric <i>Michael</i> Addition.....	183
ZSIGMOND PAPP, Unmodified and Gold-Modified Semiconductor Catalysts for Solar Light Assisted Photodegradation of Crystal Violet.....	195
MOHAMMAD HOSEIN BIGTAN, KAZEM MAHANPOOR, Preparation, Characterization, and Evaluation of the Photocatalytic Effect of α -Fe ₂ O ₃ /Sapo-34 in the Elimination Process of the Anti-Cancer Drug Doxorubicin from Aqueous Solution	203

THOMAS DIPPONG, CRISTINA MIHALI, FIRUTA GOGA, ELENA CICAL, Seasonal Evolution and Depth Variability of Heavy Metal Concentrations in the Water of Firiza-Strîmtori Lake, NW of Romania	213
DANA-ADRIANA ILUȚIU-VARVARA, DAN RĂDULESCU, VALER DONCA, Benfothiamine Administration in Patients with Dilated Cardiomyopathy and Advanced Heart Failure with Chronic Diuretic Treatment.....	229
FATMAGÜL MUTLU DEMIREL, OSMAN ISMAIL, Investigation of the Effect of a Hybrid Drying Method on the Color Quality of Nectarine Slices and Energy Consumption	237
ILDIKÓ KOVÁCS, SÁNDOR BESZÉDES, SZABOLCS KERTÉSZ, GÁBOR VERÉB, CECILIA HODÚR, IBOLYA ZITA PAPP, ÁKOS KUKOVECZ, ZSUZSANNA LÁSZLÓ, Investigation of Titanium-Dioxide Coatings on Membrane Filtration Properties	249
FIRUTA GOGA, ROXANA DUDRIC, LILIANA BIZO, ALEXANDRA AVRAM, ALEXANDRU HORATIU MARINCAS, CSABA VARHELY JR., THOMAS DIPPONG, Influence of the Ni/Mg Ratio on the Colour of Spinel Pigments Prepared by a Modified Sol – Gel Method.....	261

Studia Universitatis Babes-Bolyai Chemia has been selected for coverage in Thomson Reuters products and custom information services. Beginning with V. 53 (1) 2008, this publication is indexed and abstracted in the following:

- Science Citation Index Expanded (also known as SciSearch®)
- Chemistry Citation Index®
- Journal Citation Reports/Science Edition

FREEZE-DRYING KINETICS APPROACH OF SOLUBLE COFFEE. MASS TRANSFER PARAMETERS ESTIMATION

ADINA GHIRIŞAN^a, SIMION DRĂGAN^{a*}, VASILE MICLĂUŞ^a

ABSTRACT. The present paper presents the freeze-drying kinetics of soluble coffee in order to determine the mass transfer parameters. Several semi-theoretical and empirical models were used to find the best fit to the experimental data. The applied models were compared using the coefficient of determination (R^2), the mean relative percent error (P), the root mean square error (RMSE) and the reduced chi-square (χ^2). The Midilli model was found to fit better to the experimental freeze-drying data comparative to other models. The Fick's second law was employed to determine the effective diffusion coefficient (D_{eff}).

Keywords: coffee, freeze-drying, moisture ration, drying rate, Fick's diffusion model, effective diffusion coefficient.

INTRODUCTION

Freeze-drying or lyophilisation is the drying process used to remove the solvent (usually water) from frozen materials. Due to the absence of liquid water and the low temperatures required for the process, more of deterioration and biological reactions are stopped, the quality of materials is preserved, its shelf-life is increased, the loss of flavor and aroma is reduced, and active ingredients can be recovered [1].

The benefits of freeze-drying include also: retention of morphological, biochemical, and immunological properties, high recovery of volatiles, retention of structure, surface area, high yield, and reduced weight for storage, shipping and handling [2].

^a *Universitatea Babeş-Bolyai, Facultatea de Chimie și Inginerie Chimică, Str. Kogălniceanu, Nr. 1, RO-400084 Cluj-Napoca, Romania*

* *Corresponding author: sdragan@chem.ubbcluj.ro*

Freeze-drying was initially used for the preservation of heat-sensitive bioactive molecules (DNA, enzymes and proteins), pharmaceutical products (antibiotics) and other delicate, solvent impregnated materials [3]. Nowadays, the freeze-drying is used from relatively simple preservable food like coffee, tea, crispy fruits and vegetables, aromatic herbs, to complex biotechnological or pharmaceutical products like microorganisms, cosmetics, enzymes, fine chemicals and ceramic powders [4, 5].

By freeze-drying, the solid, semi-liquid or liquid sample is frozen to a low temperature (about -40°C) to form a thin layer and then subjected to vacuum when the ice (frozen solvent) is removed by sublimation, during the primary drying stage of the process. As the ice sublimates, the sublimation interface, which started at the outside surface, recedes, and a porous shell of dried material remains. The vaporized solvent (water) is transported through the porous layer of dried material. In contrast with mass transfer, which always flows through the dry layer, heat transfer can take place by conduction through the dry layer or through the frozen layer [6-8].

Several mathematical equations describing mass and energy transfer have been developed for modeling the freeze-drying process [9-11]. Such models account for the removal of frozen water only (sublimation model) or the removal of frozen and bound water (sorption sublimation model), examine the methods of supplying heat and the diffusion mechanisms, describe steady or unsteady state processes, or analyze both transfers under various processing conditions. Pseudo-steady state exists as long as the amount of heat entering into the product is balanced by the amount of heat removed through sublimation of ice. Under these conditions the product temperature does not change significantly.

The use of the rigorous unsteady state mathematical model of Sadikoglu and Liapis has been found to describe satisfactorily the experimental dynamic behavior of the primary and secondary drying stages of bulk solution freeze drying of pharmaceuticals in trays [10].

The diffusion of water vapor in the partially dried layer is one of the major factors affecting the mass transfer rate. The diffusivity is closely related to the pore size. Large ice crystals will be helpful for the movement of water. The pressure difference is essentially the driving force for the transport of water vapor. The smallest chamber pressure gives the highest ice sublimation rate [11].

In the present work, semi-theoretical and empirical mass transfer models used for the drying of the thin-layer samples were fitted to experimental data obtained in a laboratory freeze-dryer in order to investigate the applicability of these models to the soluble coffee freeze-drying kinetics [13, 16].

RESULTS AND DISCUSSION

Interpretation of freeze-drying behavior

The evolution of soluble coffee freeze-drying characterized by the drying curve is shown in Figure 1. The sample moisture content M was calculated on a dry basis as in other works was made [12-14]. Drying of the frozen coffee solution started with the initial moisture content of 8.54 (kg water/kg dried matter) and decreases until 0.12 (kg water/kg dried matter) in 360 minutes. The water loss was measured at intervals of 30 minutes.

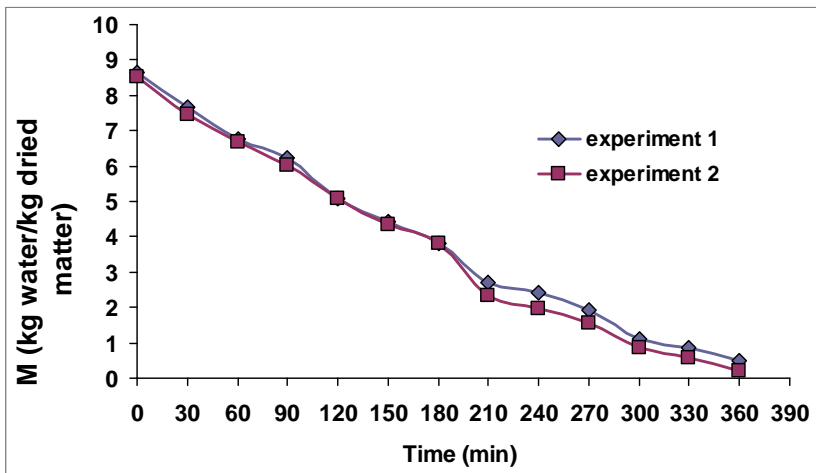


Figure 1. Drying curves

As the drying curves show, the results can be considered reproducible, as long as the drying parameters are constant. Some differences between moisture content appear in the second period, after 210 minutes from the beginning of the drying process.

In order to analyze the freeze-drying kinetics, the moisture content is forwards expressed as moisture ratio (MR), calculated by equation (1) or by the simplified form (2) applied when the equilibrium moisture contents M_e is enough low [15]:

$$MR = \frac{M - M_e}{M_0 - M_e} = e^{-kt} \quad (1)$$

$$MR = \frac{M}{M_0} = e^{-kt} \quad (2)$$

where: k is the drying constant (min^{-1}), M , M_0 and M_e - moisture content at each measured time, at the beginning and at the final/equilibrium (kg moisture/kg dried matter), t - the drying time (min).

The change of the moisture ratio (MR) during freeze-drying is presented in Figure 2.

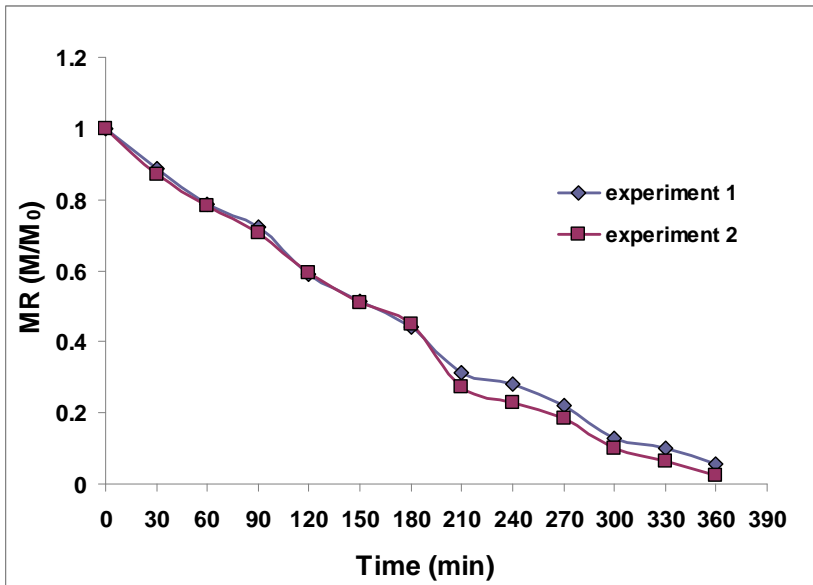


Figure 2. Moisture ration (MR) versus freeze-drying time.

The average values of moisture ratio MR obtained at each experimental time were fitted to 10 semi-theoretical or empirical drying models, usually used for convective and/or freeze-drying of thin-layer samples. The used models and the obtained drying constants, determined by **Matlab Curve Fitting** Programme, are shown in Table 1.

In order to compare the best fit for each mathematical model the next statistical parameters are used: the coefficient of determination (R^2), the mean relative percent error (P), the root mean square error (RMSE) and the reduced chi-square (χ^2). The higher values of R^2 and the lower values of P, RMSE and χ^2 will give the goodness of the fit. These parameters are calculated by equations (3) – (6), and are shown in Table 2.

Table 1. Models used for freeze-drying of soluble coffee [13, 16]

Nr. Crt.	Model name and equation	Drying constants
1	Newton $MR = e^{-kt}$	$k = 0.005457$
2	Page $MR = e^{-kt^m}$	$k = 0.0005428$ $m = 1.44$
3	Henderson & Pabis $MR = a \cdot e^{-kt}$	$k = 0.005876$ $a = 1.072$
4	Logarithmic $MR = a \cdot e^{-kt} + c$	$k = 0.002862$ $a = 1.534$ $c = -0.5142$
5	Two term $MR = a \cdot e^{-k_0t} + be^{-k_1t}$	$k_0 = 0.005502$ $k_1 = 0.00553$ $a = 0.3493$ $b = 0.661$
6	Two term exponential $MR = ae^{-kt} + (1-a)e^{-kat}$	$k = 0.005457$ $a = 0.9976$
7	Wang and Singh $MR = 1 + at + bt^2$	$a = -0.0040$ $b = 3.75 \cdot 10^{-6}$
8	Approximation of diffusion $MR = ae^{-kt} + (1-a)e^{-kbt}$	$k = 0.01112$ $a = -32.25$ $b = 0.9737$
9	Modified Henderson & Pabis $MR = ae^{-kt} + be^{-gt} + ce^{-ht}$	$a = -0.1947$ $b = 1.153$ $c = 0.0414$ $k = 0.816$ $g = 0.006346$ $h = 0.87$
10	Midilli et al. $MR = ae^{-kt^m} + bt$	$k = 0.0003916$ $a = 0.9702$ $b = -5.17 \cdot 10^{-5}$ $m = 1.488$

$$P = \frac{100}{N} \sum_{i=1}^N \frac{|MR_{\text{expi}} - MR_{\text{prei}}|}{MR_{\text{expi}}} \quad (3)$$

$$RMSE = \left[\frac{1}{N} \sum_{i=1}^N (MR_{\text{expi}} - MR_{\text{prei}})^2 \right]^{1/2} \quad (4)$$

$$\chi^2 = \frac{\sum_{i=1}^N ((MR_{\text{expi}} - MR_{\text{prei}})^2)}{N - n} \quad (5)$$

$$R^2 = 1 - \frac{\sum_{i=1}^N (MR_{\text{exp}i} - MR_{\text{pre}i})^2}{\sum_{i=1}^N (MR_{\text{pre}i})^2} \quad (6)$$

where $MR_{\text{exp}i}$ are the experimental values of moisture ratios, $MR_{\text{pre}i}$ are the predicted moisture ratios, N are the number of observations, and n is the number of constants.

Table 2. Values of statistical parameters

Model	R ²	RMSE	χ ²	P
Newton	0.9426	0.0058	3.4039*10 ⁻⁵	0.4275
Page	0.9771	0.0189	3.5833*10 ⁻⁴	0.0403
Henderson & Pabis	0.9508	0.0299	8.9187*10 ⁻⁴	0.1231
Logarithmic	0.9741	4.3325e ⁻⁰⁴	1.8771*10 ⁻⁷	0.0656
Two term	0.9448	0.0011	1.1899*10 ⁻⁶	0.3846
Two term exponential	0.9426	0.0058	3.3970*10 ⁻⁵	0.4275
Wang & Singh	0.9755	0.0110	1.2105*10 ⁻⁴	0.1391
Approximation of diffusion	0.9757	0.0189	3.5752*10 ⁻⁴	0.0013
Modified Henderson & Pabis	0.9595	0.0231	5.3364*10 ⁻⁴	0.1022
Midilli et al.	0.9785	0.0023	5.4395*10 ⁻⁶	0.0480

As the statistical results show, the highest value of R^2 and the lowest value of P , $RMSE$ and χ^2 were obtained from the Midilli et al. model, $R^2 = 0.9785$, $P = 0.0480$, $RMSE = 0.0023$ and $\chi^2 = 5.4395*10^{-6}$. Comparative results are obtained by logarithmic, Wang & Singh, and approximation of diffusion models.

The choice of these models as good models for the behavior of soluble coffee freeze-drying is confirmed by the plot of the predicted and experimental moisture ratio values, which is a straight line banding around 45°, as Figure 3 indicates.

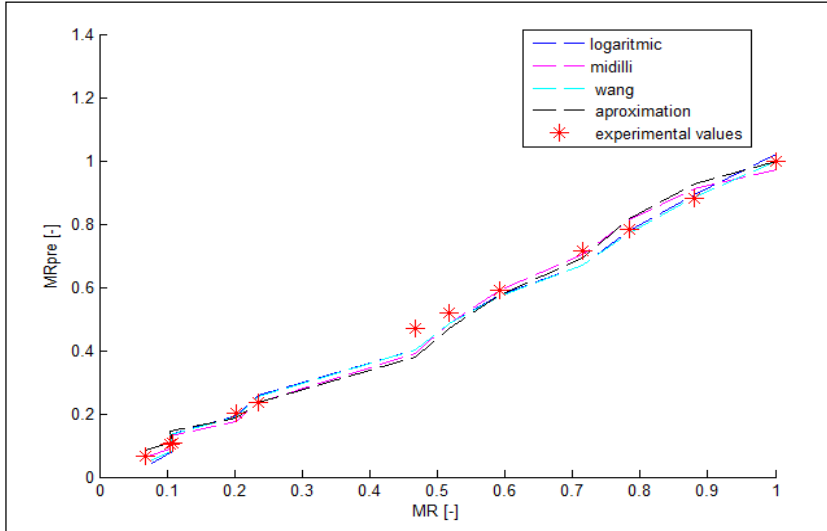


Figure 3. Comparison of experimental and predicted moisture ratio by established models

Determination of drying rate

The freeze-drying rate is expressed by equation (7) describing the amount of water loss on surface area and time.

$$DR = \frac{\Delta M}{A \cdot \Delta t} \quad (7)$$

where $A = 0.0017 \text{ m}^2$ is the surface area of the tray.

The change of the drying rate with the ratio moisture is shown in Figure 4. As it is shown, the drying process takes place in the falling rate drying period, corresponding to porous materials with low specific surface [17].

The drying rate decreases between $0.32 \text{ kg/kgm}^2\text{s}$ at $0.025 \text{ kg/kgm}^2\text{s}$, with the decrease of the moisture content from $8.54 \text{ (kg water/kg dried matter)}$ to $0.12 \text{ (kg water/kg dried matter)}$.

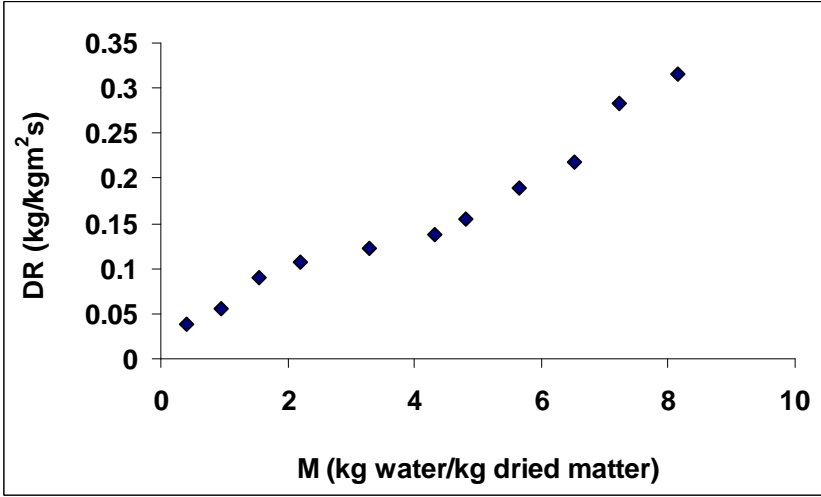


Figure 4. Drying rate versus moisture

Determination of effective diffusivity

As it was shown in the previous paper [14], the diffusion model developed for mass transfer based on Fick's second law of diffusion, more accurate than heat transfer model, was used in order to determine the diffusion coefficient during freeze-drying:

$$MR = \frac{M}{M_0} = Ae^{-kt} = Ae^{-\frac{\pi^2 D_{\text{eff}} t}{4L^2}} \quad (8)$$

where, k is known as drying constant, an important parameter in understanding the drying behavior of the material, L - the thickness of the sample, and D_{eff} - the effective diffusion coefficient [12, 14].

In order to determine the effective diffusion coefficients (D_{eff}) the experimental drying data in term of $\ln(MR)$ are plotted versus time (Figure 5). The obtained straight line has the slope given as equation (9) shows:

$$\text{Slope} = k = \frac{\pi^2 D_{\text{eff}}}{4L^2} \quad (9)$$

The Figure 5 shows two distinct drying stages, with two diffusion coefficients, that can be attributed to the change during freeze-drying process of the structure/porosity of the frozen coffee sample or to the change

of the drying mechanism. It can be considered that during the sublimation, the sample structure becomes more porous, in the place of ice appear pores with larger diameters, which improve the mass transfer. So the value of D_{eff} is higher in the second stage than in the first one, similar with other works [12, 14].

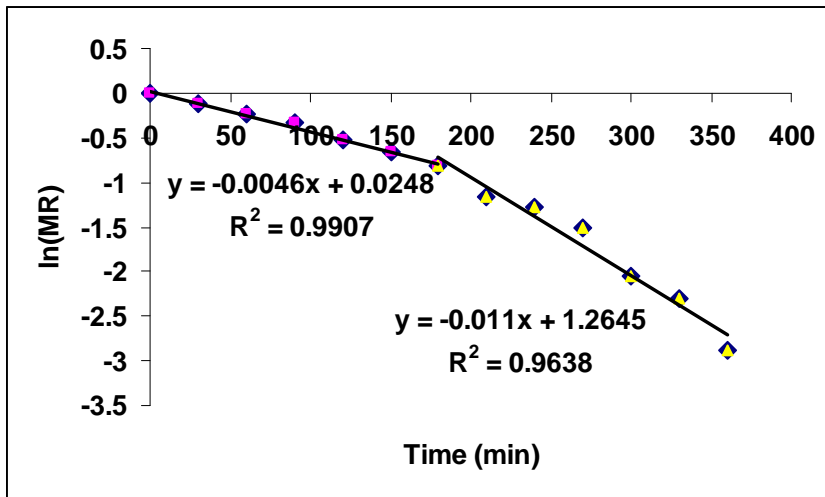


Figure 5. Determination of the diffusion coefficients

The experimental values of effective diffusion coefficient are found to vary from $2.286 \cdot 10^{-8} \text{ m}^2/\text{s}$ on the first stage to $5.467 \cdot 10^{-8} \text{ m}^2/\text{s}$ on the second stage (with an average value of $3.8765 \cdot 10^{-8} \text{ m}^2/\text{s}$).

CONCLUSIONS

The experimental data obtained for the coffee solution freeze-drying were interpreted taken 10 mass transfer models used for thin-layer samples. The models were compared considering some statistical parameters. The Midilli model was found to show the best fit to experimental data. Comparative results are obtained by logarithmic, Wang and approximation of diffusion models.

The drying rates varying from $0.32 \text{ kg}/\text{kgm}^2\text{s}$ to $0.025 \text{ kg}/\text{kgm}^2\text{s}$, have shown the decrease of drying rate with the decrease of the moisture content, specific for the porous materials with low specific surface.

The experimental values of effective diffusion coefficient, found to vary from $2.286 \cdot 10^{-8} \text{ m}^2/\text{s}$ on the first stage to $5.467 \cdot 10^{-8} \text{ m}^2/\text{s}$ on the second stage, was attributed to the change of the structure/porosity of the soluble coffee sample during the freeze-drying process.

EXPERIMENTAL SECTION

The coffee solution was prepared by boiling of 200 g pure grinded coffee from Firma Tchibo (procured from local market) in 500 mL hot water. The obtained suspension was filtered and then the concentrated solution was divided in equal samples and placed in Petri dishes. The samples with the thickness of 7 mm of concentrated coffee placed in Petri dishes were first frozen for 30 minutes at $-80 \text{ }^\circ\text{C}$ in the freezer and then the frozen samples were transferred inside the freeze dryer for a period of 6 hours under the pressure of 0.045 mbar and a shelf temperature of $20 \text{ }^\circ\text{C}$. The condenser temperature was kept to $-50 \text{ }^\circ\text{C}$. Freeze-drying was carried out using a laboratory freeze dryer ALPHA 1-2 LD_{Plus}, MARTIN CHRIST Gefriertrocknungsanlagen GmbH Germany.

The weight of each sample was measured at each 30 minutes in order to evaluate the water loss. The samples which were taken out from the freeze dryer were transferred first to the desiccators for attaining equilibrium. Two replications were done in order to verify the reproducibility of the experiment.

REFERENCES

1. C. Ratti, *Journal of Food Engineering*, **2001**, 49, 311.
2. A. Ciurzynska, A. Lenart, *Polish Journal of Food and Nutrition Sciences*, **2011**, 61(3), 165.
3. J. P. George, A. K. Datta, *Journal of Food Engineering*, **2002**, 52, 89.
4. Y. Liu, Y. Zhao, X. Feng, *Applied Thermal Engineering*, **2008**, 28, 675.
5. A. I. Liapis, M.J. Pikal, R. Bruttini, *Drying Technology*, **1996**, 14(6), 1265-1300.
6. F. Jafar, M. Farid, *Drying Technology*, **2003**, 21(2), 249.
7. S. Khalloufi, J. L., Robert, C. Ratti. *Journal of Food Processing Engineering*, **2005**, 28(2), 107.
8. W. Wang, Mo. Chen and Guohua Chen, *Chinese Journal of Chemical Engineering*, **2012**, 20(3), 551.
9. A. I. Liapis, R. J. Litcheld, *Chemical Engineering Science*, **1979**, 34, 975.
10. H. Sadikoglu, A. I. Liapis, *Drying Technology*, **1997**, 15(3/4), 791.

11. M. Karel, "Freeze Drying and Advanced Food Technology", S. A. Goldblith, L. Rey, W. W. Rothmayr, Eds. Academic Press: NY, **1975**, 177.
12. A. Muthukumaran, "Foam-mat Freeze Drying of Egg White and Mathematical Modeling", PhD Thesis, **2007**.
13. V. Kirmaci, T. Menlik, H. Usta, *Journal of Engineering and Technological Sciences*, **2013**, 1, 22.
14. A. Miclăuș (Ghirișan), *Studia UBB Chemia*, **2015**, 60(1), 147.
15. B. K. Bala, "Drying and Storage of Cereal Grains", Enfield N.H: Science Pub. **1997**, chapter 3.
16. K. Sacilik, A. K. Elicin, *Journal of Food Engineering*, **2006**, 73, 281.
17. C. Ratti, "Handbook of food powders: processes and properties", Woodhead Publishing Series in Food Science, Technology and Nutrition, Edited by: B. Bhandari, N. Bansal, M. Zhang and P. Schuck, **2013**, 57.

COMBINED KINETIC RESPONSE OF TWO SUBSTRATES WITH SIMILAR REACTIVE PATTERNS

DANA-MARIA SABOU^a AND ALEXANDRA ANA CSAVDÁRI^{a*}

ABSTRACT. The behaviour towards simultaneous oxidation by Cr(VI) in acidic environment of mixtures consisting of two structurally closely related thioethers (S-methylcysteine and DL-methionine) was tested, at $0.085 \text{ mol}\cdot\text{l}^{-1} \text{ H}^+$ and $298 \pm 0.1 \text{ K}$. The kinetic and mechanistic patterns of the two substrates when oxidized separately were already known and very similar. Based on that knowledge, the individual kinetic parameters (rate and equilibrium constants) were first computed. Theoretical predictive models for the value of the observed rate constant of a mixture, based on the kinetic data from non-mixtures, are compared with experimental findings and subsequently an empirical calibration surface obtained from all experiments is discussed. Due to differences in the kinetic parameters of the two reactions, in all models the obtained surfaces are asymmetrical, and this opens the possibility to univocally determine the concentrations of both the thioethers without separation.

Keywords: *chromium VI oxidation, DL-methionine, S-methylcysteine, combined kinetic response, kinetic modeling*

INTRODUCTION

Identification and quantification of analytes from mixed samples can be quite challenging, particularly when dealing with complex mixtures. The classical approach to the matter involves laborious steps of separating the components of the sample. It comes as no surprise that methods are sought, which could eliminate part or even all of these separation steps.

^a Babeş-Bolyai University, Faculty of Chemistry and Chemical Engineering, 11 Arany Janos str., RO-400028, Cluj-Napoca, Romania

* Corresponding author: acsavdari@chem.ubbcluj.ro

Within the overall spectrum of analytical methods, the kinetic ones have become increasingly interesting [1-4]. Besides their economic feasibility, one of their chief appeals resides precisely in the possibility of simultaneous determination of more analytical species without prior separation, although some pre-treatment of the sample (mineralising, filtering, concentrating etc.), may still be needed.

In our group, a subject of continued interest has been deciphering the kinetics and mechanism of sulphur compounds oxidation by various high valence transitional metal ions, in acidic environments. Much of our effort was directed to the oxidations by Cr(VI) of thioic type substrates such as thiols, thioacids, thioethers [5-9]. Some area studies by other groups are also found in the literature [5, 10-12] and some general patterns are now well established. Among them there is a first and often fast step in which one Cr(VI) and one or more thio compound molecules form a condensation intermediate (adduct). This subsequently decomposes in an electron transfer step that can be mono-, bi- or even trielectronic and it may or may not involve an additional thio compound molecule. In acidic media, both these steps may be assisted by H⁺ ions. The electron transfer is more often than not rate-determining. Following it, new types of intermediates are formed. They react in further steps and eventually lead to the final products: Cr(III) complexes and disulphides (S-S) or sulphoxides (-SO) respectively. These steps have sufficiently high rate constants to exert no influence on the overall rate.

With this knowledge, a new point of focus has become the study of mixtures of thio compounds. For this paper, bi-component mixtures were chosen, having as constituents two structurally closely related thioethers: DL-methionine (MET) and S-methylcysteine (MTC).

We have already reported on the kinetics and mechanisms of their individual reactions with Cr(VI) in aqueous acidic media [8,9]. Those studies benefited from very similar approaches in terms of the experimental setup (batch measurements, spectrophotometry as the tool, 350 nm as the monitoring wavelength, HClO₄ as the source for hydrogen ions, Cr(VI) as the limiting reactant, and comparable thioether and acid concentrations). The notable differences were in the work temperature and ionic strength.

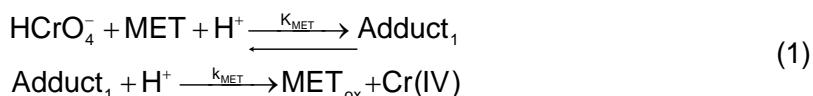
The kinetic and mechanistic features found for the two substrates are also mostly similar and are summarized below.

The thioether to Cr(VI) stoichiometric ratio was found to be 1.5 to 1 in both cases, indicating sulphoxides as the final reaction products. Also for both, four hydrogen ions are required for each reacted Cr(VI).

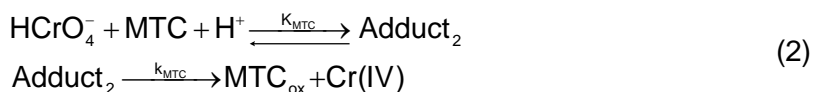
In terms of the reaction mechanism, one common feature is the initial formation of an adduct of 1 to 1 ratio between the Cr(VI) and the thio compound, in a hydrogen ion assisted equilibrium step. Another is the lack of

involvement of a second thio compound molecule in the decomposition of the adduct, which takes place with the transfer of two electrons and is the rate determining step in the case of either substrate. However, the involvement of a hydrogen ion in the rate determining step is noticed in the case of DL-methionine, but not in the case of S-methylcysteine.

Up until and including the rate determining step, the simplified reaction schemes that can be written for the two substrates are, therefore:



and:



The rate laws for the two reactions, based on the above schemes and also taking into account the fact that the total Cr(VI) (HCrO_4^- and the corresponding adduct) is experimentally monitored, are:

$$-\frac{d[\text{Cr}^{\text{VI}}]_{\text{total}}}{dt} = \frac{k_{\text{MET}} K_{\text{MET}} [\text{MET}][\text{H}^+]^2}{1 + K_{\text{MET}} [\text{MET}][\text{H}^+]} [\text{Cr}^{\text{VI}}]_{\text{total}} \quad (3)$$

in the case of DL-methionine, and:

$$-\frac{d[\text{Cr}^{\text{VI}}]_{\text{total}}}{dt} = \frac{k_{\text{MTC}} K_{\text{MTC}} [\text{MTC}][\text{H}^+]}{1 + K_{\text{MTC}} [\text{MTC}][\text{H}^+]} [\text{Cr}^{\text{VI}}]_{\text{total}} \quad (4)$$

in the case of S-methylcysteine, respectively.

The aim of this study is to assess the possibility of using the simultaneous oxidation by Cr(VI) of the two substrates with very similar reactive patterns to univocally determine both their concentrations in a mixture, without separation. This is viewed as a first and necessary step for future development of kinetic methods of analysis for multi-component mixtures of substrates with similar kinetic behaviour.

The chosen route to this end was finding suitable models to describe the oxidative behaviour of the mixtures, be they theoretical predictions derived from the kinetic data of the individual components, or empirical surfaces obtained from direct measurements of the mixtures themselves.

Also reported here is some additional insight on the individual oxidations of the two substrates acquired in the process.

RESULTS AND DISCUSSION

Before being able to draw reliable conclusions about the behaviour in the mixture of the two thioethers, the knowledge of their individual rate and equilibrium constants is important. Since these values depend on reaction conditions such as temperature or ionic strength, the figures from the literature could be of use only if the same conditions were to be employed for the mixtures. Clearly this was only partly achievable, since precisely those parameters were different for the two cases.

We decided for 298 K and constant $0.085 \text{ mol}\cdot\text{l}^{-1} \text{ HClO}_4$, the same as employed in the mechanistic study on DL-methionine. Unlike there, the ionic strength was here considered equal to the perchloric acid concentration and no further adjustment by inert salt addition was deemed necessary. Indeed, the 850-fold excess (212.5 with stoichiometry) of the acid over the Cr(VI) ensured that the contribution brought by the salt of the latter was insignificant. Also, the acid was 3 to 56 times more concentrated than the thioethers together. Since they only partly dissociate (pK_a 's of 2.28 and 9.21 for MET and 2.44 and 8.75 for MTC respectively [13,14]), and their acidic dissociation is further hindered in the presence of HClO_4 , their contribution to the total acidity and to the ionic strength, was always 1.6 % or less and could be neglected as well. With the concentration of the perchloric acid being kept the same throughout the measurements, we concluded that the constancy of the total ionic strength was sufficiently well achieved.

Further support for this decision was found by analyzing the effect of the ionic strength on the two individual reactions. Some data acquired under the same conditions as in the previously published studies and listed in Table 1 were of help in this regard. The numbers given are averages of two to three separate measurements. The errors, here and elsewhere in the paper correspond to the standard error. The individual pseudo-first order constants were obtained by the means of the least square method, from plots of the type $\ln(A_{350\text{nm}} - A_{\infty,350\text{nm}})$ vs. time, which showed good linearity (R between 0.9916 and 0.9999) over conversion regions from 5 to 90 %.

It can be seen that little change in the apparent rate constants is found in the sufficiently large range of ionic strengths covered by these measurements. The small differences are probably due to the ionic equilibria that involve the reaction participants prior to the rate determining step of the reaction (secondary salt effect). Such effects are often found to accompany the acid/base catalyzed reactions in solution.

The main group of recorded data refers to measurements of the mixtures, collected under the chosen work conditions. Also, for each varied substrate, a set at zero concentration of the other was obtained. Table 2 lists the average results of three individual runs performed in each case.

Table 1. Average k_{obs} values as a function of the ionic strength for MTC and MET oxidations by Cr(VI) (NaClO_4 added for MTC and NaNO_3 for MET).

Experimental conditions:			
$10^{-4} \text{ mol}\cdot\text{l}^{-1} \text{ Cr(VI)}; 0.012 \text{ mol}\cdot\text{l}^{-1} \text{ MTC}; 0.257 \text{ mol}\cdot\text{l}^{-1} \text{ HClO}_4; 333.0 \pm 0.1 \text{ K};$		$10^{-4} \text{ mol}\cdot\text{l}^{-1} \text{ Cr(VI)}; 0.0075 \text{ mol}\cdot\text{l}^{-1} \text{ MET}; 0.085 \text{ mol}\cdot\text{l}^{-1} \text{ HClO}_4; 298.0 \pm 0.1 \text{ K}$	
$j \text{ (mol}\cdot\text{l}^{-1})$	$k_{\text{obs,MTC}} \text{ (10}^{-3} \text{ s}^{-1})$	$j \text{ (mol}\cdot\text{l}^{-1})$	$k_{\text{obs,MET}} \text{ (10}^{-3} \text{ s}^{-1})$
0.257	7.95 ± 0.15	0.085	1.35 ± 0.02
0.437	8.70 ± 0.50	0.170	1.28 ± 0.04
0.642	8.25 ± 0.55	0.255	1.31 ± 0.03
0.848	9.23 ± 0.58	0.340	1.23 ± 0.03
1.028	9.60 ± 0.10	0.426	1.17 ± 0.05

Table 2. Average pseudo-first order rate constants for different sets of MET and MTC concentrations, at 298 K, $10^{-4} \text{ mol}\cdot\text{l}^{-1} \text{ Cr(VI)}$ and $0.085 \text{ mol}\cdot\text{l}^{-1} \text{ H}^+$ (HClO_4).

$[\text{MET}] / 10^{-3} \cdot \text{mol}\cdot\text{l}^{-1}$	$[\text{MTC}] / 10^{-3} \cdot \text{mol}\cdot\text{l}^{-1}$									
	0	1.5	3.0	4.5	6.0	7.5	9.0	12	15	18
	$k_{\text{obs}} \text{ (exp)} / 10^{-3} \text{ s}^{-1}$									
0		0.38	0.74	0.90	1.21	1.49	1.59	1.85	2.32	
		\pm								
		0.01	0.01	0.03	0.01	0.05	0.02	0.03	0.10	
1.5		0.32	0.78	0.99	1.02	1.27	1.47			
		\pm	\pm	\pm	\pm	\pm	\pm			
		0.01	0.02	0.03	0.02	0.01	0.06			
3.0		0.66	1.06	1.28	1.31	1.45	1.52	1.79	2.17	
		\pm								
		0.01	0.01	0.03	0.04	0.05	0.07	0.06	0.11	
4.5		0.86	1.23	1.25	1.44	1.88	1.82			
		\pm	\pm	\pm	\pm	\pm	\pm			
		0.01	0.02	0.02	0.01	0.05	0.01			
6.0		1.15	1.45	1.55	1.69	1.89	2.01	2.00	2.14	2.75
		\pm								
		0.01	0.02	0.03	0.01	0.03	0.01	0.10	0.10	0.05
7.5		1.30	1.50	1.73	1.91	1.97	2.10			
		\pm	\pm	\pm	\pm	\pm	\pm			
		0.02	0.03	0.01	0.01	0.01	0.05			
9.0		1.85		1.94		2.21		2.46	2.75	
		\pm		\pm		\pm		\pm	\pm	
		0.04		0.09		0.04		0.20	0.09	
12		2.22		2.32		2.69		2.55	2.43	
		\pm		\pm		\pm		\pm	\pm	
		0.09		0.04		0.14		0.16	0.10	
15		2.67								
		\pm								
		0.02								
18		2.95				3.06				
		\pm				\pm				
		0.11				0.11				

Individual kinetic response. Kinetic parameters

Figure 1 illustrates the non-linear behaviour of the rate constants when the substrates are oxidized individually, with a slight tendency of levelling of. This feature corresponds to the previous findings [8,9].

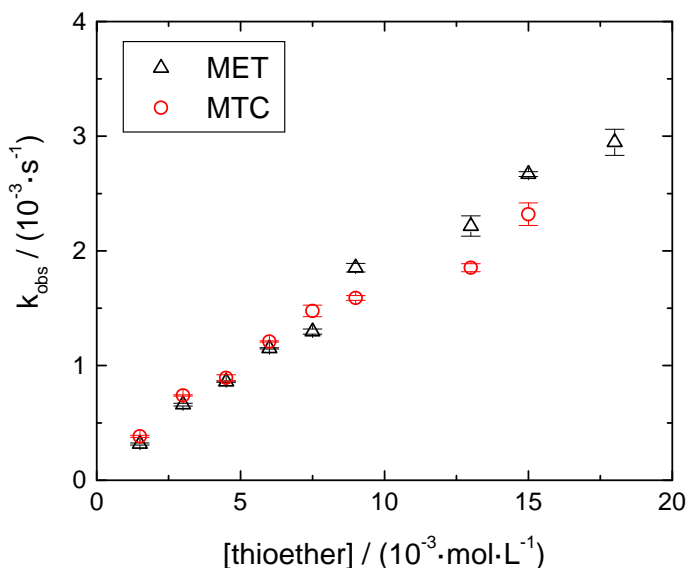


Figure 1. The non-linear increase of the rate constants with the concentration, for the two series of measurements of individual thioethers.

Based on equations 3 and 4, the data in Figure 1 were used to obtain plots of the form $1/k_{\text{obs}}$ vs. $1/[\text{thioether}]$. They were expected to be linear and indeed they were, indicating that the previously given mechanisms hold. The corresponding linear equations are:

$$\frac{1}{k_{\text{obs,MET}}} = \frac{1}{k_{\text{MET}} K_{\text{MET}} [\text{H}^+]^2} \frac{1}{[\text{MET}]} + \frac{1}{k_{\text{MET}} [\text{H}^+]} \quad (5)$$

$$\frac{1}{k_{\text{obs,MET}}} = (4.59 \pm 0.07) \frac{1}{[\text{MET}]} + (84 \pm 21); \quad R = 0.9967 \quad (5')$$

and:

$$\frac{1}{k_{\text{obs,MTC}}} = \frac{1}{k_{\text{MTC}} K_{\text{MTC}} [\text{H}^+]^2} \frac{1}{[\text{MTC}]} + \frac{1}{k_{\text{MTC}} [\text{H}^+]}; \quad (6)$$

$$\frac{1}{k_{\text{obs,MTC}}} = (3.57 \pm 0.07) \frac{1}{[\text{MTC}]} + (229 \pm 20); \quad R = 0.9960 \quad (6')$$

The parameters in the equations 5' and 6' were determined using all the individual rate constants obtained from the experimental runs, rather than the averages listed in Table 2. From these, the respective rate and equilibrium constants for the two substrates under the current reaction conditions were computed. The extracted values are listed in Table 3, as compared with the literature ones.

Table 3. Computed values for the rate and equilibrium constants of the two thioethers, at 298 K, except for those marked with *, that correspond to 333 K.

	MET		MTC	
	k_{MET} ($\text{l}\cdot\text{mol}^{-1}\cdot\text{s}^{-1}$)	K_{MET} ($\text{l}^2\cdot\text{mol}^{-2}$)	k_{MTC} (s^{-1})	K_{MTC} ($\text{l}^2\cdot\text{mol}^{-2}$)
Litt. [8,9]	0.131 ± 0.023	224 ± 45	* 0.097 ± 0.028	* 29.0 ± 7.5
This work	0.141 ± 0.035	214 ± 56	0.0044 ± 0.0004	756 ± 80

For DL-methionine the numbers are in very good agreement within the limits of the experimental errors. This comes to support further the finding that the ionic strength has little influence on the rate of this reaction.

In the case of S-methylcysteine, the comparison is not possible unless the activation energy for the electron transfer process and the free enthalpy for the intermediate formation equilibrium are known. Instead, the k_{MTC} values in Table 3 were used to estimate the activation parameters (E_a , $\ln A$, ΔH^\ddagger , ΔS^\ddagger) for the electron transfer step. These are: $73 \pm 10 \text{ kJ}\cdot\text{mol}^{-1}$, 24 ± 8.8 , $70 \pm 10 \text{ kJ}\cdot\text{mol}^{-1}$ and $-54 \pm 33 \text{ J}\cdot\text{mol}^{-1}\cdot\text{K}^{-1}$ respectively.

Kinetic response to simultaneous oxidation

With the individual reaction constants established, the evaluation of the mixtures is now possible, with the objective of developing a method to predict the concentrations of the two thioethers in an unknown mixture, based on the experimentally determined array of data. The observed rate constants found for the various mixtures and given in Table 2 are shown as well in the 3D representation of Figure 2.

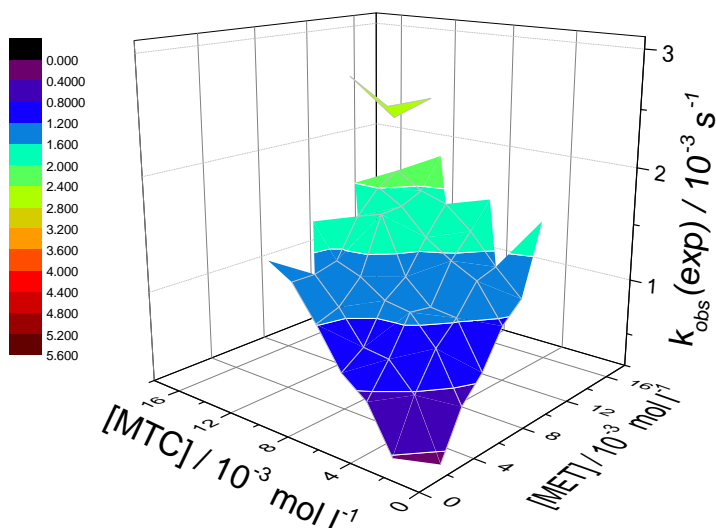


Figure 2. 3D surface plot of the experimental rate constants obtained for mixtures of MTC and MET.

Theoretical predictive models

One way to approach the task is by looking for a theoretical predictive model based on the available information for the individual compounds. Since no second molecule of this compound is expected to participate in the rate determining step or before, the two substrates could be assumed to react completely independently of each other. Therefore, the simple addition of the two terms in equations 3 and 4 was considered first. By using the values of the rate and equilibrium constants for the single-thioether experiments, it was possible to create a prediction, $k_{\text{obs}}(\text{calc})$, as a function of the two concentrations [MET] and [MTC] (equation 7).

$$k_{\text{obs}}(\text{calc}) = \frac{a_1[\text{MET}]}{1 + a_2[\text{MET}]} + \frac{a_3[\text{MTC}]}{1 + a_4[\text{MTC}]} \quad (7)$$

Here the parameters a_1 to a_4 are given as $a_1 = k_{\text{MET}} \cdot K_{\text{MET}} \cdot [\text{H}^+]^2$, $a_2 = K_{\text{MET}} \cdot [\text{H}^+]$, $a_3 = k_{\text{MTC}} \cdot K_{\text{MTC}} \cdot [\text{H}^+]$ and $a_4 = K_{\text{MTC}} \cdot [\text{H}^+]$, respectively.

COMBINED KINETIC RESPONSE OF TWO SUBSTRATES WITH SIMILAR REACTIVE PATTERNS

A 3D plot corresponding to this model is shown in Figure 3 (a) together with the difference between the predicted values and the average of the experimental ones (Figure 3 (b)), expressed as a percentage of the experimental value. The latter has been defined as:

$$\Delta k_{\text{obs}} = \frac{k_{\text{obs}}(\text{exp}) - k_{\text{obs}}(\text{calc})}{k_{\text{obs}}(\text{exp})} \cdot 100\% \quad (8)$$

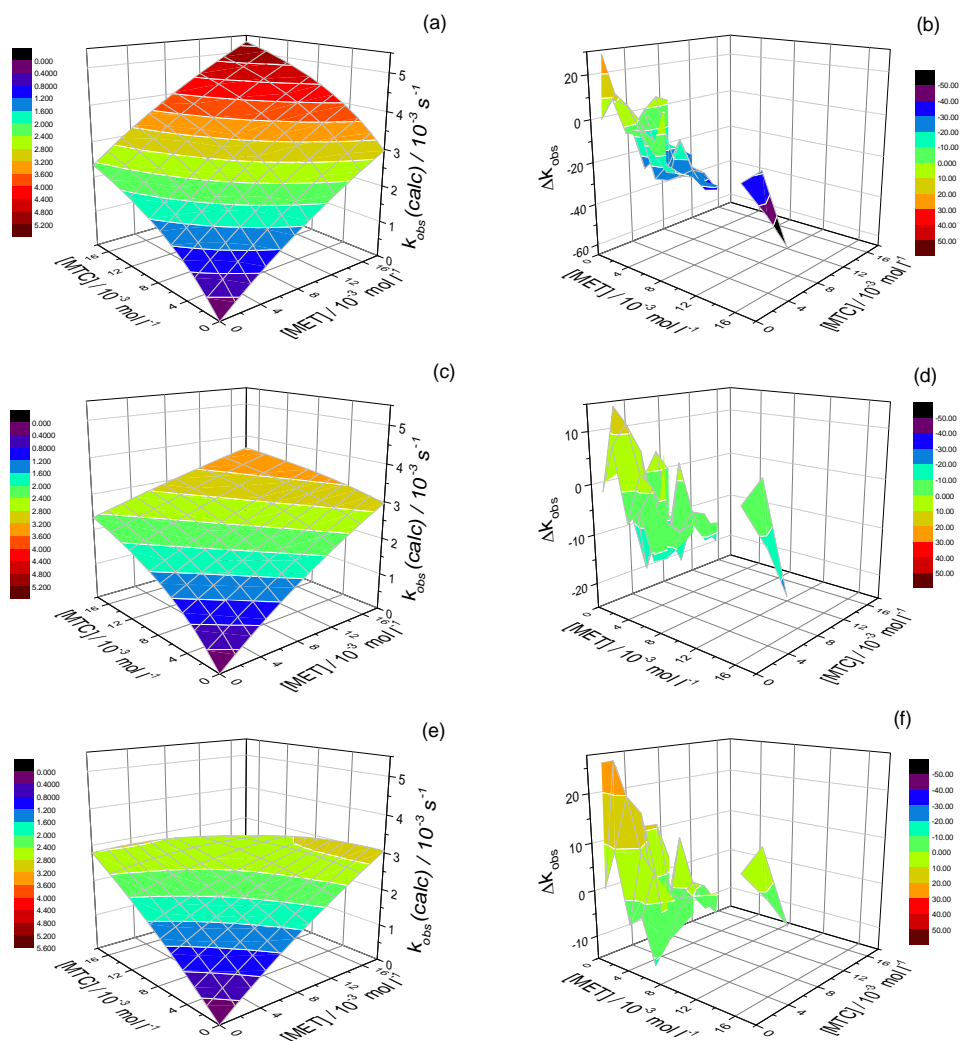


Figure 3. Surface plots for the theoretical models based on the parallel reactions rate law according to equations 7 (a) and 10 (c), as well as for the empirical model based on equation 11 (e). Corresponding plots of the percent differences between each model and the experiment (the data in Figure 2) are shown in (b), (d) and (f).

To provide a better visualisation, the plots of Δk_{obs} have been rotated about the z-axis of the coordinate system. It is clear that as both concentrations increase, the model overestimates the value of $k_{\text{obs}}(\text{exp})$ to a higher and higher degree. In other words, the experimentally investigated mixtures show overall rate constants which are significantly smaller than the simple addition model would predict.

Indeed, it comes as no great surprise that this model should not work adequately, since it does not take properly into account the fact that the analytical signal from which the pseudo-first order rate constants are obtained reflects in fact the overall consumption of all the Cr(VI) species.

Therefore, a second, improved theoretical model was obtained by writing the mass balance of the total Cr(VI) (equation 9) and solving the rate law equation for the two parallel processes while also taking this into account.

$$[\text{Cr}^{\text{VI}}]_{\text{total}} = [\text{HCrO}_4^-] + [\text{Adduct}_1] + [\text{Adduct}_2] \quad (9)$$

Note that this follows the same approach as the one used when deriving the equations 3 and 4, from which the electron transfer and equilibrium constants of the two individual processes were computed. With this, we obtained equation 10, where the parameters a_1 to a_4 are the same as in equation 7.

$$k_{\text{obs}}(\text{calc}) = \frac{a_1[\text{MET}] + a_3[\text{MTC}]}{1 + a_2[\text{MET}] + a_4[\text{MTC}]} \quad (10)$$

As it is seen from the corresponding representations in Figure 3 (c and d), this approach delivers a much better estimate of the experimental constant. At very low concentrations, the model underestimates somewhat the results of the experiments, whereas at very high concentrations the opposite is true. However, especially at high concentrations the discrepancy between experiment and calculation is much less than in the previous model.

Of course, since the predicted k_{obs} values are based only on the two sets of data describing the individual oxidations of the thioethers, an increased number of measurements from which to obtain more accurate estimates of the rate and equilibrium constants would benefit the predictions.

Empirical model

In addition to the theoretical predictive models, a more empirical approach to analysing the mixture exists. By choosing a mathematical equation which describes the experimental data adequately, it is possible to create a 3D calibration surface which allows the prediction of the rate constant

for any given mixture by interpolation, provided that the concentrations used for this mixture are within the ranges of those originally used to determine the calibration surface. The equation that was used in the present case with the better results is given below (equation 11) and is an adaptation of equation 7 by the addition of a concentration cross-term. Note that the terms in an empirical equation are not required to have a physical meaning, but are simply meant to describe the data as accurate as possible.

$$k_{\text{obs}}(\text{calc}) = \frac{b_1[\text{MET}]}{1+b_2[\text{MET}]} + \frac{b_3[\text{MTC}]}{1+b_4[\text{MTC}]} + \frac{b_5[\text{MET}][\text{MTC}]}{1+b_6[\text{MET}][\text{MTC}]} \quad (11)$$

The coefficients b_1 to b_6 were calculated using all the experimental data in MATLAB, were there used the averages of the individual values. The calculated surface is shown in Figure 3 (e) and the corresponding values of the coefficients are listed in Table 4.

Table 4. The values of coefficients b_1 to b_6 in equation 11.

Coefficient	b_1 l mol ⁻¹ s ⁻¹	b_2 l mol ⁻¹	b_3 l mol ⁻¹ s ⁻¹	b_4 l mol ⁻¹	b_5 l ² mol ⁻² s ⁻¹	b_6 l ² mol ⁻²
Value	0.213	14.165	0.194	13.973	-10.633	-19.981

In comparison to the two theoretical models, the empirical equation produces a particularly good fit at all but the lowest concentration (Figure 3 (f)). This is not surprising as it is based on a larger sample of data points than the theoretical models. In turn, one disadvantage of such empirical models is that they are strictly valid within the limits of the region covered by the experiments which generated them.

Application of the models to unknown mixtures

Once an acceptable surface is obtained, it may be used to investigate mixtures of the two thioethers where the concentrations of the individual components are unknown. A single measurement would not be sufficient to find both their concentrations, as the $k_{\text{obs}}(\text{exp})$ determined would correspond to an infinite number of concentration pairs along the level curve which corresponds to that particular value on the surface.

However, with the inclusion of a single additional measurement, the unknown concentrations can be determined, on the condition that the change in concentrations between the two measured mixtures is known. Two possible ways of achieving this are adding to the original mixture a

predetermined amount of one of the two components or diluting the mixture, for instance to half of the original concentrations, with an appropriate solution (e.g. a buffer or a solution of equal acidity).

Once the $k_{\text{obs}}(\text{exp})$ of this second mixture is known, a second infinite group of concentration pairs corresponding to this value is obtained (a second level curve). Since the surface is asymmetric in the two concentration parameters, something which is common for all three discussed models, as well as nonlinear, no pair of level curves can be “parallel”. Thus, there must be a unique solution that fits the change in $k_{\text{obs}}(\text{exp})$ at a given change in the concentrations.

It should be noted that for particularly large values of $k_{\text{obs}}(\text{exp})$ for the original mixture, it may be more appropriate to use the predictive model based on equation 10, with a physical meaning, rather than the better fitting empirical model, as there is a possibility that at least one of the compounds has a concentration which lies outside of the limits of the calibration surface.

CONCLUSIONS

As far as the insight into the individual reaction mechanisms of the two substrates goes, in the light of the new measurements the original findings do hold. Moreover, the new rate and equilibrium constants computed for DL-methionine are in very good agreement with the previously determined ones in the same temperature and acidity conditions, but different ionic strength. This is in line with the findings that the ionic strength does not have any strong effect upon the reaction rates of the two substrates in the investigated region. For S-methylcysteine, by pairing the results in this work with the literature data, it was possible to give an estimation of the thermodynamic parameters.

In mixture, the two thioethers are oxidized in parallel. Two versions of theoretical predictive models were tested against the experimental data. They were developed based on the rate law equation derived for the system of two parallel reactions and on the kinetic parameters obtained for the individual oxidations of the two substrates from the measurements of non-mixtures. Of the two models, the version that reflects the evolution of the total chromium VI concentration through the experimentally monitored parameter – the absorbance – is giving the best results, but they can only be as good as the accuracy of the estimated rate and equilibrium constants for the two individual thioethers oxidations are.

An alternative, empirical model was tested with somewhat better results. This was expected, due to the fact that its construction was based on all the available data for mixtures and non-mixtures together. However, its

application for any data belonging to unknown mixtures is limited to those that fall within the range covered by the experiments.

Even though the mechanistic patterns of the oxidations of the two substrates are quite similar, due to the differences in the individual rate constants for the two reactions, either type of model generates asymmetrical surfaces. From these, the univocal determination of the concentrations of the two thioethers is possible without separation, from only two measurements, if at least one of the species is varied by a known amount.

EXPERIMENTAL SECTION

All the reagents were of analytical purity (Merck, Aldrich) and used as received. The solutions were always prepared in demineralised and tetradistilled water (Infusion Solutions Laboratory, "Iuliu Hațieganu" University of Medicine and Pharmacy, Cluj-Napoca). Fresh batches of stock solutions of the two thioethers were prepared before each set of measurements and checked spectrophotometrically. The concentration of HClO_4 stock solution was verified by titration with NaOH solution of known factor. The aqueous stock solution of Cr(VI) was always $4 \cdot 10^{-4} \text{ mol} \cdot \text{l}^{-1}$.

In the reaction mixture, the oxidant (chromium VI) was always the reactant in the lowest concentration (the limiting component; $10^{-4} \text{ mol} \cdot \text{l}^{-1}$). The addition of an inert mineral acid (HClO_4) served to provide acidic conditions. The concentrations of the thioethers and hydrogen ions were always chosen so that pseudo-first order behaviour with respect to the chromium species was ensured. This meant a 10-fold or higher excess over the chromium VI for the thioethers and always a 212.5-fold one for the acid (taking into account the respective of 1.5 to 1 and 4 to 1 stoichiometric ratios). The total chromium concentration and acidity level were chosen such that they fell in the appropriate range, allowing that, prior to reaction, virtually all Cr(VI) was in the HCrO_4^- form [15-17]).

Spectrophotometry was employed as the main analytical tool for monitoring the reaction progress, since Cr(VI) has a well-defined absorption maximum at 350 nm, where none of the thioethers absorb. A Jasco V-530 UV/VIS spectrophotometer ("Jasco", Japan), equipped with automatic data acquisition software was used. The temperature was kept at $298.0 \pm 0.1 \text{ K}$, controlled by the means of a Lauda – M16 ("Lauda", Germany) thermostat directly connected to the cell holder.

Prior to use, all the stock solutions were kept inside the water tank of the thermostat, at the work temperature. The reaction was initiated by fast injection of 4 ml of $4 \cdot 10^{-4} \text{ mol} \cdot \text{l}^{-1}$ Cr(VI) solution over a 12 ml mixture of the other reactants already placed in a 5 cm path length quartz cuvette and the

acquisition program was simultaneously started. The mixing time did not exceed 0.5 s. Data was collected every 1 or 2 seconds, for a total of 1200 s or 2400 s respectively. The residual absorbance (A_{∞}) was measured after 24 hours from the start of the reaction. Three replicate measurements were made for each set of experimental conditions.

The Excel (Microsoft), Origin (OriginLab Corporation, USA) and MATLAB (MathWorks) programs were utilized to process the data. The pseudo-first order constants were computed by the method of least squares.

ACKNOWLEDGMENTS

The funding of the Romanian Government through UEFISCDI project “Pro-active operation of cascade reservoirs in extreme conditions (floods and droughts) using a Comprehensive Decision Support Systems (CDSS). Case study: Jijia catchment”, PN-II-PT-PCCA-2011-3-3.2-0344, contract 15/2012 is gratefully acknowledged.

The authors would also like to thank Assoc. Prof. Dr. Eng. Árpád Imre-Lucaci for developing the MATLAB program employed to determine the b_i parameters of the empirical equation (11) and Ph.D. Erzsébet-Sára Bogya for assistance with collecting part of the experimental data.

REFERENCES

1. D. Pérez-Bendito, M. Silva, “Kinetic Methods in Analytical Chemistry”, E. Horwood, **1988**.
2. H.A. Motolla, D. Pérez-Bendito, *Analytical Chemistry*, **1994**, 66, 131R.
3. N. Radić, L. Kukoc-Modun, “Kinetic Methods of Analysis with Potentiometric and Spectrophotometric Detectors – Our Laboratory Experiences”, in *Analytical Chemistry, InTech*, **2012**, chapter 3 and references therein.
4. H.B. Mark Jr. “Kinetic Methods of Analysis”, in *AccessScience*, McGraw-Hill Education, **2014**.
5. I. Bâldea, D.-M. Sabou, *Studia UBB Chemia*, **2001**, 46(1-2), 17 and references therein.
6. D.-M. Sabou, I. Bâldea, *Studia UBB Chemia*, **2013**, 58(4), 81.
7. D.-M. Sabou, *Studia UBB Chemia*, **2014**, 59(4), 183.
8. A. Csavdari, I. Bâldea, D.-M. Sabou, *Studia UBB Chemia*, **2007**, 52(3), 113.
9. I. Bâldea, D.-M. Sabou, A. Csavdari, *Studia UBB Chemia*, **2007**, 52(1), 19.
10. A. Levina, P.A. Lay, *Inorganic Chemistry*, **2004**, 43, 324.

11. A. Levina, L. Zhang, P.A. Lay, *J. Am. Chem. Soc.*, **2010**, *132*, 8720 and references therein.
12. J.F. Perez-Benito, D. Lamrhari, C. Arias, *Canadian Journal of Chemistry*, **2011**, *72(7)*, 1637.
13. R.M.C. Dawson, "*Data for Biochemical Research*", Oxford: Clarendon Pres, **1959**.
14. J.T. Edsall, J. Wyman, *Biophysical Chemistry*, Volume 1, Academic Press, New York, **1958**.
15. N.N. Greenwood, A. Earnshaw, "Chemistry of the Elements", 2nd Edition, Butterworth-Heinemann, Oxford, **1997**, chapter 23.
16. J.D. Ramsey, L. Xia, M.W. Kendig, R.L. McCreery, *Corrosion Science*, **2001**, *43*, 1557.
17. J.D. Neuss, W. Rieman III, *Journal of the American Chemical Society*, **1934**, *56*, 2238.

MODIFIED RAW MATERIALS: SYNTHESIS, CHARACTERIZATION AND APPLICATION FOR Cd²⁺ IONS REMOVAL

GULZIYA A. SEILKHANOVA^{a*}, AINUR N. IMANGALIYEVA^a,
DINA N. AKBAYEVA^a, ZHANNA ZH. KENZHALINA^a

ABSTRACT. The adsorption behavior of some lowcost adsorbents such as bentonite, meal thistle and carbonized walnut husk with respect to Cd²⁺ ions in aqueous solutions has been studied. The several process parameters (contact time, initial metal concentration, sorption capacity, extraction degree, rate constants, sorption rates and sorption energy) were found. For the Cd²⁺ ions adsorption the equilibrium time onto bentonite, meal thistle and carbonized walnut husk were found to be 2 h, 25 and 10 min, respectively. Adsorption parameters were determined using both Langmuir and Freundlich isotherms. Sorption isotherms of cadmium ions onto MBT (modified bentonite) and MTM (modified thistle meal) were the best of all described by the equation of Freundlich sorption (correlation coefficients are closest to unit). In contrast the sorption of Cd²⁺ ions onto MCWH (modified carbonized walnut husk) was described by the Langmuir isothermic model where the adsorption occurs on homogeneous surface by monolayer sorption without interaction between sorbed ions. The obtained results demonstrate that bentonite, meal thistle and carbonized walnut husk can remove Cd²⁺ ions from aqueous solutions. It means that cheap and available raw materials can be efficient adsorbents and capable to remove cationic heavy metal species from waste water. The ion-exchange mechanism of adsorption of cadmium ions by the MBT, MTM, MCWH was proposed.

Keywords: sorption, Cd, bentonite, meal thistle, carbonized walnut husk, kinetics.

^a Al-Farabi Kazakh National University, Faculty of Chemistry and Chemical Technology, 71 Al-Farabi av., 050040 Almaty, Kazakhstan

* Corresponding author: g_seilkhanova@mail.ru

INTRODUCTION

Excessive release of heavy metals into the environment due to industrialization and urbanization has posed a great problem worldwide. Unlike organic pollutants, the majority of which are susceptible to biological degradation, heavy metal ions do not degrade into harmless products. The presence of heavy metal ions is of major concern due to their toxicity to many life forms. Cadmium also exposes human health to severe risks, as it can provoke cancer, kidney damage, mucous membrane destruction, vomiting, bone damage as well as affect the production of progesterone and testosterone [1, 2]. That is why one of modern priority tasks in the field of environment protection is search of effective and environmental friendly technologies of sewage treatment.

Nowadays for removing of dissolved heavy metals the numerous processes, including ion exchange, precipitation, phytoextraction, ultrafiltration, reverse osmosis and electrodialysis exist [3]. Among them, ion exchange techniques using solid adsorbents is a promising method for treating wastewater, owing to its advantages such as operational simplicity, low cost, availability in large amount and ability to treat pollutants in a sufficiently large scale operation [3, 4]. The use of sorbents based on natural, synthetic and modified aluminosilicates can serve as a base for new technology development of heavy metal adsorption. The aluminosilicates of two-dimensional structure clay minerals (montmorillonite, vermiculite, bentonite) and three-dimensional structure of natural and synthetic zeolites as sorbents are already widely used [5, 6].

East Kazakhstan has rich deposits of bentonite clays which are suitable for sorption of heavy metal ions. Because of their availability and rather low cost the production of sorbents is economically profitable [7]. It was shown [8, 9] that the sorption processes performed by montmorillonite occurs according to the following three mechanisms:

a) substitution by cations of the exchange cationic complex locating as an between the elementary layers, and on the basal surface of mineral particles;

b) usage of hydrogen bonds of the external hydroxyl groups;

c) usage of valence "disrupted" bonds at the edges and corners, on the shifted stages of montmorillonite crystal growth.

Vegetable materials accumulating in significant quantities as various waste products in pulp and paper industry, agriculture, confectionery have of practical interest as a raw material for sorbents preparation. They can be used for solving some environmental problems such as purification of waste water, gas emissions and soil [10].

Sorbents on the basis of waste from vegetable raw materials can become even more available and cheap alternative. For the elimination of heavy metals from waste water the low cost agricultural rest by-products such as rice husk [11], nutshell [12], coconut husk [13] have been investigated by various research groups. To increase the adsorptive capacity of sorbents during processing raw plant material the various methods such as mechanical, physical, chemical methods, including thermal treatment of raw materials are used [14-18]. The effect of heat treatment of the rice husk on the adsorbent capacity of sorbents towards to Fe(III), Cu(II), Cd(II), Pb(II) ions in solution have been studied [19]. Cost is an important parameter for comparing the sorbent materials [20]. Improved sorption capacity may compensate the cost of additional processing. There is an urgent need that all possible sources of agro-based inexpensive adsorbents should be explored. Their feasibility for the removal of heavy metals should be studied in detail.

In this paper, a novel non-modified (bentonite (BT), thistle meal (TM), carbonized walnut husk (CWH)) and modified (MBT, MTM and MCWH) sorbents were developed and used to remove Cd(II) from aqueous solution. The choice of metal ion is explained that Cd(II) ions are the most widespread and dangerous on toxicity degree as pollutant. Also, the possibility of usage of low-cost adsorbents for removal of heavy metals from aqueous solution was found. The chemical composition of TM and CWH was determined using the X-ray phase analysis. The morphology of BT, MBT, TM, MTM and MCWH was characterized by scanning electron microscopy (SEM). The adsorption performance of Cd(II) onto MBT, MTM and MCWH was investigated. The adsorption conditions pH value, adsorption time and initial concentration were investigated in detail. The adsorption isotherms and adsorption kinetics were discussed.

RESULTS AND DISCUSSION

Characterization of sorbents

Figure 1 presents the typical SEM images of non-modified BT, TM, WHC and modified sorbents MBT, MTM and MCWH. Non-modified BT, TM, (Fig. 1 a, c, e) had a substantially uniform texture provided predominantly by micropores with diameter in the range of 1-4 μm . From the SEM images, the modified sorbent has a developed microporous structure, an increase of pores size in comparison with the non-modified sorbents. As a result of acid-base modification, the surface structure of TM is changed, possibly due to the formation of Na-O groups. The surface morphology indicates that the BT and TM are easily modified after the acid-base treatment, washing and drying

procedures. The surface of MCHW particles underwent to profound changes (Fig. 1 e, f) after carbonization and mechanical activation to comparison with CHW, which had the ordered macroporous structure.

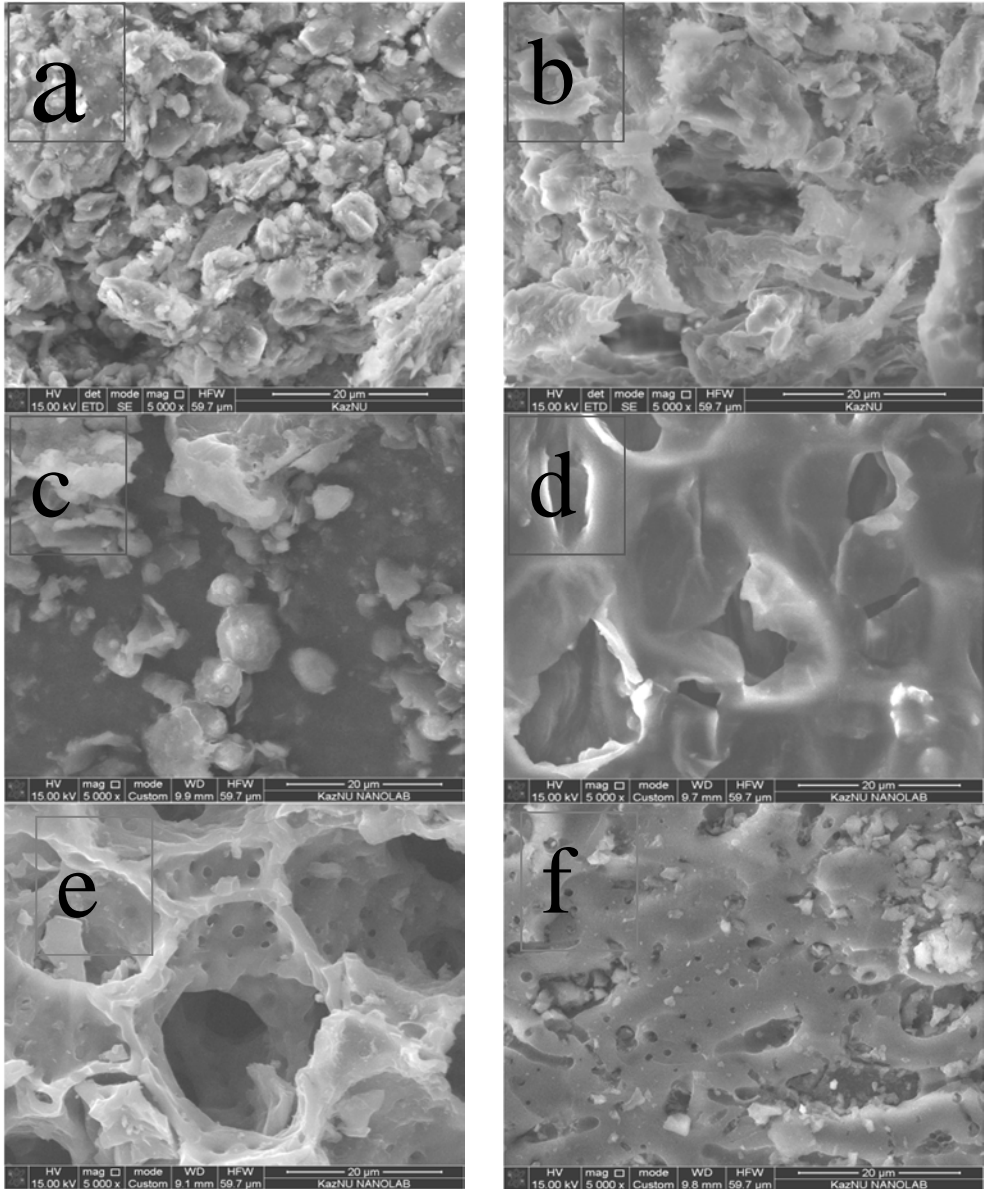


Figure 1. SEM images of non-modified and modified sorbents: (a) BT, (b) MBT, (c) TM, (d) MTM (e) CWH and (f) MCWH.

Adsorption of Cd ions by modified sorbents

Effect of total contact time

The effect of total contact time on the adsorption of Cd(II) ions by MB, MTM, MCWH was investigated at 25°C in the time range 15-180 min and the results were presented in Fig. 2. It can be seen that the capacity of MB, MTM and MCWH for Cd²⁺ ions was depended from contact time. The adsorption of MB, MTM, MCWH for Cd(II) ions increased sharply during the first 15 min and then tended to be equilibrium. It can be seen from Fig. 2, that the values of adsorption capacity of Cd(II) were 61, 50, 95%, respectively. So, the sorption equilibrium of MB, MTM, MCWH was set at 120, 25 and 10 min, respectively.

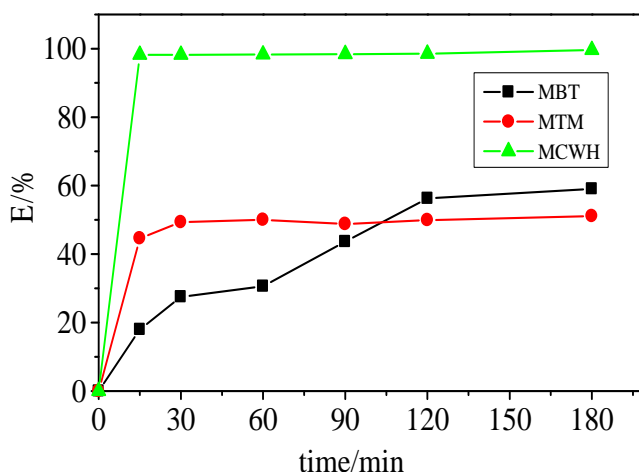


Figure 2. Effect of total contact time on the adsorption of Cd(II) by MBT, MTM, MCWH at 25°C.

Effect of initial concentration of Cd(II) ions

The effect of the initial concentration of Cd(II) ions on the adsorption can be established on the basis of the sorption isotherms. The adsorption of Cd(II) by MB, MTM, MCWH was studied at 25°C in the concentration range 4-9 mg/L while keeping all other parameters constant. The results were presented in Figure 3. The adsorption of MB, MTM, MCWH for Cd(II) ions increased sharply and then gradually tended to be equilibrium. This is in accordance with the observations reported for natural adsorbents, that the adsorption increases with rising initial concentration of heavy metal ions [21, 22].

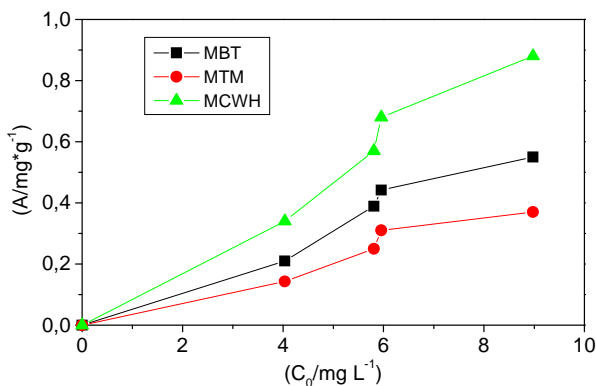


Figure 3. Effect of initial concentration of Cd(II) on the adsorption by MBT, MTM, MCWH at 25°C.

In the case of microporous sorbents, the sorption of metal ions consists of the following stages:

1. Rapid transportation of Cd(II) ions onto the surface of MB, MTM, MCWH;
2. Intraparticle diffusion as the rate-limiting step;
3. Final equilibrium step due to the lower concentration of metal ions in aqueous solution [23].

One of these stages is a limiting factor. To obtain of the rate determining step applies the equation proposed by Weber and Morris [24], which is follows:

$$A = K_p * t^{1/2} \quad (1)$$

where, A is the amount of the metal absorbed (mg/g) at time t and K_p is the interparticle diffusion rate constant.

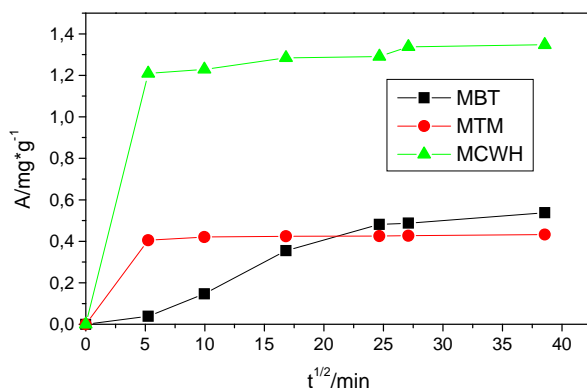


Figure 4. Plots for intra particle diffusion for Cd (II) adsorption by MBT, MTM, MCWH at 25°C.

The plots of A versus $t^{1/2}$ (Fig.4) are not linear over the entire time range, indicating that more than one process is affecting the adsorption. This type of non-linearity has been reported previously by various authors [25, 26] and has been interpreted as showing that both boundary layer diffusion (the initial curved portion) and intra-particle diffusion (the final linear portion) are occurring.

Adsorption kinetics

The kinetics of metal ions sorption by modified sorbents MBT, MTM, MCWH was studied for its possible importance in treatment of metal-bearing industrial effluents. In the present study, pseudo-first-order and pseudo-second-order kinetic models were employed to test the experimental data [27, 28]. The pseudo-first-order and pseudo-second-order models are respectively described by the following equations:

$$\ln(C_0 - C_x) = \ln C_0 - k_1 t \quad (2)$$

$$\ln \frac{C_x^a}{C_x^b} = -\ln \frac{C_0^b}{C_0^a} + k_2 (C_0^a - C_0^b) t \quad (3)$$

where C_0 and C_x are the quantities of adsorbate adsorbed on the adsorbents at the beginning and time t (mg/g), respectively; k_1 (min^{-1}) and k_2 ($\text{L mg}^{-1} \text{min}^{-1}$) are the rate constants of pseudo-first-order and pseudo-second-order models, respectively.

The kinetic data were linearized using the pseudo-first-order and pseudo-second-order models, and plotted between $\ln(C_0 - C_x)$ versus t and $\ln \frac{C_x^a}{C_x^b}$ versus t , respectively.

For definition of kinetic characteristics, such as energy of activation and rate constant, the sorption was carried out at 25 and 35°C for definition of temperature influence. The obtained results are presented in Table 1. As the sorption is exothermic process, the increase in temperature leads to shifting of equilibrium towards the desorption. Data in Table 1 shows that rise of temperature has negative impact on the sorption of Cd(II) ions.

As the adsorption process is exothermic [29], so that with increasing temperature the equilibrium shifts towards reagents, i.e. amplifies desorption process, which is likely to lead a reduction the rate of the direct reaction - sorption of metal ions.

The results given in Table 1 show that, for all sorbents the correlation coefficients values for pseudo-second-order model were much lower than those obtained using the pseudo-first-order model. Thus, it means that the pseudo-first-order model explains the kinetic process better. As seen from the Table 1, the highest rate of sorption is inherent to MTM.

Table 1. Kinetic parameters for the adsorption of Cd(II).

Sorbent	t (°C)	c ₀ (mg L ⁻¹)	Pseudo-first order model		Pseudo-second order model		E _a (kJ mol ⁻¹)
			k ₁ (min ⁻¹)	R ²	k ₂ (L mg ⁻¹ min ⁻¹)	R ²	
MBT	25	10	0.004	0.913	5.35735·10 ⁻⁷	0.847	-21.95
	35	10	0.003	0.987	2.42080·10 ⁻⁷	0.545	
MTM	25	10	0.013	0.963	1.26761·10 ⁻⁶	0.708	-28.06
	35	10	0.009	0.953	1.27255·10 ⁻⁶	0.895	
MCWH	25	14	0.004	0.998	5.54012·10 ⁻⁶	0.931	-52.89
	35	14	0.002	0.915	6.05081·10 ⁻⁶	0.767	

From Table 1, all the values of E_a were between -21.95 and -52.89 KJ mol⁻¹ for the Cd(II) ions adsorption of MBT, MTM, MCWH, which revealed that both chemisorption and physisorption coexisted during the adsorption processes. The negative sorption energy indicates on decreasing of process rate with temperature increase. This is probably due to the shift of the chemical equilibrium towards the initial components. Consequently, the desorption process is dominated by the metal ions with the surface of the sorbents.

Adsorption isotherms

Adsorption isotherm has a great importance at the description of sorption process. It demonstrates the adsorption as a function of the equilibrium concentration of the adsorbates in solution. Figure 5 shows the adsorption isotherms of Cd(II) onto MBT (a), MTM (b) and MCWH (c) at adsorbent dose 1.0g/100 ml, contact time 180 min, pH 6 and at 25°C. As seen from Fig. 5, the isotherm results indicated a good adsorption capacity of MBT, MTM and MCWH for Cd(II) ions. In additional, the capacity of MBT, MTM and MCWH for Cd(II) ions followed the sequence of MCWH > MBT > MTM. The Langmuir and Freundlich isotherms were used to normalize the adsorption.

The parameters of the Langmuir and Freundlich isotherms were shown in Table 2. The correlation coefficients values (R²) indicated that the adsorption of Cd(II) ions onto MBT and MTM was fitted better by the Freundlich isotherm equation (R² = 0.964–0.974) than the Langmuir isotherm equation (R² = 0.901). Therefore, the adsorption of MBT and MTM of Cd(II) ions can be mainly considered as monolayer adsorption. But the adsorption of Cd(II) ions onto MCWH was fitted better by the Langmuir isotherm equation (R² = 0.964–0.974) than the Freundlich isotherm equation (R² = 0.823).

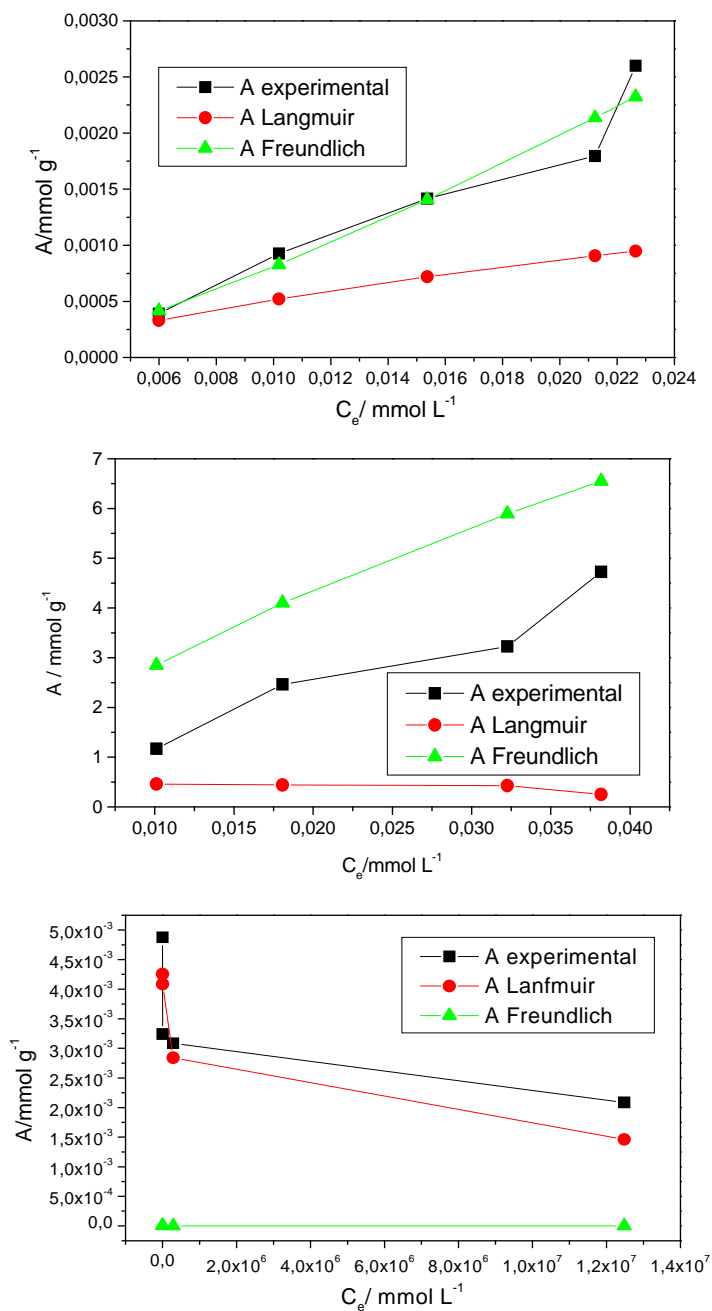


Figure 5. Adsorption isotherms of Cd(II) onto MBT (a), MTM (b) and MCWH (c) at adsorbent dose 1.0g/100 ml, contact time 180 min, pH 6 and at 25°C.

The low correlation coefficients values (R^2) indicate that the surface of adsorbent is non-uniform, between the adsorbed particles interaction takes place, and the active centers are not completely independent from each other.

Table 2. Parameters of adsorption isotherms of Cd^{2+} ions.

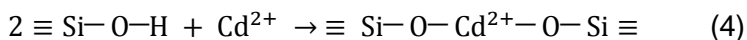
Sorbent	Langmuir isotherm			Freundlich isotherm		
	$K \times 10^3$ (L mmol ⁻¹)	$A_{\infty} \times 10^3$ (mmol g ⁻¹)	R^2	$K \times 10^{-3}$ (L mmol ⁻¹)	1/n	R^2
MBT	0.001	142850.00	0.651	0.196	1.037	0.974
MTM	0.026	5.35	0.822	0.051	0.626	0.964
MCWH	8.170	4.71	0.901	407.380	3.649	0.823

Adsorption mechanism

Sorption by the MBT

It is known that the bentonite clays (BC) are the cheap sorbents for extraction of heavy metals ions [30] and the main mineral, being their part is montmorillonite. The structure of montmorillonite represents layers of silicon-oxygen tetrahedrons between which the aluminium-oxygen octahedrons are concluded. Replacement of Al^{3+} ions by Mg^{2+} and $\text{Fe}^{2+}/\text{Fe}^{3+}$ ions leads to emergence of a structural negative charge which is compensated by interlayered (exchange) cations (Ca^{2+} , Na^+). Montmorillonite has a 2:1 alumino silicate semi-basic unit layer, where 2:1, ratio refers to two tetrahedral sheets sandwiching an octahedral sheet in between. The composition of montmorillonite is presented by the following formula: $(\text{OH})_4\text{Si}_8(\text{Al}_{3.34}\text{Mg}_{0.66})\text{O}_{20}$ [31].

Acid activation of layered silicates is a widespread way of modifying which is necessary for increasing of material porosity [32]. The mechanism of acid processing is reduced to dissolution and washing away of alkaline and the alkaline-earth metals cations (Ca^{2+} , Na^+ , Mg^{2+}) from a mineral framework. Adsorption of cadmium ions the modified bentonite clay of the Dinovavrovoe field (East Kazakhstan) is caused by interaction the silanolic groups with metal ions. Adsorption proceeds on the ion-exchange mechanism which is presented as follows:



Sorption by the MTM

It is known that a component of a thistle meal is cellulose. Cellulose – polysaccharide which molecules are presented in the form of long chains with spatially correct structure, consisting of β-D-glucose (β-D-glucopirane) links connected by glucosidic bonds [33].

Extreme adsorptive capacity of adsorbent is characterized by concentration of carboxyl groups. Carboxyl groups can be present at cellulose, generally because of oxidation of alcohols and carbonyl groups in positions 1,2,3 and 6 of a polysaccharidic chain as a result of isolation and purification of cellulose. The cellulose modified by alkali is characterized by higher reaction ability in comparison with initial object:



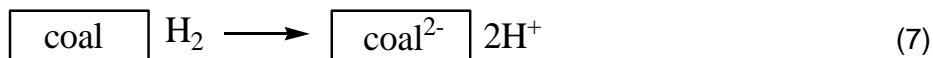
It is agreed with literature data for the cellulose-containing polymeric materials [34]. The obtained sorbent can be classified as cation exchanger. The sorption mechanism of cadmium ions by the modified thistle meal also is ion-exchange with formation of the chelate complexes:



Sorption by the MCWH

Among of the porous carbon materials one of perspective sorbents is the walnut shell. This type of vegetable cellulose is characterized by the high content of carbon, existence by primary transport porous structure and the low maintenance of mineral part. The commercial analogs obtained on the basis of a walnut shell are valuable active coals let out industrially. The most important purpose of application of carbonization process is increase of carbon specific content, removal of easily volatile compounds from composition of initial vegetable cellulose, creation of porous material with the big porosity which is evenly distributed on all material volume. Heat treatment of a walnut shell is resulted by increase available and formation of new pores, merge of two or several pores in one, increase in a surface and volume of pores due to burning out of carbon part.

The chemical nature of a coal surface in many respects defines the extraction extent of heavy metals ions from solutions. Experience shows that coal not only is capable to selective adsorption of metals ions, but also the phenomena of exchange adsorption can proceed on it. It is explained by the electrochemical theory [35]. The surface of coal can absorb hydrogen which is formed during coal production and its activation. At the same time coal behaves as acid adsorbent:



CONCLUSIONS

In summary, MBT, MTM, MCWH were prepared successfully from bentonite of the Dinovavrovoe field, thistle meal and carbonized walnut husk and used as adsorbents for removing Cd(II) from aqueous solutions. Adsorption kinetic and isotherm processes for adsorption of Cd(II) ions onto MBT and MTM were found to correlate with pseudo-first-order model and Freundlich isotherm equation, respectively. Comparison of the regression coefficients R^2 shows that the Freundlich model better describes the experimental data of the adsorption on MBT and MTM. This indicates that the adsorption of Cd(II) occurs on a heterogeneous surface and that the majority of active sites have different quantities of energy. But the adsorption of Cd(II) ions onto MCWH was fitted better by the Langmuir isotherm equation than the Freundlich isotherm equation. This can indicate the applicability of monolayer coverage of Cd ions on the surface of adsorbent. In addition, the capacity of MBT, MTM and MCWH for Cd(II) ions followed the sequence of MCWH > MBT > MTM. Furthermore, energy changes were -21.95 , -28.06 and -52.89 KJ/mol for the Cd(II) ions adsorption of MBT, MTM, MCWH at 25°C , which revealed that the adsorption processes including chemisorption and physisorption were complicated. Negative values of the activation energy are probably associated with the shift of the chemical equilibrium towards the initial components. Consequently, the desorption process is dominated by the metal ions with the surface of the sorbents. Adsorption of cadmium ions by the MBT, MTM, MCWH is characterized by the ion-exchange mechanism. In conclusion, these low cost natural adsorbents show efficiency and selectivity for the removal of Cd(II) ions from aqueous solutions.

EXPERIMENTAL SECTION

Materials and methods

All used chemicals and solvents were of analytical grade quality. Cadmium chloride, ($\text{CdCl}_2 \cdot 6\text{H}_2\text{O}$) was used as source for Cd(II).

Concentration of cadmium ions before and after sorption was monitored by nuclear-absorbing spectrophotometer Shimadzu 6200. Definition of structure changes and morphology of particles surface of a natural sorbents after modification was carried out on a Quanta 200i 3D by the SEM (scanning electronic microscopy). The X-ray phase analysis was performed using computerized diffractometer DRON-2 with the modernized collimation on the filtered CuK α -radiation.

Natural sorbents preparation

Natural sorbents preparation consists of mechanical cleaning of initial raw material and modification of the obtained product.

Preparation of MBT

Bentonite from Dinozavrovoe field (East Kazakhstan) was used, the main characteristics of which are listed in Table 3. As seen from Table 3, BT practically represents monomineral raw material which contains 95% of montmorillonite.

Table 3. Characteristics of BT from Dinozavrovoe field

Physical characteristics	Fraction (mm)	Montmorillonite (%)	Moisture content (%)	Sand (%)	Swelling number (on 2 g)
Value	0,07	90-95	12	1-2	24

In a 500 mL beaker was added 40 g of crude wood sawdust and 200 mL of 4,5-5,5% phosphoric acid. The obtained mixture was kept for 23-25 h at ambient temperature and washed by distilled water until the pH was neutral. Then, the wood sawdust, BT and water were mixed in ratio 2:1:2 and then stirred until the uniform structure suspension was not formed. The final mixture was dried at 80-85°C for 3,5-4 h, then crushed to form a particles of 3-15 mm in size. Obtained MBT was dried in a oven at 90-95°C for 0,75-1 h.

Preparation of MTM

The chemical composition of TM was determined using the X-ray phase analysis, which is listed in Table 4.

Table 4. The chemical composition of TM.

Content, %									
C	O	Mg	Al	Si	P	S	K	Ca	Fe
42,20	53,94	0,44	0,12	0,38	0,38	0,09	1,42	0,75	0,11

The obtained data indicate that TM contains organic substances 42.20% and oxygen 53.94%.

In a 1 L beaker was added 10 g of TM and 500 mL of sodium hydroxide water solution (1 g of NaOH was dissolved). The pH 8 was used. Then, the mixture was heated at 100°C for 30 min and cooled at ambient temperature. The desired pH 5 was adjusted by using aqueous solution of diluted HCl. The obtained product was filtered, washed by distilled water and dried.

Preparation of MCWH

The chemical composition of CWH was determined using the X-ray phase analysis, which is listed in Table 5.

Table 5. Technical and elemental analysis of the CWH.

Technical analysis, %				Elemental analysis, %			
moisture	ash	volatile	C	H	S	N	O
7,2	0,3	76,1	56,4	6,5	0,2	0,3	36,6

As seen from the data listed in Table 5, CWH have a relatively high content of carbon. This indicates that CWH can be a promising porous carbon material as TM.

For preparation of MCWH a walnut husk was used, which is withdrawal of food confectionery production [10]. As the walnut husk had the big sizes therefore at the initial stage before treatment it was crushed. This procedure allows obtain sorbent with high sorption ability and increase its specific surface. In a 200 mL beaker was added 20 g of walnut husk and 100 ml of 10% sulfuric acid. The treatment by sulfuric acid activates a surface and increases the size of a husk pores. The obtained walnut husk was washed by the distilled water. Then, the drying of walnut husk in a oven at 400±5°C for 30 min gives MCWH.

Sorption experiment

For the adsorption kinetics study, 1 g of adsorbent was weighed into the flasks with 100 mL solution of metal ion at the concentrations of 2-14 mg L⁻¹. The temperature was maintained at 25°C. The process was carried out statically without agitation. The equilibration was defined according to the curves of the adsorption capacity changes on the interaction time of the sorbent with a solution.

The equilibrium adsorption capacity A (mg g⁻¹) was calculated using the following equation.

$$A = \frac{c_0 - c_e}{m} * V, \quad (9)$$

where c_0 and c_e are the initial and equilibrium concentrations of metal ions in the liquid phase (mg L⁻¹), respectively, A is the adsorption capacity of metal ions (mg/g), V is the volume of the solution (L), and m is the mass of the adsorbent used in adsorption experiments (g).

ACKNOWLEDGMENTS

This work was supported by the grant of Ministry of Education and Science of Republic of Kazakhstan 3444/GF4 “Scientific bases development of phosphorus-containing compounds obtaining on the basis of technogenic mineral raw materials”.

REFERENCES

1. U. Wingenfelder, G. Furrer, R. Schulin, *Micropor. Mesopor. Mat.*, **2006**, *95*, 265.
2. Y. Wang, F. Lin, W. Pang, *J. Hazard. Matter.*, **2007**, *142*, 160.
3. R. Petrus, J.K. Warchol, *Water Res.*, **2005**, *39*, 819.
4. M. Sprynskyy, B. Buszewski, A.P. Terzyk, J. Namiesnik, *J. Colloid Interface Sci.*, **2006**, *304*, 21.
5. Sh.-Ch. Tsai, Sh. Ouyang, Ch.-N. Hsu, *Appl. Radiat. Isot.*, **2001**, *54*, 209–215.
6. M. Gutierrez, H.R. Fuentes, *Appl. Radiat. Isot.* **1993**, *13*, 327.
7. P. Chutia, S. Kato, T. Kojima, S. Satokawa, *J. Hazard. Matter.*, **2009**, *162*, 440
8. M.V. Eyrish, “Crystallochemical and structural features of montmorillonite and their influence on the properties of bentonite clay”, Nauka, Moscow, **1980**, 117. (in Russian)

9. T.N. Frolova, K.A. Kozlov, A.V. Bondarenko, Regulation of ion exchange capacity of the layered silicates by cation substitution, Abstracts XIII of the regional scientific and technical conference. Improving the efficiency of steel production, Lipetsk, **2004**, 39. (in Russian)
10. V.I. Sergienko, L.A. Zemnukhova, A.G. Egorov, E.D. Shkorina, N.S. Vasylyuk, *Ross. Khim. Zh.*, **2004**, *48*, 116. (in Russian)
11. W.E. Marshall, E.T. Champagne, W.J. Evans, *J. Environ. Sci. Health, Part A: Toxic/Hazard. Subst. Environ. Eng.*, **1993**, *28*, 1977.
12. M. Ahmedna, W.E. Marshall, A.A. Hussein, R.M. Rao, I. Goktepe, *Water Res.*, **2004**, *38*, 1062–1068.
13. W.T. Tan, S.T. Ooi, C.K. Lee, *Environ. Technol.*, **1993**, *14*, 277.
14. E.Yu. Belyaev, L.E. Belyaeva, *Chemistry in interests of a sustainable development*, **2000**, *8*, 763. (in Russian)
15. T.E. Nikiforova, V.A. Kozlov, *J. Appl. Chem.*, **2008**, *81*, 428.
16. S.S. Stavitskaya, T.I. Myronyuk, N.K. Kartel, V.V. Strelko, *J. Appl. Chem.*, **2001**, *74*, 531.
17. Patent 2217231 (Russia), The method of extraction of heavy metal ions from aqueous solutions / T.E. Nikiforova, N.A. Bagrovskaya, S.A. Lilin, V.A. Kozlov, A.I. Maximov, V.A. Titov, *Bl. 33*, **2003**, 389. (in Russian)
18. V.C. Srivastava, I.D. Mall, I.M. Mishra, *Colloids Surf., A.*, **2008**, *312*, 172–184.
19. I.V. Shevelev, A.N. Holomeydik, A.V. Voight, L.A. Zemnukhov, *Chemistry of plant raw materials*, **2009**, *4*, 171. (in Russian)
20. Ch. Li, H. Zhong, Sh. Wang, J. Xue, Zh. Zhang, *Colloids Surf., A.*, **2015**, *470*, 258.
21. M. Prasad, H.Y. Xu, S. Saxena, *J. Hazard. Mater.*, **2008**, *154*, 221.
22. O.S. Amuda, A.A. Giwa, I.A. Bello, *Biochem. Eng. J.*, **2007**, *36*, 174.
23. Q. Li, J. Yu, F. Zhou, X. Jiang, *Colloids Surf., A.*, **2015**, *482*, 306.
24. M.T. Yagub, T.K. Afroze, H.M. Ang, *Adv. Colloid Interface Sci.*, **2014**, *209*, 172.
25. O. Keskinan, M.Z. L. Goksu, M. Basibuyuk, C.F. Forster, *J. Bioresour. Technol.*, **2004**, *92*, 97.
26. Y.S. Ho, D.A. Johnwase, C.F. Forster, *Wat. Res.*, **1995**, *29*, 1327.
27. F. Pagnanelli, S. Mainelli, F. Vegliò, L. Toro, *Chem. Eng. Sci.*, **2003**, *58*, 4709.
28. M.L. Zhang, H.Y. Zhang, D. Xu, L. Han, D.X. Niu, B.H. Tian, J. Zhang, Y. Zhang, W.S. Wu, *Desalination*, **2011**, *271*, 111.
29. R.N. Meretin, *Natural Sciences*, **2013**, *2*, 168. (in Russian)
30. R. Waseem, S.S. Tahir, *Wat. Res.*, **2001**, *35*, 3982.
31. M.S. Nocon, "Inorganic Sorption in Polymer Modified Bentonite Clays", Graduate Thesis and dissertations, University of South Florida, **2006**.
32. R. Suarya, A.A. Bawa Putra, D.D. Wisudawan, *Journal Kimia*, **2010**, *1*, 43.
33. T.E. Nikiforova, V.A. Kozlov, M.K. Islyaikin, *Russ. J. Phys. Chem. A.*, **2012**, *86*, 1836.
34. N.I. Nikitin, "Chemistry of wood and cellulose", Moskow-Leningrad: Akad. Nauk SSSR, **1962**, 711. (in Russian).
35. A.N. Frumkin, "Selected works: Electrode processes", Moscow: Nauka, **1987**, 336. (in Russian).

BIOGAS PRODUCTION USING WASTE WATERS – INFLUENCE OF PROCESS PARAMETERS FOR TEST RIG AT LABORATORY SCALE

ADRIAN EUGEN CIOABLĂ^a, ALEKSANDAR DJURIC^b,
GABRIELA-ALINA DUMITREL^{c,*}, DANIEL CHIRILĂ^d, VASILE PODE^c

ABSTRACT. Biogas production by anaerobic digestion of residual waters from different sources (a treatment plant and a beer factory) was investigated in laboratory small scale batch reactors. Both wastewaters represent efficient biogas substrates. As concern the methane composition, the value is slightly higher in the case of biogas produced by anaerobic digestion of wastewater from beer factory. In the second part of this study, anaerobic co-digestion of wastewater and cow whey was performed. Addition of cow whey to wastewater from beer factory increase the biogas yield, while the addition of cow whey to wastewater from treatment plant decrease the biogas yield. In both cases of co-digestion, the methane content in biogas was higher than in the single digestion processes.

Keywords: *wastewater, anaerobic digestion, biogas, methane yield*

INTRODUCTION

The rapid development of human society increased the energy demands, which will lead to the depletion of conventional energy sources [1].

^a Politehnica University of Timisoara, Faculty of Mechanical Engineering, 1 M. Viteazu Blvd., RO-300222, Timisoara, Romania

^b University of Novi Sad, Technical Faculty "Mihajlo Pupin", Djure Djakovica bb, 23000 Zrenjanin, Serbia

^c Politehnica University of Timisoara, Faculty of Industrial Chemistry and Environmental Engineering, 6 V. Parvan Blvd., RO-300223, Timisoara, Romania

^d Politehnica University of Timisoara, Physical Education and Sports Department, 1 M. Viteazu Blvd., RO-300222, Timisoara, Romania

* Corresponding author: alina.dumitrel@upt.ro

Meanwhile, in the world, huge amounts of wastewater coming from agriculture, industry or domestic activities are generated. The composition of these wastewaters depends on the source and its characteristics, but the main constituents are: organic matter, nutrients (nitrogen, phosphorus and potassium), inorganic matter (dissolved minerals), toxic chemicals and pathogens [2]. Releasing of an untreated wastewater effluent into environment can have negative impact on ecosystem and human health. Now, there are a variety of strategies used to treat the wastewaters [3,4]

Anaerobic digestion is an interesting solution to this problem which leads to biogas and digestate [5]. The biogas is generally composed of ca. 48–65% methane, ca. 36–41% carbon dioxide, up to 17% nitrogen, <1% oxygen and traces of hydrogen sulphide or other gases [6]. The process works at cryophilic, mesophilic (25–37°C) and thermophilic (45–55°C) temperatures.

According to literature, higher biogas quantities were obtained in the case of wastewater co-fermentation with percentages of other residual materials from dairy industry, sugar industry, brewery industry [7-9].

The dairy industry is divided into several sectors, which are associated to the production of contaminated wastewaters. These effluents have different characteristics, according to the product obtained (yogurt, cheese, butter, milk, ice cream, etc.). Moreover, the wastewater management, climate, operating conditions and types of cleaning-in-place, also influence the dairy effluents characterization [10]. The dairy effluents show a relatively high organic load, monitored by biological oxygen demand (BOD) and chemical oxygen demand (COD) in the range of 0.1-100 kg/m³ with an index of biodegradability (BOD5/COD) typically in the range 0.4 - 0.8. Organic matter content is mainly due to the presence of milk carbohydrates and proteins such as lactose and casein, respectively [11].

The composition of whey resulting from the white cheese making process is presented in table 1.

Table 1. Constituents of whey resulting from white cheese making process [12]

Constituent	Percentage, [%]
Water	94
Protein	0.8 – 1.0
Lactose	4.5 – 5.0
Fat	<0.1
Minerals	<0.1
pH	4.5 - 5

From a wastewater treatment point of view, anaerobic digestion of cheese whey offers an excellent approach. However, raw whey is known to be quite problematic to be treated anaerobically, because of its low bicarbonate

alkalinity, high COD concentration and its tendency to get acidified very rapidly [13]. Supplemental alkalinity is required so as to avoid acidification and subsequently anaerobic process failure [14].

By comparison with other types of biomass, whey general properties are presented in Table 2 [15].

Table 2. Comparative properties of whey with other biomass types

Biomass	pH	TS, [%]	VS, [% TS]	TN, [% TS]
Tomato skin and seeds	4.7	32.0	97.8	3.34
Barley straw	7.87	90.5	94.3	0.99
Rice straw	8.14	88.7	91.9	0.88
Grape stalks	4.4	31.1	91.9	1.99
Maize drying up residues	5.05	81.8	97.5	1.29
Whey	5.2	6.86	91.1	1.83
Grape marcs	3.58	61.4	90.7	2.30
Inoculum	8.00	7.62	70.0	5.93

where: TS - total solids, VS - volatile solids, TN - total nitrogen.

The protein profile of whey is presented in Table 3.

Table 3. Protein profile of whey and primary structure basic properties [16]

Protein	Concentration, [g/L]	Molecular weight, [kDa]	Number of amino acids residues
β -Lactoglobulin	1.3	18.277	162
α -Lactalbumin	1.2	14.175	123
Bovine serum albumin	0.4	66.267	582
Immunoglobulins (A, M and C)	07	25000 (light chain) + 50000 (heavy chain)	-
Lactoferrin	0.1	80000	700
Lactoperoxidase	0.03	70000	612
Glycomacropetide	1.2	6700	64

As it can be observed, this material can be used in co fermentation processes in order to produce biogas.

This work evaluates the feasibility of anaerobic digestion of two wastewater types from a treatment plant and from a beer factory. For this purpose, laboratory experiments were conducted. The performance of the reactor was monitored and evaluated in terms of pH, methane content, carbon dioxide content and biogas production. In addition, the anaerobic fermentation efficiency of wastewaters co-fermented with cow whey was also evaluated.

RESULTS AND DISCUSSION

The small scale anaerobic installation was used to test the digestion performances of residual waters from water treatment plant and beer factory and, also the combination between those two materials and cow whey (90% waste waters and 10% cow whey).

The time variation for pH is presented in figure 1. In the figure it can be observed that during the fermentation process, the pH in the reactor containing only wastewater from the beer factory (WW2) was relatively stable with values in the range of 6.5 – 7. The co-fermented material (WW2+CW) presented a pH variation between 6 and 6.8 due to acid influences of the cow whey inside the first period of the process. The pH during the fermentation process of wastewater from treatment plant (WW1) had an initial acid tendency, but after corrections the values raised slowly from 6.1 to 7.1 at the end of the process. The co-fermented batch (WW1+CW) had at the beginning of the process an oscillated pH around 6. After correction it was raised at 7.5 – 7.7 and remained constant along the study.

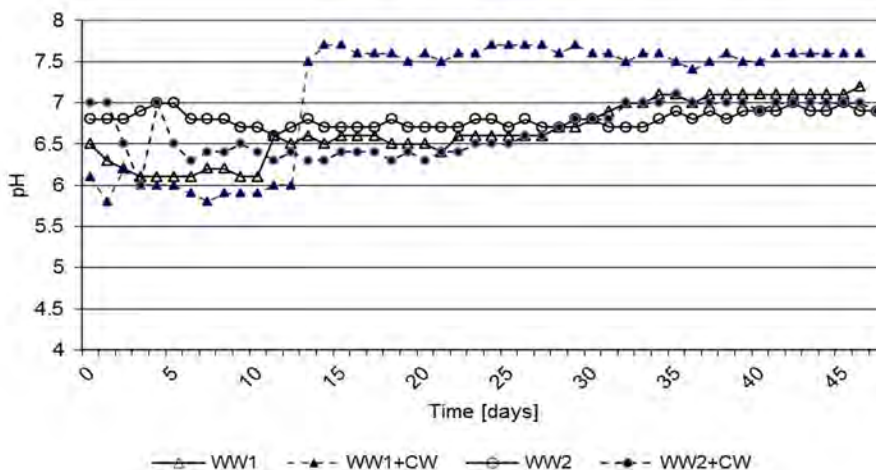


Figure 1. pH variation for the studied batch

During the anaerobic digestion process the following parameters were monitored: the total quantity of biogas produced and its partial composition (in terms of CH_4 and CO_2 concentrations).

The total quantity of biogas produced at the end of each anaerobic fermentation process is presented in figure 2.

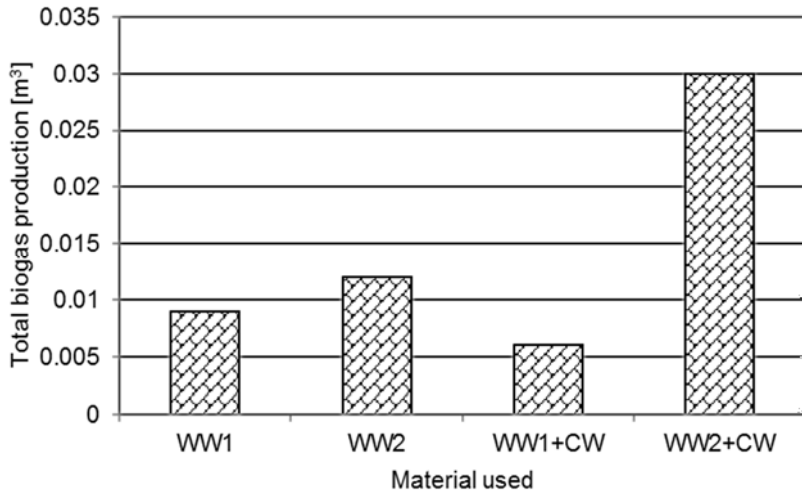


Figure 2. Total biogas produced in the case of each material used

The figure revealed that the addition of cow whey to wastewater from beer factory increased the production of biogas by 2.5 times, while the same addition to the wastewater from treatment plant inhibited partially the anaerobic digestion process. Total biogas production was found in the order: 90% wastewater from bear factory + 10% cow whey (0.03 m³) > wastewater from bear factory (0.012 m³) > wastewater from treatment plant (0.009 m³) > 90% wastewater from treatment plant + 10% cow whey (0.006 m³).

According to literature [23,24], the biogas and methane production efficiency is influenced by the total solids (TS) content of the substrate used in the anaerobic digestion process. In our study the TS content of the substrates investigated is around 2% for WW1, 2.4% for WW1+CW, 3% for WW2 and 3.5 % for WW2+CW. The quantity of biogas produced by anaerobic digestion increase with the increasing of TS content. Exception was the co-substrate wastewater from treatment plant and cow whey which generated an unusual low quantity of biogas. The anomaly can arise from the fact that, in this situation, the cow whey partially inhibited the biogas production process due to lack of a previous environment adapted for co-fermentation of wastewater with cow whey.

In the next step of the study, the quality of biogas was evaluated. In this purpose, the methane and carbon dioxide composition was evaluated.

The CH₄ composition of biogas for the four studied substrates is presented in figure 3.

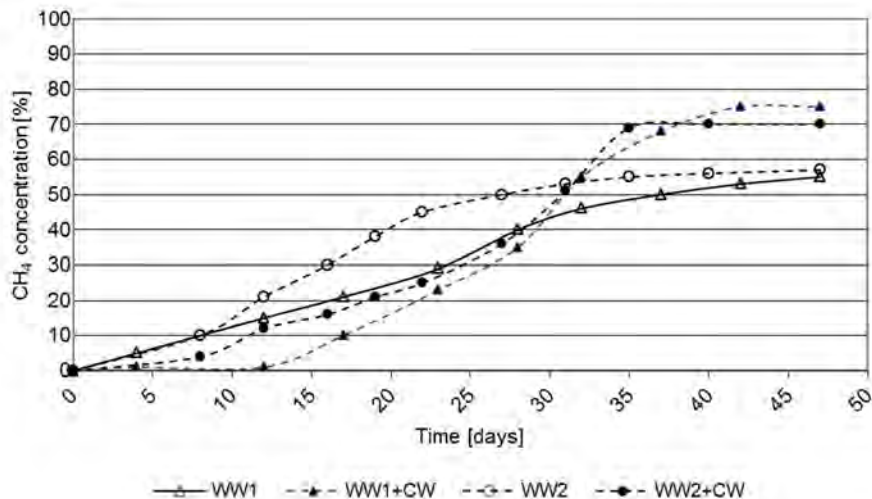


Figure 3. Evolution of CH₄ concentration during anaerobic digestion of studied batch

The methane concentration showed an increasing trend over time for all the studied situations. In the first 30 days of the process, the methane quantity is higher in the biogas produced from WW1 and WW2. After 30 days, the concentration of methane became higher in the biogas generated by anaerobic digestion of wastewaters co-fermented with cow whey. A maximum of 55% and 57% methane was reached during wastewater WW1 and WW2 fermentation, while the maximum methane production for co-fermented material WW1+CW was 75 % and for WW2+CW was 70 %.

The CO₂ composition of biogas for the four studied substrates is presented in figure 4.

The CO₂ concentration in the biogas varies between 40% and 20% for the wastewater WW1 and between 50% and 35% for the wastewater WW2. The co-fermented batches show higher CO₂ concentrations in the first 30 days and, in the end of the process the concentration decrease in the range 25 - 30%.

Relative to the residence time of materials inside the anaerobic fermenters, the experiment was made using a stationary batch type reactor, in this case the total residence time for the used materials being equal to the period of time of the experiment (approximately 47 days). WW1 and WW2 batches started to produce methane after 24-48 hours of process, in small concentrations, while the process of methane production was slow for the other two batches – between 5 and 12 days.

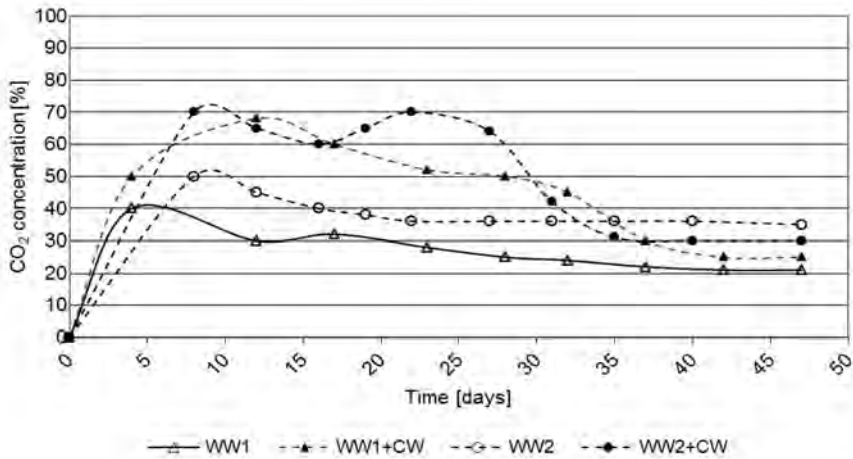


Figure 4. Evolution of CO₂ concentration during anaerobic digestion of studied batch

The overall efficiency of the process was relatively low for the WW1 and WW2 batches in terms of quality for the obtained biogas, and relatively high for the other two studied batches, showing an improvement over the biogas quality – high percentage in methane. This aspect is a key factor in terms of further using the produced biofuel inside firing processes.

The higher quantity of biogas was exhibit by the mix of 90% wastewater from beer factory and 10% cow whey but the wastewater from beer factory had better results in terms of biogas quality over time.

CONCLUSIONS

Anaerobic digestion of wastewaters from a treatment plant and a beer factory was performed in laboratory batch reactors during 47 days. The feasibility of the anaerobic co-digestion of mixed residual water and cow whey was also investigated.

Single substrate digestion of wastewaters showed higher biogas production for residual water coming from treatment plant. Addition of cow whey to wastewater from beer factory increases the production of biogas, while addition to wastewater from treatment plant decreases the biogas production. In the meantime, the co-digestion process increases the concentration of methane in biogas for both case studies.

The results showed potential for all materials, with accent on combinations between residual waters and cow whey, both in terms of results and way of process control.

EXPERIMENTAL SECTION

1. Characteristics of wastewaters

The studied wastewaters were collected from a water treatment plant located in Timisoara City (WW1) and from a beer factory (WW2). The characteristics of these materials were determined according to the procedures of the standard methods [17-22] and are presented in table 4. All analyses were performed in duplicate and the results were expressed as mean values.

Table 4. General characteristics of wastewater

	WW1	WW2
Measured parameter	Value	Value
Carbon content, [%]	32	36.4
Sulphur content, [%]	5.1	4.4
Chlorine content, [mg/kg]	1.1	2.7
Volatile content (dry basis), [%]	37.9	42.3
Hygroscopic moisture content, [%]	5.85	5.1
Ash content (dry basis), [%]	36.2	26.7
Mean calorific value (dry basis), [MJ/kg]	15.2	17.4

As it can be observed from the table above, the carbon content is relatively high, close to the range specific to agricultural waste materials (40 – 45%). The sulphur and chlorine content show that the used materials cannot be used inside firing processes, at least not alone, because of the risk to affect the combustion chamber negatively – there is a high possibility of forming acid components during oxidizing process. Even if the mean calorific value for the wastewaters shows increased energetic potential in terms of capitalization, the ash content is very high, proving to be not fit to be used in any type of firing or co-firing processes. The resulting residual quantity is too high, rising the problem of properly managing the obtained waste material.

In a second study, the wastewaters were co-fermented with cow whey (CW). The percentage of cow whey was 10% of the total suspension volume inside the fermentation tanks.

2. Experimental set-up

Two laboratory scale anaerobic reactors with a total volume of 6L were used in this study.

The schematic of the experimental set-up is presented in figure 5.

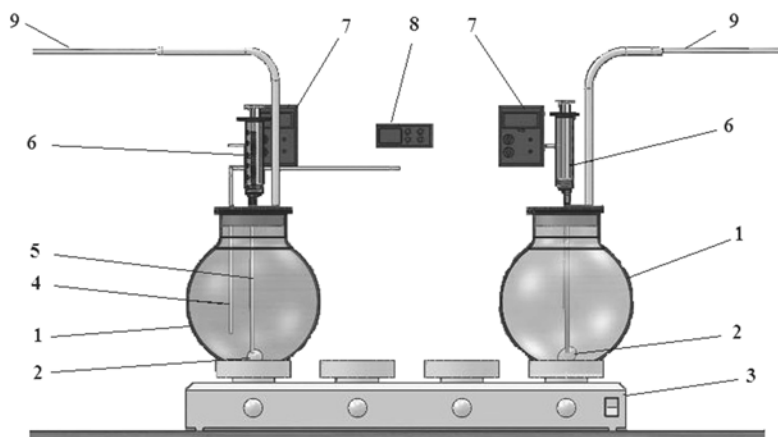


Figure 5. Schematic experimental setup

The components of the small scale installation are: 1 – thermal glass reactors with a total volume of 6L used for dark fermentation; 2 – magnets used for magnetic stirring of the material suspensions; 3 – device used for heating the suspension inside the glass reactors; 4 – thermocouple; 5 – system for sampling and pH correction of the suspensions inside the vessels; 6 – syringe used for sampling and pH correction system; 7 - pH controllers connected to pH sensors inside the glass reactors in order to determine in real time the pH value of the suspension; 8 – temperature controller connected with the thermocouple for temperature control to a determined range; 9 – gas bags with a total volume of 2L used to collect the biogas from the fermentation process.

In order to obtain a good fermentation process the glass reactors used for anaerobe fermentation were covered with a layer of black paint.

The fermentation process was held for 47 days in order to observe the pH, the biogas yield and its composition in terms of CH₄ and CO₂ concentration. The temperature was kept constant in a range between 36 and 37 °C. In order to correct the pH values during the process, it was used a solution of NH₃, 10% concentration.

For measuring the methane and carbon dioxide concentration of biogas a DELTA 1600 S IV gas analyzer was used.

ACKNOWLEDGMENTS

This work was supported by a grant of the Romanian National Authority for Scientific Research and Innovation, CNCS – UEFISCDI, project number PN-II-RU-TE-2014-4-1043.

REFERENCES

1. D.A. Ilutiu-Varvara, *Environmental Engineering and Management Journal*, **2010**, 9, 6, 813.
2. M.-H. Huang, Y.-M. Li, G.-W. Gu, *Desalination*, **2010**, 262(1–3), 36.
3. P.P. Kalbar, S. Karmakar, S.R. Asolekar, *Journal of Environmental Management*, **2012**, 113, 158.
4. P.R. Gogate, A.B. Pandit, *Advances in Environmental Research*, **2004**, 8(3–4), 501.
5. S. Connaughton, G. Collins, V. O'Flaherty, *Water Research*, **2006**, 40, 2503.
6. S. Rasi, A. Veijanen, J. Rintala, *Energy*, **2007**, 32, 1375.
7. M.R.J. Daelman, Van E. M. Voorthuizen, U.G.J.M. Van Dongen, E.I.P. Volcke, M.C.M. Van Loosdrecht, *Water Research*, **2012**, 46, 3657.
8. S. Luostarinen, S. Luste, M. Sillanpää, *Bioresource Technology*, **2009**, 100, 79.
9. L. Appels, J. Baeyens, J. Degreve, R. Dewil, *Progress in Energy and Combustion Science*, **2008**, 34, 755.
10. R. Pattnaik, R.S. Yost, G. Porter, T. Masunaga, T. Attanandana, *Ecological Engineering*, **2007**, 32, 1.
11. A.R. Prazeres, F. Carvalho, J. Rivas, *Journal of Environmental Management*, **2012**, 110, 48.
12. T. Spachos, A. Stamatis, *Renewable Energy*, **2011**, 36, 2097.
13. F. Malaspina, C.M. Cellamare, L. Stante, A. Tilche, *Bioresource Technology*, **1996**, 55, 131.
14. N. Venetsaneas, G. Antonopoulou, K. Stamatelatu, M. Kornaros, G. Lyberatos, *Bioresource Technology*, **2009**, 100, 3713.
15. E. Dinuccio, P. Balsari, F. Gioelli, S. Menardo, *Bioresource Technology*, **2010**, 101, 3780.
16. A.R. Madureira, C.I. Pereira, A.M.P. Gomes, M.E. Pintado, F.X. Malcata, *Food Research International*, **2007**, 40, 1197.
17. European Standard EN 14774: **2009**, Solid biofuels – Determination of moisture content – Oven dry method.
18. European Standard EN 14775: **2009**, Solid biofuels - Determination of ash content.
19. European Standard EN 14918: **2010**, Solid biofuels – Determination of calorific value.
20. European Standard EN 15290: **2011**, Solid biofuels – Determination of major elements.
21. European Standard EN 15104: **2011**, Solid biofuels – Determination of total content of carbon, hydrogen and nitrogen – Instrumental methods.
22. European Standard EN 15148: **2010**, Solid biofuels – Determination of the content of volatile matter.
23. J. Yi, B. Dong, J. Jin, X. Dai, *PLoS ONE*, **2014**, 9(7), e102548. doi:10.1371/journal.pone.0102548.
24. S. Maamri, M. Amrani, *Energy Procedia*, **2014**, 50, 352.

EVALUATION OF BLEACHING ON A CAD/CAM HYBRID CERAMIC MATERIAL

BOGDAN CULIC^a, CRISTINA GASPARIK^{a*}, MIHAI VARVARA^a,
CARINA CULIC^a, CRISTIAN DRAGOS^b,
LAURA SILAGHI-DUMITRESCU^c, DIANA DUDEA^a

ABSTRACT. The objective of our study was to test the bleaching effect of two whitening gels, on stained hybrid ceramic material used for Computer Aided Design/ Computer Aided Manufacturing technology. 40 rectangular specimens 12/14/1mm were prepared from Vita Enamic blocks. All specimens were accelerated stained, and distributed in two groups. Group 1 was bleached using Opalescence PF 15% (Ultradent, USA), group 2 was bleached using an experimental gel containing natural products. ΔE^* (used to assess the color changes) was above the perceptibility threshold of 1.2 in 40%; and the WID (used to assess the bleaching process in dentistry) showed high units for both bleaching gels. Hybrid ceramics staining showed moderate results, while the bleaching effect was present, with no statistical difference between the discolorations produced by the two bleaching gels ($p < 0.05$). SEM images showed that the bleaching gels did not affect the surface structure of the material.

Keywords: CAD/CAM, hybrid ceramics, polymer, bleaching, color, SEM

INTRODUCTION:

In the last years CAD/CAM technologies (Computer Aided Design/ Computer Aided Manufacturing) become one of the most important component of dental medicine. The technique is orientated to the future, being mainly focused on high efficiency and standardization of prosthodontics

^a Department of Prosthetic Dentistry and Dental Materials, Faculty of Dentistry, "Iuliu Hatieganu" University of Medicine and Pharmacy, Cluj-Napoca, Romania

^b Department of Statistics, Faculty of Economics, Babes-Bolyai University, Cluj-Napoca, Romania

^c Raluca Ripan Chemistry Institute, Department of Polymer Composites, Babes-Bolyai University, Cluj-Napoca, Romania

* Corresponding author: gasparik.cristina@umfcluj.ro

treatment. The advantages of CAD/CAM technologies consist in the quality of the materials, industrially processed, reproducibility and low cost [1]. The available CAD/CAM systems are: "in office" systems, and laboratory systems, used in the dental lab. All CAD/CAM systems have three main components:

- A scanner - for image acquisition, transforming images into data;
- An Imaging software – data processing and restoration 3D design
- A milling unit – for transforming the virtual design into a finite product (veneers, inlays, onlays, crowns, bridges) [2,3]

Innovative materials were developed in order to fulfill researchers, clinicians and patient's demands. A great variety of dental ceramics and a large selection of composite resin materials can be found on the market. Among the advantages of ceramics are a high flexural strength and great color stability, while disadvantages are high antagonistic tooth wear and high incidence of failure due to its brittle nature [4,5]. These two parameters are much improved in the case of composite resins, but the wear of the material itself is higher. While ceramics are stiffer and harder than natural tooth structure, composite resins show lower values [6,7].

Manufacturers have been developing new materials for CAD/CAM systems in order to combine the advantages of ceramic materials (durability, color stability) with the ones of composites (improved flexural strength and low abrasiveness) [5,8]. Recent materials like Vita Enamic (Vita, Bad Sackingen, Germany) represent such great improvements. The material has a three-dimensional interconnected geometry with two penetration networks. One network is a glass ceramic material and the other a polymer (methacrylate for dental applications), with a proportion of 84% and 16 % respectively (by weight). Material indications are for long term restorations in the anterior and lateral areas for full coverage crowns, veneers, inlay and onlays [5,7,8].

Nowadays, dental bleaching is one of the most current treatments in dentistry. The treatment provides higher self-esteem to patients, with minor consequences to the teeth if correctly performed. During bleaching procedure restorative materials are bleached together with the tooth structures [9,10].

The effects of bleaching agents on the surface of composite restorative materials have been studied over the years. Different bleaching products and systems have been used for at home and in in-office procedures, containing up to 38 percent hydrogen peroxide. However, 10 to 15% carbamide peroxide bleaching agents are the most widely used as at home products. The literature contains several reports of their safety and effectiveness of hydrogen peroxide releasing agents like carbamide

peroxide or sodium perborate [11]. Unfortunately the bleaching procedure can be responsible for causing alterations of enamel surface, or dental materials, and tooth sensitivity [12]. Several studies showed that nanofill and hybrid composite resins are affected by the bleaching gel [13,14]. Other studies observed that the effect on the surface of the restorative materials were material dependent. The effects to the pulp were also studied, but with no clinical significance [15,16].

Development of the new tooth bleaching agents based on natural products with minimal side effects on tooth structures and dental materials is beneficial in order to minimize the side effects, but only if it's clinically effectiveness is demonstrated.

In our study we evaluate the chromatic changes produced by two bleaching gels with different chemical composition, on a new CAD/CAM hybrid ceramic material. No studies were published so far, to evaluate CAD/CAM hybrid ceramics bleaching effect. The objective of our study was to test the bleaching effect of two whitening gels, on stained hybrid ceramic CAD/CAM material.

RESULTS AND DISCUSSION

40 Vita Enamic (VE) specimens were accelerated stained, and distributed in two groups (n=20). Group 1 was bleached using Opalescence PF, (OP), group 2 was bleached using a non-peroxide experimental gel containing natural ingredients (EG). The CIEL*a*b* color parameters of the VE specimens were measured at baseline, after staining and after bleaching, using Vita Easy Shade Spectrophotometer (Vita, Germany). Color variation obtained after staining (ΔE_1) and after bleaching (ΔE_2), were calculated. ΔE^* mean values for the CIELab color space and the WI_D (whitening index for dentistry) were also calculated in order to assess color parameters after staining and after bleaching (Table1).

Table 1. Color changes (ΔE^*) and Whitening Index (WI_D). Mean values and standard deviation

	ΔE^*		WI_D after staining	WI_D after bleaching	p-value
	Staining	Bleaching			
Group 1 (OP)	1.668 (0.742)	1.687 (0.608)	21.29 (0.946)	23.85 (0.612)	< 0.001
Group 2 (EG)	2.195 (1.403)	1.878 (0.946)	20.71 (2.050)	23.59 (1.049)	<0.001

A powerful correlation (Pearson coefficient $R = 0.819$) and a significant statistical correlation ($p < 0.001$) were obtained between the staining and the bleaching effect of all VE samples figure 1.

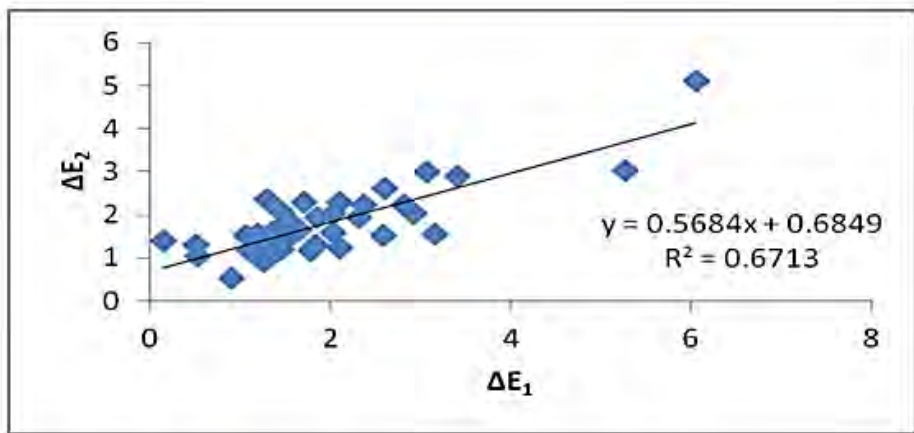


Figure 1. Correlation between ΔE values obtained after staining and bleaching (ΔE_1 and ΔE_2)

The staining effect was visible for 17.5 % of the samples (ΔE^* above the acceptability threshold of 2.7).

40% of ΔE^* (used to assess the discoloration process) were above the perceptibility value of 1.2. However 90% were below the acceptability threshold of 2.7, fig. 2a.

The WID showed similar bleaching effect with an average of 23.85 units (st.dev. 0.612) for the OP gel, and 23.59 units (st.dev. 1.049) for EG gel. (fig. 3) The existence of a hypothesis that there is a statistical difference between the whitening effect produced by the OP and EG gels was rejected ($p=0.310$), fig. 2b.

ΔL^* was also calculated in order to indicate the increasing or decreasing of lightness for bleaching - fig. 2c.

The SEM images at baseline, after staining and after bleaching performed at different magnifications indicate that the surface of the samples showed a complex structure, with a uniform distribution of the polymer filler and ceramic network. The red arrows indicate the organic phase, the yellow arrows the inorganic phase fig. (4-7).

EVALUATION OF BLEACHING ON A CAD/CAM HYBRID CERAMIC MATERIAL

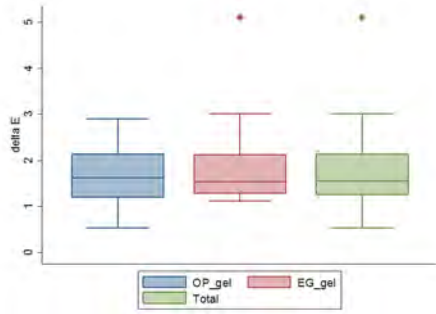


Figure 2a. ΔE^* values found after bleaching for the two groups.

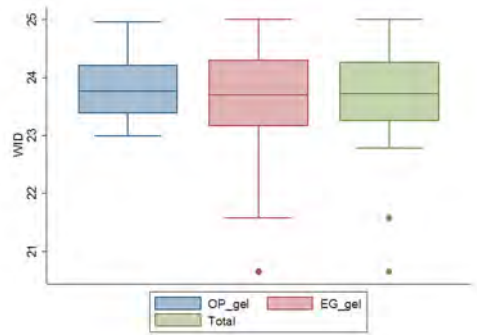


Figure 2b. WID_B values for the two groups

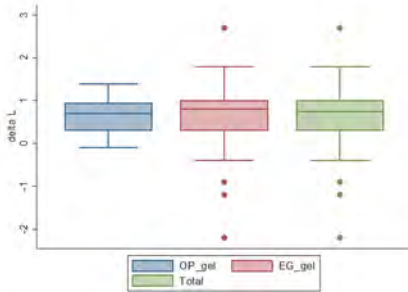


Figure 2c. ΔL^* after bleaching

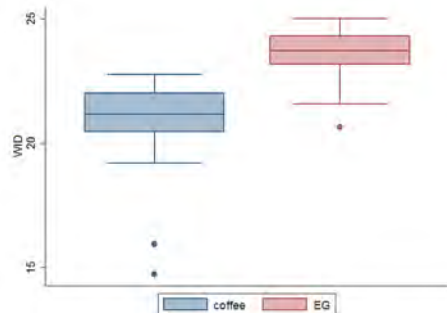
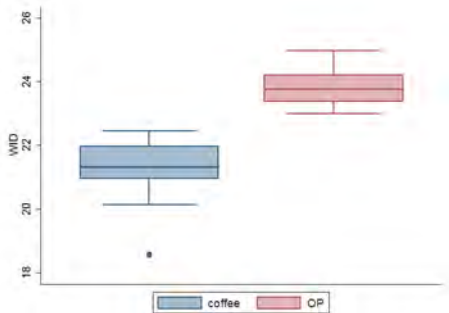


Figure 3. WID_B after bleaching the stained hybrid ceramic

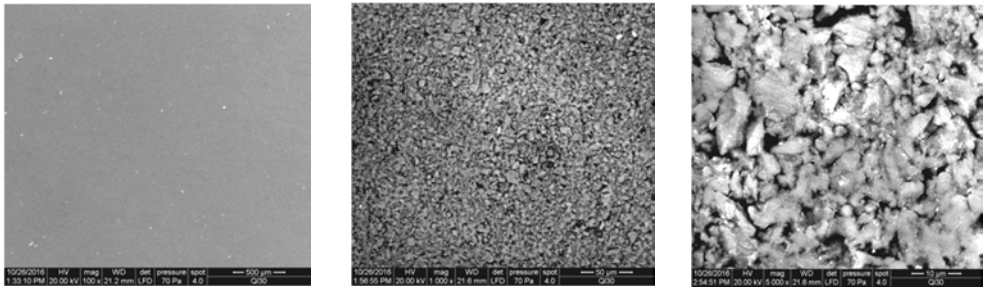


Figure 4. SEM examination at magnification of 100, 1000 and 5000 - at baseline

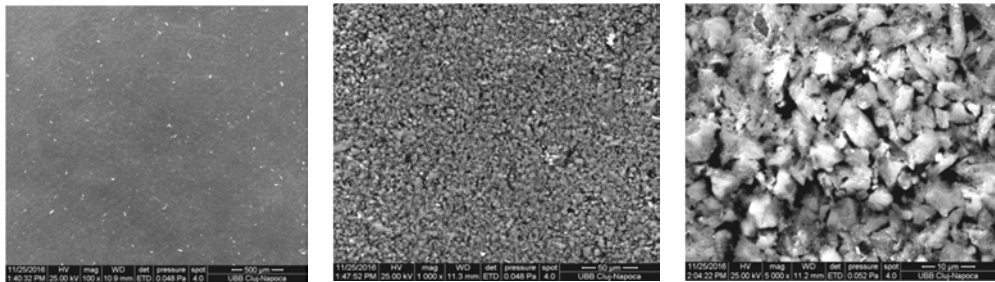


Figure 5. SEM examination at magnification of 100, 1000 and 5000 - after staining

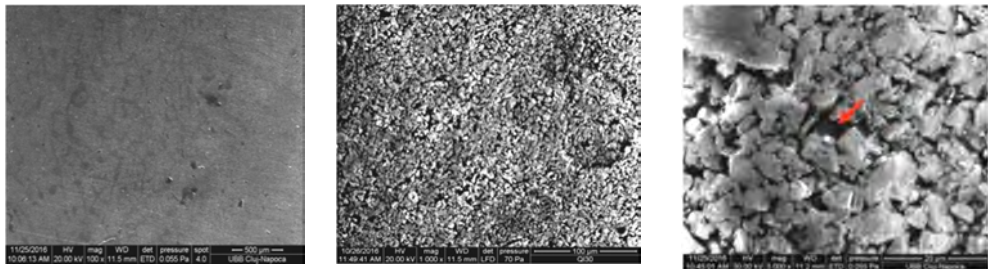


Figure 6. SEM examination at magnification 100, 1000 and 5000 - after bleaching with OP gel

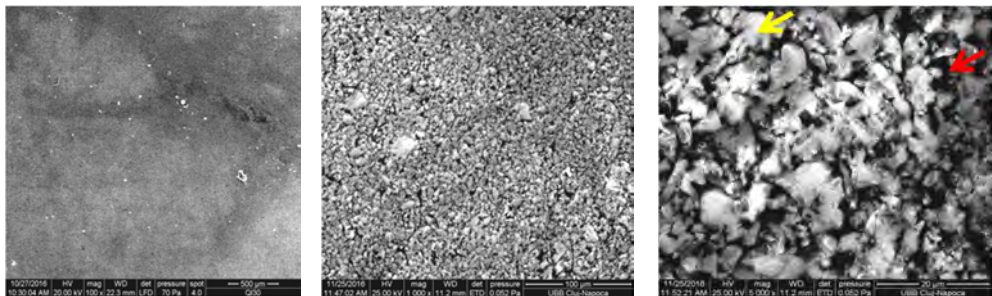


Figure 7. SEM examination at magnification 100, 1000 and 5000 - after bleaching with EG gel

The purpose of our in vitro study was to evaluate the effect of the two bleaching gel on the surface of CAD/CAM hybrid ceramic material. Discoloration was assessed using an instrumental method (spectrophotometer), used to obtain L^* , a^* , b^* values from the CIE Lab* color space, with high level of accuracy and repeatability [17].

During color measurements both light and the color of the background under which the sampled will be measured can influence the result [20,21]. In our study a standardized grey back was used for the measurements standardization [22].

CIE Lab* color space is composed by the positive x axis that extends out from the center toward its maximum value of +60 at red is named the a^* axis. Perpendicular to this and going toward the yellow hue is the positive y axis called b^* . The $-a^*$ axis extends toward green and $-b^*$ toward blue. The value (or lightness) axis which is the z axis extends upward with values ranging from 0 (black) to 100 (white) and is given the name L^* [23]

CIE Lab* color difference ΔE^* is a value introduced to evaluate color changes. A ΔE^* below 1.2 is not perceptible to human eyes; while values up to 2.7 are considered clinically acceptable. [17,18]

In order to use the ΔE^* in bleaching evaluation, it has to be associate with ΔL^* calculation otherwise false results of the bleaching effect can be obtained. A decrease of ΔL^* , will show a ΔE^* variation, that can be interpreted as bleaching, even the process was opposite. ΔE^* calculation is a sum of perfect squares and will give always positive results, it will not indicate the direction of color variation, but only the amount.

WID was introduced in order to eliminate the inconveniences of other indices recommended for the assessment of bleaching. This index can have both positive and negative values. A greater value than the baseline will show a positive effect of the bleaching agent [18].

A positive WID correlated with delta ΔE^* values give us the direction of color variation and also the quantitative level [18,19].

Based on the testing conditions applied for our study design, the results showed a moderate staining of the hybrid CAD/CAM composite, 17.5% of the samples were above the acceptability threshold. The color of the stained specimens return to baseline, for both test groups, but without obtaining a discoloration above the acceptability values. Bleaching agents are effective to remove the staining for the hybrid ceramic when 15% carbamide peroxide or experimental gel was used. The whitening result produced by the two bleaching gels were similar, thus that bleaching agents based on natural products can be regarded as less aggressive alternatives to commercial gels based on carbamide peroxides [16].

The SEM microscope is a type of microscope used for the study of surface morphology, which use electrons for illuminating the sample and create a 3D image. Electronic microscopes have a higher resolution and magnification when compared to light microscopes.

Although conventional dental ceramics is considered the most inert of all dental restorative materials, their surfaces may present damages in contact with acidic fluoride gels or other solutions. In addition, the contact and possible diffusion of free radicals produced by bleaching agents can selectively extract the alkaline ions of ceramic network, causing damage [11,24]. The polymer network may also be affected by the erosion on the surface of the matrix and is dependent on resin matrix components and filler size [14,25].

Dental restorations must be resistant to degradation caused by a broad range of solutions. Prolonged exposure to hydrogen peroxide affects the restoration surface and cause changes. In addition, an increase in the surface roughness may produce an increase in the accumulation of dental plaque, thus increasing the risk of secondary caries, periodontal inflammation [25,26].

In general, roughness change of the restorative materials depends on the material, on the concentrations of whitening gels, but also on the exposure times, all these factors can cause greater roughness. After bleaching, color changes on the restorative materials can be different than the enamel response. Refinishing or replacement of these restorations may be necessary to enable regain of esthetics and to prevent microorganism colonization [26,27,28].

In our study, the stained samples analyzed with SEM behaved well with no changes in the morphology of the surface of the hybrid ceramics, compared to the control. After bleaching with the 2 whitening gels (OP and EG) qualitative analysis of SEM images at magnification of 100x shows a slight deterioration of the surfaces, suggesting that the roughness of CAD/CAM hybrid ceramic changed after exposure to bleaching agents. Our results are in agreement with those of previous studies (Turker, Biskin, Yap, Wattanapayungkul) [9,14].

In the staining and bleaching procedures we did not notice the existence of micro particles expelled or cracks on the surface of studied samples.

CONCLUSIONS

The bleaching effect of VE samples was present, but with moderate results.

No statistical difference between the discolorations produced by the two bleaching gels ($p=0.310$).

The Hybrid ceramics tested showed good color stability for accelerate staining.

Bleaching gels did not affect the surface structure of hybrid CAD/CAM ceramic.

EXPERIMENTAL SELECTION:

40 rectangular shaped specimens 12/14/1mm were prepared from Vita Enamic CAD/CAM blocks 1M1 shade, high translucency (HT), EM14 size. The specimens were sectioned using a diamond-wafering blade mounted on a saw (Isomet Precision 1000, Buehler, USA), at 1.2 mm thickness. The samples were subsequently polished using sandpaper with grit size of 600, 800 and 1200 (CbC). The final polishing was performed using the manufacturer polishing kit (Vita Enamic Polishing Set, Vita, Bad Sackingen, Germany). At the end, a 1mm thickness was achieved. All specimens with out-of- range dimensions ($\pm 60\mu\text{m}$) were discarded. The thickness was checked with an electronic digital caliper (Pittsburg, USA) for all samples. The specimens were ultrasonically cleaned in distilled water for 10 minutes and then were allowed to dry for 24 hours. All specimens were accelerated stained, and distributed in two groups ($n=20$).

Staining process

The specimens were immersed in coffee, 50 ml of coffee for each sample (prepared in a drip coffeemaker) using 32 grams of ground coffee / 8 cups of water). The immersion time was 3 hours per day in the colorant solution and the rest of the time in artificial saliva at 37°C. The protocol was carried out for 21 days. Afterwards, they were rinsed in distilled water, air dried and stored in distilled water.

Bleaching process

Group 1 was bleached using Opalescence PF, containing 15% carbamide peroxide (Ultradent, USA) (OP), group 2 was bleached using a non-peroxide experimental gel containing natural ingredients (EG). (Hydroxyapatite with Zn 15% and strawberries/quinces juice). The bleaching agents were applied on test specimens 8 hours per day for 14 days (total 112 hours).

The CIEL*a*b* color parameters of the VE specimens were measured at baseline, after staining and after bleaching, using Vita Easy Shade Advanced 4.0 Spectrophotometer (Vita, Germany). The measurements were performed against an 18% gray card background. Several pairs of color parameters were obtained for each sample (L_x^* , a_x^* , b_x^* values from the CIE Lab color space) - at baseline, after staining; after bleaching) which allowed to calculate the ΔE_{ab}^* values and the new whitening index for dentistry (WI_D). [17]. The results were statistically analyzed using the SSPS 16.0 for Windows.

E_{ab}^* was calculated using the following formula:

$$\Delta E_{ab}^* = \sqrt{(\Delta L^*)^2 + (\Delta a^*)^2 + (\Delta b^*)^2},$$

where ΔL^* - is the difference in lightness, Δa^* - is the difference in the chromatic parameter a^* on the red-green axis, Δb^* - is the difference in the chromatic parameter b^* on the yellow-blue axis from the CIEL*a*b* color space.

The CIE*Lab color space WI_D was calculated using the formula:

$$WI_D = 0.511L^* - 2.324a^* - 1.100b^*$$

The samples were examined under SEM with FEI Inspect model S microscope, in functional High and low vacuum, with an accelerating tension between 200V-30KV. The microscope is equipped with infrared CCD-IR camera and electrons detector, having a max resolution of 4096x3536 pixels. The measurements were recorded at baseline, after staining and after bleaching. Images were recorded in three different magnifications (100x, 1000x and 5000x). The images were obtained at three different locations for each sample.

ACKNOWLEDGEMENTS

The research was supported by the UMF "Iuliu Hatieganu" Cluj Napoca Internal Grant nr. 4994/10/2016.

REFERENCES

1. F. Beuer, J. Schweiger, D. Edelhoff, *British Dental Journal*, **2008**, 204, 505.
2. S.B. Nathan, B. Aaronson Heidi, *Compedium*, **2008**, 29, 494.
3. P. Feuerstein, S. Puri, *Oral Health*, **2009**, 99, 65.
4. A. Coldea, M.V. Swain, N. Thiel, *Dental Materials*, **2013**, 29, 419.
5. A. Awada A., D. Nathanson, *Journal of Prosthetic Dentistry*, **2015**, 144, 587.
6. N.D. Ruse, M.J. Sadoun, *Journal of Dental Research*, **2014**, 93, 1232.
7. A. Della Bona, P. Corazza, Yu Zhang, *Dental Materials*, **2014**, 30, 564.
8. D. Fasbinder, G. Neiva, *Journal of Esthetic and Restorative Dentistry*, **2016**, 28, 66.

9. S.B. Turker, T. Biskin, *Journal of Prosthetic Dentistry*, **2003**, 89, 466.
10. O. Polydorou, E. Hellwig, TM Auschill, *Operative Dentistry*, **2006**, 31, 473.
11. S. Ourique, C. Arrais, A. Cassoni, C. Tsuzuki-Ota, J.A. Rodrigues, *Brazilian Oral Research*, **2011**, 25, 453.
12. M. Goldberg, M. Grootveld, E. Lynch, *Clinical Oral Investigations*, **2010**, 14, 1.
13. T. Attin, C. Hanning, A. Wiegand, R. Attin, *Dental Materials*, **2004**, 20, 852.
14. P. Wttanapayungkul, A.U. Yap, *Operative Dentistry*, **2004**, 29, 398.
15. A.F. Lima, A.P. Ribeiro, D.G. Soares, N.T. Sacono, J. Hebling, C.A. De Souza, *Acta Odontologica Scandinavica*, **2013**, 71, 1319.
16. I. Baldea, D. Olteanu, A. Filip, M. Cenariu, D. Ducea, A. Tofan, C. Alb, M. Moldovan, *Clinical Oral Investigation*, **2016** [Epub ahead of print]. DOI:10.1007/s00784-016-1882-4
17. R. Ghinea, MM. Pérez, L.J. Herrera, M.J. Rivas, A. Yebra, R.D. Paravina, *Journal of Dentistry*, **2010**, 38, 57.
18. M.M. Pérez, R. Ghinea, M.J. Rivas, A. Yebra, A. Ionescu, R.D. Paravina, L.J. Herrera, *Dental Materials*, **2016**, 32, 461.
19. A. Petran, T. Radu, B. Culic, R. Turcu, *Applied Surface Science*, **2016**, 390, 1.
20. A.U. Guler, F. Yilmaz, T. Kulunk, E. Guler, S. Kurt, *Journal of Prosthetic Dentistry*, **2005**, 94, 118.
21. R. Bagheri, M.F. Burrow, M. Tyas, *Journal of Dentistry*, **2005**, 33, 389.
22. A. Alharbi, S. Ardu, T. Bortolotto, I. Krejci, *Odontology*, **2016**, DOI:10.1007/s10266-016-0258-1.
23. C. Gaspari, A.G. Grecu, B. Culic, M.E. Badea, D. Ducea, *Journal of Esthetic and Restorative Dentistry*, **2015**, 27, 285.
24. K.J. Anusavice, *Degradability of Dental Ceramics*, **1992**, 6, 82.
25. S. Marto, C. Coito, A. Pequeno, Al. Cavalheiro, *Revista Portuguesa de Estomatologia, Medicina Dentaria Cirurgia Maxillofacial*, **2012**, 53, 7.
26. A.A. Zaki, N.Z. Fahmy, *Journal of Prosthodontics*, **2009**, 18, 223.
27. A.D. Vanderlei, S.P. Passos, S.M. Salazar-Marcho, S.M. Pereira, V.Z. Vásquez, M.A. Bottino, *Acta Odontologica Latinoamericana*, **2010**, 23, 257.
28. A.V. Burde, S. Cuc, A. Radu, M.A. Rusu, C.S. Cosma, R.S. Câmpian, D. Leordean, *Studia UBB Chemia*, **2016**, 61, 205.

IN VITRO DEGRADATION AND PHASE COMPOSITION OF COSMETIC EMULSIONS

RAMONA I. CHELCEA^a, DUMITRIȚA MOLDOVAN^a, DAN E. DEMCO^a,
EUGEN CULEA^a AND RADU FECHETE^{a*}

ABSTRACT. Microscopic properties like network dynamics and phase compositions were studied for a series of commercially available cosmetics emulsions like hair shampoo, anti-UV shielding creams and hand and body creams. Proton longitudinal and transverse nuclear magnetic relaxations were measured by recording the 1D CPMG and 2D saturation recovery–CPMG echoes decays. The one and bi-dimensional inverse Laplace transformations reveals subtle features which characterize the microscopic dynamic behaviour associated with the *in vitro* natural degradation of cosmetics. The IR and UV–VIS spectra were recorded and correlated with the NMR measurement.

Keywords: *commercial cosmetics; NMR; T_2 relaxation; T_1 - T_2 correlation; NMR-MOUSE[®], IR and UV-VIS spectroscopy.*

INTRODUCTION

Daily the human body is assaulted by food, cosmetic or pharmaceutical products and can develop a significant sensitivity in interaction with these consumer products. For example N-Nitrosamines are expected to be human carcinogens because of evidence of carcinogenicity in experimental animals [1]. Humans can be exposed to Nitrosamines exogenously and via endogenous formation. Exogenous exposure can occur from a variety of products like: food and drink (beer), inhalation of tobacco smoke, use of rubber products (balloons, teats and soothers) and cosmetics [2–4].

^a *Technical University of Cluj-Napoca, Department of Physics and Chemistry, 25 G. Baritiu Str., RO-400027, Cluj-Napoca, Romania*

* *Corresponding author: rfechete@phys.utcluj.ro*

The *stratum corneum* (10-20 μm) is the most upper layer of the epidermis which together with dermis and subcutaneous fat tissues forms the skin. This is composed of intracellular lipids and dead cells (corneocytes – flat cells of keratin-containing structures enveloped in proteins) and has a protective role against environmental aggression, being also a barrier to water loss and foreign body penetration. In *stratum corneum* (SC) a substantial amount of water is bounded by the keratin and by so called natural moisturizing factors (humectants) like some amino acids, lactate, urea, uric acid, glucosamine, creatine, citrate, formate or ions (Cl^- , Na^+ , K^+ , Ca^{2+} , Mg^{2+}) etc. The hair fibres are composed from a central cortex enveloped into 6 to 10 layers of overlapping cells named cuticle. In order to prevent degradation of skin or hair a large variety of specialized cosmetics emulsions with multiple targets (cleansers, humectants, emollients, sunscreen and occlusive agents or antipuretic and/or antiacne medicaments) are produced and are commercially available. Thus, for example glycerol and urea are well-known humectants, which are highly water soluble and therefore difficult to be deposited into skin, and petroleum which is a common occlusive agent [5 and references therein].

An emulsion is usually defined as an opaque, heterogeneous system of two immiscible liquid phases where one of the phases is dispersed in the other as drops of microscopic or colloidal size (around 1 μm) and stabilized against separation [6]. Common cosmetic emulsions can be found as: i) oil in water (o/w) - which are the majority; ii) water in oil (w/o); iii) aqueous gel or iv) silicone in water. Thus, many types of silicone can be used to create cosmetics with the appropriate degree of hair conditioning. Among these, the dimethicone copolyols have a light conditioning effect but are largely used due to their reduced eye irritation and to boost the foaming properties of shampoos [5].

Cleanser products are mainly designated to remove unwanted materials (e.g. dirt, oil or sebum) from skin and hair. Unfortunately charged surfactants like anionic (e.g. phosphoric, sulfonic or acyl amino acids and salts) and cationic are aggressive, they can reduce the skin moisture and can increase the skin's irritation. Fortunately, there are other commercially available surfactants (nonionic and amphoteric derivate from anionic variants) that are mild to the skin [5]. Aqueous polymeric dispersions are used extensively as thickeners in cosmetics and pharmaceutical products to improve their rheological properties [7–10]. For example the cross-linked thickeners can form a networked microgel structure in solutions and are also very useful as platforms in drug delivery applications because of a better control release of medicaments [11, 12]. The UV filters (sunscreens) in skin care products bring important benefit to cosmetic formulations. For classification of such products function of the degree of protection, a sun protection factor (SPF) is defined as the dose of UV radiation required to produce 1 minimal erythema dose on protected skin surface on which is applied 2 mg/cm^2 of product [5].

In the last two decades, strongly inhomogeneous static and radio frequency magnetic fields becomes a prosperous environment for quality NMR techniques to evolve. More and more NMR applications have been proposed and operate successfully in these fields [13, 14]. These can includes the stray field NMR [15,16], as well as the development of surface NMR spectrometers [17, 18] and sensors [19, 20] for material testing [21-24], imaging [25, 26] and well logging [27-29]. Moreover, approaches toward high-resolution *ex-situ* NMR spectroscopy have been also recently discussed [30, 31].

The present work proposes a study of the cosmetic compounds phases' stability when they are subjected to external natural degradation factors. As example, three cosmetics categories were chosen: hair shampoo, anti-UV shielding creams and hand and body creams (see Table 1).

RESULTS AND DISCUSSION

The recorded 1D NMR signal, $S_{T_2}(t_2)$, the decay of a CPMG echoes trains is analysis by an one-dimensional Laplace inversion algorithm, using Prospa software [32], to extract the transversal relaxation time distribution function $f(T_2)$ from,

$$S_{T_2}(t_2) = \int f(T_2) \exp\left\{-\frac{t_2}{T_2}\right\} dT_2 \cdot \quad (1)$$

A cosmetic product usually consists of a large number of ingredients which can interact with each other forming a smaller number of phases. In the following we will name an emulsion phase that component of the sample which presents a similar microscopic network dynamic, quantified in our experiments with a similar value of relaxation time. In time, during the use or conservation, these phases can present various changes leading to an altered product with modified properties. The study of phase alteration, via the changes in the transverse relaxation times distributions in controlled laboratory conditions to simulate the daily use (up to 24 h), is presented in Fig. 1, for the series of cosmetic samples listed in Table 1. The cosmetic samples used in this study can be grouped in three categories: i) hair shampoos; ii) anti-UV shielding creams and iii) hand and body creams.

In the analysis of such T_2 distributions the main interest is on the peak position (changes of peaks positions) and area under the peaks. Then the peaks located at largest values of T_2 time can be associated with a low viscous

emulsion phase or volatile component while the low T_2 value peak can be associated with high viscous emulsion phase characterized by a more restricted molecular motion. In time, we are expecting to observe on cosmetic samples two opposite effects: i) the loose of moisture by water and volatile components (like perfumes) evaporation and ii) to increase of water amount for the cosmetic sample containing hygroscopic components like glycerin. The area under the peaks which is proportional with the number of ^1H is a good indication of the amount of each component in the measured sample.

The shampoos and anti-UV creams presents, at least initially, three main T_2 peaks (see Figs 1a-1d). The time-dependent T_2 distributions for both shampoos and anti UV shielding cream with SPF 15 (Figs 1a-1c) are shifted towards smallest T_2 values, becoming in this way more viscous. This is due probably by losing water, since in shampoos the amount of volatile components like perfumes is small. For these samples the most viscous component (characterize by a small T_2) becomes in time more rigid and looks for both hair shampoos (see Figs 1a and 1b) to have the same area; while the middle and largest T_2 component seems to suffer an *interaction* process, more visible for hair shampoo 1 (Fig. 1a).

Thus, for this sample, after approximately 10 hours, the largest T_2 -component became smaller and is moved toward the middle peak. Contrary, the hair shampoo 2 after approximately 6 hours looks to present an exchange between the middle and the high T_2 -value peaks, both becoming closer and higher, probably on account of rigid component.

It is of interest to compare the dynamic behavior of the two anti-UV shielding creams with standard protection factor, SPF 15 and 25. The most mobile components (large T_2 -value peak), appears to not be too much affected. Since the anti-UV creams have also the role to hydrate the skin, and assuming that the moisture is associated with the more mobile component (or high T_2 -value peak) then is perfectly reasonable that this component to be less affected in time. The behavior of the other two components is completely different. The middle peak of the SPF 15 cream remain unchanged for almost 10 hours when starts to merge with the rigid component (see Fig 1c). The last one, at the beginning is increasing in rigidity (observed as a decrease of the T_2 value) but then after 5-6 hours start to became more and more mobile. Contrary, for the SPF 25 cream, in a time of 3 hours, the left peak (more rigid component – small T_2 value) and middle peak merges with the right peak (most mobile component), excepting a small residue component at T_2 value around 0.01 s (see Fig. 1d).

IN VITRO DEGRADATION AND PHASE COMPOSITION OF COSMETIC EMULSIONS

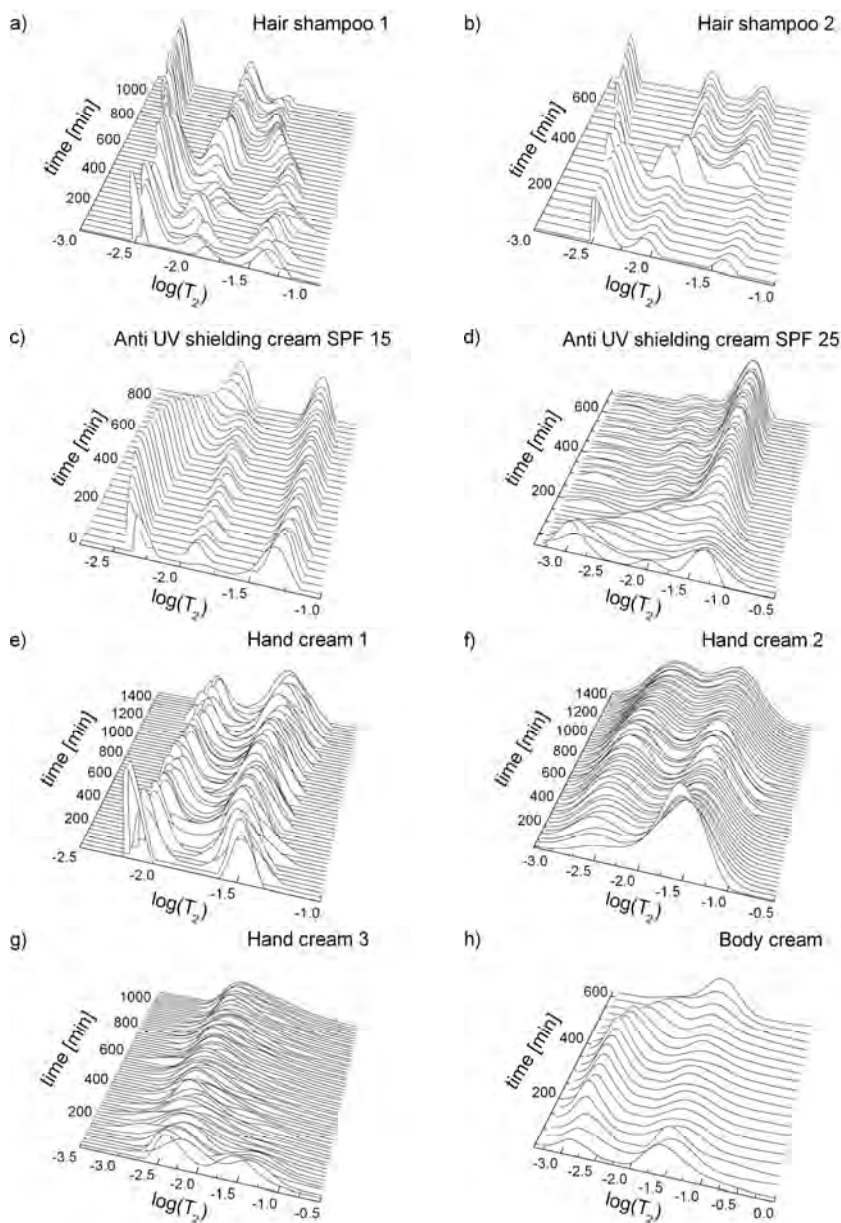


Figure 1. The time dependent normalized probability distribution functions of $\log(T_2)$ for a series of commercial samples like: two hair shampoos a) and b) two anti-UV shielding creams c) and d); three hand creams e), f) and g); and one body cream h).

The dynamics reflected in the time evolution of recorded Laplace spectra is different for those three hand cream samples (Fig. 1e-1g). All three samples present only two components, which can be differentiated by their dynamics by the two peaks observed in their T_2 -distribution functions. While, for the hand cream 1, the dynamic phases can be clearly differentiated, for the hand cream 2 and 3 we cannot distinguish between these phases. No spectacular changes in time are to be reported. In the experimental and data analysis errors, the hand cream 1 seems to be unaffected (see Fig. 1e). A small transitory process, up to 2-3 hours, can be identified for the hand cream 2, where the amount of mobile component percentage decrease with the increase of the rigid component amount (see Fig. 1f). A different, but fast, transitory process can be observed for hand cream 3 where only in the initial time regime a mobile peak is observed (see Fig. 1g). This became very fast so small that is hidden by the more broaden middle peak, which covers several orders of magnitude in the T_2 -distribution. This is an indication of a sample with heterogeneous dynamic components, but stable in time. In fact all hand creams can be characterized as stable in the measurement time window.

The body cream presents also two dynamic components (see Fig. 1h). As a particularity, for this sample one can observe a component with a restricted dynamics compared with the rest of cosmetic samples characterized by a T_2 value around 1 ms. After a transitory regime of several hours, in which this peak increase in amplitude without a change in position, then starts to decrease and to be shifted toward larger T_2 -values, indicating an increase in mobility. Finally, both peaks merge into a single dynamic component with the characteristics of the initial mobile phase.

Up to this point we were able to identify two or three components but we estimate that the T_2 measurements alone are generally insufficient to distinguish and associate entirely the phase components of studied cosmetics samples. For a better characterization of our colloids we need a new approach, based on the correlation of T_1 - T_2 relaxation times. Here, the 2D NMR measured signal, $S_{T_1, T_2}(\tau_1, t_2)$ is function of i) the measurement parameters (see the pulse sequence from experimental and sample section) like the magnetization recovery time, τ_1 and total echo time $t_2(\tau_2 + \tau'_2)$ starting after excitation pulses and ii) depends on the sample parameters like longitudinal, T_1 and transversal, T_2 relaxation times, respectively [33],

$$S_{T_1, T_2}(\tau_1, t_2) = \iint f(T_1, T_2) \left(1 - \exp\left\{-\frac{\tau_1}{T_1}\right\} \right) \exp\left\{-\frac{t_2}{T_2}\right\} dT_1 dT_2, \quad (2)$$

where $f(T_1, T_2)$ is the T_1 - T_2 distribution function.

The measured T_1 – T_2 correlation maps for the series of sample listed in Table 1 are presented in Fig. 2. Many more dynamic phases can be observed in these distribution functions compared with the 1D T_2 -distributions. The peak projections in the T_2 dimension correspond with the range of similar peaks presented in Fig. 1, however the 2D extension in the T_1 domain can reveal particular characteristics. As general features we can observe: i) well defined peaks around $T_1 = 0.1$ s or between $T_1 = 0.1$ – 1 s; ii) excepting two cases two large peaks extended over several order of magnitude in both T_1 and T_2 ; iii) the large distribution at largest value of T_1 is due to the lack of sufficient data points to describe a complete relaxation, therefore, we will consider only the peak maximum of these distributions. The dashed diagonal line indicates the $T_1 = T_2$ values and the thin diagonal lines indicated the constant T_1/T_2 ratios of 10, 100 and 1000. The peaks with the T_1/T_2 ratios closed to 1 can be associated with aqueous phases and those with large T_1/T_2 ratio can be associated with more viscous phases. Moreover, for all samples, the phases for which the T_2 relaxation is significantly faster than T_1 relaxation indicate an exchange of molecules which contain protons, possibly in majority, water [33].

There are several features that must be underlined. The anti-UV cream with SPF 25 (see Fig. 2d) present the sharpest peaks and less extended. Only in this case the maximum T_1 value is around 1 s. In contrast, the hand cream 2 has the largest T_1 values around 100 s (see Fig. 2f).

Sharp distributions presents also the hand cream 1 located close to the $T_1/T_2 = 10$ ratio (see Fig. 2e). In half of the cases there are some components into a so called *forbidden* region where $T_1 < T_2$. If these peaks are real, then this can be a consequence of proton exchange between different dynamic components. The T_1 – T_2 correlation maps were found to be an important source of information but we steel need information for a better interpretations and peak assignment. Additional spectroscopic measurements were performed into attempt to identify the phase compositions and physico-chemical properties.

The FT/IR spectra of the series of cosmetics samples listed in Table 1 are presented in Fig. 3 together with the water spectrum. Water presents three main peaks (Fig. 3 sample W): i) a main asymmetric and broad (3000 – 3700 cm^{-1}) peak centred at ~ 3450 cm^{-1} (due to the O-H bond); ii) a narrow peak centred at ~ 1600 cm^{-1} and iii) a broad band at wavenumber smaller than 1000 cm^{-1} . Excepting some features, all these spectra are similar to water spectra. This is an indication of the large amount of water that can form the aqueous phases of studied cosmetics. The particular features presented by all spectra are smallest, indicating a smallest concentration in the sample product.

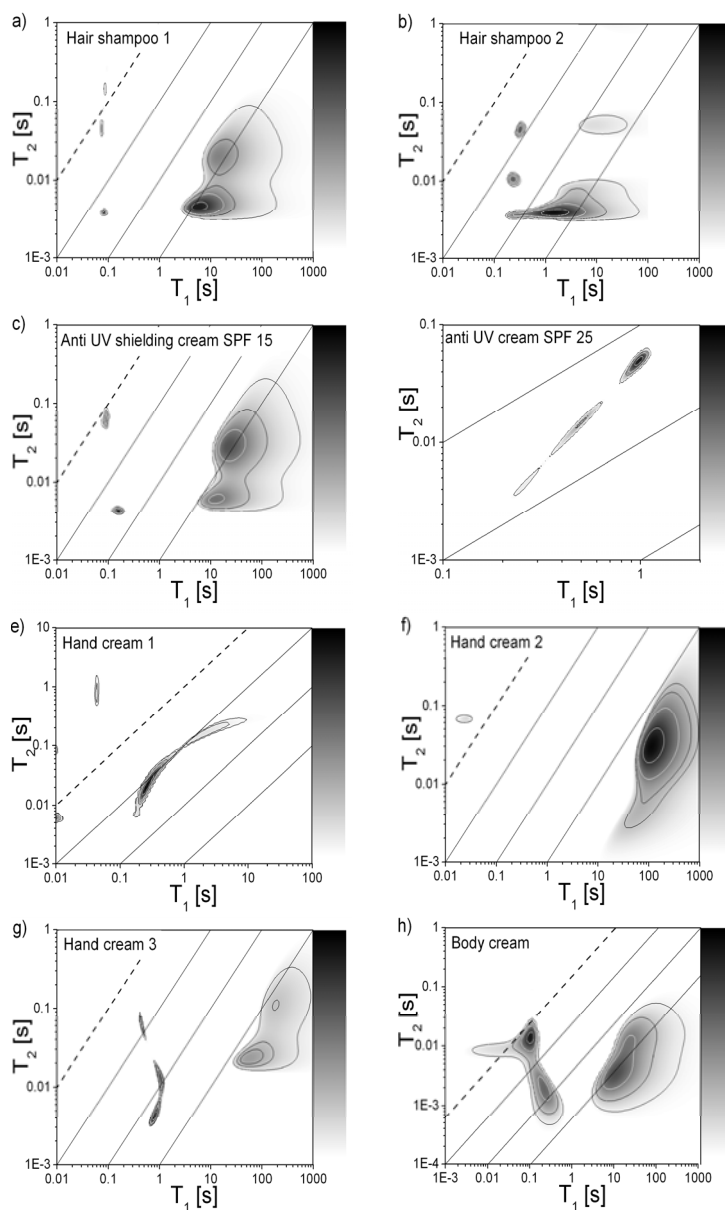


Figure 2. The T_1 - T_2 correlation maps for a series of commercial cosmetic emulsions like: two hair shampoos (a) and (b) two anti-UV shielding creams with (c) SPF 15 and (d) SPF 25; three hand creams (e), (f) and (g); and one body cream (h).

The viscous emulsion dynamics is manifested at lower wave number $1000 - 1600 \text{ cm}^{-1}$ associated with the skeleton vibration of entire molecule (the fingerprint region) and at large wave number from $2800 - 3700 \text{ cm}^{-1}$ associated with group characteristic frequencies. Here a broad peak centred $\sim 3200 \text{ cm}^{-1}$ appears as a right shoulder on the water peak, overlapping on this peak, therefore for the majority of samples is identifiable only by comparison with the measured water IR spectra.

All spectra present two relatively large peaks at $\sim 2850 \text{ cm}^{-1}$ and 2925 cm^{-1} and other left shoulders around them. These can be associated, for example with stearic acid, citric acid, glycerol or other similar ingredients. Many of these compounds present IR peaks between $2800 - 3000 \text{ cm}^{-1}$ and from $1000 - 1500 \text{ cm}^{-1}$ and less, then positive final identifications are not possible. Nevertheless, comparing the database ATR-IR spectra of glycerol and paraffin [34] one can identify specific bands (doublet at 2880 and 2934 cm^{-1}) of $-C-H$ (stretching) bonds and $\sim 1500 \text{ cm}^{-1}$, in our measured ATR-TF/IR spectra.

The anti-UV shielding cream with SPF 15 labelled with C, present a particular peak as a left shoulder on the water peak around 1750 cm^{-1} may be an indication of a carbonyl compound ($C=O$). Moreover, the small peaks at $\sim 1560 \text{ cm}^{-1}$ observed for the samples labelled with C and D (SPF 15 and 25) may be an indication of the presence of aromatic compounds in the anti-UV shielding creams. The same indices can be found also for the measured hand cream 1 (see the ATR-FT/IR spectrum labelled with E in Fig. 3). Amines

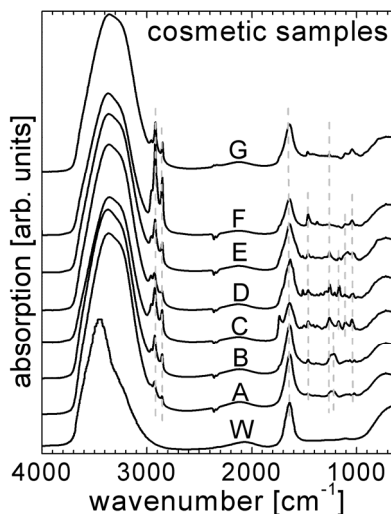


Figure 3. Compared ATR (Attenuated Total Reflection) FT/IR absorption spectra of the series of cosmetics presented in Table 1 together with water (W) IR spectrum.

(C-N bonds) and alcohols (C-O bonds) functional groups can be found as components in samples presenting peaks between $1030\text{--}1230\text{ cm}^{-1}$ and $1050\text{--}1150\text{ cm}^{-1}$, respectively.

Compared with the time dependent 1D T_2 distributions (Figs. 1) and 2D $T_1\text{--}T_2$ correlation maps (Figs. 2) ^1H NMR data the ATR-FT/IR spectra are more similar. In these spectra the major features appear grace at the presence of water which for all our samples is found into an amount larger than 50 % (curve W compared with the rest of spectra in Fig. 3). Such amount of water in the cosmetic sample means that the water has to be distributed into mobile phases, characterized by large T_2 values, but has to be found also in less mobile phases (characterized by smaller T_2 values) as bound water.

The transmission/absorption characteristics in ultraviolet and visible domains of the distilled colloidal samples are presented in Fig. 4, for comparison together with the UV-VIS water spectra. These present a large absorption peak around 970 nm and began to be absorbed in the UV domain starting with 300 nm. In addition to water, the cosmetic samples present a continuously increased absorption with no significant features in the visible domain when moving to small wavelength. Starting with $\sim 450\text{ nm}$ for anti-UV shielding cream with SPF 15 (sample C), $\sim 400\text{ nm}$ for hand cream 1 (sample E) and $\sim 350\text{ nm}$ for hair shampoo 2 (sample B) the samples present broadens and features absorption characteristics in the UV domain. Such characteristics may be associated with the presence of paraffin (of which UV characteristic absorption is manifested for wavelength smaller than $350\text{--}400\text{ nm}$) rather than

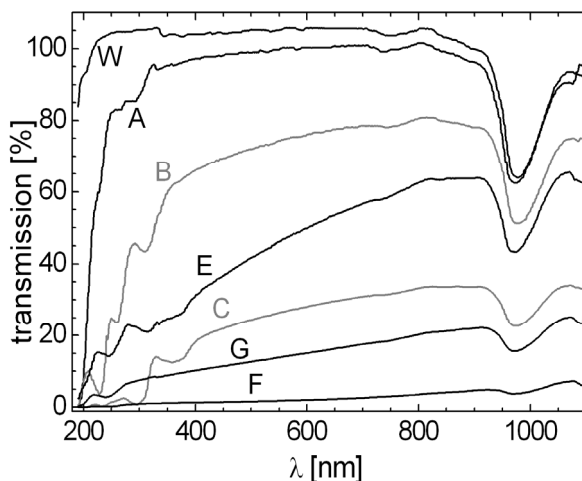


Figure 4. Compared UV-VIS transmission spectra of the series of cosmetics presented in Table 1 and compared with water (W).

glycerol which present absorption bands up to 550 nm. Diverse features observed as unresolved shoulders in this domain suggest the existence of different ingredients that can absorb the UV radiation, which are in concordance with their use especially the anti-UV creams. The shampoos emulsions present the largest transmission characteristics in near UV and VIS domains.

Contrary to the ATR-FT/IR spectra (Fig. 3), for which the main features are given by the water content, the main features of the UV-VIS spectra (Fig. 4) and of the ^1H NMR 1D T_2 distributions (Fig. 1) and 2D T_1 - T_2 correlation maps (Fig. 2) are due to the rest of the components (which for many cosmetic samples the number of this components is larger than 20). Moreover, we can observe that the hair shampoos (samples A and B) with the highest transmittance in UV-VIS spectra (Fig. 4) presents initially (few minutes after the application of the thin film) three balanced peaks in the T_2 distributions (Figs. 1a and 2b) associated with three dynamic phases. Three T_2 peaks are observed in the initial regime also for the anti-UV creams (Figs 1d and 1e) and a medium transmittance was measured in the UV-VIS spectra (sample C in Fig. 4). Contrary the samples with the lower transmittance in UV and visible light (as measured from UV-VIS spectra – samples F and G in Fig. 4) presents a quasi-two component T_2 distribution (poorly resolved distributions – Figs. 1f and 1g). Probably, the large phase heterogeneity (wide T_2 distributions) can be correlated with large distributions of electrons levels in cosmetic molecules which will lead to a sample more absorptive in UV-VIS region of the electromagnetic domain.

CONCLUSIONS

Low field NMR, originally developed to characterize the fluid filled porous media and well-logging, can play now an important role in the characterization, monitoring and quality control of cosmetic products. When accompanied by the new algorithms of Laplace inversion the NMR measurements are a reach source of information about colloidal materials. Thus, the combination of 1D and 2D NMR methods that involve transversal and longitudinal relaxation and Laplace inversion data analysis together with IR and UV-VIS spectroscopy was found to be a useful new tool in the characterization of various commercially available cosmetic products. The time dependent T_2 relaxation distribution functions, which are sensitive to structural composition, texture mobility and interactions of various emulsion components, provided useful information's about cosmetic's phases stability: i) non-stable like the shampoos sample; ii) very stable like hand and body creams or iii) with good hydrating properties like anti UV shielding creams.

EXPERIMENTAL AND SAMPLE

The one-dimensional (1D) and two-dimensional (2D) Nuclear Magnetic Resonance relaxometry correlated with advance data processing by the 1D and 2D Laplace inversions and IR and UV-VIS spectroscopy are methods largely used in the study of this class of materials. An appropriate NMR experimental set-up uses a unilateral NMR sensor, the NMR-MOUSE® [13, 14]. In this case (in contrast with the classical in tube measurement) the tested sample can be subjected to similar conditions as in the case of ordinary use of a thin layer applied on a large surface and with the opposite surface, in contact with the air.

An important tool in highly inhomogeneous magnetic fields NMR experiments is the combination of dedicated pulses sequences like CPMG, which can refocus the linear spin inhomogeneities, with the signal processing by Laplace inversion [13, 14, 27, 29, 32, 33, 35-38]. An elaborate study was performed by Hürlimann et al., on the characterization of food products by two-dimensional $D-T_2$ and T_1-T_2 distribution function obtained by Laplace inversion [33]. These functions exhibits also distinct components associated there with aqueous and liquid fat content phases. An important step was made by Marigheto et al. by giving several methods for peak assignment in complex T_1-T_2 maps of low-resolution 2D NMR cross-correlation relaxometry [36].

For the NMR measurement a BRUKER Minispec spectrometer with a unilateral NMR-MOUSE® sensor working at 19.2 MHz frequency, was used [20, 37]. The cosmetic samples were placed directly on the top of the NMR sensor coil on a laboratory ultra-thin glass (0.1 mm) as a film of 3 mm thick, covering the entire surface of the radio-frequency coil. For the reproducibility a perforated stencil was used as holder, removed during the measurements. In order to simulate better the contact between the cosmetic sample and the human body the temperature was increased and kept constant at 32°C. The atmospheric pressure of 990 mm Hg and 60 % relative humidity was also monitored.

The molecular dynamics and phase composition of a thin film of emulsion samples subjected to one day degradation in natural conditions was studied by applying the CPMG pulse sequences and recording the spin system response, see Fig. 5 up [37]. A total number of 1000 echoes were recorded with 2s recycle delay and 512 scans to improve the signal to noise ratio. The duration of excitation pulse and refocusing pulses were 5 μ s too.

® NMR-MOUSE is a registered trademark of RWTH-Aachen.

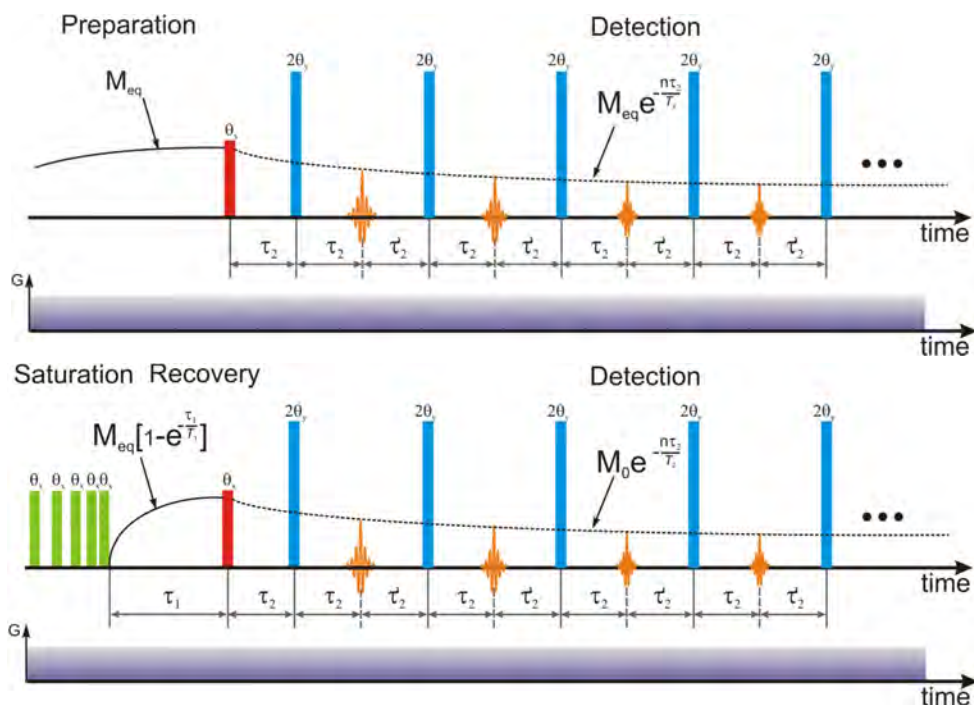


Figure 5. The classical CPMG pulse sequence (up) and (down) saturation recovery followed by detection via CPMG pulse sequence designated for recording the T_1 – T_2 correlations maps.

The 2D, T_1 – T_2 correlations maps were obtained by recording the spin system response during the CPMG that follow a saturation–recovery pulse sequence with re-magnetization time, τ_1 , (see Fig. 5 down) [37]. The echo time, $\tau_2 + \tau_2'$ was between 100 – 300 μs , in function of the measured sample, while the τ_1 time was increased in equal steps with 100 ms up to 5–6 s. For the NMR-MOUSE[®] sensor, the static magnetic fields gradient across the sample is higher than the strength of the radiofrequency magnetic field. Therefore, all pulses are slice selective (~ 0.2 mm per slice) leading to an initial transient regime in CPMG [33, 37]. In order to avoid this effect to affect the T_2 -distribution, the first 10 CPMG echoes were eliminated. The NMR measurements were analyzed using the Prospa software for inverse Laplace transform [32].

The absorption IR spectra were recorded using a single beam FT/IR Jasco 6200 spectrometer with Fourier Transform and an ATR (Attenuated Total Reflection) device. The samples were placed into a 10 cm long, 5 mm large and 3 mm deep holder on top of a special crystal accessory dedicated

to measurement of liquid samples. The ATR correction procedure was applied in order to obtain similar spectra with those obtained by transmission spectroscopy. Finally, a base line correction procedure was applied. The signal to noise ratio was 16 times improved by recording 256 scans for each sample. The resolution of recorded spectra was 1.928 cm^{-1} and a full range from 349.05 cm^{-1} to 4002.57 cm^{-1} .

The UV-VIS spectra were recorded using a single beam CAMSPEC M501 UV-VIS spectrophotometer, and a quartz cell of 1 cm path length. Due to a high absorbance a smallest droplet of cosmetic samples was mixed with distilled water obtaining solutions with the ratio of emulsion/distilled water presented in Table 1. As an illustration, we present measurements for a variety of cosmetics samples that includes two types of hair shampoo, anti-solar ultraviolet radiation creams with different standard protection factor, SPF of 15 and 25, three types of hand creams and one body cream. All these products are commonly commercially available, belong to different cosmetics producers and were purchased from the local specific market. The observed cosmetics present dispersed into dispersion phases with similar or different network dynamics according to i) their compositions, common components like water, glycerol, liquid paraffin or particular components like perfumes and ii) most important, the interactions between these components. For example, glycerin is a neutral, sweet-tasting, colorless, thick liquid which freezes to a gummy paste and which has a high boiling point and can be dissolved into water or alcohol, but not oils. On the other hand, many things will dissolve easier into glycerin so can be characterized as a good solvent. Glycerin is also highly hygroscopic, which means that it absorbs water from the air, an important characteristic for moistening the cosmetics [5].

Table 1. The investigated cosmetic samples: name, associated label and emulsion/distilled-water ratio for UV-VIS measurements.

Sample Name	Sample Label	emulsion/distilled-water [mg/ml]
Hair shampoo 1	A	3.56
Hair shampoo 2	B	1.66
Anti UV shielding cream SPF 15	C	1.53
Anti UV shielding cream SPF 25	D	-
Hand cream 1	E	0.93
Hand cream 2	F	3.56
Hand cream 3	G	1.33
Body cream	H	-

ACKNOWLEDGMENTS

This work was supported by CNCSIS –UEFISCDI, project number PN II – IDEI code 307/2011. R.F. would like to thank Prof. Dr. B. Blümich for useful dissections related to NMR-MOUSE applications.

REFERENCES

1. Report on Carcinogens U.S. Department of Health and Human Services, 10th edn. Public Health Service, National Toxicology Program, **2002**.
2. G. Ellen, In: Eisenbrand G, Bozler G, Nicolai HV (eds) The significance of N-nitrosation of Drugs. Gustav Fischer Verlag, Stuttgart, **1997**, 19–46.
3. Ellen G, Egmond E, van Loon JW, Sahertian ET, Tolsma K, *Food Addit Contam*, **1990**, 7, 207–221.
4. Stephany RW, Schuller PL, *Oncology*, **1980**, 37, 203–210.
5. A.O. Barel, M. Paye, H.I. Maibach, Informa Healthcare USA, New York, **2009** (and references therein).
6. Bernard P. Binks, Modern aspects of Emulsion Science, The Royal Society of Chemistry, Cambridge, **1998**.
7. Gary E. LeGrow, W. Leonard Terry, US Patent No 6, **2002**, 351, 867.
8. M. Sjöberg, L. Bergström, A. Larsson, and E. Sjöström. *Colloids Surf. A, Physicochemical Eng. Asp.*, **1999**, 159, 197–208.
9. K.D. Bremecker, B. Koch, W. Krause, and L. Neuenroth. *Pharm. Ind.*, **1992**, 54, 182.
10. J.Y. Kim, J.Y. Song, E.J. Lee, and S.K. Park. *Colloid and Polymer Science*, **2003**, 281, 614.
11. M. Yonese. In Y. Osada and K. Kajiwara (eds.), *Gels Handbook*. Vol. 3, Academic Press, San Diego, CA, **2001**, 230–240.
12. S. Ding, *Pharmaceutical. Science. Technology Today*, **1998**, 1, 328.
13. N. Cioica, R. Fechet, R. Chelcea, C. Cota, M. Todica, C.V. Pop, O. Cozar, *Studia UBB Chemia*, **2015**, 60 (1), 45-55.
14. D. Moldovan, M. Pop, A. Baudouine, M. Todica, *Studia UBB Chemia*, **2011**, 56 (3) 103.
15. F. Balibanu, K. Hialu, R. Eynaël, D.E. Demco, B. Blümich, *Journal of Magnetic Resonance*, **2000**, 145, 246.
16. P.J. McDonald, *Progress in Nuclear Magnetic Resonance Spectroscopy*, **1997**, 30, 69 (and references therein).
17. R.L. Klinberg, A. Sezginer, D.D. Griffin, M. Fukuhara, *Journal of Magnetic Resonance*, **1992**, 97, 466-485.
18. G. Eidmann, R. Savelsberg, P. Blümmler, B. Blümich, *Journal of Magnetic Resonance. A.*, **1992**, 122, 104-109.

19. B. Blümich, V. Anferov, S. Anferova, M. Klein, R. Fechete, M. Adams, F. Casanova, *Magnetic Resonance Engineering*, **2002**, 15(4), 255.
20. B. Blümich, V. Anferov, S. Anferova, M. Klein, R. Fechete, *Macromolecular Materials Engineering*, **2003**, 288(4), 312.
21. G. Guthausen, A. Guthausen, F. Balibanu, R. Eymael, K. Hailu, U. Schmitz, and B. Blümich. *Macromolecular Materials Engineering*, **2000**, 276/277, 25.
22. K. Hailu, R. Fechete, D.E. Demco B. Blümich, *Solid State Nuclear Magnetic Resonance*, **2002**, 22, 327.
23. N.O. Goga, A. Pirnau, L. Szabo, R. Smeets, D. Riediger, O. Cozar, B. Blumich, *Journal Optoelectronic Advanced Materials*, **2006**, 8(4), 1430.
24. M. Todica, *Journal Optoelectronic Advanced Materials*, **2007**, 9(3), 633.
25. H. Heise, D. Sakellariou, C.A. Meriles, A.J. Moulé, *Journal of Magnetic Resonance*, **2001**, 156, 146.
26. B. Blümich, F. Casanova, J. Perlo, S. Anferova, V. Anferov, K. Kremer, N. Goga, K. Kupferschläger, M. Adams, *Magnetic Resonance Imaging*, **2005**, 23, 197–201.
27. G. Goelman, and M.G. Prammer, *Journal of Magnetic Resonance. A.*, **1995**, 113, 11.
28. Y.Q. Song, L. Venkataramanan, M.D. Hürlimann, M. Flaum, P. Frulla, and C. Straley, *Journal of Magnetic Resonance*, **2002**, 154, 261.
29. M.D. Hürlimann, M. Flaum, L. Venkataramanan, C. Flaum, R. Freedman, G.J. Hirasaki, *Magnetic Resonance Imaging*, **2003**, 21, 305.
30. C.A. Meriles, D. Sakellariou, H. Heise, A.J. Moulé, A. Pines, *Science*, **2001**, 293, 82-85.
31. J. Perlo, F. Casanova, B. Blümich, *Science*, **2007**, 315, 1110 – 1112.
32. P.T. Callaghan, *Translational Dynamics and Magnetic Resonance*, **2011**, Oxford University Press.
33. M. Hürlimann, L. Burcaw, Y.Q. Song, *Journal of Colloid Interface Science*, **2006**, 297, 303.
34. S. Pasiczna-Patkowska, T. Olejnik, *Annales Universitatis Mariae Curie-Skłodowska Lublin – Polonia*, **2013**, 68, 95-106.
35. K.E. Washburn, P.T. Callaghan, *Journal of Magnetic Resonance* **2007**, 186, 337.
36. N. Marigheto, L. Venturi, D. Hibberd, K.M. Wright, G. Ferrante, B.P. Hills, *Journal of Magnetic Resonance*, **2007**, 186, 327.
37. R.I. Chelcea, R. Fechete, E. Culea, D.E. Demco and B. Blümich, *Journal of Magnetic Resonance*, **2009**, 196, 178.
38. G.C. Borgia, R.J.S. Brown, and P. Fantazzini, *Journal of Magnetic Resonance*, **1998**, 132, 65.

RESVERATROL AND LORATADINE EFFECTS ON OXIDATIVE STRESS INDUCED BY EXPERIMENTAL INFLAMMATION

DANIELA-RODICA MITREA^{a,*}, SIMONA CLICHICI^a,
ADRIANA FILIP^a, DIANA OLTEANU^a, IOANA BÂLDEA^a,
REMUS MOLDOVAN^a, NICOLETA DECEA^a, OANA-ALINA HOTEIUC^a

ABSTRACT. Resveratrol is a polyphenol with important antioxidant and anti-inflammatory roles. Loratadine, as a selective inverse-agonist of peripheral receptor H₁, is described as an anti-allergic substance with potential anti-inflammatory effects. We aimed to assess the protective capacity of loratadine against oxidative stress produced by inflammation with carrageenan in comparison with a well-known antioxidant compound, resveratrol.

Our results showed that resveratrol and loratadine had no protective anti-inflammatory effects in inflamed skin. As expected, resveratrol had antioxidant effects in serum and in liver. Loratadine developed oxidative stress in tegument and serum.

In this experimental model, our results do not sustain the initial hypothesis that loratadine could have a protective effect in inflammation, and, in the contrary, is capable of increasing it, by producing an oxidative stress.

Keywords: *antioxidants, inflammation, loratadine, oxidative stress, resveratrol*

INTRODUCTION

Inflammation is a common process characterized by vasodilation, leukocytes infiltration and cytokines release and, also by reactive oxygen species production that in turn can initiate or maintain the inflammatory process. Histamine is one of the chemical mediators that are immediately

^a Iuliu Hațieganu University of Medicine and Pharmacy, Department of Physiology, 1 Clinicilor Street, 400006 Cluj-Napoca, Romania

* Corresponding author: rdmitrea@yahoo.co.uk

released after basophils and mast cells activation that occurs during inflammation. Histamine interacts with histamine receptors that are part of GPCRs (G-protein coupled receptors) that will stimulate the Ca^{++} release from endoplasmic reticulum. The intracellular increase of Ca^{++} concentration allows the amplification of inflammation [1]. Resveratrol (trans-3,4',5-trihydroxystilbene) is a natural polyphenol with antioxidant and some anti-inflammatory effects. Resveratrol has anti-inflammatory effects due to its capacity of inhibiting the pro-inflammatory mediators and the enzymes responsible for the synthesis of these mediators. Resveratrol inhibits transcription factor NF- κ B (Nuclear Factor kappa-light chain enhancer of activated B cells), a protein complex involved in cellular response to noxious stimuli that regulates genes responsible for immunity and oxidative stress [2] [3]. Resveratrol also inhibits some activated immune cells [4]. Loratadine (selective inverse-agonist of peripheral receptor H_1) is used in allergy treatment. Desloratadine, the active metabolite of loratadine, also inhibits the basal and histamine-increased activity of NF- κ B [5].

Our study used resveratrol and loratadine to test their efficiency in neutralization of the oxidative stress generated by inflammation, induced by carrageenan injections. The study has on its basis the idea that resveratrol has an important antioxidant role and anti-inflammatory effects. Loratadine was described in literature as anti-inflammatory agent in several allergic diseases and based on these data, the study aim to explore the antioxidant and anti-inflammatory effect of loratadine on a model of experimentally induced inflammation, in comparison with the well-studied effect of resveratrol.

In our study, oxidative stress was evaluated through the measurement of the parameters of pro-oxidant and anti-oxidant statuses and a paw inflammation was produced to assess if the pre-treatment using these compounds can be useful in the reducing of the development of inflammatory lesions.

RESULTS AND DISCUSSION

Plethysmometry

The measurements made at two hours after inflammation of the posterior right paw, presented a significant increase of the paw volume in rats that received resveratrol and in the group that received loratadine, in comparison with the Control group that suffered only inflammation without treatment. There were not recorded significant differences between the rats treated with resveratrol or with loratadine.

The plethysmometric values at 24 hours after inflammation showed minor modifications among the groups, without significant differences (Figure 1).

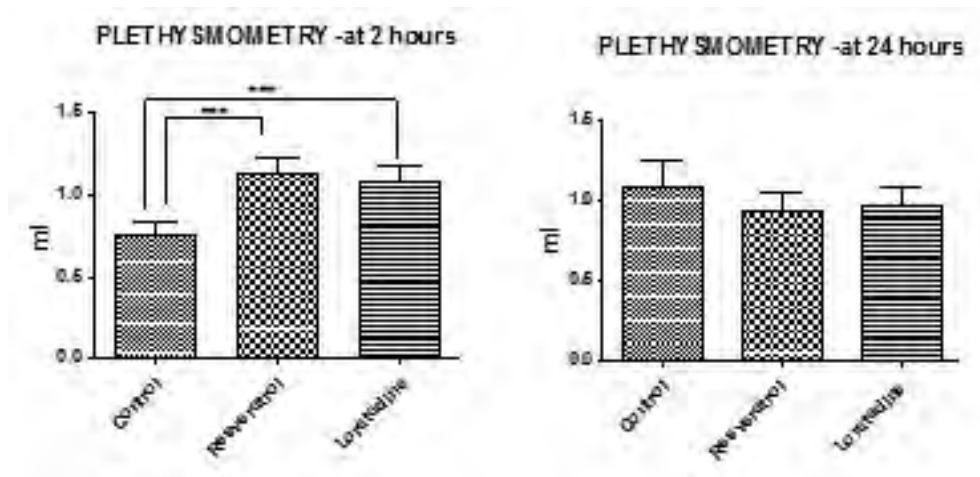


Figure 1. Plethysmometry at 2 hours and 24 hours after inflammation with carrageenan.

Oxidative stress investigation

Inflamed tegument

Loratadine significantly increased the MDA (malondialdehyde) levels in inflamed tissue, in comparison with the Control group, rats that suffered inflammation of the paw, without any other treatment ($p < 0.001$).

The concentration of glutathione (GSH) enhanced significantly in inflamed paws, in rats treated with resveratrol ($p < 0.01$) and in rats treated with loratadine ($p < 0.05$), in comparison with Control group. The group that previously received resveratrol had significant increases of the glutathione disulfide (GSSG) in comparison with the group that did not receive medication, but also in comparison with Loratadine group ($p < 0.05$). GSSG is a compound that gives information about the usage of GSH during oxidative stress reactions. The ratio between GSH (glutathione) and GSSG (glutathione disulfide) did not have significant results among the groups of rats ($p > 0.05$).

The 2,2-diphenyl-1-picrylhydrazyl (DPPH) free radical scavenging and catalase activity did not have significant modifications among the groups ($p>0.05$) (Figure 2).

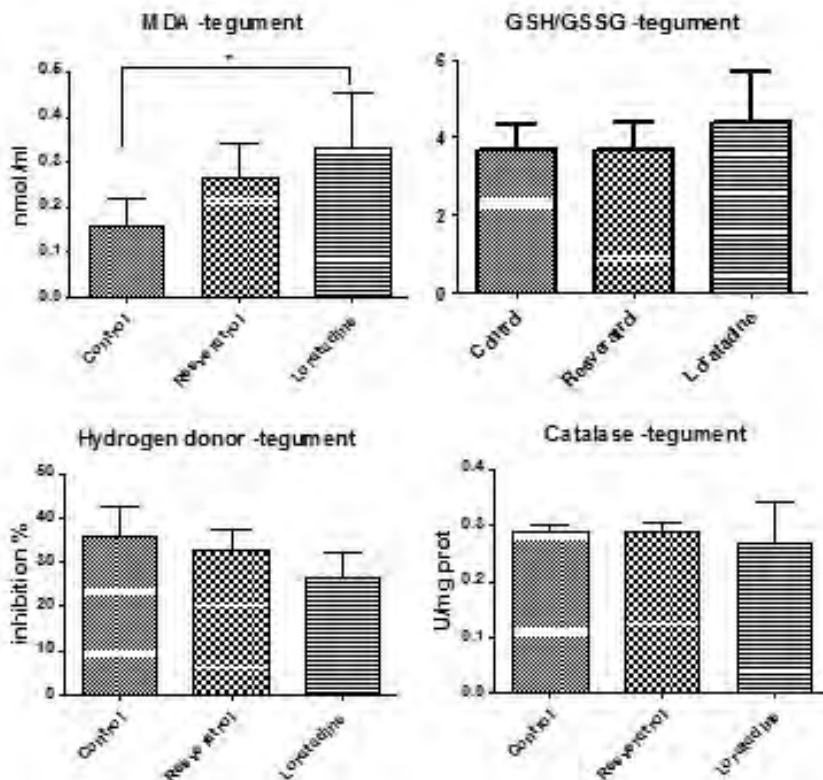


Figure 2. Malondialdehyde, ratio between glutathione and glutathione disulfide, hydrogen donor and catalase variations in inflamed tegument.

Serum

In serum, loratadine significantly increased the MDA level in comparison with resveratrol group ($p<0.05$). The modifications between Control and Loratadine groups, and the variations between Resveratrol and Control groups were not significant ($p>0.05$).

The serum level of glutathione significantly increased after both treatments used (resveratrol, loratadine), in comparison with Control group ($p<0.05$). Glutathione disulfide had no significant variation among the groups. The ratio between glutathione reduced and glutathione disulfide in serum was not influenced by the treatment with resveratrol or loratadine.

Hydrogen donor and catalase modifications were not significant in rat's serum ($p>0.05$) (Figure 3).

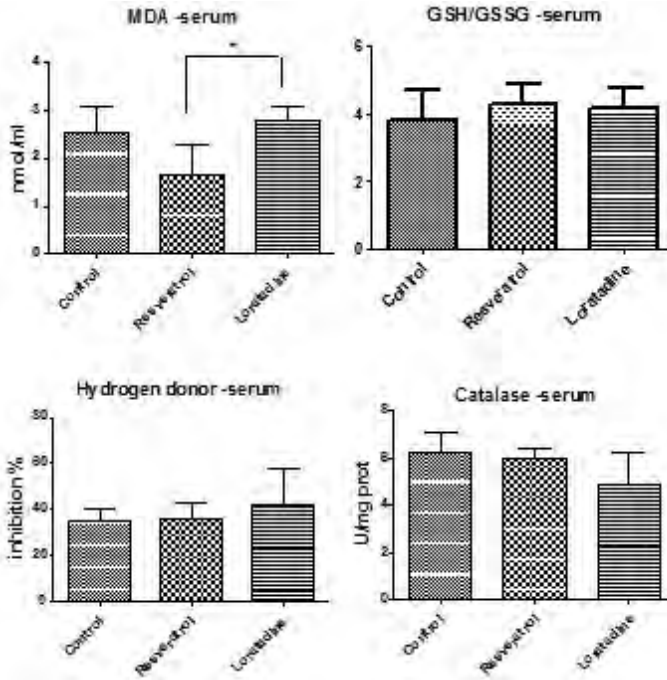


Figure 3. Malondialdehyde, ratio between glutathione and glutathione disulfide, hydrogen donor and catalase variations in serum of rats with paw tissue oedema.

Liver

Resveratrol and Loratadine groups did not present significant modifications in hepatic MDA level, in comparison with the Control group.

In liver, resveratrol and loratadine induced significantly decreases of GSH in comparison with Control group ($p<0.001$). There were no significant modifications between the Resveratrol and Loratadine groups for GSH concentration. Glutathione disulfide concentrations in rats that received medication (Resveratrol and Loratadine groups) decreased significantly in comparison with Control group. There were no significant variations between Resveratrol and Loratadine groups for GSSG concentration. The ratio GSH/GSSG presented a significant increase in Resveratrol group, in comparison with the Control group ($p<0.01$) (inflammation without medication). The ratio was not significantly increased in Loratadine group.

The DPPH free radical scavenging test had not significant modifications.

Resveratrol produced significant increases of liver catalase activity in comparison with the Control group ($p < 0.05$) and Loratadine group ($p < 0.01$) (Figure 4).

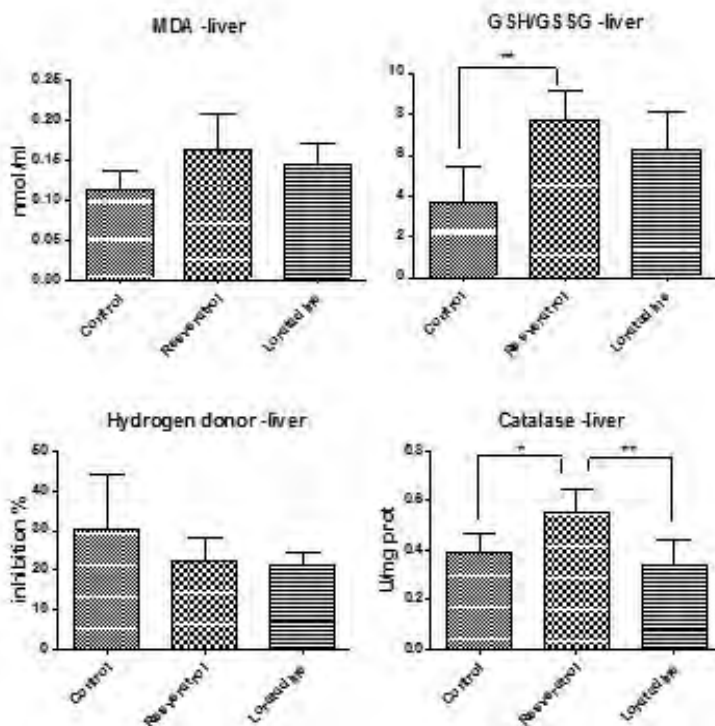


Figure 4. Malondialdehyde, ratio between glutathione and glutathione disulfide, hydrogen donor and catalase variations in the liver of rats with inflamed paw.

Histamine represents the main mediator in inflammation. Loratadine, being a selective inverse-agonist of peripheral receptor H_1 , could present some anti-inflammatory effects. Knowing the relationship between inflammation and oxidative stress, we decided to evaluate the loratadine effects on these processes, and at the same time, to compare its effects with those of a well-known antioxidant: resveratrol.

In our research, we investigated the oxidative stress parameters in serum, hepatic tissue and tegument tissue in rats with daily administration of resveratrol or loratadine, in experimental inflammation induced by carrageenan in rats.

It is known that carrageenan produces free radicals that can lead to lipid peroxidation (MDA production), histamine, serotonin and bradykinin release, NO synthesis (through activation of NF- κ B that leads also to IL_s and TNF α release), and tissue infiltration with neutrophils. Nitric oxide (NO) is reactive nitrogen specie that can react with many other molecules, increasing the oxidative stress; nitric oxide also produces oedema (through vasodilation) and PG release [6].

Resveratrol is a polyphenol known for its antioxidant and some pro-oxidant effects [7]. In our study, after resveratrol administration, GSH was increased in serum and inflamed paw's tegument, without a significant variation of the ratio GSH/GSSG, proving an antioxidant potential. In the liver, both GSH and GSSG are reduced, with the significantly increase of GSH/GSSG ratio. The glutathione increase in comparison with glutathione disulfide, in our experiment, is in concordance with the study that was made by Martins et al [8] using resveratrol in activated hepatic stellate cells, that established that this polyphenol does not induce GSH oxidation. The significant decrease of GSH in the liver is realized through the GSH action against the reactive oxygen species (e.g. peroxyxynitrite) as it was also seen in many other studies [9][10][11]. Reduced glutathione ensures cellular protection against intracellular pro-oxidant molecules. The same results were seen in literature, with the hypothesis that resveratrol can modulate the expression of genes and proteins that are involved in tolerance to oxidative stress [12]. The catalase activity in the liver is significantly increased by resveratrol, in comparison with all other groups. This result is in concordance with studies performed in diabetic rats with liver injury [13] and in senescence-accelerated mice [14] that proved that resveratrol increases the CAT and GSH concentration in liver.

The data concerning the role of resveratrol upon inflammation are contradictory. Poulsen et al [15] and Semba et al [16] established through their researches that resveratrol does not have effects on inflammation. In addition, Gentilli et al [17] established on their model developed on rats that resveratrol administration in inflammation with carrageenan did not have effects on swelling of the paw. On the other hand, Martin et al [18] found that administration of 10 mg/kg/day of resveratrol reduced chronic inflammation developed on a colitis model. Resveratrol significantly reduces in serum IL-6 and the expression of IL-1 β and TNF α [19].

In our study, plethysmometry performed at 2 hours after carrageenan injection shown an increase of paw's oedema under the treatment with resveratrol, indirectly emphasizing the absence of a beneficial effect upon the inflammatory process.

Loratadine, as a selective inverse agonist of peripheral H₁-receptors, binds to H₁-receptors and reduces their activity [20]. Loratadine has no effect on the histamine concentration in the tissue; it does not prevent the histamine release from an inflamed tissue. Histamine is released from damaged cells and, in comparison with other tissues, its concentration in the tegument is higher.

In our experiment, loratadine significantly increased the paw's oedema measured through plethysmometry at 2 hours after carrageenan injection. Carrageenan produced free radicals that activate nuclear Factor kappa light chain enhancer of activated B cells (NF-κB) that regulates inflammation through nitric oxide synthesis (NO can promote prostaglandin release, vasodilation, oedema, new reactive species synthesis), cyclooxygenase activation, the release of TNFα, IL-1β. Desloratadine, the metabolite of loratadine can inhibit the activity of H₁-receptors, blocking the NF-κB activation, leading to an inhibition of cytokines release [21]. Histamine, serotonin, and bradykinin are the first measurable mediators produced in carrageenan inflammation. Later, prostaglandin, lysosomal enzymes and protease are released. The significant increase of paw inflammation in rats that received loratadine cannot be explained by these mechanisms presented in literature. However, carrageenan, through free radicals, promotes lipid peroxidation that can lead to oedema, and it directly causes neutrophil infiltration that can produce new oxygen species (like superoxide) that continue the inflammation processes. Cheng et al [22] established on an experimental model performed on A549 cells that loratadine has anti-inflammatory effects through inhibition of IL-8. Amsellen et al [23] evaluated the loratadine effects on PMN co-cultured with HAEC and assessed that anti-inflammatory effect is realized through reduction of LTB₄ synthesis by neutrophils. From the best of our knowledge, loratadine was not used in a study on inflammation with carrageenan in rats, and in our study, we established that the administration of this selective inverse agonist of peripheral H₁-receptors increases the paw's oedema. These differences between our experiment and other studies can be explained through the following effects. Loratadine increases the cytosolic calcium by releasing it from intracellular stores (calcium activates NF-κB, increases the cytokines release), partially inhibits the leukotrienes as Letari et al [24] assessed in their research performed in vitro on rat peritoneal macrophages. Naclerio [25] in a study performed on nasal challenge antigen model and Shroeder et al [26] in their research in vitro on human basophils established that loratadine reduces the release of histamine and PGD₂, but not significantly. The anti-inflammatory effects of loratadine are not efficient in reducing the inflammation, and it promotes a supplementary oxidative stress in the inflamed tissue. Loratadine inhibits H₁-receptors but does not inhibit the

histamine release. Loratadine and its metabolite desloratadine do not inhibit the release of PGD₂, cytokines, LTC₄ -factors that promote inflammation. In our study, loratadine administration significantly increased MDA concentration in comparison with the rats that suffered inflammation without treatment. This lipid peroxidation promoted the oedema that was found significantly increased through plethysmometry.

Regarding the effects of loratadine upon oxidative stress in our study, loratadine increased the GSH level in serum. These results are similarly to those found by Sadowska-Woda [27] in a study performed in vitro on human erythrocytes.

In liver, loratadine significantly decreased GSH and GSSG levels, without the modification of the GSH/GSSG ratio. These results indirectly prove the occurrence of oxidative stress, but the reactive species that were formed, were scavenged by GSH. Loratadine is processed in liver, and Yumibe et al [28] established through their experiment performed on human liver microsomes that at the first passage through this organ, loratadine is almost complete metabolized by cytochrome P450 to several substances, and one of these is desloratadine. CYP3A4 and CYP2D6 are the enzymes of the cytochrome P450 that mediate the metabolism of loratadine till the important active metabolite: decarboethoxyloratadine [29]. In literature, loratadine and its metabolites are presented like medications that can affect rarely the liver structures, and they can cause liver modifications when they are administrated with substances that can interfere with the cytochrome P450 enzymes. Our study assessed the presence of an oxidative stress that is neutralized by the scavenger activity made by GSH.

The performed experimental study is useful because our results complete the other researches data.

For the clinicians, the obtained data can help them in choosing the treatment. Anti-allergic treatment in persons that also develop an inflammation should be done with another anti-histaminic (loratadine administration gave discouraging results).

Further studies should be performed to identify more markers of inflammation that are stimulated or inhibited by resveratrol and loratadine.

CONCLUSIONS

In *inflamed skin*, resveratrol did not ensure protection, increasing the inflammation, and loratadine developed a supplementary oxidative stress increasing lipid peroxidation and inflammation.

In *serum*, resveratrol and loratadine had antioxidant effects, stimulating the production of GSH.

In *liver*, resveratrol had antioxidant activity, while loratadine developed a minor oxidative stress.

EXPERIMENTAL SECTION

Methods

24 adult male rats, Wistar breed, with weight 200-220 g, were randomly allocated into 3 groups, with eight rats in each group.

The cages were kept in the same room, in the same environmental standard conditions at 22 +/- 1° C, a daylight cycle of 12 hours, having, before the study, one week for adaptation to these conditions. The substances were administered by oral gavage, between 7 a.m. - 8 a.m. to all the rats. The experiments were done in the biobase of U.M.Ph. "Iuliu Hațieganu" Cluj-Napoca. All the procedures were performed with the approval of the Ethical Committee of U.M.Ph. "Iuliu Hațieganu" Cluj-Napoca and respected the Directive 86/609/EEC.

The groups were the following:

Control group -received physiological salt, 0.5 ml/day by oral gavage, for 14 days, at the same hour when the test groups received medication

Resveratrol group - for 14 days, received 50 mg/kg/day of resveratrol, through oral gavage (resveratrol gelatinous capsule, each capsule containing 100 mg dry extract 200:1 from *Polygonum cuspidatum* root, standard resveratrol 50%, Polypharma Industries S.R.L.)

Loratadine group - received 0.5 ml of solution containing 0.14 mg/kg/day of loratadine (Claritin) in physiological salt, by oral gavage, for 14 days. (Claritin: 10 mg of loratadine, Schering-Plough Labo N.V. Belgium).

On the 14th day of the treatment, after 30 minutes from the medication administration, all the rats were intraplantar injected with 0.2 ml of carrageenan 1% (fresh prepared solution of 1 % carrageenan in saline, Sigma-Aldrich Co. LLC, Germany), in the posterior right paw, to produce them a paw inflammation. The inflammation of the rat's paw was measured through plethysmometry using a (plethysmometer UGO BASILE North America, 7140). For all the rats, measures of the injected paw were done at 2 hours and 24 hours after the carrageenan administration. After the plethysmometry was done, the obtained values were used in the following formula:

$$\text{Anti-inflammatory activity (\%)} = [1 - \frac{\text{treated paw volume}}{\text{untreated paw volume}}] \cdot 100$$

In the day 15, the blood samples were taken and under anaesthesia with ketamine and xylazine (90 mg/kg b.w. ketamine and 10 mg/kg b.w. xylazine) paw's skin and liver were collected.

The oxidative stress was investigated in serum, inflamed paw's tissue and liver through the following parameters: malondialdehyde (MDA), glutathione (GSH), oxidised glutathione (GSSG), ratio GSH/GSSG, DPPH free radical scavenging method and catalase activity.

Malondialdehyde (MDA), product of lipid peroxidation was determined using the method of Conti [30]. Reduced glutathione (GSH) was determined using the method described by Hu [31] and oxidized glutathione (GSSG) using Vats' method [32]. The ratio GSH/GSSG was calculated, because it is an indicator of the oxidative stress. For DPPH test, the method of Janaszewska was used [33]. For evaluation of catalase activity the method described by Pippenger et al [34] was used.

The obtained data were statistically processed using GraphPad Prism version 5.03 for Windows, GraphPad Software, (San Diego California USA), performing One-way ANOVA followed by the Post-test Bonfferoni. It was set the threshold significance level at $p < 0.05$.

REFERENCES

1. M. Matsubara, *Biochem Pharmacol*, **2005**, 69, 433.
2. B. Tian, A.R. Brasier, *Recent Prog Horm Res*, **2003**, 58, 95.
3. A.R. Brasier, *Cardiovascular Toxicology*, **2006**, 6(2), 111.
4. S. Sas, D.K. Das, *Inflamm Allergy Drug Targets*, **2007**, 6 (3), 168.
5. R.L.Wu, J.C. Anthes, W. Kreutner, A.G. Harris, R.E. Jr. West, *Int Arch Allergy Immunol*, **2004**, 135 (4), 313.
6. F.R.F. Silva, C.M.P.G. Dore, C.T. Marques et al, *Carbohydrate Polymers*, **2010**, 79, 26.
7. C.A. De la Lastra, I. Villegas, *Biochemical Society Transactions*, **2007**, 35 (Pt 5), 1156.
8. L.A. Martins, B.P. Coelho, G. Behr, et al., *Cell Biochem Biophys*, **2014**, 68, 247.
9. C. Harris, J.M. Hansen, *Methods in Molecular Biology*, **2012**, 889, 325.
10. L. Yuan, N. Kaplowitz, *Molecular Aspects of Medicine*, **2009**, 30(1-2), 29.
11. H.J. Forman, H. Zhang, A. Rinna, *Molecular Aspects of Medicine*, **2009**, 30 (1-2), 1.
12. M. Ruweler, M. Gulden, E. Maser, M. Murias, H. Seibert, *Chemico-Biological Interactions*, **2009**, 182 (2-3), 128.
13. N. Hamadi, A. Mansour, M.H. Hassan, F. Khalifi-Touhami, O. Badary, *J Biochem Molecular Toxicology*, **2012**, 26(10), 384.

14. G. Liu, Z. Zhang, B. Yang, W. He, *Journal of Medicinal Plants Research*, **2012**, 6(2), 325.
15. M.M. Poulsen, P.F. Vestergaard, B.F. Clasen, et al., *Diabetes*, **2013**, 62, 1186.
16. R.D. Semba, L. Ferrucci, B. Bartali, et al., *JAMA Intern Med*, **2014**, 174(7), 1077.
17. M. Gentili, J.X. Mazoit, H. Bouaziz, et al., *Life Sci*, **2001**, 68(11), 1317-21.
18. A.R. Martin, I. Villegas, M. Sánchez-Hidalgo, C. Alarcón de la Lastra, *Br J Pharmacol*, **2006**, 147(8), 873.
19. J. Tomé-Carneiro, M. Larossa M, M.J. Yáñez-Gascón, et al., *Pharmacol Res*, **2013**, 72, 69.
20. R. Leurs, M.K. Church, M. Tagliatela, *Clinical and Experimental Allergy*, **2002**, 32(4), 489.
21. G.W. Canonica, M. Blaiss, *World Allergy Organ J*, **2011**, 4(2), 47-53.
22. K.C. Cheng, J.Y. Hsu, L.S. Fu, W.C. Chang, J.J. Chu, C.S. Chi, *J Microbiol Immunol Infect*, **2006**, 39, 206.
23. C. Amsellen, W. Czarlewski, M. Lagarde, Y. Pachéco, *Pulmonary Pharmacology & Therapeutics*, **1998**, 11(4), 245.
24. O. Letari, A. Miozzo, G. Folco, P.A. Belloni, A. Sala, G.E. Rovati, S. Nicosia, *Eur J Pharmacol*, **1994**, 15, 266(3), 219.
25. R.M. Naclerio, *Ann Allergy*, **1993**, 71(3), 292.
26. J.T. Schroeder JT, R.P. Schleimer, L.M. Lichtenstein, W. Keutner, *Clin Exp Allergy*, **2001**, 31(9), 1369.
27. I. Sadowska-Woda, B. Sychta, M. Rachel, E. Bieszczad-Bedrczuk, *Environmental Toxicology and Pharmacology*, **2010**, 30(2), 141.
28. N. Yumibe, K. Huie, K.J. Chen, M. Snow, R.P. Clement, M.N. Cayen, *Biochem Pharmacol*, **1996**, 51, 165.
29. B. Katchen, J. Crame, M. Chung, *Ann Allergy*, **1985**, 55, 393.
30. M. Conti, P.C. Morand, P. Levillain, A. Lemonnier, *Clinical Chemistry*, **1991**, 37, 1273.
31. M.L. Hu, *Methods in Enzymology*, **1994**, 233, 380.
32. P. Vats, V.K. Singh, S.S. Sing, *Aviation, Space and Environmental Medicine*, **2008**, 79 (12), 1106.
33. A. Janaszewska, G Bartosz, *Scandinavian Journal of Clinical and Laboratory Investigation*, **2002**, 62 (3), 231.
34. C.E. Pippenger, R. W. Browne, D. Armstrong, *Methods in Molecular Biology*, **1998**, 108, 299.

VALIDATION OF AN ALTERNATIVE METHOD FOR TOTAL NITROGEN ANALYSIS IN WATER SAMPLES

ADRIANA MUNTEAN^a, IRINA SMICAL^{b*}, ZOLTÁN TÖRÖK^c

ABSTRACT. The current study presents the analytical validation method and performance characteristics of visible molecular adsorption spectrophotometry in determining the nitrogen concentration in water samples after the catalytic oxidation under controlled temperature and pressure conditions, using potassium peroxodisulfate, according to Romanian standard SR EN ISO 11905-1:2003. The quality of the calibration range (the determination coefficient of the calibration curve, the linearity and homogeneity tests), the limit of detection, the limit of quantification, selectivity, robustness, recovery tests and the uncertainty calculation of the method allow the successful use of the method, using the specific conditions imposed by the analytical standard method.

Keywords: *total nitrogen, potassium peroxodisulfate, validation.*

INTRODUCTION

The Romanian regulation of monitoring the quality of surface waters [1] and various discharges of wastewaters into surface water [2] requires an analytical determination of nitrogen concentrations in various forms: ammonia, nitrate, nitrite, organic nitrogen, Kjeldhal nitrogen and total nitrogen (TN).

The analytical techniques for determining the various nitrogen forms are multiple (volumetric analysis, potentiometry, spectrophotometry, liquid chromatography etc.), but the applied procedures must be standardized, fully validated and internationally accepted.

^a *Maramureş Water Management System, Someş-Tisa Basinal Water Administration, 2 Aleea Hortensiei, Baia Mare City, Maramureş County, Romania*

^b *Faculty of Engineering, Technical University of Cluj-Napoca, North University Centre of Baia Mare, 62A Victor Babeş Street, Baia Mare City, Maramureş County, Romania*

^c *Faculty of Environmental Science and Engineering, Babeş-Bolyai University of Cluj-Napoca, 30 Fântânele Street, Cluj County, Romania*

* *Corresponding author: irina.smical@yahoo.com*

In many laboratories, the streamline of the analytical process refers to the implementation of the safe analytical procedures, and efficient cost reduction of the analysis. Thus, the determination of total nitrogen by catalytic oxidation up to nitrates (NO_3^-) under controlled temperature and pressure conditions using potassium peroxodisulfate ($\text{K}_2\text{S}_2\text{O}_8$), in accordance with the analysis SR EN ISO 11905-1: 2003, Annex C4 [4], has become usually applied as an alternative analytic method at digestion of water samples with Devarda alloy.

To ensure the results with high confidence level the implementation of a standardized method in an accredited laboratory is not enough, an assessment of fitness-for-purpose of the method by in-house confirmation is „sine-qua-non” [5, 6].

RESULTS AND DISCUSSION

The characteristics assessment of the calibration curve

The calibration was performed according to the standard method [4], in compliance with the scope of the work over the interval (0.5-5.0) $\text{mg L}^{-1}(\text{N-NO}_3^-)$. The working standard solutions were obtained by appropriate dilutions of the stock solution of 1000 $\text{mg N-NO}_3^-/\text{l}$ concentration, derived from potassium nitrate (extra-pure salt, Merck, Germany). The calibration curve (Figure 1) fits to the Beer's law and was drawn by plotting the typical values of the absorbance due to NO_3^- (obtained by subtracting the absorbance value measured at 275 nm from that at 210 nm) against N-NO_3^- concentration of the standards. By using the corrected absorbance of a sample, concentration was directly obtained from the calibration curve.

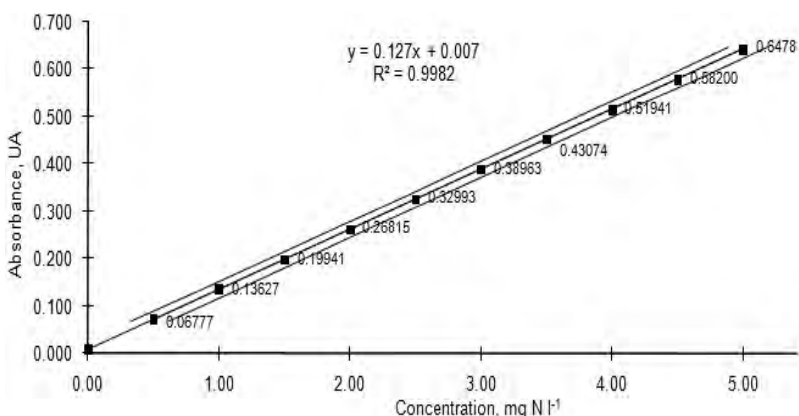


Figure 1. Regression curve and confidence interval

The assessment of the performance characteristics of the calibration curve (Table 1) fulfills the performance criteria [7, 8] in terms of linear range: slope, intercept, coefficient of determination, standard deviation, variation coefficient of the method, tests of homogeneity dispersion and linearity.

Table 1. The performance characteristics of the calibration function

Coefficient of determination (R^2)		0.9982	
The slope of the calibration function (sensitivity, b), *abs l mg ⁻¹		0.127	
The intercept (a, intersection with the axis Oy), *abs		0.007	
The residual standard deviation (s_y), mg l ⁻¹		0.009	
The standard deviation (s_{x0})		0.067	
The coefficient variation of the method (V_{x0}), %		0.025	
The homogeneity dispersions test			
$s_1^2 * 10^{-5}$	$s_{10}^2 * 10^{-5}$	PG**	F**(9;9;99%)
3.993	1.713	4.29	5.351
The linearity test			
PD***	DS ²	s_{y2}	F**(8;7;99%)
0.5778	0.00522	0.0090	6.719
Note: *abs – absorbance units; **PG - ratio factor of the homogeneity dispersions test (s_1/s_{10}); ***PD - ratio factor of the linearity test; **F (9; 9; 99%) – Fischer value, at significance level (99%) with 9, 8; and 7 degrees of freedom, respectively.			

The limit of detection (LOD) and the limit of quantification (LOQ)

The Romanian regulation in force [1] provides a maximum concentration of 1.5 mg L⁻¹ for the first class of surface waters. In accordance with this regulation, a target value for the quantification limit (LOQ) was set to 1.00 mg L⁻¹. The „3s criteria” - standard deviation multiplied by multiples of 3 - respectively 3, 6 or 9 times - was applied to determinate LOD and LOQ, respectively [10, 23, 24].

To estimate LOD, the standard deviation was multiplied by 6 times and to estimate LOQ, the standard deviation was multiplied by 9 times [10, 23, 24], from an experiment using simple replication of standard solution, at below of the expected LOD = 0.5 mg N-NO₃⁻¹ L⁻¹, as it is shown in Table 2.

10 individual samples of a mixed solution (MS) containing nitrogen from glycine, ammonium, nitrite and nitrate (each one with a contribution of 25% nitrogen, from reference material, NIST traceable) were analysed in order to determine the precision at the assumed LOQ level to $1 \text{ mg N-NO}_3^{-1} \text{ L}^{-1}$. The relative standard deviation (RSD, %), in terms of reproductibility, was 4.29% (<10%), the recovery was 103.1% (between 95% and 105%), both meeting the criteria of acceptability requirements imposed by the laboratory, as shown in the brackets.

Table 2. Results of the estimation of LOD and LOQ limits, using a standard solution of $0.5 \text{ mg N-NO}_3^{-1} \text{ L}^{-1}$

Minimum value, $\text{mg N-NO}_3^{-1} \text{ L}^{-1}$	0.430
Maximum value, $\text{mg N-NO}_3^{-1} \text{ L}^{-1}$	0.691
Mean value, $\text{mg N-NO}_3^{-1} \text{ L}^{-1}$	0.545
Median value, $\text{mg N-NO}_3^{-1} \text{ L}^{-1}$	0.538
Standard deviation (s), $\text{mg N-NO}_3^{-1} \text{ L}^{-1}$	0.0817
LOD = $6*s$, $\text{mg N-NO}_3^{-1} \text{ L}^{-1}$ (calculated)	0.4903
LOQ = $9*s$, $\text{mg N-NO}_3^{-1} \text{ L}^{-1}$ (calculated)	0.7354
Assumed LOD, $\text{mg N-NO}_3^{-1} \text{ L}^{-1}$	0.500
Assumed LOQ, $\text{mg N-NO}_3^{-1} \text{ L}^{-1}$	1.000

The specificity of the method was verified by testing the interference of the organic substances, in accordance with the standard method [4]. Five determinations were conducted using the synthetic samples with a concentration of 2 mg L^{-1} (N-NO_3^{-}), enriched in potassium hydrogen phthalate (it inhibits the ability of the potassium peroxodisulfate in oxidation reaction) with the following concentrations, expressed as COD: $50 \text{ mg O}_2/\text{l}$, $120 \text{ mg O}_2/\text{l}$ and $200 \text{ mg O}_2/\text{l}$. The test results (table 3) verify the standard provisions [4] and impose the recommendation to use the method only for water matrices having the chemical oxygen demand less than $120 \text{ mg O}_2/\text{l}$ or dilutions of them.

The selectivity of the method was verified by comparing the total nitrogen (TN) concentrations obtained by using two methods and analyzing two samples of water with different matrices: surface water and household wastewater. Admitting a bias of 5% between these two methods, the selectivity of this method can be confirmed.

Table 3. The specificity of the method

Characteristics	Mean, mg N L ⁻¹	Standard deviation, mg N L ⁻¹	RSDr, %	Acceptance condition [4]: RSDr, % ≤ 2.364
2 mg L ⁻¹ (N- NO ₃ ⁻) + 50 mg O ₂ /l	2.017	0.033	1.637	Fulfilled
2 mg L ⁻¹ (N- NO ₃ ⁻) +120 mg O ₂ /l	1.969	0.045	2.309	Fulfilled
2 mg L ⁻¹ (N- NO ₃ ⁻) +200 mg O ₂ /l	1.806	0.089	4.492	Not fulfilled

The first method allows the calculation of the total nitrogen by summing the nitrogen mineral forms: N-NH₄⁺ [19], N-NO₃⁻ [20], N-NO₂⁻ [21], and organic nitrogen, calculated from the difference of Kjeldahl nitrogen [22] and ammonia nitrogen. The second method - water samples mineralization with potassium peroxodisulphate - allows the direct determination of total nitrogen using the calibration curve (Figure 1). From each matrices of water, 3 replicates of the original sample were individually analyzed.

The results (table 4) show that the method is applicable to the proposed aim.

Table 4. The selectivity of the method

Water matrix	The analyzed nitrogen form	Concentration (mean of 3 replicates) mg N L ⁻¹	Acceptance condition: Bias, % ≤ ±5.00
Surface water	TN – present method	1.017±0.144*	1.017 = 0.968+4.82%
	Mineral nitrogen:	0.360	
	Ammonium (N-NH ₄ ⁺)	0.306	
	Nitrites (N-NO ₂ ⁻)	0.012	
	Nitrates (N-NO ₃ ⁻)	0.042	
Organic nitrogen	0.608		
Household wastewater	TN – present method	6.401±0.825*	6.401 = 6.544 - 2.23%
	Mineral nitrogen:	4.796	
	Ammonium (N-NH ₄ ⁺)	2.606	
	Nitrites (N-NO ₂ ⁻)	0.744	
	Nitrates (N-NO ₃ ⁻)	1.446	
Organic nitrogen	1.748		
Note: * - value of standard deviation in terms of repeatability			

For accuracy a certified reference material was used [15]. Usually, the difference between the certified value and the measured value (Δ_m) must be lower than the expanded uncertainty obtained by combining the certified uncertainty (u_{CRM}) with the uncertainty of repeatability measurements (u_m) [17, 23]. For evaluating the results obtained for CRM (Battle-02, River Water Sample, Environment Canada) the „2-sigma limit” criterion was used, because this criterion was used by the producer (Table 5).

Table 5. The results obtained by using CRM (mean \pm 2 sigma limit)

Certified value, mg N L ⁻¹	Measured value, mg N L ⁻¹
0.57 \pm 0.17	0.600 \pm 0.07

The precision of the method in terms of the repeatability (same operator, and equipment, on the same day) and reproducibility (different operators and equipment, in different days) was evaluated by the coefficient of variation and in accordance with the provisions of Appendix A of the standard method [4]. The results obtained from analyzing the 6 independent samples, are presented in Table 6.

Table 6. The precision method in terms of the repeatability and reproducibility

Sample	Standard, 2 mg L ⁻¹	Estuary (2.02 mg L ⁻¹) with addition of 15 mg L ⁻¹	Final effluent (6.401 mg L ⁻¹) with addition of 10 mg L ⁻¹
Mean, mg L ⁻¹	1.986	17.226	16.522
Found *s _r , mg L ⁻¹	0.038	0.327	0.171
Found **CV _r %	1.913	1.898	1.035
Imposed CV _r , %	2.364	2.252	1.195
Found **s _r , mg L ⁻¹	0.066	0.883	0.761
Found **CV _R %	3.323	4.662	4.605
Imposed CV _R , %	3.558	5.117	5.313

Note: *s_r, s_R – standard deviation in terms of repeatability or reproducibility; **CV_r, CV_R – coefficient of variation, in terms of repeatability or reproducibility

The recovery was verified in compliance with the standard method [4] provisions (Annex B) using solutions with nitrogen originated from ethylenediaminetetraacetic acid disodium salt (EDTANa₂) and urea (Table 7). Recovery fulfill the conditions of the standard method [4] in Annex B.

Table 7. Recovery of total nitrogen

EDTANa ₂ solution, 2 mg L ⁻¹	Urea solution, 2 mg N L ⁻¹	Glycine solution, 2 mg N L ⁻¹
Average of the 6 determination		
Recovery, %	Recovery, %	±0.20 mg N L ⁻¹
95.5	98.1	+0.16
93.2	95.8	+0.12
92.6	94.8	-0.10
Recommended: 87% ÷ 98%	Recommended: 91% ÷ 103%	2.00±0.20, mg N L ⁻¹
Fulfilled criterium.	Fulfilled criterium.	Fulfilled criterium.

The **uncertainty** of the method was assessed [9, 10, 14] using synthetic samples with a concentration at a quantification limit, LOQ = 1 mg N L⁻¹, and real matrices: surface water and wastewater.

All possible sources of uncertainty were identified. Using propagation of uncertainty the combined standard uncertainty was calculated. The extended uncertainty was calculated by multiplying the combined standard uncertainty with a coverage factor ($k = 2$ for a level of confidence of 95%) [9].

The sources of uncertainty during the analysis identified and quantified [9] by processing a surface water sample are: the mean concentration (of repeatability) of 10 samples, the calibration curve plotting (preparation standard and calibration), equipment (UV-VIS), laboratory glassware and degree of recovery.

For the mentioned samples the expanded relative uncertainty for determination of the total nitrogen by catalytic oxidation with potassium peroxodisulfate is 13.8 %.

The expanded relative uncertainty for determination of the total nitrogen by catalytic oxidation with potassium peroxodisulfate was assumed at 15 %.

CONCLUSIONS

The method presents an adequate alternative for the determination of the nitrogen in water samples in a relative short time, minimizing the analysis cost. The implementation of the method for current use in laboratory imposed the necessity of verifying of all the method performance characteristics so that the results provide a high level of confidence.

The performance parameters established and verified in laboratory, give objective evidences that the method is suitable for the purpose, and also that the standard method specifications are complied with and might provide results with a high confidence level.

EXPERIMENTAL SECTION

Method, equipment and materials

The principle of the standardized method [4] provides the oxidizing of the nitrogen forms up to nitrates (free and ammonia nitrogen, nitrates, nitrites and organic compounds with nitrogen) in water samples.

The mineralization of water samples (maximum of 50 ml of the water sample or dilution of sample) is carried out in heat-resistant glass bottles, in alkaline medium (pH = 9.7) with a mix solution (10 ml at 50 ml water samples) of potassium peroxodisulfate, boric acid and sodium hydroxide, in precise conditions of temperature (120 °C) and pressure (maximum 40 kP), in an autoclave, for 30 minutes.

After mineralization, the nitrogen concentration in the obtained solutions is determined from a calibration curve previously drawn using potassium nitrate solution (p.a., Merck manufacturer), in a concentration range of 0.5-5.0 mg N-NO₃⁻ L⁻¹. The procedure consists in measuring the net absorbance (nm) (subtract the value of the absorbance reading at 275 nm from the reading at 210 nm), by using ChemLab software of the molecular absorption spectrophotometer Agilent, type 8453, metrological tested and calibrated.

Analytical purity reagents (p.a.), certified solutions as reference materials, CertiPur Merck [11, 12, 13] and certified reference materials - Battle-02, River Water Sample, Environment Canada [11, 12, 13], glassware A class and benchmarked measurement equipment were used.

The performance characteristics of the calibration curve were established by the statistical testing of the dispersion linearity and homogeneity [7, 8]. The acceptability criteria of the other parameters analysed for the fitness-for-purpose are in accordance with the standard method [4], the European and international guides [9-18] regarding the quality assurance of analytical chemistry measurements.

REFERENCES

1. Ministerial Order no. 161 of 16 February **2006**, for approval of the *Norms on surface water quality classification in order to establish ecological status of the water bodies* (in Romanian).
2. Technical Framework of the Romanian Government for approval of the maximum limits loading with pollutant allowed at industrial and urban waste water evacuation in the natural receptors, **2002** web link: <http://www.gnm.ro/otherdocs/nsbhrtjqp.pdf>
3. SR ISO 10048:2001, *Water quality. Determination of nitrogen. Catalytic digestion after reduction with Devarda`s alloy.*
4. SR EN ISO 11905-1:2003, *Water quality. Determination of nitrogen. Part 1: method using oxidative digestion with peroxodisulfate. Annex C4 – Nitrates determination.*
5. SR EN ISO/CEI 17025:2005, *General requirements for the competence of testing and calibration laboratories.*
6. M., Omota, L., Lazarescu, C., Neamtu, *Bioflux, Proenvironment*, **2011**, 4, p. 131-138, web link: <http://journals.usamvcluj.ro/index.php/promediu/article/viewFile/6204/5637>.
7. SR ISO 8466-1:1999, *Water quality. Calibration and evaluation of analytical methods and estimation of performance characteristics. Part 1: Statistical evaluation of the linear calibration function.*
8. SR ISO 8466-2:1999, *Water quality. Calibration and evaluation of analytical methods and estimation of performance characteristics. Part 2: Calibration strategy for nonlinear second calibration function.*
9. Eurachem/CITAC Guide: *Quantifying Uncertainty in Analytical Measurement*, **2012**, available from: <http://www.eurachem.org>.
10. B. Magnusson and U. Örnemark (eds.) Eurachem Guide: *The Fitness for Purpose of Analytical Methods – A Laboratory Guide to Method Validation and Related Topics*, 2nd edition, **2014**, web link: <http://www.eurachem.org>.
11. Guide ISO 30:1992/Amd.1:2008, *Revision of definitions for references material and certified reference material.*
12. Guide ISO 32:1997, *Calibration in analytical chemistry and use of certified reference materials.*
13. Guide ISO 33:2000, *Uses of certified references materials.*
14. Guide ISO/CEI 98-3:2010, *Uncertainty of measurement - Part 3: Guide to the expression of uncertainty in measurement.*

15. SR ISO 5725-6:2002 – *Accuracy (trueness and precision) of measurement methods and results – Part 6: Use in practice of accuracy values.*
16. H., Hovind, B., Magnusson, M., Krysell, U., Lund, I., Makinen, „*Internal Quality Control – Handbook of Chemical Laboratories*”, **2011**, ed. 4th, p. 3- 25.
17. T., Linsinger, *Application Note 1, Comparison of a measurement results with certified value*, European Commission-Joint Research Center Institute for Reference Material and Measurements, **2005**, web link:
http://www.bam.de/en/fachthemen/referenzmaterialien/referenzmaterialien_m edien/erm_application_note_1_en.pdf
18. Journal AOAC Int, *Official Methods of Analysis Guidelines for Standard Method Performance Requirements*, **78(5)**, **2012**, web link:
http://www.aoac.org/imis15_prod/AOAC_Docs/StandardsDevelopment/Collab orative_Study_Validation_Guidelines.pdf
19. SR ISO 7150-1:2001 - *Water quality. Determination of ammonium. Part 1: Manual spectrometric method.*
20. SR EN 26777/C91:2006 - *Water quality - Determination of nitrite - Molecular absorption spectrometric method.*
21. SR ISO 7890-3:2000 - *Water quality. Determination of nitrate. Part 3: Spectrometric method using sulfosalicylic acid.*
22. SR EN 25663: 2000 - *Water quality. Determination of Kjeldahl nitrogen. Method after mineralization with selenium.*
23. L. Senila, M. Miclean, O. Cadar, M. Senila, M. Kovacs, M.A. Hoaghia, *Studia UBB Chemia*, **2016**, 61, 345.
24. C. Drăghici, C. Jelescu, C. Dima, C. Sică, E. Chirilă, S. Dobrinaș, A. Soceanu, *Studia UBB Chemia*, **2012**, 58, 93.

AFRICAN BAOBABS WITH A VERY LARGE NUMBER OF STEMS AND FALSE STEMS: RADIOCARBON INVESTIGATION OF THE BAOBAB OF WARANG

ADRIAN PATRUT^{a,*}, SÉBASTIEN GARNAUD^b, OUMAR KA^c,
ROXANA T. PATRUT^d, TOMAS DIAGNE^e, DANIEL A. LOWY^f,
EDIT FORIZS^a, JENŐ BODIS^a, KARL F. VON REDEN^g

ABSTRACT. The article presents the AMS (accelerator mass spectrometry) radiocarbon dating results of the baobab of Warang, Senegal. The investigation of the baobab revealed that it consists of 18 partially fused stems, which represents the largest number of stems reported for an African baobab. Three stems build the ring that closes a false cavity, while 15 stems grow outside the ring. Seven wood samples were collected from the false cavity and from the outer part of other stems. The dating results evinced that the stems belong to four different generations, out of which the first generation is around 500 years old. We also documented the presence of false stems, which emerge from a large adjacent stem, are triangular in horizontal section and act as an anchor. The baobab of Warang possesses 12 ordinary stems and 6 false stems.

Keywords: AMS radiocarbon dating, *Adansonia digitata*, tropical trees, multiple stems, age determination, inner cavity.

^a Babeş-Bolyai University, Faculty of Chemistry and Chemical Engineering, 11 Arany Janos, RO-400028, Cluj-Napoca, Romania

^b INECOBA, 8 Charles Vaillant, 93600 Aulnay-sous-Bois, France

^c Faculty of Sciences and Techniques, Cheikh Anta Diop University, Dakar, Senegal

^d Babeş-Bolyai University, Faculty of Biology and Geology, 44 Gheorghe Bilascu, RO-400015, Cluj-Napoca, Romania

^e African Chelonian Institute, P.O.Box 449, 33022 Ngaparou, Mbour, Senegal

^f Nova University, 5000 Dawes Ave., Alexandria, VA 22311, U.S.A.

^g NOSAMS Facility, Dept. of Geology & Geophysics, Woods Hole Oceanographic Institution, Woods Hole, MA 02543, U.S.A.

* Corresponding author: apatrut@gmail.com

INTRODUCTION

The African baobab (*Adansonia digitata* L.), which belongs to the Bombacoideae, a subfamily of Malvaceae, is the best-known and the biggest of the nine *Adansonia* species [1-3]. The African baobab has a natural distribution in the savanna regions of mainland Africa between the latitudes 16° N and 26° S. It is also found in African islands and outside Africa in tropical areas, where it has been introduced [1,2,4-7].

In 2005, we started an in-depth research in order to elucidate several controversial aspects regarding the architecture, growth and age of the African baobab. The research is based on our approach which also allows to investigate and date standing and live specimens. This approach involves the AMS radiocarbon dating of small wood samples collected from inner cavities and/or from deep incisions/entrances in the stems, fractured stems and from the outer part/exterior of large baobabs [8,9].

Due to the special ability of baobabs to produce stems periodically during their life cycle, over time they develop architectures of increasing complexity. The dating results have demonstrated that all large baobabs are multi-stemmed. We identified the open and closed ring-shaped structures, which are the most significant architectures that enable African baobabs to reach old ages and large sizes. We also disclosed for the first time the presence of false cavities, which are large natural empty spaces between fused stems that are disposed in a closed ring-shaped structure. The oldest investigated and dated *A. digitata* specimens were found to have ages greater than 2000 yr [10-13]. Dated growth rings of several African baobab specimens, which may act as a proxy climate archive, were used for past climate reconstruction in southern Africa [14,15].

The scientific name *Adansonia digitata* honours Michel Adanson, the French naturalist and explorer who documented and described the African baobab in its native habitat after his voyage to Senegal from 1749 to 1754. Even if Senegal possesses more baobab specimens than all countries from southern Africa, the number of significant surveys and scientific articles about the Senegalese baobabs was scarce over the past 50 years [16].

Here we present the investigation and the AMS radiocarbon dating results of the African baobab with the largest known number of stems, the baobab of Warang, Senegal.

RESULTS AND DISCUSSION

The baobab of Warang and its area. The large baobab is located in Warang village, at 7 km south of Mbour, in Thiès region, Senegal. The GPS coordinates of the tree are 14°22.250' N, 016°56.330' W and the altitude is 7 m. Mean annual rainfall in the area is 496 mm.

The baobab of Warang has a maximum height of 22.1 m, the circumference at breast height (cbh; at 1.30 m above ground level) is 28.69 m and the overall wood volume is around 250 m³ (**Figures 1 and 2**). It consists of 18 partially fused stems that can be relatively easily counted. Hence, it becomes the African baobab with the highest known number of stems. The baobab has a closed ring-shaped structure, with a false cavity defined by three stems, as well as other 15 additional stems. The false cavity is accessible via an opening that leads into a corridor delimited by two stems and then into the cavity. The false cavity is bell shaped, with a maximum height of 2.74 m and an ellipsoidal base with the axes of 2.02 x 2.13 m (**Figure 3**). The horizontal canopy dimensions are 33.6 x 29.1 m.

Wood samples. Two wood samples (labelled 1, 2) were collected from the walls of the false cavity. Other three samples (labelled 3-5) were collected from three different stems. Finally, two samples (labelled 6, 7) were collected from the deepest end/origin and from the middle of the largest false stem FS1. All samples were collected at convenient heights, between 0.96 and 1.28 m.

A number of eight small pieces/segments, of the length of 0.001 m each, were extracted from determined positions of the seven samples. Seven segments (1b, 2a, 3a, 4a, 5a, 6a, 7a, 8a) are close to the calculated pith and/or point of maximum age of the corresponding stems, while one segment (1a) correspond to an intermediate position inside stem 1.

AMS results and calibrated ages. Radiocarbon dates of the eight segments are listed in Table 1. Radiocarbon dates and errors were rounded to the nearest year. The radiocarbon dates are expressed in ¹⁴C yr BP (radiocarbon years before present, i.e., before the reference year AD 1950).

Calibrated (cal) ages, expressed in calendar years, are also disclosed in Table 1. The 1- σ probability distribution was selected to derive calibrated age ranges. For all sample segments, the 1- σ distribution is consistent with two, three or four ranges of calendar years. For these segments, the confidence interval of one range is considerably greater than that of the other(s); therefore, it was selected as the cal AD range of the segment for the purpose of this discussion. For obtaining single calendar age values of sample segments, we derived a mean calendar age of each segment from the selected range (marked in bold). Calendar ages of segments represent the difference between AD 2017 and the mean value of the selected range, with the corresponding error. Calendar ages and errors were rounded to the nearest 5 yr.



Figure 1. General view of the baobab of Warang taken from the west. The false stem 1 and the sampling positions 3 and 4 are marked.

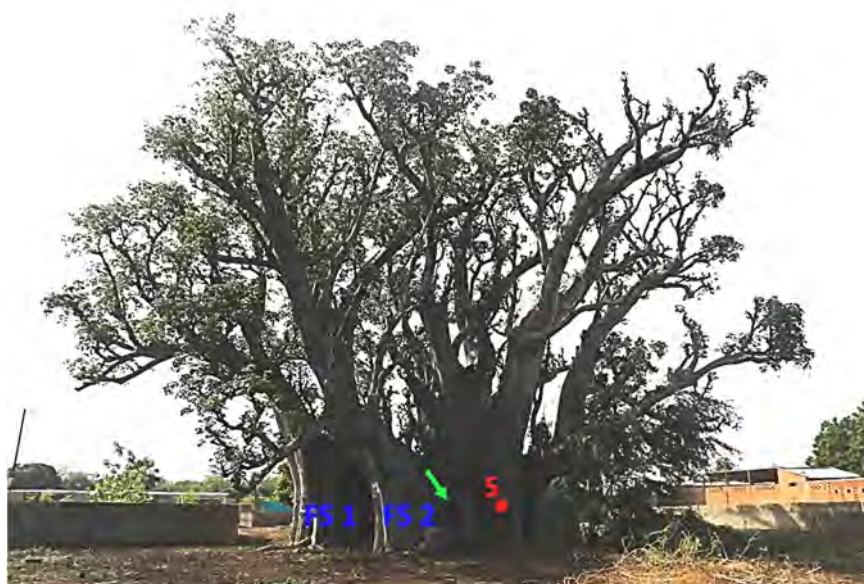


Figure 2. Another general view of the baobab of Warang taken from the east. The false stems 1 and 2 and the sampling position 5 are marked.

Table 1. AMS Radiocarbon dating results and calibrated calendar ages of samples/segments collected from the baobab of Warang.

Sample (Segment)	Depth ¹ [height ²] (10 ⁻² m)	Radiocarbon date [error] (¹⁴ C yr BP)	Cal AD range 1-σ [confidence interval]	Sample age [error] (cal yr)
1a	18 [96]	113 [± 22]	1692-1710 [10.6%] 1718-1728 [6.2%] 1812-1890 [45.7%] 1910-1920 [5.7%]	165 [± 40]
1b	40 [96]	324 [± 25]	1516-1596 [55.2%] 1618-1636 [13.0%]	460 [± 40]
2a	36 [104]	308 [± 20]	1522-1574 [52.9%] 1626-1642 [15.3%]	470 [± 30]
3a	44 [105]	235 [± 25]	1649-1666 [45.1%] 1784-1794 [23.1%]	360 [± 10]
4a	35 [110]	110 [± 21]	1694-1710 [10.7%] 1717-1726 [6.2%] 1813-1890 [46.6%] 1910-1917 [4.7%]	165 [± 40]
5a	54 [128]	330 [± 20]	1512-1528 [12.1%] 1544-1600 [42.2%] 1616-1636 [13.9%]	445 [± 30]
6a	30 [110]	262 [± 22]	1532-1536 [3.4%] 1636-1664 [64.8%]	365 [± 15]
7a	30 [110]	157 [± 24]	1670-1690 [12.4%] 1729-1779 [35.7%] 1798-1810 [7.8%] 1925-1943 [12.4%]	265 [± 25]

¹ Depth in the wood from the sampling point.

² Height above ground level.

Dating results of samples (segments). The oldest dated segments, 1b and 2a, that originate from two stems that build the false cavity, are close to the estimated points of maximum age. Their radiocarbon dates of 324 ± 25 and 308 ± 20 BP correspond to calibrated ages of 460 ± 40 and 470 ± 30 calendar yr. The segment 5a has a comparable age, i.e., 330 ± 20 BP, which corresponds to an age of 445 ± 30 calendar yr. The segment 3a has a lower radiocarbon date of 235 ± 25 BP and a calibrated age of 360 ± 10 yr. The radiocarbon date of 110 ± 21 BP of the youngest dated segment 4a corresponds to an age of only 165 ± 40 yr. We also dated two segments 6a and 7a, which originate from samples collected from the deepest end/origin and from the middle of the false stem FS1. Their radiocarbon dates of 262 ± 22 and 157 ± 24 BP correspond to calibrated ages of 365 ± 15 and 265 ± 25 calendar yr.



Figure 3. View of the false cavity which is defined by three stems. The sampling positions 1 and 2 are shown.

Ordinary and false stems. Prior to our research, the phenomenon of multiple stems among baobabs was mentioned only occasionally [1,17]. Visual observations suggest that typically only 15-25% of baobabs younger than 150-200 years have multiple stems. Nevertheless, radiocarbon results demonstrate that the vast majority of large and old baobabs are multi-stemmed. This is a consequence of the fact that, as baobabs age, single-stemmed specimens usually become multi-stemmed owing to the baobabs' ability to generate new stems periodically, such as other tree species produce branches. This phenomenon usually occurs naturally, when new stems periodically shoot from the roots or may emerge from fallen stems. In time, the new stems may fuse with older stem(s) or among them. Our investigations have revealed that all large baobabs, with a circumference over 16 m (corresponding to a formal diameter over 5 m), are multi-stemmed. Therefore, any attempt to estimate the baobab's age by measuring its size/circumference is meaningless.

The structure of old baobabs with fused stems can be determined by using radiocarbon dates and age sequences of samples collected from inner cavities and different areas of the trunk. In addition, one can perform a careful inspection of the multi-stemmed trunk, the canopy structure and the area/platform where the trunk divides into branches.

While often fused stems of multi-stemmed baobabs may prove to be difficult to identify, radiocarbon results indicate that several reported stems are in fact false stems. Hence, some large baobabs have peculiar structures that are triangular in horizontal section. Radiocarbon dating evinced that the oldest age can be found toward the upper contact with the larger adjacent stem, while the age decreases toward the opposite sharp extremity. This false stem, that plays the role of an anchor, is a special type of buttress, very different from the so-called buttress branch [1]. We named it also long triangular stem buttress (LTSB). The false stems emerge from a large trunk/stem and may reach horizontal lengths up to 3-5 m. The upper part extends upward obliquely and branches out, while the lower part merges with the root system. Certain baobabs have two adjacent false stems disposed in V-shape, with an opening of 30-60°. Such false stems are able to offer a much better stability in sandy soils. The false stems are much more common in northern Africa than in southern Africa.

The baobab of Warang possesses 12 ordinary stems and 6 false stems. Two of them are long false stems disposed in V-shape, which are marked FS1 and FS2 (**Figures 1, 2, 4**). Their horizontal lengths are 3.90 m (FS1) and 2.47 m (FS2). The radiocarbon dating results of segments 6a and 7a, extracted from the false stem FS1 (see Table 1), demonstrate that its oldest age is at the upper contact (6a) with the adjacent stem from which it emerged.

Age of the baobab of Warang. The ages of the oldest dated segments, 1b, 2a and 5a, which originate from three different stems, are between 445-470 yr. These values suggest an age of 500 ± 50 yr for the oldest stems of the baobab of Warang. The ages of segments 3a and 4a, i.e., 360 and 165 yr, indicate the existence of two other generations of stems that may be 350-400 and 150-200 yr old. The age of segment 6a shows that the longest false stem FS1 belongs to the generation which is 350-400 yr old. Other two stems of the baobab are much smaller and they seem to be up to 100 yr old. However, these stems are too young for an accurately dating by AMS radiocarbon.

Observations. Ten years ago, this large baobab was on a vacant land of Warang village, only 300 m away from the ocean shore. Over time, it was surrounded by a fence; in 2014, a local resident built a house at only 20 m from the baobab, thereby damaging some roots. We strongly believe that the national and local authorities should take urgent action for protecting this unique baobab and for preventing any further damage.

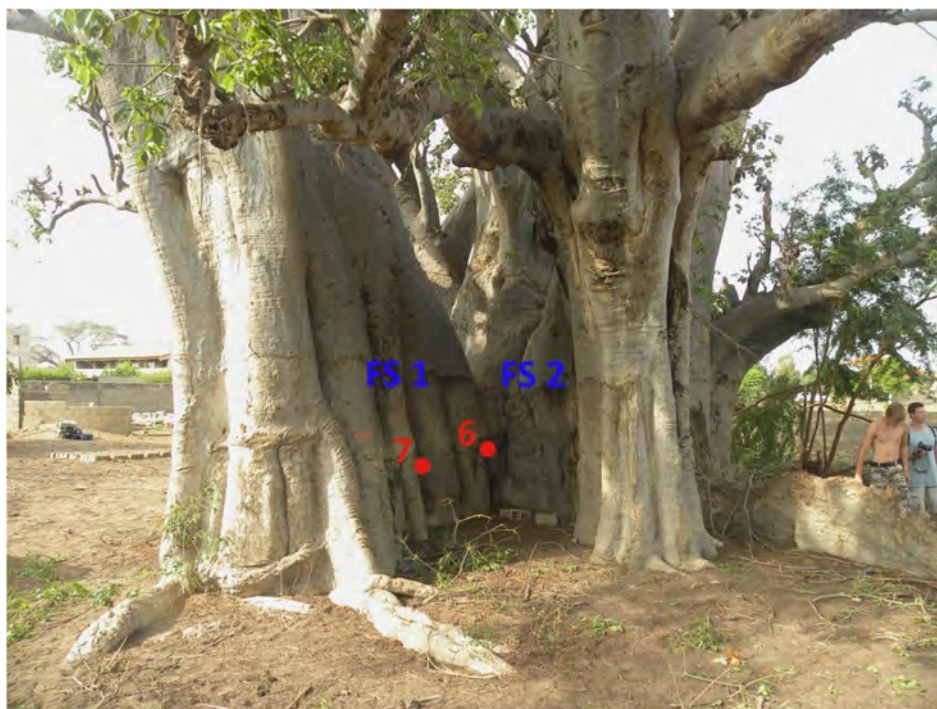


Figure 4. View of the two long false stems, FS1 and FS2, disposed in V-shape with an opening of 50°. The sampling positions 6 and 7 are shown.

One should also mention that, at a distance of only 103 m toward SW from the big baobab, stands another beautiful large baobab (14°22.232' N, 016°56.378' W; h = 24.2 m, cbh = 19.24 m), which is located on a private property.

CONCLUSIONS

The research discloses the AMS radiocarbon investigation results of the stoutest Senegalese baobab, the baobab of Warang. The investigation of this large tree shows that it has a closed ring-shaped structure defined by three stems, with a false cavity inside, as well as 15 additional stems. Seven wood samples were collected from the false inner cavity and from the outer part of stems. The dating results indicate that the stems belong to three different generations, to which a very young generation can be added.

The oldest stems, that belong to the first generation, are 500 ± 50 yr old. We documented for the first time the existence of false stems, which emerge from a larger adjacent stem. False stems, which are triangular in horizontal section, play the role of an anchor and offer a better stability, especially in sandy soils. The baobab of Warang has 12 ordinary stems and 6 false stems.

EXPERIMENTAL SECTION

Sample collection

The seven wood samples were collected with a Haglöf CH 600 increment borer (0.80 m long, 0.0054 m inner diameter). A number of eight tiny pieces/segments of the length of 0.001 m were extracted from predetermined positions along the wood samples. The segments were processed and investigated by AMS radiocarbon dating.

Sample preparation

The standard acid-base-acid pretreatment method was used for removing soluble and mobile organic components. The pretreated samples were combusted to CO_2 by using the closed tube combustion method. Then, CO_2 was reduced to graphite on iron catalyst, under hydrogen atmosphere. Finally, the resulting graphite samples were analysed by AMS [4, 18, 19].

AMS measurements

AMS radiocarbon measurements were performed at the NOSAMS Facility of the Woods Hole Oceanographic Institution (Woods Hole, MA, U.S.A.) by using the Pelletron ® Tandem 500 kV AMS system. The obtained fraction modern values, corrected for isotope fractionation with the normalized $\delta^{13}\text{C}$ value of -25‰ , were ultimately converted to a radiocarbon date.

Calibration

Radiocarbon dates were converted into calendar ages with OxCal v4.2 for Windows [20], using the IntCal13 atmospheric set [21].

ACKNOWLEDGMENTS

Authors thank The Ministry of Environment and of Nature Protection of Senegal and its Direction of National Parks for authorising the investigation and sampling of the baobab of Warang. The research was funded by the Romanian Ministry of National Education CNCS-UEFISCDI under grant PN-II-ID-PCE-2013-76.

REFERENCES

1. G.E. Wickens, P. Lowe, "The Baobabs: Pachycauls of Africa, Madagascar and Australia", Springer, Dordrecht, **2008**.
2. D.A. Baum, *Annals of the Missouri Botanical Garden*, **1995**, *82*, 440.
3. J.D. Pettigrew, L.K. Bell, A. Bhagwandin, E. Grinan, N. Jillani, J. Meyer, E. Wabuyele, C.E. Vickers, *Taxon*, **2013**, *61*, 1240.
4. A. Patrut, K.F. von Reden, D.A. Lowy, A.H. Alberts, J.W. Pohlman, R. Wittmann, D. Gerlach, L. Xu, C.S. Mitchell, *Tree Physiology*, **2007**, *27*, 1569.
6. A. Patrut, D.H. Mayne, K.F. von Reden, D.A. Lowy, R. Van Pelt, A.P. McNichol, M.L. Roberts, D. Margineanu, *Radiocarbon*, **2010**, *52*, 717.
7. A. Patrut, R.T. Patrut, L. Rakosy, J. Bodis, D.A. Lowy, E. Forizs, K.F. von Reden, *Studia UBB Chemia*, **2016**, *LXI*, *4*, 21.
8. A. Patrut, D.H. Mayne, K.F. von Reden, D.A. Lowy, S. Venter, A.P. McNichol, M.L. Roberts, D. Margineanu, *Radiocarbon*, **2010**, *52*, 727.
8. A. Patrut, K.F. von Reden, R. Van Pelt, D.H. Mayne, D.A. Lowy, D. Margineanu, *Annals of Forest Science*, **2011**, *68*, 993.
9. A. Patrut, S. Woodborne, K.F. von Reden, G. Hall, M. Hofmeyr, D. Lowy, R.T. Patrut, *PLoS ONE*, **2015**, *10(1)*, e0117193, doi: 10.1371/journal.pone.0117193.
10. A. Patrut, K.F. von Reden, D.H. Mayne, D.A. Lowy, R.T. Patrut, *Nuclear Instruments and Methods in Physics Research Section B*, **2013**, *294*, 622.
11. A. Patrut, S. Woodborne, R.T. Patrut, G. Hall, L. Rakosy, K.F. von Reden, D. Lowy, D. Margineanu, *Studia UBB Chemia*, **2015**, *LX*, *4*, 7.
12. A. Patrut, L. Rakosy, R.T. Patrut, I.A. Ratiu, E. Forizs, D.A. Lowy, D. Margineanu, K.F. von Reden, *Studia UBB Chemia*, **2016**, *LXI*, *4*, 7.
13. A. Patrut, S. Woodborne, K.F. von Reden, G. Hall, R.T. Patrut, L. Rakosy, P. Danthu, J-M. Leong Pock-Tsy, D.A. Lowy, D. Margineanu, *Radiocarbon*, **2016**, in press.
14. S. Woodborne, G. Hall, I. Robertson, A. Patrut, M. Rouault, N.J. Loader, M. Hofmeyr, *PLoS ONE*, **2015**, *10(5)*, e0124202. doi: 10.1371/journal.pone.0124202.
15. S. Woodborne, P. Gandiwa, G. Hall, A. Patrut, J. Finch, *PLoS ONE* **2016**, *11(7)*, e015936. doi:10.1371/journal.pone.0159361.
16. J.G. Adam, *Notes Africaines*, **1962**, *94*, 33.
17. N. Esterhuysen, J. von Breitenbach, H. Söhnge, "Remarkable Trees of South Africa", Briza, Pretoria, 2001.
18. A. Patrut, D.H. Mayne, K.F. von Reden, D.A. Lowy, S. Venter, A.P. McNichol, M.L. Roberts, D. Margineanu, *Radiocarbon*, **2010**, *52*, 727.
19. A. Patrut, S. Woodborne, K.F. von Reden, G. Hall, M. Hofmeyr, D. Lowy, R.T. Patrut, *PLoS ONE*, **2015**, *10(1)*, e0117193, doi: 10.1371/journal.pone.0117193.
20. C. Bronk Ramsey, *Radiocarbon*, **2009**, *51*, 337.
21. P.J. Reimer, E. Bard, A. Bayliss, J.W. Beck, P.G. Blackwell, C. Bronk Ramsey, C.E. Buck, H. Cheng, R. Lawrence Edwards, M. Friedrich, P.M. Grootes, T.P. Guilderson, H. Hafflidason, I. Hajdas, C. Hatté, T.J. Heaton, D.L. Hoffmann, A.G. Hogg, K.A. Hughen, K.F. Kaiser, B. Kromer, S.W. Manning, M. Niu, R.W. Reimer, D.A. Richards, E.M. Scott, J.R. Southon, R.A. Staff, C.S.M. Turney, J. van der Plicht, *Radiocarbon*, **2013**, *55*, 1869.

THE MINIMAL SET OF INTERMOLECULAR INTERACTIONS IN THE STRUCTURES OF SUBSTITUTED PROLINES

ALEXANDRU BANARU^{a,*}, ALEXANDER KOCHNEV^a

ABSTRACT. In this paper the calculation of intermolecular interaction energy based on Gavezzotti–Filippini semi-empirical method was performed for the series of substituted prolines. The initial structural data were mined from Cambridge Structural Database. The topology of each structure was analyzed with respect to a minimal generator set of the space group. It was shown that the least number of strong symmetrically independent interactions required to generate a crystal structure is likely to exceed the cardinality of a minimal generator set.

Keywords: *intermolecular interaction, lattice energy, space group generator, minimal generator set*

INTRODUCTION

Up to the moment the most powerful retrieval tool for structural data of organic compounds is Cambridge Structural Database, CSD [1]. Statistics based on CSD has following applications: crystal structure prediction, prediction of polymorphs, crystal engineering, a quantitative estimation of intermolecular interactions, justification of phase transitions, an insight into evaluable material properties etc. The database was established in 1965 and initially contained published results on structure determination by X-ray and neutron diffraction for compounds having at list one “organic” carbon atom. Thereafter this ambiguous criterion was moderated, and nowadays CSD contains, for instance, carbonyl complexes $M(\text{CO})_n$ of transition metals. Since the late 1990th, an unpublished data is also permitted if it satisfies certain requirements to the reliability. According to some estimates [2], the capacity

^a *Moscow State University, Chemistry Faculty, 1/3 Lenin Hills, 119991, Moscow, Russia*

* *Corresponding author: banaru@phys.chem.msu.ru*

of CSD may reach a million of crystal structures in the nearest future. Each structure is supplemented by a refcode of 6 letters, polymorphs having the same refcodes with slightly different numeric endings. A compound may have several refcodes attributed to, since the structure may be studied by different workgroups and under different conditions.

In the beginning of the XXth century Kitaigorodsky derived crystallographic symmetries favorable for a molecular packing [3]. Preferential symmetries lead to non-uniform distribution of crystal over the space groups [4, 5]. In particular, about a half of organic racemates crystallize in the space group $P2_1/c$ [5]. However, a molecular packing is hardly governed solely by the stereometric preferences that are more substantial for comparatively poor chemical interactions among molecules. More generally, interacting molecules do not recognize space groups but adapt to each other to minimize lattice energy. A space groups just restricts the number of symmetrically independent interactions formed by a given molecule in the crystal structure. In this work we gain an insight into correlation between the energy of intermolecular interactions and the space group.

SPACE GROUP GENERATORS

Space group generators are symmetry operations, whose various products (compositions) generate the whole space group [6]. A minimal generator set is that of the minimal cardinality N_G for a given space group, and $2 \leq N_G \leq 6$ [7]. Such sets are not presented in International crystallographic tables [6] but their cardinalities were calculated [8]. If a crystal consists of symmetrically equal molecules occupying a so-called general position (with the site symmetry of the point group C_1), then N_G equals the minimal number of symmetrically independent intermolecular interactions required for the formation of the corresponding crystal structure [7, 8]. Since such interactions are necessary, one could expect that they are the strongest by the energy of intermolecular interaction. In order to test this hypothesis, we are performing analysis of intermolecular interactions in the series of similar compounds. Do interaction energies satisfy the “broken stick model” [9]? According to this model, widely applicable in social sciences, the distribution of some discrete variable over sequence numbers should exhibit an extremum at the number setting bound to the most principal part of that sequence. The greatest intermolecular interaction energies U_1, U_2, \dots, U_n might exhibit a “brake of the stick” at $n = N_G$.

METHOD

Crystal structures were selected among proline derivatives because this amino acidic frame entails significant variety of intermolecular interactions. The search was performed in CSD ver.5.36 [1]. The following restrictions were applied to the molecular structure: 1) each is a proline ester, 2) each has less than 20 carbon atoms, 3) the chemical unit is sole (no hydrates, solvates etc.). Additionally, structures with no atomic coordinates were rejected. Totally 10 structures were found (Figure 1) and 2 pairs of polymorphs among them (3, 4 and 7, 8).

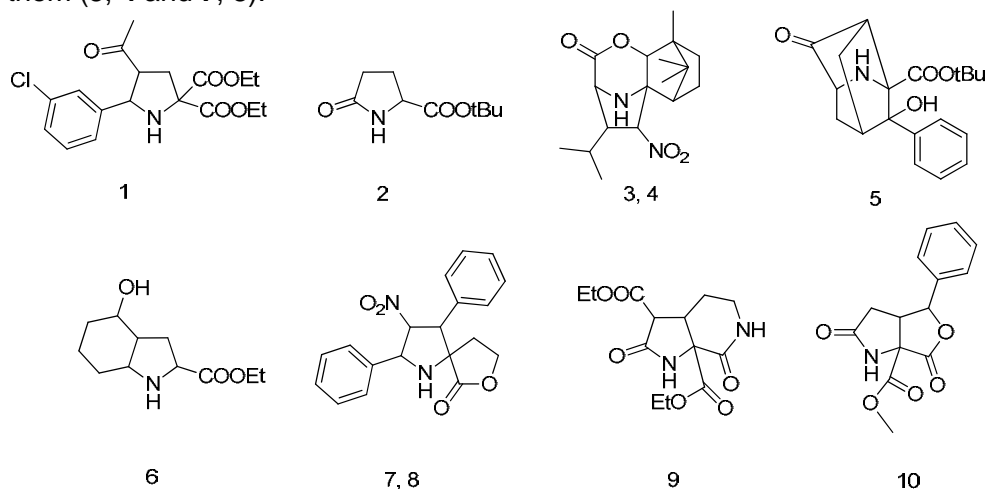


Figure 1. The structural formulas of 1-9

The computation of interaction energy was performed in Mercury [10] with the use of Gavezzotti–Filippini potential 6–exp [11]. In this approach the potential of intermolecular interaction U is the sum of all interatomic potentials between two molecules. Intramolecular interactions were being neglected. For the chart the 10 strongest contacts with the energies U_1, U_2, \dots, U_{10} were considered, because less strong contacts commonly share less than 1% of the lattice energy U_Σ . Denote $U_1 + U_2 + \dots + U_{10} = U_{\text{tot}} \approx U_\Sigma$. The “broken stick” implies that at some n the value of $\Delta U_n / U_{\text{tot}}$, where $\Delta U_n = U_{n+1} - U_n$, should change dramatically.

Each intermolecular interaction corresponds to some symmetry operation. Combining these operations, one can obtain a minimal generator set of the space group. In fact, this is a minimal set of interactions to form the crystal structure. Although for any space group there can be various minimal

sets, we select the only one in the following manner. Assume that such minimal set of interactions has an advantage if it contains interactions with the highest energy. Thus, we select a minimal set of interactions such that its 1st strong interaction is the strongest among all sets. If this point does not lead to a definite set, we select a set such that its 2nd strong interaction is the strongest among those in other sets, etc.

RESULTS AND DISCUSSION

In 6 structures there is an intermolecular H-bond forming either a molecular chain along a screw axis 2_1 (**2**, **5**, **8-9**) and along a translation (**6**), or a center-symmetric dimer (**10**). In each case, assuming that the strongest interaction is necessary for the observed molecular arrangement, the symmetry operator of the H-bond has to be also included in the minimal generator set of the space group (Table 1). If this operator was missing, the generator set would not be minimal. It is surprising that among polymorphs **7-8** H-bond is present just in the latter structure despite they have much more in common.

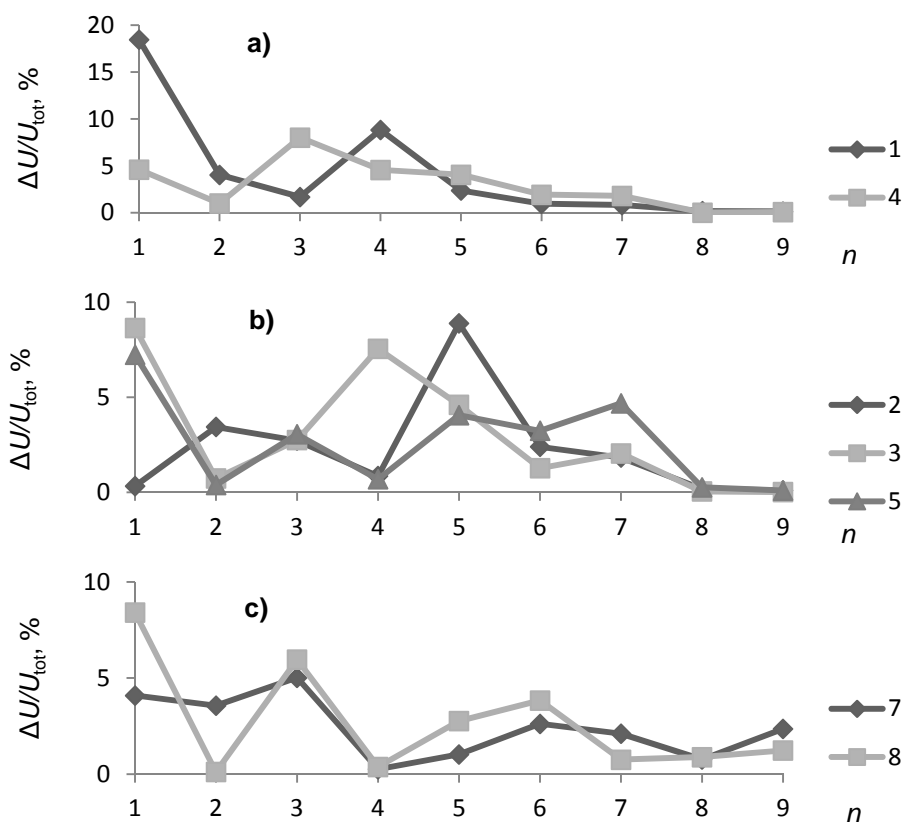
Table 1. Space group, Z , N_G and essential interactions* for the structures **1-10**

No	CSD refcode	Space group, Z	N_G	Essential intermolecular interactions along**
1	AZEFER	$P2_1, Z = 2$	3	I. Y II. $2_1 (1 y \frac{1}{2})$ III. $2_1 (1 y 0)$ IV. $2_1 (\frac{1}{2} y \frac{1}{2})$
2	DICXET	$P2_12_12_1, Z = 4$	2	I. X II. $2_1 (\frac{1}{2} y \frac{3}{4})$ III. $2_1 (x \frac{1}{4} 1)$
3	FONYUD	$P2_12_12_1, Z = 4$	2	I. X II. $2_1 (0 y \frac{1}{4})$ III. $2_1 (x \frac{1}{4} 0)$
4	FOXCUR	$P2_1, Z = 2$	3	I. Y II. $2_1 (0 y 0)$ III. $2_1 (\frac{1}{2} y \frac{1}{2})$ IV. $2_1 (\frac{1}{2} y 0)$
5	GUDBEM	$P2_12_12_1, Z = 4$	2	I. $2_1 (x \frac{1}{4} 1)$ II. $2_1 (1 y 1\frac{1}{4})$
6	HEQRIG	$P-1, Z = 2$	4	I. $X+Y$ II. Y III. $i (\frac{1}{2} \frac{1}{2} 0)$ IV. X V. $i (1 1 0)$ VI. $i (1 \frac{1}{2} 0)$ VII. $i (\frac{1}{2} 1 0)$ VIII. $i (\frac{1}{2} \frac{1}{2} \frac{1}{2})$
7	LOGHEV	$P2_1/c, Z = 4$	3	I. $2_1 (\frac{1}{2} y \frac{1}{4})$ II. $i (\frac{1}{2} \frac{1}{2} 0)$ III. X

8	LOJNOO	$P2_1/c$, $Z = 4$	3	<u>I. 2_1 ($\frac{1}{2} y \frac{1}{4}$)</u> II. i ($\frac{1}{2} \frac{1}{2} \frac{1}{2}$) III. X
9	MALREX	$Pbca$, $Z = 8$	3	<u>I. 2_1 ($x \frac{3}{4} 1$)</u> II. b ($\frac{3}{4} y z$) III. a ($x y \frac{3}{4}$)
10	POSMIV	$Pbca$, $Z = 8$	3	<u>I. i ($\frac{1}{2} \frac{1}{2} \frac{1}{2}$)</u> II. X III. i ($0 \frac{1}{2} \frac{1}{2}$) IV. a ($x y \frac{1}{4}$) V. b ($-\frac{1}{4} y z$)

*Assuming that stronger interactions are more advantageous as generators (see explanation in **METHOD**), the interactions are listed as energy decrease (I, II, etc.) till the space group is generated by the symmetry operations (generators) accounting for those interactions. The minimal set is shown in bold.

**X, Y, X+Y denote interactions of a molecule with those related by a corresponding translation; 2_1 – related by a screw axis; i – related by a center of inversion; a, b – related by a glide plane. Intermolecular H-bonds are shown underlined.



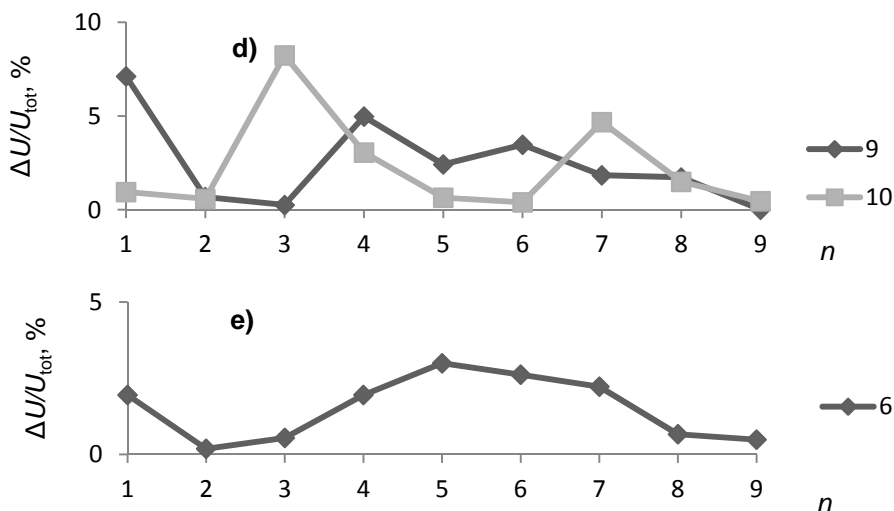


Figure 2. $\Delta U/U_{tot}$ (see explanation in **METHOD**) for the structures of space groups $P2_1$ (a), $P2_12_12_1$ (b), $P2_1/c$ (c), $Pbca$ (d), and $P-1$ (e)

In 4 structures (**1-4**) the 1st strong interaction cannot be included in the minimal generator set because this interaction corresponds to a translation, but not to a screw axis 2_1 in the same direction. While the screw axis can generate the translation: $2_{1(Y)}^2 = Y$, the screw axis cannot be generated by the translation itself. The mentioned result disproves the hypothesis that there should be a “brake of the cane” at the $(N_G + 1)$ th strong contact on the energy chart. On the other hand, in 4 structures (**5, 7-9**) the minimal set includes the 1st, 2nd, etc. strong contacts in a row. In other cases essential interactions are formed in addition to the minimal set, either one interaction (**1-4**), or more than one (**6, 10**). This means that actually the value of the minimal coordination number is commonly more than the number of generators of the space group.

There are intermolecular energy charts shown in Figure 2. Sometimes the maximal value of $\Delta U_n/U_{tot}$ without consideration of the 1st one indicates $n = N_G$ (**1, 7, 8**), but more commonly doesn't. The chart usually has a wavy shape with the floating “wavelength”. As a rule, falling from $n = 1$ to 2, the “wave” rises again at $n = 3$ or 4, and the next rise is at $n = 6$ or 7. As the average energy drops, the “wave” fades out. Since the maximal $\Delta U_n/U_{tot}$ in the majority of structures is located farther than $n = N_G$, distant interactions are to play a very important role in the formation of the crystal structure.

The structure **6** has the crucial intermolecular interaction with the extremely distant location ($n = 8$). It is the interaction over the center of inversion i ($\frac{1}{2} \frac{1}{2} \frac{1}{2}$). There is no possibility to exclude the 8th interaction from the minimal generator set. If it were not for this interaction, **6** would be a layered 2D crystal (XY). Actually, $P-1$ is itself a rather complicated group ($N_G = 4$), and a complicated system of interactions formed by its molecules is not so surprising. Nevertheless, this space group is commonly thought of as one of the simplest, because it belongs to the least symmetric crystal system (triclinic). These opposite points of view should be reconciled.

CONCLUSION

As it follows from the above section, the minimal number of intermolecular interactions is rarely equal to the N_G . It would be more definitive to count the least number of strong contacts sufficient to form a given structure. This entails enduring interest in the manual analysis of intermolecular interactions in a crystal structure.

ACKNOWLEDGEMENTS

The authors are thankful to L. Vasilieva for her help in preparing of this manuscript.

REFERENCES

1. F.H. Allen, *Acta Crystallographica*, **2002**, B58, 380.
2. C.R. Groom, F.H. Allen, *Angewante Chemie International Edition*, **2014**, 53, 662.
3. A.I. Kitaigorodsky, "Molecular Crystals and Molecules", Academic Press, New York, **1973**.
4. L.N. Kuleshova, M. Yu. Antipin, *Russian Chemical Reviews*, **1999**, 68, 1.
5. P.M. Zorkii, P.N. Oleinikov, *Journal of Structural Chemistry*, **2001**, 42, 24.
6. Th. Hahn (ed.), "International Tables for Crystallography, Volume A: Space-group symmetry, 1st online ed.", International Union of Crystallography, **2006**, part 2.2.10.
7. A.M. Banaru, *Moscow University Chemistry Bulletin*, **2009**, 64, 80.
8. E.A. Lord, A.M. Banaru, *Moscow University Chemistry Bulletin*, **2012**, 67, 50.

9. R.H. MacArthur, *Proceedings of National Academy of Sciences USA*, **1957**, *43*, 293.
10. C.F. Macrae, I.J. Bruno, J.A. Chisholm, P.R. Edgington, P. McCabe, E. Pidcock, L. Rodriguez-Monge, R. Taylor, J. van de Streek, P.A. Wood, *Journal of Applied Crystallography*, **2008**, *41*, 466.
11. A. Gavezzotti, G. Filippini, *Journal of Physical Chemistry*, **1994**, *98*, 4831.

VERTEX-ECCENTRICITY DESCRIPTORS IN DENDRIMERS

MAHDIEH AZARI^{a*}, ALI IRANMANESH^b AND MIRCEA V. DIUDEA^{c*}

ABSTRACT. In this paper, we present graph theoretical methods to compute several vertex-eccentricity-based molecular descriptors such as the eccentric connectivity index, total eccentricity, average eccentricity and first and second Zagreb eccentricity indices for the generalized and ordinary Bethe trees and some dendrimer graphs. Also, we study the behavior of these descriptors under the rooted product of graphs and apply our results to compute these indices for some classes of molecular graphs, designed by attaching copies of ordinary Bethe trees to paths and cycles.

Keywords: *Vertex eccentricity, Molecular descriptor, Molecular graph, Bethe tree, Dendrimer, Rooted product of graphs.*

INTRODUCTION

Chemical graph theory is a branch of mathematical chemistry dealing with the study of chemical graphs [1]. Chemical graphs, particularly molecular graphs, are models of molecules in which atoms are represented by vertices and chemical bonds by edges of a graph. Physico-chemical or biological properties of molecules can be predicted by using the information encoded in the molecular graphs, eventually translated in the adjacency or connectivity matrix associated to these graphs. This paradigm is achieved by considering various graph theoretical invariants of molecular graphs (also known as topological indices, molecular descriptors, etc.) and evaluating how strongly are they correlated with various molecular properties. In this way, chemical

^a *Department of Mathematics, Kazerun Branch, Islamic Azad University, P. O. Box: 73135-168, Kazerun, Iran, azari@kau.ac.ir*

^b *Department of Pure Mathematics, Faculty of Mathematical Sciences, Tarbiat Modares University, P. O. Box: 14115-137, Tehran, Iran, iranmanesh@modares.ac.ir*

^c *Department of Chemistry, Faculty of Chemistry and Chemical Engineering, "Babes-Bolyai" University, Arany Janos 11, 400028, Cluj, Romania, Diudea@gmail.com*

* *Corresponding authors: azari@kau.ac.ir, Diudea@gmail.com*

graph theory plays an important role in mathematical foundation of QSAR and QSPR research. A graph invariant is any function calculated on a molecular graph, irrespective of the labeling of its vertices. Many invariants have been proposed and employed to date with various degrees of success in QSAR/QSPR studies. We refer the reader to consult the monographs [1,2].

In the recent years, some invariants based on vertex eccentricity such as eccentric connectivity index [3], total eccentricity, average eccentricity [4], and first and second Zagreb eccentricity indices [5] have attracted much attention in chemistry. These invariants are successfully used for mathematical modeling of biological activity of diverse nature [6-8]. They were also proposed as a measure of branching in alkanes [9].

Dendrimers are highly ordered hyper-branched molecular structures [10-12] reaching the nano-dimensions. The end-groups (the pendant groups reaching the outer periphery) can be functionalized, thus modifying their physico-chemical or biological properties. Dendrimers have gained a wide range of applications in supra-molecular chemistry, particularly in catalysis, host-guest reactions, and self-assembly processes [13,14]. Promising applications come to cancer therapy [15] but their applications are unlimited.

In this paper, we present graph theoretical methods to compute these descriptors for generalized and ordinary Bethe trees and several classes of molecular graphs and dendrimers derived from them.

DEFINITIONS AND PRELIMINARIES

Let G be a simple connected graph with vertex set $V(G)$ and edge set $E(G)$. The degree $d_G(u)$ of a vertex $u \in V(G)$ is the number of first neighbors of u in G . The (topological) distance $d_G(u, v)$ between the vertices $u, v \in V(G)$ is defined as the length of any shortest path in G connecting u and v . The eccentricity $\varepsilon_G(u)$ of a vertex u is the largest distance between u and any other vertex v of G , $\varepsilon_G(u) = \max\{d_G(u, v); v \in V(G)\}$.

The best known and widely used topological index is the Wiener index, W , introduced in 1947 by Wiener [16], who used it for modeling the thermodynamic properties of alkanes. The Wiener index of a molecular graph G represents the sum of topological distances between all pairs of atoms/vertices of G . Details on the Wiener index can be found in [17-20].

Zagreb indices are among the oldest topological indices, and were introduced in 1972 by Gutman and Trinajstić [21] within the study about the dependence of total π -electron energy of molecular structures. The first and the second Zagreb indices of a graph G , $M_1(G)$ and $M_2(G)$, respectively, are defined as:

$$M_1(G) = \sum_{u \in V(G)} d_G(u)^2 \text{ and } M_2(G) = \sum_{uv \in E(G)} d_G(u)d_G(v).$$

The eccentric connectivity index $\xi(G)$ was introduced by Sharma *et al.* [3] in 1997; it is defined as:

$$\xi(G) = \sum_{u \in V(G)} d_G(u)\varepsilon_G(u).$$

It is sometimes interesting to consider the sum of eccentricities of all vertices of a given graph G . This quantity is called the total eccentricity of G and denoted by $\zeta(G)$.

The average eccentricity [4] of G is denoted by $\eta(G)$ and defined as:

$$\eta(G) = \frac{\zeta(G)}{|V(G)|}.$$

The Zagreb eccentricity indices were introduced by Vukičević and Graovac [5] in 2010. They are defined, analogously to the Zagreb indices, by replacing the vertex degree with the vertex eccentricity, as:

$$\xi_1(G) = \sum_{u \in V(G)} \varepsilon_G(u)^2, \quad \xi_2(G) = \sum_{uv \in E(G)} \varepsilon_G(u)\varepsilon_G(v).$$

RESULTS AND DISCUSSION

Let us compute some vertex-eccentricity-based invariants for path and cycle. The results follow easily by direct calculations, so the proofs are omitted.

Lemma 1. Let P_n and C_n denote the n -vertex path and cycle, respectively.

(i) If n is even, then

$$\xi(P_n) = \frac{3n^2 - 6n + 4}{2}, \quad \zeta(P_n) = \frac{n(3n - 2)}{4}, \quad \eta(P_n) = \frac{3n - 2}{4},$$

$$\xi_1(P_n) = \frac{n(n - 1)(7n - 2)}{12}, \quad \xi_2(P_n) = \frac{n(7n^2 - 21n + 20)}{12},$$

and if n is odd, we have

$$\xi(P_n) = \frac{3(n - 1)^2}{2}, \quad \zeta(P_n) = \frac{(n - 1)(3n + 1)}{4}, \quad \eta(P_n) = \frac{(n - 1)(3n + 1)}{4n},$$

$$\xi_1(P_n) = \frac{(n - 1)(7n^2 - 2n - 3)}{12}, \quad \xi_2(P_n) = \frac{(n - 1)(7n^2 - 14n + 3)}{12}.$$

(ii) For every $n \geq 3$,

$$\xi(C_n) = 2n \left\lfloor \frac{n}{2} \right\rfloor, \quad \zeta(C_n) = n \left\lfloor \frac{n}{2} \right\rfloor, \quad \eta(C_n) = \left\lfloor \frac{n}{2} \right\rfloor, \quad \xi_1(C_n) = \xi_2(C_n) = n \left\lfloor \frac{n}{2} \right\rfloor^2.$$

A generalized Bethe tree [22] of k levels, $k > 1$, is a rooted tree in which vertices lying at the same level have the same degree (Figure 1). The level of a vertex in a rooted tree equals its distance from the root vertex plus one.

Let B_k be a generalized Bethe tree of k levels. For $i = 1, 2, \dots, k$, let d_{k-i+1} and n_{k-i+1} denote the degree of the vertices at the level i of B_k and their number, respectively. Also, suppose $e_k = d_k$ and $e_i = d_i - 1$ for $i = 1, 2, \dots, k-1$.

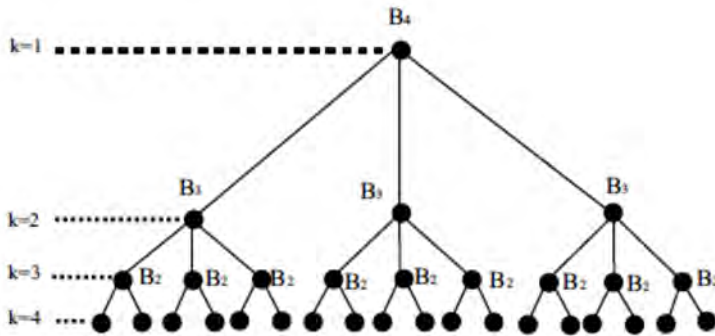


Figure 1. A generalized Bethe tree of 4 levels.

In the following theorem, some vertex-eccentricity-based invariants of the generalized Bethe tree B_k are computed.

Theorem 2. Let B_k be a generalized Bethe tree whose root vertex has degree $d_k > 1$. Then

$$\begin{aligned} \text{(i)} \quad \xi(B_k) &= \sum_{i=1}^k d_i (2k-1-i) \prod_{j=i+1}^k e_j, \\ \text{(ii)} \quad \zeta(B_k) &= \sum_{i=1}^k (2k-1-i) \prod_{j=i+1}^k e_j, \\ \text{(iii)} \quad \eta(B_k) &= \frac{\sum_{i=1}^k (2k-1-i) \prod_{j=i+1}^k e_j}{\sum_{i=1}^k \prod_{j=i+1}^k e_j}, \end{aligned}$$

$$(iv) \xi_1(B_k) = \sum_{i=1}^k (2k-1-i)^2 \prod_{j=i+1}^k e_j,$$

$$(v) \xi_2(B_k) = \sum_{i=2}^k (2k-1-i)(2k-i) \prod_{j=i}^k e_j.$$

Proof. We just prove parts (i) and (v); other parts can be proven similarly. To prove part (i), let v be an arbitrary vertex of the level $k-i+1$ of B_k , where $1 \leq i \leq k$. It is easy to see that, $\varepsilon_{B_k}(v) = (k-i) + (k-1) = 2k-1-i$. So,

$$\xi(B_k) = \sum_{i=1}^k n_i d_i (2k-1-i). \tag{1}$$

On the other hand, the number of vertices of the level $k-i+1$ is equal to $n_i = n_{i+1} e_{i+1}$, $1 \leq i \leq k-1$. Thus,

$$n_i = n_{i+1} e_{i+1} = (n_{i+2} e_{i+2}) e_{i+1} = ((n_{i+3} e_{i+3}) e_{i+2}) e_{i+1} = \dots = n_k e_k e_{k-1} \dots e_{i+1} = \prod_{j=i+1}^k e_j.$$

Now using (1), we can get the formula for $\xi(B_k)$. To prove part (v), let E_{k-i+1} , $2 \leq i \leq k$, denote the set of all edges of B_k which connect vertices of the level $k-i+1$ and level $k-i+2$ of B_k . It is easy to see that,

$$|E_{k-i+1}| = n_i e_i = e_i \prod_{j=i}^k e_j = \prod_{j=i}^k e_j,$$

and if $uv \in E_{k-i+1}$, then $\varepsilon_{B_k}(u) \varepsilon_{B_k}(v) = (2k-1-i)(2k-i)$. Now, by definition of the second Zagreb eccentricity index, we can get the formula for $\xi_2(B_k)$.

The ordinary Bethe tree $B_{d,k}$ is a rooted tree of k levels whose root vertex has degree d , the vertices from levels 2 to $k-1$ have degree $d+1$ and the vertices at level k have degree 1 (Figure 2). Note that $B_{1,k} = P_k$ and $B_{d,2} = S_{d+1}$.

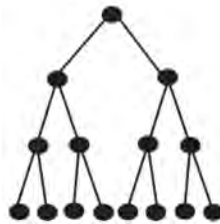


Figure 2. The ordinary Bethe tree $B_{2,4}$.

Using Theorem 2, we easily arrive at:

Corollary 3. For the ordinary Bethe tree $B_{d,k}$ with $d > 1$, we have:

$$(i) \xi(B_{d,k}) = d(k-1)(2d^{k-2} + 1) + (d+1) \sum_{i=1}^{k-2} (k-1+i)d^i,$$

$$(ii) \zeta(B_{d,k}) = \sum_{i=0}^{k-1} (k-1+i)d^i,$$

$$(iii) \eta(B_{d,k}) = \frac{\sum_{i=0}^{k-1} (k-1+i)d^i}{\sum_{i=0}^{k-1} d^i},$$

$$(iv) \xi_1(B_{d,k}) = \sum_{i=0}^{k-1} (k-1+i)^2 d^i,$$

$$(v) \xi_2(B_{d,k}) = \sum_{i=1}^{k-1} (k-2+i)(k-1+i)d^i.$$

A dendrimer tree $T_{d,k}$ [23] is a rooted tree having the degree of its non-pendent vertices equal to d and the distance between the root (central) vertex and the pendent vertices equal to k (Figure 3). Thus, $T_{d,k}$ can be seen as a generalized Bethe tree with $k+1$ levels and the non-pendent vertices have the same degree. Note that $T_{2,k} = P_{2k+1}$ and $T_{d,1} = S_{d+1}$.

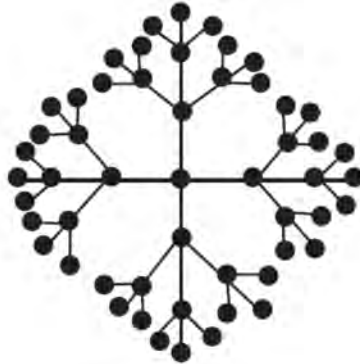


Figure 3. The dendrimer tree $T_{4,3}$.

Using Theorem 2, we easily arrive at:

Corollary 4. For the dendrimer tree $T_{d,k}$ with $d > 1$, we have:

$$(i) \xi(T_{d,k}) = kd(2(d-1)^{k-1} + 1) + d^2 \sum_{i=0}^{k-2} (k+1+i)(d-1)^i,$$

$$(ii) \zeta(T_{d,k}) = k + d \sum_{i=0}^{k-1} (k+1+i)(d-1)^i,$$

$$\begin{aligned}
 \text{(iii)} \quad \eta(T_{d,k}) &= \frac{k + d \sum_{i=0}^{k-1} (k+1+i)(d-1)^i}{1 + d \sum_{i=0}^{k-1} (d-1)^i}, \\
 \text{(iv)} \quad \xi_1(T_{d,k}) &= k^2 + d \sum_{i=0}^{k-1} (k+1+i)^2 (d-1)^i, \\
 \text{(v)} \quad \xi_2(T_{d,k}) &= d \sum_{i=0}^{k-1} (k+i)(k+1+i)(d-1)^i.
 \end{aligned}$$

The formula of part (i) of Corollary 4 has also been obtained in [24].

Now, we introduce a class of dendrimers constructed from copies of ordinary Bethe trees. This molecular structure can be encountered in real chemistry, e.g. in some tertiary phosphine dendrimers. Let D_0 be the graph depicted in Figure 4. For $d, k > 0$, let $D_{d,k}$ be a series of dendrimers obtained by attaching d pendent vertices to each pendent vertex of $D_{d,k-1}$ and let $D_{d,0} = D_0$. Some examples of these graphs are shown in Figure 5.

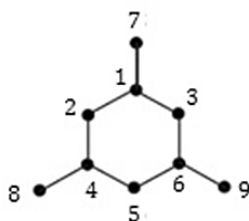


Figure 4. The dendrimer graph D_0 with a numbering for its vertices.

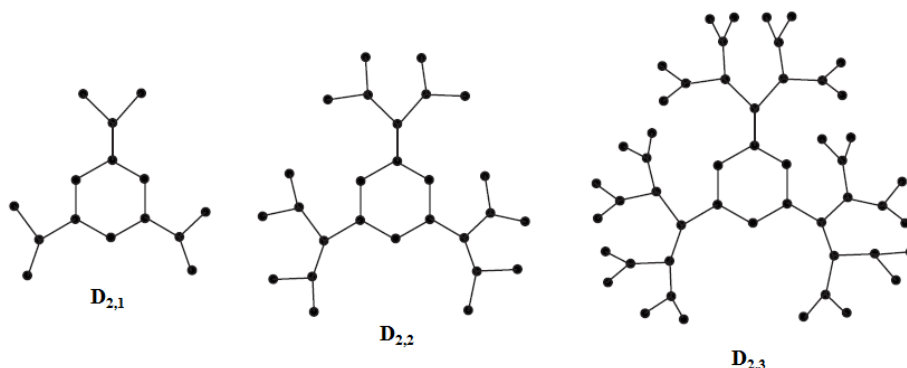


Figure 5. Dendrimer graphs $D_{2,k}$, for $k=1,2,3$.

We can also introduce the dendrimer graph $D_{d,k}$ as the graph obtained by identifying the root vertex of the ordinary Bethe tree $B_{d,k+1}$ with all three pendant vertices of the graph D_0 . In the following theorem, some vertex-eccentricity-based invariants of the dendrimer graph $D_{d,k}$ are calculated.

Theorem 5. For the dendrimer graph $D_{d,k}$ with $k \geq 0$, we have:

$$(i) \quad \xi_5(D_{d,k}) = 15k + 51 + 6(k+2)d^k + 3(d+1) \sum_{i=0}^{k-1} (k+4+i)d^i,$$

$$(ii) \quad \zeta(D_{d,k}) = 6k + 21 + 3 \sum_{i=0}^k (k+4+i)d^i,$$

$$(iii) \quad \eta(D_{d,k}) = \frac{6k + 21 + 3 \sum_{i=0}^k (k+4+i)d^i}{6 + 3 \sum_{i=0}^k d^i},$$

$$(iv) \quad \xi_1(D_{d,k}) = 3(2k^2 + 14k + 25) + 3 \sum_{i=0}^k (k+4+i)^2 d^i,$$

$$(v) \quad \xi_2(D_{d,k}) = 9(k+3)(k+4) + 3 \sum_{i=1}^k (k+3+i)(k+4+i)d^i.$$

Proof. Consider a subgraph of $D_{d,k}$ isomorphic to the graph D_0 and choose a numbering for its vertices as shown in Figure 4. It is easy to see that:

$$\varepsilon_{D_{d,k}}(1) = \varepsilon_{D_{d,k}}(4) = \varepsilon_{D_{d,k}}(6) = k+3, \quad \varepsilon_{D_{d,k}}(2) = \varepsilon_{D_{d,k}}(3) = \varepsilon_{D_{d,k}}(5) = k+4.$$

Now, let G be a subgraph of $D_{d,k}$ isomorphic to the ordinary Bethe tree $B_{d,k+1}$ and let v be an arbitrary vertex of the level i , $1 \leq i \leq k+1$ of G . Then

$$\varepsilon_{D_{d,k}}(v) = (i-1) + 4 + k = k+3+i,$$

and the number of vertices of this level is equal to d^{i-1} . Next, using the definition of the eccentric connectivity index, total eccentricity, average eccentricity, and Zagreb eccentricity indices, the proof is obvious.

Let now consider two other molecular graphs constructed from copies of the ordinary Bethe tree $B_{d,k}$ and compute some of their vertex-eccentricity-based invariants. Recall that the rooted product $G_1\{G_2\}$ of simple connected graphs G_1 and G_2 is the graph obtained by taking one copy of G_1 and $|V(G_1)|$ copies of the rooted graph G_2 , and identifying the root vertex of the i -th copy of G_2 with the i -th vertex of G_1 , for $i=1,2,\dots, |V(G_1)|$. More about topological indices of rooted product of graphs can be found in [25-29]. In what follows, we denote the root vertex of G_2 by w , and the copy of G_2 whose root is identified with the vertex $u \in V(G_1)$ by $G_{2,u}$. The degree of a vertex x of $G_1\{G_2\}$ is calculated as:

$$d_{G_1\{G_2\}}(x) = \begin{cases} d_{G_2}(x) & x \in V(G_{2,u}) - \{w\} \\ d_{G_1}(u) + d_{G_2}(w) & x = w \in V(G_{2,u}) \end{cases}.$$

Also, if $x \in V(G_{2,u})$ then the eccentricity of the vertex x is:

$$\varepsilon_{G_1\{G_2\}}(x) = d_{G_2}(x, w) + \varepsilon_{G_1}(u) + \varepsilon_{G_2}(w).$$

Let G be a simple connected graph and $u \in V(G)$. In order to express our next formulas in more compact forms, we introduce some quantities related to graph G as follows:

$$D_G(u) = \sum_{x \in V(G) - \{u\}} d_G(x, u), \quad D_G^2(u) = \sum_{x \in V(G) - \{u\}} d_G(x, u)^2,$$

$$DD_G(u) = \sum_{x \in V(G) - \{u\}} \deg_G(x) d_G(x, u), \quad DD_G^*(u) = \sum_{xy \in E(G)} d_G(x, u) d_G(y, u).$$

In the following lemma, we compute the above quantities in case G is the ordinary Bethe tree $B_{d,k}$ and u is its root vertex. The proof follows immediately from definitions, so is omitted.

Lemma 6. Let w denote the root vertex of $B_{d,k}$. Then

- (i) $D_{B_{d,k}}(w) = \sum_{i=1}^{k-1} id^i,$
- (ii) $D_{B_{d,k}}^2(w) = \sum_{i=1}^{k-1} i^2 d^i,$
- (iii) $DD_{B_{d,k}}(w) = (d+1) \sum_{i=1}^{k-2} id^i + (k-1)d^{k-1},$
- (iv) $DD_{B_{d,k}}^*(w) = \sum_{i=1}^{k-1} i^2 d^i - \sum_{i=1}^{k-1} id^i.$

In the following theorem, some vertex-eccentricity-based invariants of the rooted product $G_1\{G_2\}$ are computed.

Theorem 7. Let G_1 and G_2 be simple connected graphs with $|V(G_i)|=n_i, |E(G_i)|=m_i, 1 \leq i \leq 2$, and let the copies of G_2 used in the construction of $G_1\{G_2\}$ be rooted in w . Then

- (i) $\xi(G_1\{G_2\}) = \xi(G_1) + 2m_2\zeta(G_1) + 2(m_1+n_1m_2)\varepsilon_{G_2}(w) + n_1DD_{G_2}(w),$
- (ii) $\zeta(G_1\{G_2\}) = n_2\zeta(G_1) + n_1D_{G_2}(w) + n_1n_2\varepsilon_{G_2}(w),$
- (iii) $\eta(G_1\{G_2\}) = \eta(G_1) + \frac{1}{n_2}D_{G_2}(w) + \varepsilon_{G_2}(w),$
- (iv) $\xi_1(G_1\{G_2\}) = n_2\xi_1(G_1) + 2(D_{G_2}(w) + n_2\varepsilon_{G_2}(w))\zeta(G_1) + n_1D_{G_2}^2(w) + n_1n_2\varepsilon_{G_2}(w)^2 + 2n_1\varepsilon_{G_2}(w)D_{G_2}(w),$

$$(v) \xi_2(G_1\{G_2\}) = \xi_2(G_1) + m_2\xi_1(G_1) + \varepsilon_{G_2}(w)\xi(G_1) + 2m_2\varepsilon_{G_2}(w)\zeta(G_1) + (m_1 + n_1m_2)\varepsilon_{G_2}(w)^2 + (n_1\varepsilon_{G_2}(w) + \zeta(G_1))DD_{G_2}(w) + n_1DD_{G_2}^*(w).$$

Proof. We prove part (i); other parts can be proven similarly.

$$\begin{aligned} \xi(G_1\{G_2\}) &= \sum_{x \in V(G_1\{G_2\})} d_{G_1\{G_2\}}(x) \varepsilon_{G_1\{G_2\}}(x) \\ &= \sum_{u \in V(G_1)} \sum_{x \in V(G_2, u) \cup \{w\}} d_{G_2}(x) [d_{G_2}(x, w) + \varepsilon_{G_1}(u) + \varepsilon_{G_2}(w)] \\ &\quad + \sum_{u \in V(G_1)} [d_{G_1}(u) + d_{G_2}(w)] [\varepsilon_{G_1}(u) + \varepsilon_{G_2}(w)] \\ &= [n_1 DD_{G_2}(w) + (2m_2 - d_{G_2}(w))\zeta(G_1) + n_1(2m_2 - d_{G_2}(w))\varepsilon_{G_2}(w)] \\ &\quad + [\xi(G_1) + 2m_2\varepsilon_{G_2}(w) + d_{G_2}(w)\zeta(G_1) + n_1d_{G_2}(w)\varepsilon_{G_2}(w)] \\ &= \xi(G_1) + 2m_2\zeta(G_1) + 2(m_1 + n_1m_2)\varepsilon_{G_2}(w) + n_1DD_{G_2}(w). \end{aligned}$$

Denote by $P(d, k, n)$, the tree obtained by attaching the root vertex of $B_{d,k}$ to the vertices of P_n (Figure 6 and ref. [30]).

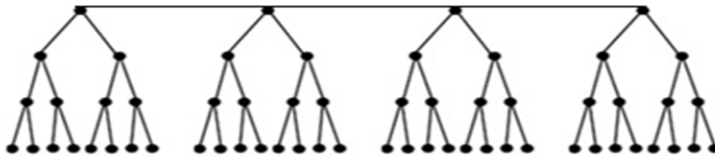


Figure 6. The chemical tree $P(2,4,4)$.

The graph $P(d, k, n)$ can be considered as the rooted product of P_n and $B_{d,k}$. So, we can apply Theorem 7 and Lemmas 1 and 6 to get the formulas for the eccentric connectivity index, total eccentricity, average eccentricity, and Zagreb eccentricity indices of $P(d, k, n)$.

Corollary 8. For the tree $P(d, k, n)$ with $d > 1$, the following hold:

(i) If n is even, then

$$\begin{aligned} \xi(P(d, k, n)) &= n(d + 1) \sum_{i=1}^{k-2} id^i + n \left[\frac{3n-2}{2} + 2(k-1) \right] \sum_{i=1}^{k-1} d^i \\ &\quad + [2(n-1) + nd^{k-1}](k-1) + \frac{3n^2 - 6n + 4}{2}, \end{aligned}$$

and if n is odd, then

$$\begin{aligned} \xi(P(d, k, n)) &= n(d + 1) \sum_{i=1}^{k-2} id^i + \left[\frac{(n-1)(3n+1)}{2} + 2n(k-1) \right] \sum_{i=1}^{k-1} d^i \\ &\quad + [2(n-1) + nd^{k-1}](k-1) + \frac{3(n-1)^2}{2}, \end{aligned}$$

(ii) If n is even, then

$$\zeta(P(d, k, n)) = n \sum_{i=1}^{k-1} id^i + n \left[\frac{3n-2}{4} + k-1 \right] \sum_{i=0}^{k-1} d^i,$$

and if n is odd, then

$$\zeta(P(d, k, n)) = n \sum_{i=1}^{k-1} id^i + \left[\frac{(n-1)(3n+1)}{4} + n(k-1) \right] \sum_{i=0}^{k-1} d^i.$$

(iii) If n is even, then

$$\eta(P(d, k, n)) = \frac{\sum_{i=1}^{k-1} id^i}{\sum_{i=0}^{k-1} d^i} + \frac{3n-2}{4} + k-1,$$

and if n is odd, then

$$\eta(P(d, k, n)) = \frac{\sum_{i=1}^{k-1} id^i}{\sum_{i=0}^{k-1} d^i} + \frac{(n-1)(3n+1)}{4n} + k-1.$$

(iv) If n is even, then

$$\begin{aligned} \xi_1(P(d, k, n)) &= n \sum_{i=1}^{k-1} i^2 d^i + n \left[\frac{3n-2}{2} + 2(k-1) \right] \sum_{i=1}^{k-1} id^i \\ &+ n \left[\frac{(n-1)(7n-2)}{12} + \frac{(k-1)(3n-2)}{2} + (k-1)^2 \right] \sum_{i=0}^{k-1} d^i, \end{aligned}$$

and if n is odd, then

$$\begin{aligned} \xi_1(P(d, k, n)) &= n \sum_{i=1}^{k-1} i^2 d^i + \left[\frac{(n-1)(3n+1)}{2} + 2n(k-1) \right] \sum_{i=1}^{k-1} id^i \\ &+ \left[\frac{(n-1)(7n^2-2n-3)}{12} + \frac{(k-1)(n-1)(3n+1)}{2} + n(k-1)^2 \right] \sum_{i=0}^{k-1} d^i. \end{aligned}$$

(v) If n is even, then

$$\begin{aligned} \xi_2(P(d, k, n)) &= n \sum_{i=1}^{k-1} i^2 d^i + n \left[(d+1) \left(\frac{3n-2}{4} + k-1 \right) - 1 \right] \sum_{i=1}^{k-2} id^i \\ &+ n \left[\frac{(n-1)(7n-2)}{12} + \frac{(k-1)(3n-2)}{2} + (k-1)^2 \right] \sum_{i=1}^{k-1} d^i \\ &+ n(k-1)d^{k-1} \left(\frac{3n-2}{4} + k-2 \right) + \frac{n(7n^2-21n+20)}{12} \\ &+ \frac{(k-1)(3n^2-6n+4)}{2} + (n-1)(k-1)^2, \end{aligned}$$

and if n is odd, then

$$\begin{aligned} \xi_2(P(d,k,n)) &= n \sum_{i=1}^{k-1} i^2 d^i + [(d+1)\left(\frac{(n-1)(3n+1)}{4} + n(k-1)\right) - n] \sum_{i=1}^{k-2} id^i \\ &+ \left[\frac{(n-1)(7n^2 - 2n - 3)}{12} + \frac{(k-1)(n-1)(3n+1)}{2} + n(k-1)^2\right] \sum_{i=1}^{k-1} d^i \\ &+ (k-1)d^{k-1} \left[\frac{(n-1)(3n+1)}{4} + n(k-2)\right] + \frac{(n-1)(7n^2 - 14n + 3)}{12} \\ &+ \frac{3(k-1)(n-1)^2}{2} + (n-1)(k-1)^2. \end{aligned}$$

Denote by $C(d,k,n)$, the dendrimer graph obtained by attaching the root vertex of $B_{d,k}$ to the vertices of C_n (Figure 7 and ref. [22]). It is easy to see that, $C(d,k,n)$ is the rooted product of C_n and $B_{d,k}$. So, using Theorem 7, and Lemmas 1 and 6, we get the following results for $C(d,k,n)$.

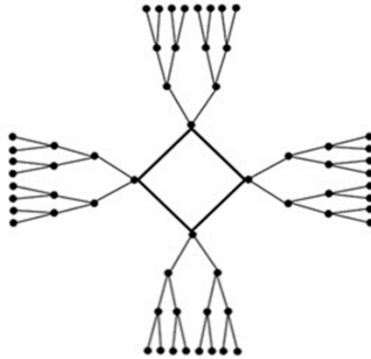


Figure 7. The dendrimer graph $C(2,4,4)$.

Corollary 9. For the dendrimer graph $C(d,k,n)$ with $d > 1$, we have:

- (i) $\xi(C(d,k,n)) = n(d+1) \sum_{i=1}^{k-2} id^i + 2n \left\lfloor \frac{n}{2} \right\rfloor + k-1 \left[\sum_{i=1}^{k-1} d^i + 1 \right] + n(k-1)d^{k-1}$,
- (ii) $\zeta(C(d,k,n)) = n \sum_{i=1}^{k-1} id^i + n \left\lfloor \frac{n}{2} \right\rfloor + k-1 \sum_{i=0}^{k-1} d^i$,
- (iii) $\eta(C(d,k,n)) = \frac{\sum_{i=1}^{k-1} id^i}{\sum_{i=0}^{k-1} d^i} + \left\lfloor \frac{n}{2} \right\rfloor + k-1$,

$$\begin{aligned}
 \text{(iv)} \quad \xi_1(C(d, k, n)) &= n \sum_{i=1}^{k-1} i^2 d^i + 2n \left[\left\lfloor \frac{n}{2} \right\rfloor + k - 1 \right] \sum_{i=1}^{k-1} i d^i + n \left[\left\lfloor \frac{n}{2} \right\rfloor + 2 \left\lfloor \frac{n}{2} \right\rfloor \right] \\
 &\quad + (k-1)^2 \sum_{i=0}^{k-1} d^i + n \left[\left\lfloor \frac{n}{2} \right\rfloor + 2 \left\lfloor \frac{n}{2} \right\rfloor + (k-1)^2 \right] \sum_{i=0}^{k-1} d^i, \\
 \text{(v)} \quad \xi_2(C(d, k, n)) &= n \sum_{i=1}^{k-1} i^2 d^i + n[(d+1) \left(\left\lfloor \frac{n}{2} \right\rfloor + k - 1 \right) - 1] \sum_{i=1}^{k-2} i d^i + n \left[\left\lfloor \frac{n}{2} \right\rfloor \right]^2 \\
 &\quad + 2(k-1) \left\lfloor \frac{n}{2} \right\rfloor + (k-1)^2 \left(\sum_{i=1}^{k-1} d^i + 1 \right) + n(k-1) d^{k-1} \left[\left\lfloor \frac{n}{2} \right\rfloor + k - 2 \right].
 \end{aligned}$$

CONCLUSIONS

In this paper, we performed a topological study on several molecular graphs constructed from copies of Bethe trees, by applying graph theoretical methods, to obtain explicit formulas for calculation of the eccentric connectivity index, total eccentricity, average eccentricity, and first and second Zagreb eccentricity indices of these structures. These descriptors can be used in topological analysis of enzymes (in general, proteins) to identify structural similarities and ways of reactions.

ACKNOWLEDGMENTS

The authors would like to thank the referee for the valuable comments. Partial support by the Center of Excellence of Algebraic Hyper-structures and its Applications of Tarbiat Modares University (CEAHA) is gratefully acknowledged by the second author (AI).

REFERENCES

1. I. Gutman, O.E. Polansky, "Mathematical Concepts in Organic Chemistry", Springer, Berlin, **1986**.
2. M.V. Diudea (Ed.), "QSPR/QSAR Studies by Molecular Descriptors", Nova, New York, **2001**.
3. V. Sharma, R. Goswami, A.K. Madan, *J. Chem. Inf. Comput. Sci.*, **1997**, *37*, 273.
4. P. Dankelmann, W. Goddard, C.S. Swart, *Util. Math.*, **2004**, *65*, 41.

5. D. Vukičević, A. Graovac, *Acta Chim. Slov.*, **2010**, 57, 524.
6. H. Dureja, S. Gupta, A.K. Madan, *J. Mol. Graphics Modell.*, **2008**, 26, 1020.
7. S. Sardana, A.K. Madan, *J. Mol. Model.*, **2002**, 8, 258.
8. A. Alizadeh, M. Azari, T. Došlić, *J. Comput. Theor. Nanosci.*, **2013**, 10(6), 1297.
9. A. Ilić, I. Gutman, *MATCH Commun. Math. Comput. Chem.*, **2011**, 65(3), 731.
10. M.V. Diudea, G. Katona, "Molecular Topology of Dendrimers", in: G. A. Newcome (Ed.) *Advances in Dendritic Macromolecules*, **1999**, 4, 135.
11. G.A. Newcome, V.K. Gupta, G.R. Baker, Z-Q Yao, *J. Org. Chem.*, **1985**, 50, 2003.
12. D.A. Tomalia, *Sci. Am.*, **1995**, 272, 42.
13. G.R. Newcome, C.N. Moorefield, F. Vogtle, "Dendritic Macromolecules: Concepts, Syntheses, Perspectives", VCH, Weinheim, Germany, **1996**.
14. C. Deraedt, N. Pinaud, D. Astruc, *J. Am. Chem. Soc.*, **2011**, 136(34), 12092.
15. Y. Cheng, L. Zhao, Y. Li, T. Xu, *Chem. Soc. Rev.*, **2011**, 40, 2673.
16. H. Wiener, *J. Am. Chem. Soc.*, **1947**, 69(1), 17.
17. I. Gutman, D. Vidović, B. Furtula, *Indian J. Chem.*, **2003**, 42A(06), 1272.
18. M.V. Diudea, *MATCH Commun. Math. Comput. Chem.*, **1995**, 32, 71.
19. M. Eliasi, B. Taeri, *J. Theor. Comp. Chem.*, **2008**, 7(5), 1029.
20. M.V. Putz, O. Ori, F. Cataldo, A.M. Putz, *Curr. Org. Chem.*, **2013**, 17(23), 2816.
21. I. Gutman, N. Trinajstić, *Chem. Phys. Lett.*, **1972**, 17, 535.
22. O. Rojo, *Lin. Algebra Appl.*, **2007**, 420, 490.
23. A.A. Dobrynin, R. Entringer, I. Gutman, *Acta Appl. Math.*, **2011**, 66, 211.
24. J. Yang, F. Xia, *Int. J. Contemp. Math. Sciences*, **2010**, 5(45), 2231.
25. A. Iranmanesh, M. Azari, *Curr. Org. Chem.*, **2015**, 19(3), 219.
26. M. Azari, *Appl. Math. Comput.*, **2014**, 239, 409.
27. M. Azari, A. Iranmanesh, *MATCH Commun. Math. Comput. Chem.*, **2013**, 70, 901.
28. M. Azari, A. Iranmanesh, *Discrete Appl. Math.*, **2013**, 161(18), 2827.
29. T. Došlić, *Ars Math. Contemp.*, **2008**, 1, 66.
30. M. Robbiano, I. Gutman, R. Jimenez, B. San Martin, *Bull. Acad. Serbe. Sci. Arts (Cl. Sci. Math. Natur.)*, **2008**, 137, 59.

MODELING BOILING POINTS OF ALKANE DERIVATIVES

ESMAT MOHAMMADINASAB^a

ABSTRACT. Relationship between the boiling points of a series of alkanes and some topological indices and geometrical descriptors is investigated using the multi linear regression MLR method. The results revealed that Wiener, Randić and volume descriptors play a more important role in the description of boiling points of alkanes, in comparison to the other molecular descriptors.

Keywords: *Graph theory, MLR method, Alkane Derivatives.*

INTRODUCTION

Alkanes, with general formula C_nH_{2n+2} , are organic compounds that only contain carbon and hydrogen atoms and only carbon-carbon single bonds. Alkanes react very poorly to ionic or other polar chemical species. The boiling point of alkanes, as a physico-chemical parameter, is of great importance in chemical engineering and chemical reactions [1].

Chemical graph theory is a branch of mathematics which combines graph theory and chemistry and has been extensively applied to predict the physico-chemical and biological properties of organic compounds through the quantitative structure-activity/property relationship (QSAR/QSPR). These are mathematical models which relate the physico-chemical properties of a set of molecules to structural indices or other types of molecular descriptors [2-10]. It is worth mentioning that many properties of chemical compounds are closely related to topological indices of their molecular structures; therefore, the correlational studies, enabling the prediction of molecular properties are of practical importance.

Hence, the necessity of finding formulas for calculating some topological indices and then performing QSAR/QSPR studies.

^a *Department of Chemistry, Faculty of Sciences, Islamic Azad University, Arak Branch, Arak, Iran*

* *Corresponding author: e-mohammadinasab@iau-arak.ac.ir*

TOPOLOGICAL INDICES

WIENER INDEX

Harold Wiener in 1947, introduced one of the first molecular descriptors, of topological nature, for acyclic saturated hydrocarbons. Wiener index of the graph G is the half-sum of all entries in the distance matrix D [11]:

$$W = \frac{1}{2} \sum_{i=1}^n \sum_{j=1}^n D_{ij} \quad (1)$$

where the entries D_{ij} denote the (topological) distance between any two vertices i and j in the graph G .

HYPER-WIENER INDEX

A related distance-based topological index is called the Hyper-Wiener index, $WW(G)$; it is defined as:

$$WW(G) = \frac{1}{2} \sum d_{ij} + \frac{1}{2} \sum (d_{ij})^2 \quad (2)$$

where d_{ij} denotes the topological distance between the vertices i and j in the graph G and the summation runs over all (unordered) pairs of vertices of G [12,13].

BALABAN INDEX

Balaban index, $J=J(G)$, of a graph on n node and m edges, is calculated by using the sum of all distances, D_i , from i to all the other vertices of G ; it was defined in 1982 by the Romanian chemist, A. T. Balaban, as follows [14]:

$$J = \frac{m}{\mu + 1} \sum_{i=1}^n \sum_{j=1}^n [(D_i)(D_j)]^{-0.5} \quad (3)$$

where $\mu = m - n + 1$ is the cyclomatic number.

RANDIC INDEX

In 1975, the Croatia scientist, Milan Randić introduced the first connectivity index [15], named nowadays the "Randić index"; it was defined

as the sum of all the bonds contribution, by means of d_i and d_j (being the degrees of the vertices/atoms "i", "j"):

$$\chi = \sum_{(i,j) \in D(G)} (d_i d_j)^{-1/2} \quad (4)$$

HARARY INDEX

The Harary index, $H(G)$, was introduced independently in 1993 by Plavsic *et al.* [16] and Ivanciuc *et al.* [17]. In fact, this index was introduced by Ciubotariu and the QSAR Group of Timisoara (Romania) since 1987 [18,19]. The Harary index is defined as:

$$H = \frac{1}{2} \sum_{i=1}^n \sum_{j=1}^n (1/D_{i,j}) \quad (5)$$

where $1/D_{i,j}$ represents the reciprocal distances in the graph.

GEOMETRIC INDICES

Geometric analysis provides characteristic values related to the geometrical structure of a molecule such as minimal and maximal z length, minimal and maximal projection area, force field energies or van der Waals volume. The Dreiding energy related to the 3D structure of a molecule was determined using the Dreiding force field.

A quantitative structure–property relationship (QSPR) study was herein performed for prediction of boiling points of 66 aliphatic alkane derivatives using topological and geometric indices.

RESULTS AND DISCUSSION

The experimental data of boiling point of alkanes and their derivatives are shown in Table 1.

The values of related molecular indices of 66 different types of alkanes and their derivatives were calculated using formulas (1 to 5); the values of geometry descriptors of all the mentioned compounds were extracted from book and web book [20].

The relationship between the boiling point of molecules used in the search and 11 different types of geometric and topological indices was investigated using the Excel software (equations 6-16).

Table 1. The values of experimental boiling point of the set of 66 alkanes

No	Compound	T _{bp} (K)	No	Compound	T _{bp} (K)
1	propane	231.05	34	2,3,3-trimethylpentane	387.85
2	n-butane	272.65	35	2,3,4-trimethylpentane	386.80
3	2-methylpropane	261.45	36	2-methyl-3-ethylpentane	388.80
4	n-pentane	309.25	37	3-methyl-3-ethylpentane	391.50
5	2-methylbutane	300.95	38	2,2,3,3-tetramethylbutane	379.60
6	2,2-dimethylpropane	282.65	39	n-nonane	423.90
7	n-hexane	342.15	40	2-methyloctane	415.95
8	2-methylpentane	333.45	41	3-methyloctane	416.45
9	3-methylpentane	336.45	42	4-methyloctane	415.00
10	2,2-dimethylbutane	322.85	43	2,2-dimethylheptane	405.85
11	2,3-dimethylbutane	331.15	44	2,3-dimethylheptane	413.65
12	n-heptane	371.55	45	2,4-dimethylheptane	406.65
13	2-methylhexane	363.15	46	2,5-dimethylheptane	408.00
14	3-methylhexane	365.15	47	2,6-dimethylheptane	408.35
15	2,2-dimethylpentane	352.35	48	3,3-dimethylheptane	410.45
16	2,3-dimethylpentane	362.95	49	3,4-dimethylheptane	413.25
17	2,4-dimethylpentane	353.65	50	3,5-dimethylheptane	409.15
18	3,3-dimethylpentane	359.25	51	4,4-dimethylheptane	408.35
19	2,3,3-trimethylpentane	354.05	52	3-ethylheptane	416.15
20	3-ethylpentane	366.65	53	2,2,4-trimethylhexane	399.65
21	n-octane	398.85	54	2,2,5-trimethylhexane	397.15
22	2-methylheptane	390.75	55	2,3,3-trimethylhexane	410.90
23	3-methylheptane	391.15	56	2,3,4-trimethylhexane	412.15
24	4-methylheptane	390.85	57	2,3,5-trimethylhexane	404.45
25	2,2-dimethylhexane	379.95	58	2,2,3,3-tetramethylpentane	413.42
26	2,3-dimethylhexane	388.75	59	2,2,3,4-tetramethylpentane	406.15
27	2,4-dimethylhexane	382.55	60	2,3,3,4-tetramethylpentane	414.65
28	2,5-dimethylhexane	382.15	61	2,2,4,4-tetramethylpentane	395.85
29	3,3-dimethylhexane	385.15	62	2,4-dimethyl-3-ethylpentane	409.88
30	3,4-dimethylhexane	390.85	63	3,3-diethylpentane	419.35
31	3-ethylhexane	391.50	64	n-decane	447.27
32	2,2,3-trimethylpentane	387.85	65	3-methylnonane	440.95
33	2,2,4-trimethylpentane	372.40	66	4-methylnonane	438.85

The following equations indicate the relationship between T_{bp} and the values of calculated molecular indices.

$$\text{Bp}=0.36 \text{ WW} + 322 \quad \text{R}^2=0.68 \quad (6)$$

$$\text{Bp}=1.15 \text{ W} + 296.47 \quad \text{R}^2=0.84 \quad (7)$$

$$\text{Bp}=9.92 \text{ H} +236.82 \quad \text{R}^2=0.92 \quad (8)$$

MODELING BOILING POINTS OF ALKANE DERIVATIVES

$$Bp=47.88 J +231.94 \quad R^2 =0.29 \quad (9)$$

$$Bp=58.10 X +172.05 \quad R^2 =0.97 \quad (10)$$

$$Bp=6.41P +277.31 \quad R^2 =0.55 \quad (11)$$

$$Bp=1.64 V +142.90 \quad R^2 =0.96 \quad (12)$$

$$Bp=7.00 \text{ Min P A} +173.19 \quad R^2 =0.50 \quad (13)$$

$$Bp=16.69 \text{ Min Z L} +214.1 \quad R^2 =0.49 \quad (14)$$

$$Bp=4.86 \text{ Max P A} +149.02 \quad R^2 =0.85 \quad (15)$$

$$Bp=25.99 \text{ Max Z L} +224.5 \quad R^2 =0.13 \quad (16)$$

According to eqs. (6 to 16), and the square correlation coefficients one can see that there are better correlations between T_{bp} with: Randic > Volume > Harary > Max P A > Wiener of this class of alkanes, respectively. A poor correlation was obtained between T_{bp} and Max Z L, Min Z L, Min P A, Platt, HyperWiener and the Balaban index of mentioned alkanes.

In the next step, SPSS software, multiple linear regression (MLR) method (eq. 17) and backward procedure were used.

$$Y = \beta_0 + \beta_1 X_1 + \beta_2 X_2 + \dots + \beta_p X_p + \epsilon \quad (17)$$

Whether or not the regression model explains a statistically significant proportion of data was ascertained through the ANOVA Table of output based on the MLR model in terms of the relationship between T_{bp} and effective molecular indices.

Therefore, different models were examined and the best model was defined using correlation coefficient, coefficient of determination, standard error of estimate, mean square, the Fischer statistics, and Durbin-Watson significance values. (Table 2).

Table 2. MLR statistics: Predictors X_i , Pearson correlation coefficient R^2 , R^2_{Adjust} , standard error of estimate s , Fisher Coefficient F , Mean Square MS , Significance of models Sig .

	X_i	R^2	R^2_{Adj}	s	F	MS	Sig
1	X, H, Volume, Mx P A, W	0.992	0.991	4.009	1.485E3	23860.749	0.000
2	X, Volume, Mx P A, W	0.992	0.991	3.988	1.875E3	29824.436	0.000
3	X, Volume, W	0.992	0.991	4.001	2.483E3	39758.370	0.000

To predict the T_{bp} values, three models were used with $\text{sig} = 0.000$, $F: 1.485E3 < 1.875E3 < 2.483E3$, $M-S: 23860.749 < 29824 < 39758.370$; respectively (Table 2).

$$Bp = 109.615 + 42.683x + 1.038V - 0.971H + 0.199\text{Max P A} - 0.383W \quad (18)$$

$$Bp = 116.715 + 43.730x + 0.837V + 0.303\text{Max P A} - 0.393W \quad (19)$$

$$Bp = 121.780 + 48.452X + 0.778V - 0.380W \quad (20)$$

Finally, one model with a compromise between the highest square correlation coefficient ($R^2 > 0.99$), Fisher coefficient ($F = 2.483E3$), standard error of estimate (4.001) with significance level = 0.000 and the lowest number of descriptors was opted for further analysis, as reported in MLR eq. (20). Therefore, the best model with $R^2 = 0.992$, $R^2_{\text{Adjust}} = 0.991$, $F = 2.483E3$, $\sigma = 4.002$ K, $MS = 39758.370$ K, $DW = 1.651$ was used for prediction of alkanes T_{bp} . The best two descriptors are shown as predictors in the third model in terms of non-standardized coefficients.

This equation has three common descriptors X , V , W with high calibration statistics and prediction ability.

It is known that, the adjust coefficient (R^2_{Adjust}) indicates the percentage of dependent variable that is justified by the independent variable. The less distinction between R^2_{adjust} and R^2 indicates that the independent variables added to the model have been chosen more appropriately. The slight difference between the above amounts in the proposed model verifies the precision and accuracy of the model for predicting the critical properties. The coefficient which has been used in the statistical method is called the significance level. The more the significance level closes to zero, the smaller the significance level and the more meaningful the linear model will be. Therefore, a higher Fisher coefficient leads to a smaller significance coefficient.

Durbin-Watson (DW) statistics is a number giving information about the autocorrelation in the residuals. The statistical coefficient of Durbin-Watson test ranges between 0 and 4. The more this coefficient closes to zero, the less correlation between the errors will be. However, the amount of this number indicates there is no caution using the proposed models.

Table. 3 lists the T_{bp} of considered molecules predicted by eq. (20).

Figure 1 shows the linear correlation between the predicted T_{bp} by using eq. (20) compared with the experimental T_{bp} . The results indicate that the equation (20) can be used effectively for predicting the T_{bp} of alkanes. Therefore, the results are satisfactory.

MODELING BOILING POINTS OF ALKANE DERIVATIVES

Table 3. $T_{bp(Pred)}$ (K) with Eq. 20 and Residual (K) of Alkanes

No	$T_{bp(Pred)}$ (K)	Residual (K)	No	$T_{bp(Pred)}$ (K)	Residual (K)
1	236.93	-5.88	34	382.93	4.91
2	272.07	0.57	35	384.01	2.78
3	263.82	-2.37	36	391.46	-2.66
4	305.72	3.52	37	390.75	0.74
5	299.78	1.17	38	372.64	6.96
6	287.66	-5.01	39	417.43	6.46
7	337.50	4.64	40	413.09	2.86
8	331.96	1.48	41	416.60	-0.15
9	334.29	2.15	42	417.39	-2.38
10	323.53	-0.68	43	406.92	-1.07
11	327.02	4.12	44	413.68	-0.03
12	366.83	4.71	45	412.46	-5.8
13	361.79	1.35	46	411.79	-3.79
14	364.55	0.59	47	408.74	-0.39
15	354.15	-1.79	48	412.29	-1.83
16	360.05	2.90	49	417.17	-3.92
17	356.64	-2.98	50	415.22	-6.07
18	357.84	1.40	51	413.01	-4.66
19	350.09	3.95	52	420.89	-4.74
20	367.30	-0.65	53	405.72	-6.07
21	393.69	5.15	54	402.58	-5.43
22	388.99	1.76	55	409.75	1.14
23	392.11	-0.96	56	413.17	-1.02
24	392.49	-1.63	57	409.10	-4.65
25	382.05	-2.54	58	403.99	9.42
26	388.29	0.45	59	404.39	1.75
27	386.86	-4.31	60	406.96	7.69
28	384.23	-2.08	61	396.74	-0.89
29	386.60	-1.45	62	414.02	-4.13
30	391.07	-0.21	63	422.06	-2.71
31	395.59	-4.09	64	437.77	9.49
32	381.59	6.25	65	437.72	3.23
33	377.37	-4.97	66	438.89	-0.03

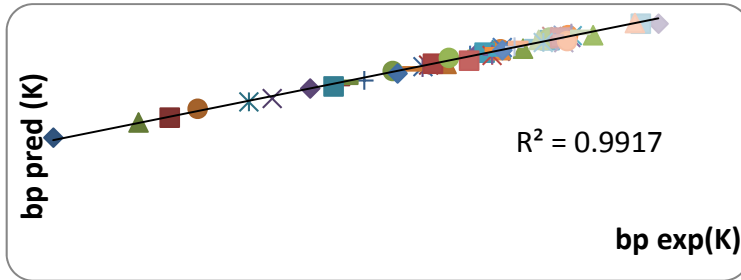


Figure 1. The plot of predicted bp vs experimental bp

Figure 2 shows the differences between the experimental and predicted boiling points of alkanes.

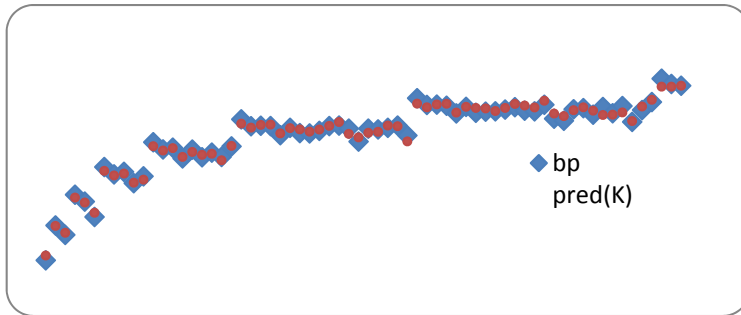


Figure 2. Comparison between the experimental and predicted of T_{bp} by MLR method

The residual values are represented at a fairly random pattern (Figure 3). Residuals are used to assess the normality of assumption. This random pattern indicates that a linear model provides a decent fit to the data.



Figure 3. The scatter plot of residuals against experimental values of alkanes boiling points

CONCLUSIONS

Mathematical regression models are very important in QSAR modelling and the regression method, particularly MLR, can be used in this respect.

The results of this study indicated that the boiling points of alkane derivatives have a strong correlation with Wiener, Randić and volume descriptors.

EXPERIMENTAL

To analyse the relationship between boiling point and molecular descriptors, the research data were collected in two stages:

First, the structures and the values of experimental available boiling points of 66 various types of alkanes and their derivatives used in the present investigation were taken from National Institute of Standard and Technology Chemistry web book and listed in Table 1.

Second, the values of Randic (χ), Harary (H), Balaban (J), Wiener (W), Platt (P) and HyperWiener (WW) topological indices related to the mentioned molecular graphs were calculated using the above formulas. Also the values of geometry descriptors such as the minimal z length (Min.z.L/A^o), the maximal z length (Max.z.L/A^o), the minimal projection area (Min. P.A/A^{o2}), the maximal projection area (Max.P.A/A^{o2}), the van der Waals volume (V/A^{o3}) for these 66 compounds were extracted from book and web book [20].

Third, the relationship between boiling points and 11 various types of molecular descriptors was investigated for the set of alkanes derivatives, using excel software, and the relevant equations were extracted.

Finally, the boiling points of these alkanes and their derivatives were estimated using SPSS software (version 16) by multiple linear regression method and backward procedure. The best molecular indices were determined for prediction of the boiling points of mentioned compounds in terms of important parameters such as Fisher statistics, Durbin Watson, correlation coefficient, square correlation coefficient, adjust square correlation coefficient, etc. (Table 2).

REFERENCES

1. A. Arora, "Hydrocarbons, Alkanes, Alkenes and Alkynes", Discovery Publishing House, **2006**.
2. L. Blaha, J. Damborsky, M. Nemeč, *Chemosphere*, **1998**, 36(6), 1345.
3. N. Trinajstić, I. Gutman, *Croatica Chemica Acta*, **2002**, 75, 329.

4. N. Gutman, Trinajstic, *Chemical Physics Letters*, **1972**, 17, 535.
5. I. Gutman, B. Furtula (eds), "Novel molecular structure descriptors-theory and applications I and II", Univ. Kragujevac, **2010**, 3.
6. I. Gutman, B. Ruscic, N. Trinajstic, C.F. Wicox, *Journal of Chemical Physics*, **1975**, 62, 3399.
7. E. Mohammadinasab, and M. Goodarzi, *Fullerenes, Nanotubes, and Carbon Nanostructures*, **2011**, 19, 550.
8. A.A. Taherpour, E. Mohammadinasab, *Fullerenes, Nanotubes and Carbon Nanostructures*, **2010**, 18, 76.
9. M. Monajjemi, E. Mohammadinasab, F. Shafiei, *Journal Physical&Theoretical Chemistry*, **2009**, 6, 125.
10. M. Goodarzi, E. Mohammadinasab, *Fullerenes, Nanotubes and Carbon Nanostructures*, **2013**, 21, 102.
11. H. Wiener, *Journal of American Chemical Society*, **1947**, 69, 17.
12. M. Randić, *Chemical Physics Letters*, **1993**, 211, 478.
13. G. Cash, S. Klavzar, M. Petkovsek, *Journal Chemical Information and Computer Science*, **2002**, 42, 571.
14. A.T. Balaban, *Chemical Physics Letters*, **1982**, 89(5), 399.
15. M. Randic, *Journal American Chemical Society*, **1975**, 23, 6606.
16. D. Plavsic, S. Nikolic, N. Trinajstic and Z. Mihalic, *Journal of Mathematical Chemistry*, **1993**, 12(1), 235.
17. O. Ivanciuc, T.S. Balaban, and A.T. Balaban, *Journal of Mathematical Chemistry*, **1993**, 12, 309.
18. D. Ciubotariu, "Structură-reactivitate în clasa derivațiilor acidului carbonic", PhD Thesis, Timisoara, Romania, **1987**.
19. D. Ciubotariu, M. Medeleanu, V. Vlaia, T. Olariu, C. Ciubotariu, D. Dragos and C. Seiman (2004) *Molecules*, **2004**, 9, 1053.
20. Web search engine developed by ChemAxon; software available at [http:// www. Chemicalize. Org](http://www.Chemicalize.Org).

PRACTICAL INVESTIGATION OF GELS CONTAINING ARISTOLOCHIA (*ARISTOLOCHIA CLEMATITIS*) EXTRACT

PAUL ATYIM^{a*}, NELI KINGA OLAH^a, GYÖNGYI OSSER^a,
CLAUDIA CRINA TOMA^a, CLAUDIU MORGOVAN^{a*},
ELISABETA ATYIM^b

ABSTRACT. The aim of this study is to embed the active ingredients of the hydroalcoholic extract from the aristolochia (*Aristolochia clematitidis*) into a new semisolid preparation and a viscoelastic methylcellulose based hydrogel in order to broaden the topical applicability of the palette's range. The methylcellulose based hydroalcoholic gel formulation, preparation and quality evaluation was realized by continuously measuring the product's physico-chemical parameters. The evaluated physico-chemical parameters: the swelling degree, the equilibrium swelling degree, the swelling rate and the swelling fraction, the swelling rate parameter, the swelling kinetics order, the speed constant.

Keywords: *Aristolochia clematitidis*, hydrogel, methylcellulose, pH, swelling parameters

INTRODUCTION

Over the last two decades, gels, in general, and hydrogels in particular, have been extensively studied as semi-solid pharmaceutical products, capable of ensuring an efficient delivery of the drug, after its oral, rectal, vaginal, ocular, cutaneous or subcutaneous administration.

Thus, hydrogels have become widely used in the biomedical and pharmaceutical fields, as transportation systems and biomedical devices, due to their biocompatibility, their network structure and due to the molecular stability of the incorporated bioactive compound [1]. Hydrogels can be prepared from a

^a Vasile Goldis Western University of Arad, Faculty of Pharmacy, Department of Pharmaceutical Sciences, Liviu Reberanu Street 86, Arad, Romania

^b Kölcsey Ferenc National College, Mihai Eminescu Street 1, Satu Mare, Romania

* Corresponding authors: dpatyim@yahoo.co.uk, claudiumorgovan@yahoo.com

wide range of materials, such as semi-synthetic polymers (eg. Cellulose derivatives), whose practical applications are increasing day by day [2, 3]. Due to the high water content, hydrogels can dissolve hydro soluble drugs, resulting in aqueous, transparent gels.

Hydrogels are characterized by the following aspects: they chemically stable in general, but they may dissolve or disintegrate in water. The classic hydrogels are highly valued in dermatology due to their transparency and their high water content which confers them a refreshing sensation when applied, which is sought after in the treatment of some types of acute dermatitis. Hydrogels are physiological, they dry up on the application site and form a protective coating, conferring softness to the skin and they are preferred by patients with seborrheic skin. They are easily removed by washing the area. The pH of the hydrogels can be easily adjusted by adding buffer solutions. A great advantage is that temperature does not influence the consistency of hydrogels, with the exception of the thermo sensitive ones. They are well tolerated by the skin and mucous membranes and also have a cooling effect [4].

The birthwort can be used only externally for various conditions, as a tincture, cream, poultice or sitting baths. The birthwort tincture is prepared from thoroughly crushed or ground leaves, which are mixed with alcohol over 70°; it is then left to soak for two weeks. The resulting tincture may be used for up to two years since the date the plants were harvested on.

The hydro alcoholic extract has antiseptic, healing and detoxifying properties due to chemical composition in bioactive substances [5]. It is recommended in allergies, thrush, angina, bronchitis, an irritable bowel syndrome, hemorrhoids, varicose veins, varicose ulcers, psoriasis, vaginal candidiasis, gonorrhea, uterine fibroids, breast cysts, abscesses, breast infections, tonsillitis, rhinitis, lymphangitis, adnexitis (pelvic inflammatory disease), eczemas, dermatitis, ulcerative infections, wounds, cuts, burns, scalding, skin regeneration, hair loss and cancer diseases [6, 7].

It is used as a compress on the affected areas, thus healing severe, festering wounds, which have withstood other treatments.

RESULTS AND DISCUSSIONS

The Organoleptic Analysis

The organoleptic analysis tells us that the hydrogel is washable, that it has a homogenous, translucent aspect with a smell characteristic to the hydroalcoholic medicinal plant extract. The organoleptic characteristics: aspect, viscosity, aroma and color of the freshly prepared hydrogel were preserved up to 6 months.

The pH variation

The pH variation of the freshly prepared hydrogel, after 3 months and 6 months since its preparation is depicted in Figure 1.

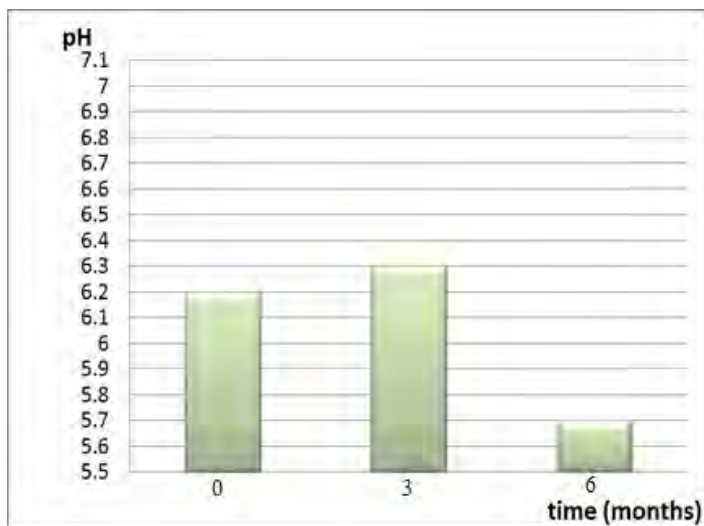


Figure 1. The pH variation depending on the time, at 0, 3 and 6 months

Probably the pH varies because of the partial hydrolysis processes of methyl 4-coumarate, magnoflorine iodide in the presence of aristolochic acid, ferulic and 4-coumaric acids. One should observe that, after a slight increase at 3 months, after 6 months since its preparation, it still is within the RP X (Romanian Pharmacopoeia X) provisions

The spreading capacity

The spreading capacity of an ointment is a very important property since it provides information regarding the ease with which the ointments can be applied on the skin or on the mucous membranes. It is characterized by the force that needs to be applied in order to spread the ointment and it depends on the viscosity and consistency of the semi-solid product.

As shown in Figure 2, even after 6 months, the circle surfaces fall within the accessibility limits regarding the spreading capacity of the semi-solid products, according to the RP X.

One can observe a stabilization of the consistency and of the spreading capacity of the hydrogel containing the hydroalcoholic birthwort extract, after 6 months as well.

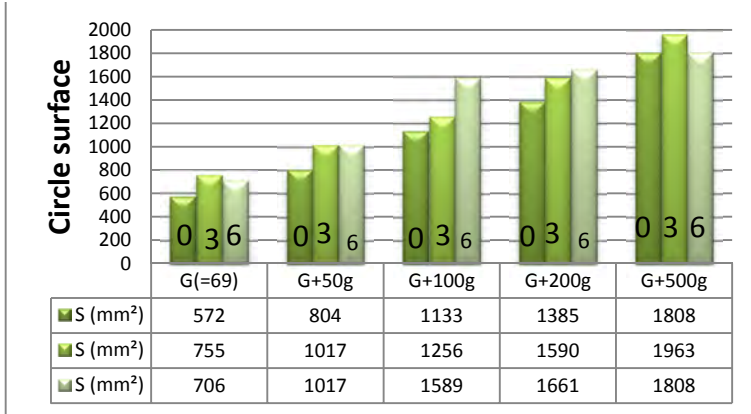


Figure 2. Determining the spreading capacity of the hydrogel containing the hydroalcoholic birthwort extract, via the Ojeda-Arbussa method

Determining the physico-chemical swelling parameters of the hydrogel

The degree of swelling (**Q**) represents the amount of liquid absorbed by the mass unit of the hydrogel:

$$Q = \frac{m_t - m_0}{m_0} \quad (1)$$

where m_0 is the mass of dry hydrogel and m_t is the mass of swollen hydrogel at the time t . Table 1 shows the data on the degree of swelling of the *Aristolochia clematitis* extract hydrogel.

Table 1. The degree of swelling of the *Aristolochia clematitis* extract hydrogel

Hydrogel mass (g)	Time (min.)	Degree of swelling Q (%)
$m_0=1.3344$	0	-
$m_1=3.0894$	30	131.51
$m_2=3.6317$	60	172.15
$m_3=3.8805$	90	190.80
$m_4=3.8207$	120	186.32
$m_5=3.8947$	150	191.86
$m_6=3.8621$	180	189.42
$m_7=3.8561$	210	188.97
$m_8=3.5456$	240	165.70 Obs.: hydrolyses

Figure 3 shows the variation of the hydrogel's swelling degree over time.

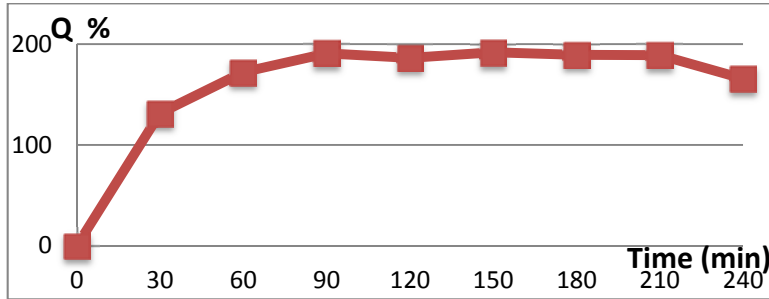


Figure 3. The variation of the hydrogel's swelling degree over time

The equilibrium water content (EWC%) [9] is calculated using the formula (2):

$$Q_e \% = \frac{m_{tf} - m_0}{m_{tf}} \cdot 100 \quad (2)$$

where m_{tf} is the mass of the swollen hydrogel in equilibrium (in the end) and m_0 is the mass of the dry hydrogel and is 189,47%.

The variation of the swelling content, per time unit, of the hydrogel is known as **swelling rate**, Q_R [10] and is calculated using the formula (3):

$$Q_R = \frac{Q_{t+\Delta t} - Q_t}{\Delta t} \quad (3)$$

where Q_t is the swelling degree at any given time and $Q_{t+\Delta t}$ is the swelling degree based on the dry content at $t+\Delta t$. For Δt (min) = 30 it is 0,0103 and for Δt (min) = 60 its value is 0,0015.

Based on the Davidson – Peppas model [14] the swelling of the hydrogels can be characterized by the **F swelling fraction** equation (4)

$$F = \frac{Q_t}{Q_e} = kt^n \quad (4)$$

where F is the swelling fraction, Q_e is the equilibrium swelling degree, n is the solvent's diffusion exponential and k is the constant that changes depending on the structure of the gel's network [10,13]. In order to determine the type of diffusion, one must know the value of n . The diffusion's exponential can be determined from the slope of the line obtained from the graphic representation

of the $\ln F$, depending on the $\ln t$; one should take into consideration the data from the graph in the region where the swelling has not reached equilibrium, where just 60% of the solvent's mass has permeated the gel's structure. The n , k values are calculated using the slope of the resulting line. If the value of n is below 0,5, we are talking about a Fickian diffusion; anything above 0,5 implies a non-Fickian diffusion of the water. **Figure 4** represents the $\ln F$ variation, depending on the $\ln t$, only for 60% of the solvent's mass which permeated the gel's structure.

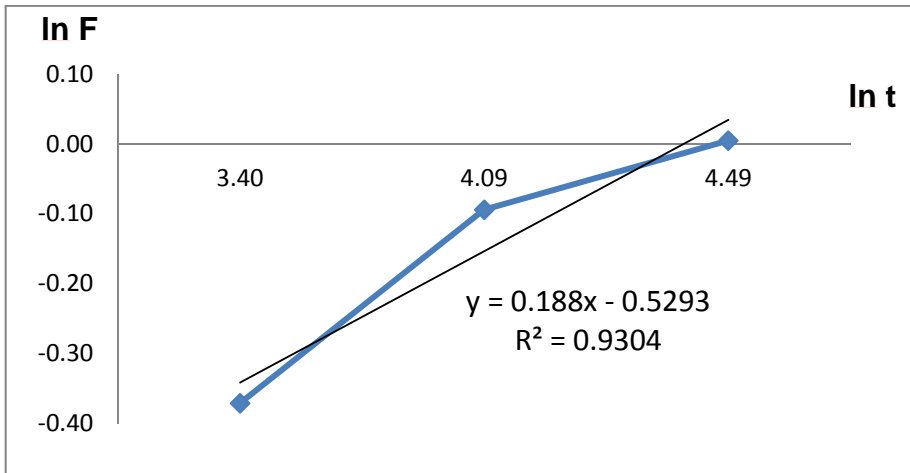


Figure 4. The $\ln F$ variation depending on the $\ln t$ for 60% of the solvent's mass which permeated the gel's structure.

Calculations showed $n=0,33$ and the diffusion constant (the front factor) $k=1,65$ (min^{-n}).

In order to study the swelling kinetics of hydrogels, one must apply the Voigt-Kelvin viscoelastic kinetic model [11], having the following equation:

$$Q_t = Q_e \left(1 - e^{-\frac{t}{\tau}}\right) \quad (5)$$

where Q_t is the swelling degree for the t period, Q_e is the equilibrium swelling degree and τ is the **swelling rate parameter (time retardation)**. The τ value is the measure of the swelling rate in the sense that: the lower the τ value is, the higher the swelling rate will be. In order to calculate the parameter of the swelling rate τ , by the linearization of the equation (5) $\ln\left(1 - \frac{Q_t}{Q_e}\right)$ one must graphically represent it, depending on the time t . Using the slope of the line

(slope = $-1/\tau$) we can calculate the τ swelling rate parameter. The swelling rate represents the time necessary to obtain a swelling degree equal to 0,6321 of the equilibrium swelling degree's value. Figure 5 shows the evaluation of the swelling rate.

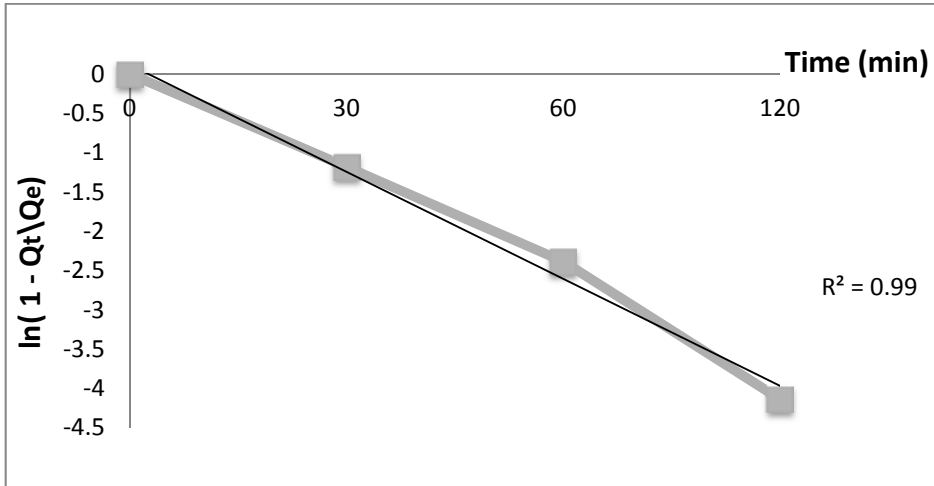


Figure 5. The evaluation of the swelling rate.

After the calculations, $\tau = 26,5$ min.

In order to determine the order of the swelling kinetics, we must resort to the procedure of Quintana & al. [11,12], regarding the model – dependency approach. For a **level one kinetics**, the differential of the swelling speed is as equation (6):

$$\frac{dQ}{dt} = K(Q_e - Q) \quad (6)$$

where Q is the swelling degree at the time t. By integrating the (6) equation, we have the formula (7):

$$\ln\left(\frac{Q_e}{Q - Q_e}\right) = K \cdot t \quad (7)$$

If the swelling occurs via a level one kinetics, through a graphical representation of $\ln\left(\frac{Q_e}{Q - Q_e}\right)$ depending on the time, **Figure 6**, we need to analyze the value of the regression coefficient R, which should be close to 1;

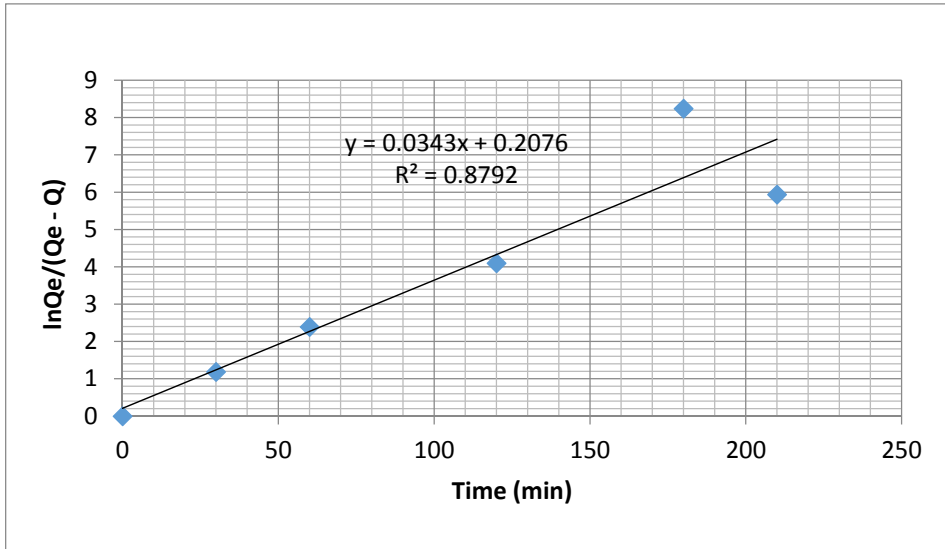


Figure 6. Graphical representation of the $\ln\left(\frac{Q_e}{Q_e - Q}\right)$ variation, depending on the time

otherwise, the kinetics of the swelling is not a level one. A level two swelling kinetics has the differential equation (8)

$$\frac{dQ}{dt} = K(Q_e - Q)^2 \quad (8)$$

After the integration and linearization of the equation, we obtain the following:

$$\frac{1}{Q} = \frac{1}{K \cdot Q_e^2} + \frac{1}{Q_e} \cdot t \quad (9)$$

If, for the graphic representation of $1/Q$, depending on the time t , the linear regression coefficient is close to 1 more than in the case of a level one kinetics, the swelling kinetics is a level two type. Figure 7 shows the variation of the reciprocal value of the swelling degree, depending on the time. The graph also allows us to determine the speed constant.

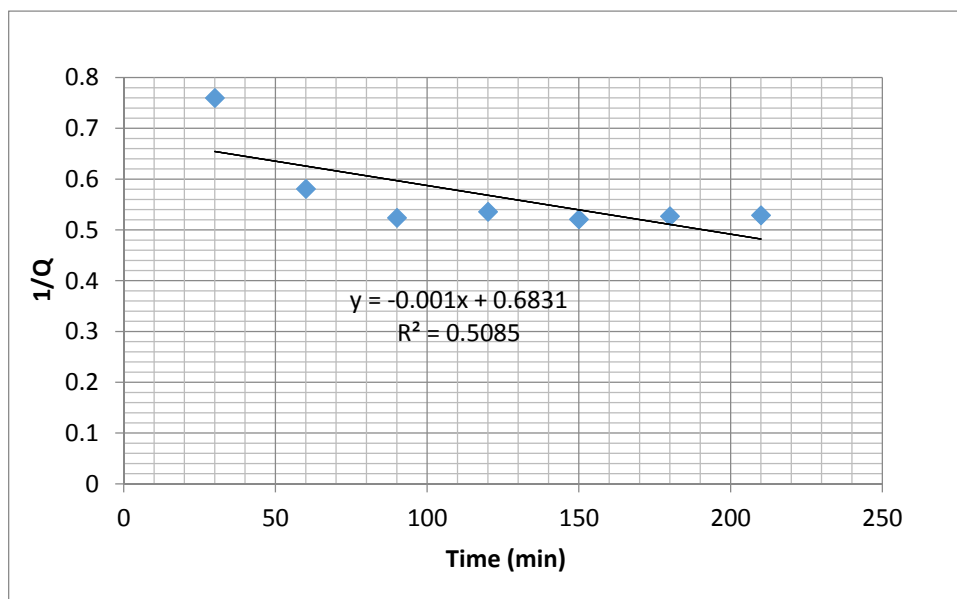


Figure 7. The variation of the reciprocal value of the swelling degree, depending on the time.

Due to the fact that, in the case of this model, R has a value less close to 1 when compared to the level I kinetics model, the swelling of the birthwort extract hydrogel follows a level I kinetics, with a speed constant of $K = 3,33 \cdot 10^{-2} \text{ min}^{-1}$. This model can be found among other swelling kinetics models [17], therefore suggesting the complexity of this process's kinetics.

CONCLUSIONS

The hydroalcoholic birthwort extract, turned into gel with methylcellulose, forms a stable product, with an optimal release of the active ingredient.

After a slight acidification process, the pH changes remain within the scope of the safety requirement's applicability.

The Ojeda – Arbussa diagram indicates a softening of the product, over time, which becomes stable after 3 and 6 months.

The evaluated physico-chemical parameters: the swelling degree, the equilibrium swelling degree, the swelling rate and the swelling fraction, the swelling rate parameter, the swelling kinetics order, the speed constant; all these demonstrate the presence of a physical hydrogel structure.

EXPERIMENTAL SECTION

The preparation of the hydroalcoholic *Aristolochia clematitis* extract hydrogel, for one hundred grams of product, was done as follows: for 50 g of distilled water – vehicle, heated to 70⁰ C, 5 g of methylcellulose with DS = 1,5 – 1,9 were added (Parma Produkt Srl. 1145 Budapest, Hu) as a viscosity-increasing agent under continuous stirring. In order to cool down the solution, we added 10 g of glycerol (SC Stera Chemicals Srl, Jilava, Ro) as a humectation agent [16] and 10 g of 96⁰ ethyl alcohol (SC Medchim TM Srl, București, Ro) as a dispersing agent [8]. The remaining 15 g of distilled water are to be added and one should wait until the system takes a gel-like form, which is when the 10 g of birthwort tincture need to be added (Aroma Plant – Ion Bonchiș, Buntești nr. 83, Bihor, Ro) 27% (V/V) as a therapeutic agent.

The organoleptic examination ensures that the most important characteristics of the hydrogel are determined, such as its aspect, consistency, its smell and its color [8].

The determination of the pH was done with a potentiometrically, according to the RP X [18]. provisions, by using a portable, digital pH-meter of the *pHep®+* by *Hanna pH* type. The measurements were performed on samples taken from the freshly prepared hydrogel, after 3 and 6 months since its preparation.

In order to determine the spreading capacity, the Ojeda – Arbussa method was used. The method is based on the principle of measuring the spreading surface of an ointment, under the action of a determined force. The measurement is made with a common device known as an extensometer, suggested by A. Pozo-Ojeda and J.M. Sune-Arbussa. The device consists of two glass plates, with sides of 11 cm. The external part of the lower plate is covered in scale paper, with 5 concentric circles drawn on it. Starting with the first circumference, the perpendicular diameters are graduated in mm, which intersect in the center, where the first circle has been drawn, with a 1 cm diameter. On the lower plate, in the center of the first circle, 1 g of ointment is placed, over which the second plate is placed. The diameter of the circle created by the ointment is noted, a circle which resulted after the ointment was applied pressure with a glass plate weighing 69 g. After 1 minute, on the top plate of the extensometer, weights are added, in an ascending order – 50, 100, 200 and 500 g. The radiuses of the circles created by the investigated sample are read and they are noted down with r_1 , r_2 , r_3 etc. Afterwards, the surfaces are calculated, which are noted with S_1 , S_2 , S_3 etc.

In order to determine the main physico-chemical swelling parameters of this hydrogel, after its preparation it is dried to a constant weight, at a temperature of 50⁰ C, after which a cylindrical shaped piece is cut out [15],

which has $m_0 = 1.3344$ g. This sample is immersed by means of a plastic bag in a glass containing 500 ml of distilled water and it is removed from said glass at intervals of 30 minutes; the excess water is removed from the surface of the hydrogel in the swollen phase, after which the mass is weighed with the analytical scale. This procedure is repeated until the hydrogel starts disintegrating, which is signaled by the loss in mass, after a long interval in which the mass was constant. Table 2 represents the starting values for the evaluation of the other physico-chemical swelling parameters. All the measurements of the physico-chemical parameters derived from the swelling degree were made on the hydrogel, after six months since its preparation.

Average values were reported for at least three measurements made for each sample, separately.

REFERENCES

1. Lavinia Vlaia, Ioana Olariu, Georgeta Coneac, Ana Maria Muț, V. Vlaia, Z. Szabadai, D. Lupuleasa, *Practica farmaceutica*, **2015**, 8, 5.
2. N.A. Peppas, P. Bures, W. Leobandung, H. Ichikawa, *European Journal of Pharmaceutics and Biopharmaceutics*, **2000**, 50, 27.
3. J. Siepmann, R. Siegel, M. Rathbone, Fundamentals and Applications of Controlled Release Drug Delivery, Eds. Springer, New York, NY, **2012**, 75.
4. Iuliana Popovici, D. Lupuleasa, Tehnologie farmaceutică, Eds. Polirom, **2008**, Tom 2, 1500.
5. D. Košťálová, V. Hrochová, N. Pronayová, J. Leško, *Chemical Papers*, **1991**, 45 (5), 713.
6. Heinrich, M., Chan, J., Wanke, S., Neinhuis, C., & Simmonds, M.S., *Journal of Ethnopharmacology*, **2009**, 125 (1), 108.
7. Camelia Papuc, Maria Crivineanu, G. Goran, V. Nicorescu, Nicoleta Durdun, *Revista de Chimie*, **2010**, 61, 7, 619.
8. Laura Vicaș, *Practica farmaceutică*, **2012**, 5, 23.
9. A. Barati, H. Norouzi, S. Sharafoddinzadeh, R. Davarnejad, *World Applied Sciences Journal*, **2010**, 11 (11): 1336.
10. A.S. Kipcak, O. Ismail, I. Doymaz, S. Piskin, *Journal of Chemistry*, **2014**, Volume 2014, Article ID 281063, 8 pages.
11. M. Sadeghi, G. Koutchakzadeh, *Journal of Sciences (Islamic Azad University)*, **2007**, 17, 19.
12. J.R. Quintana, N.E. Valderruten, I. Katime, *Langmuir*, **1999**, 15, 4728.
13. F. Ganji, S. Vasheghani-Farahani, E. Vasheghani-Farahani, *Iranian Polymer Journal*, **2010**, 19 (5), 375.
14. G.W. Davidson, N.A. Peppas, *Journal of Controlled Release*, **1986**, 3, 243.

15. Ch. Chang, B. Duan, J. Cai, L. Zhang, *European Polymer Journal*, **2010**, *46*, 92.
16. Elena Dinte, M. Todica, C.V. Pop, S. E. Leucuta, *Studia UBB Physica*, **2008**, *LIII*, 55.
17. A. Kostić, B. Adnadjević, A. Popović, Jelena Jovanović, *Journal of the Serbian Chemical Society*, **2007**, *72* (11), 1139.
18. *** Romanian Pharmacopoeia X (RP X), Eds. Editura Medicală, Bucuresti, **1993**, 1315.

INVESTIGATING THE IMPACT OF SOILS' PHYSICOCHEMICAL COMPOSITION ON CHLORSULFURON PEDOSPHERIC SORPTION

KHURAM SHAHZAD AHMAD^a

ABSTRACT. Chlorsulfuron (1-(2-chlorophenyl) sulfonyl-3-(4-methoxy-6-methyl-1, 3, 5- triazin-2-yl)), a Sulfonyl herbicide was investigated for its sorption behaviour in soils from various geographical locations. The results, fitting Freundlich and Linear equations, depicted a C type curve. Linear distribution coefficient value (K_d) spanned in a range of 8.2-23.0 $\mu\text{g/ml}$ while Freundlich distribution coefficient value (K_f) was found to be 7.06 -17.41 $\mu\text{g/ml}$. Low Gibbs free energy values (-14.9 to -16.0 kJ/mol) are indicative of physisorption process. The regression and correlation analysis depicted pH to be negatively correlated ($r=-0.936$) while organic matter and organic carbon to be positively correlated with K_d ($r=0.989$ and $r=0.988$ respectively). However the soil texture rendered positive correlation with clay ($r=0.897$) and negative correlation with sand and silt ($r=-0.990$ and $r=-0.820$ respectively). Desorption hysteresis coefficient (H), in all four soil was found to be less than 1 (0.44 to 0.62). Results have been statistically evaluated by ANOVA and the accuracy of fit has been calculated by plotting residual graphs in Minitab. This study is a milestone for further investigation based on Chlorsulfuron degradation and mobility patterns.

Keywords: Chlorsulfuron methyl, Soil, Adsorption, Correlation, Regression

INTRODUCTION

Weed control is an imperative factor for an effective crop production and therefore the prevention of weed-crop competition at an early stage plays a very paramount role [1]. Sulfonylurea (SU) herbicides are group of herbicides,

^a Department of Environmental Sciences, Fatima Jinnah Women University, The Mall, 46000, Rawalpindi, Pakistan. Tel #:92 (051) 9292900, Email: chemist.phd33@yahoo.com

recently manufactured and the preeminent qualities of these weedicides include their rather immensely active nature and very low application rates [2]. Long term application of sulfonylurea herbicides often cause curtailment in crop yield annually as well as emergence of resistant weed species to herbicides application [3,4]. Boost in crop yields has been observed by using pesticides yet it also posed challenges to food and environmental contamination [5]. Chlorsulfuron has been the first sulfonylurea herbicide in terms of commercialization. Chlorsulfuron finds major applicability for wiping out multiple weed species and is also used as a pre-emergent and post-emergent herbicide on variety of weeds attacking the cereal crops [6, 7, 8]. Chlorsulfuron possess minor toxicity for mankind and other faunal species. It is known for obstructive response for enzyme acetolactate synthase (ALS) which is aimed at biosynthetic protein pathways in floral and microbial species. Chlorsulfuron application rates for weed destruction can have an influential impact on microbe mediated processes thus different doses rates have been recommended for Chlorsulfuron use [9]. Several floral and microbial populations exhibited resistance towards Chlorsulfuron which is mostly associated with point mutations rendered in ALS thus causing hindrance between Chlorsulfuron and acetolactate synthase attachment [10,11]. Recently number of floral species i.e. 103 monocotyledonous and 143 dicotyledonous has been found resistant to ALS impeder like Chlorsulfuron [12]. Like all other ALS-impeder herbicides, Chlorsulfuron toxicity towards plants and persistence is influentially governed by organic matter. Higher quantity of organic matter favors alleviated toxicity and reduced dispersal in soil compartment [13]. Residual herbicide quantities have given rise to their use particularly in case of grain and leguminous crops. Chlorsulfuron migratory patterns enabling its occurrence away from areas of application has been influenced by several factors. Thus Chlorsulfuron application has been completely restricted in several regions [14, 15]. Despite massive use of pesticides in an agricultural country like Pakistan, the reported data is scant in many aspects [16]. Drawing a clear cut trend for Chlorsulfuron mitigation in contaminated soils on larger scale is impossible without comprehension of its sorption behaviour. Thus present study took into account this scant knowledge by investigating sorption behaviour of Chlorsulfuron in selected soils and to draw a clear environmental trend depicting the dependence of sorption on soils' physicochemical characteristics.

RESULTS AND DISCUSSION

Variation in soils' physicochemical make up

Table 1. Physicochemical parameters of selected soils

Soil	pH	OM (%)	TOC (%)	N (%)	Clay (%)	Sand (%)	Silt (%)	CEC	Texture	EC ($\mu\text{s}/\text{cm}$)
1	7.41	2.29	1.33	0.137	26	20.48	53.52	7.1	Silty loam	707
2	6.2	3.5	2.03	0.14	60.52	15	24.48	7.4	Clay	272
3	6.60	2.82	1.63	0.092	57	19	24	7.83	clay	232
4	7.38	2.74	1.59	0.083	40.94	6.3	52.76	7.9	Silty loam	189

(OM: organic matter, TOC: Total Organic Carbon, CEC: Cation exchange capacity, EC: Electrical conductivity)

Soils sampled from geographically diverse zones were tested for variation in physicochemical characteristics (Table 1). This degree of variation was expressed in terms of all tested parameters with Soil 2 exceeding all samples in lowest pH (6.2), highest OM and TOC (3.5% and 2.03%), highest clay content (60.52%). This was due to the fact that the sample was taken from an agricultural region and the vegetation results in an increase in the soil OM. The value of kinetic parameters increases with the increasing clay content [17]. Selected soils followed the trend Soil2> Soil3> Soil4> Soil1 for above mentioned parameters. The values of EC varied among all soils and were in the range 189-707 $\mu\text{s}/\text{cm}$. Higher variability in EC values has been reported for several soils thus altering pesticide adsorption [18]. The organic matter (OM) in all the samples was found not to be in a higher range (2.29-3.5%).

Variable sorptive affinities

Table 2. Adsorption coefficients of Chlorsulfuron in selected soils

Soils	K_d ($\mu\text{g}/\text{ml}$)	R^2	K_{oc}	K_f ($\mu\text{g}/\text{ml}$)	R^2	K_{foc}	n_a	K_{om}	ΔG (kJ/mol)
1	8.2	0.92	850.0	7.06	0.83	732.35	1.22	425.80	-14.9
2	23.0	0.98	1440.5	17.41	0.87	1093.39	1.60	635.70	-15.9
3	15.1	0.9	1271.6	13.6	0.99	1137.03	1.32	661.70	-16.0
4	12.0	0.95	1121.0	9.32	0.74	867.27	1.90	504.23	-15.4

Photometric determination of Chlorosulfuron adsorption and desorption was done at λ_{\max} 230 nm on UV-Vis Spectrophotometer BMS 1602. The adsorption and desorption isotherms of Chlorosulfuron in all tested soil samples yielded nonlinear and Freundlich isotherm that resemble to C-type isotherm shape (figure 1-4). This type of isotherm usually depicts the interaction of hydrophobic adsorbate with hydrophobic adsorbent (e.g. pesticide–organic matter interactions). Adsorption equilibrium distribution co-efficient ($K_{d(ads)}$) was calculated by plotting the adsorbed pesticide concentration (C_s) against the equilibrium pesticide concentration (C_e) and are shown in the Table 2. Similarly the desorption equilibrium distribution co-efficient ($K_{d(des)}$) was calculated by plotting the desorbed pesticide concentration (C_s) against the equilibrium pesticide concentration (C_e). The distribution coefficients (K_d), Freundlich constant (K_f), Gibbs free energy (ΔG) and hysteresis (H) were calculated from the obtained isotherms.

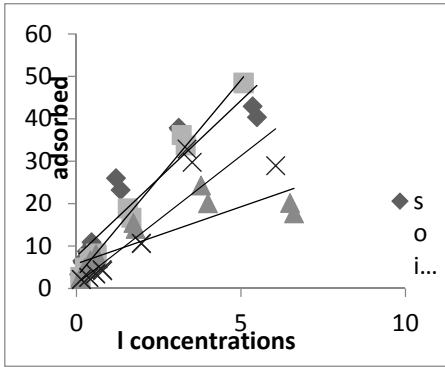


Figure 1. Comparative linear adsorption isotherms of Chlorosulfuron on studied soils

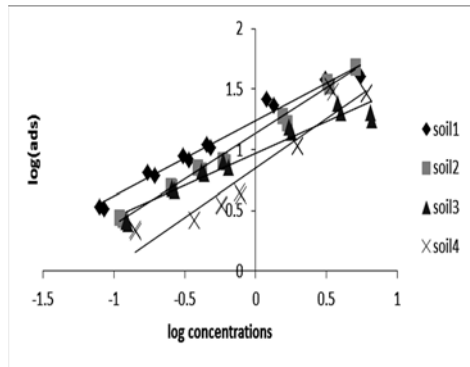


Figure 2. Comparative Freundlich adsorption isotherms of Chlorosulfuron on studied soils

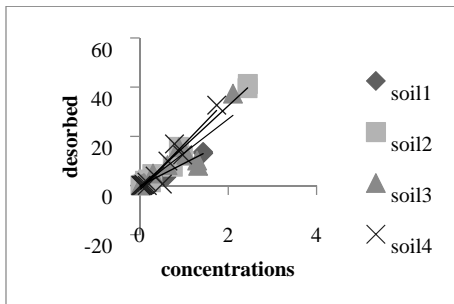


Figure 3. Comparative linear desorption isotherms of Chlorosulfuron on studied soils

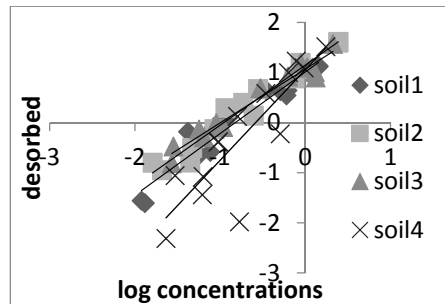


Figure 4. Comparative Freundlich desorption isotherms of Chlorosulfuron on studied soils

ΔG values (-14.9 to -16.0 kJ/mol) of soil in the current investigation falls in lower range, indicating the fact that lower values of Gibbs free energy results in weak interaction between soil and pesticide. Thus they experience Van der-Waals forces among them. Consequently we can say that the phenomenon of physisorption is existent. The value of $\Delta G < 0$ is indicative that the reaction is favourable and spontaneous. It also predicts the duration of Chlorsulfuron endurance in soil as factors like transportation, bioavailability and degradation are influenced by adsorption. A positive correlation has been observed between Freundlich constant (K_f) and the distribution coefficient (K_d). Both were observed to be increasing in a similar pattern. K_d also represents the sorption of Chlorsulfuron in soil. The range of R^2 of K_d is from 0.9-0.98 while that of K_f was seen to be 0.74-0.99. R^2 can be used to select the best fitting model for adsorption and desorption. Soil 2 showed highest value of linear distribution coefficient K_d 23 $\mu\text{g/ml}$ and Freundlich distribution coefficient (K_f) (17.4 $\mu\text{g/ml}$) which is indicative of high rate of adsorption. A positive correlation has been observed between K_d/K_f and OM. So it can be inferred that the highest K_f in soil 2 may be due to the fact that it contains the highest amount of OM (3.5%), this trend has been reported for other pesticides [19, 20]. $K_{f(\text{ads})}$ ranges for adsorption of Chlorsulfuron from 7.06-17.41 $\mu\text{g/ml}$. The rise in K_f is because of higher Soil Organic Matter (SOM), pH, CEC and clay percentage in soils makes soil 2 best adsorbent as reported [21]. The overall trend of increasing K_f and K_d for present investigation was Soil2 > Soil3 > Soil4 > Soil1.

Desorption

Table 3. Desorption coefficients of Chlorsulfuron in selected soils

Soils	$K_{d(\text{des})}$ ($\mu\text{g/ml}$)	R^2	S	$K_{f(\text{des})}$ ($\mu\text{g/ml}$)	R^2	S	n_d	H
1	11.67	0.98	1.76	14.10	0.95	0.174	0.83	0.62
2	7.83	0.91	2.79	11.50	0.72	0.631	0.55	0.44
3	8.24	0.97	0.789	10.28	0.92	0.238	0.81	0.50
4	11.42	0.80	4.492	11.80	0.95	0.161	0.93	0.48

Soils that succeeded in having good adsorption rates i.e. Soil 2 and 3 were found poor for desorbing the attached Chlorsulfuron molecules. Stronger adsorption inhibited these soils from desorbing the molecules readily. While Soil 1 and 4 expressed higher desorption values owing to higher pH and

lower OM, TOC and clay contents. One more factor affecting the adsorption of Chlorsulfuron in soil is its n_a value which is inversely proportional to adsorption process of soil. It depicts the intensity of adsorption. Similarly the n_d value depicts the intensity of desorption. The desorption hysteresis coefficient (H) of all soil samples specify slight differences among adsorption and desorption isotherms (Table 3). It was found to be ranging from 0.44 to 0.62. However the value of H close to 1 indicates that the process of desorption occurred almost as quickly as adsorption. Highest value of H was perceived in soil2 (0.62) indicating quick desorption. This might be due to the fact that the sand content in soil2 is fairly high. The order of soil samples for desorption process was Soil1> Soil4> Soil3> Soil2.

Chlorsulfuron Leaching and mobility pattern

The K_{oc} values of the soil samples in the study Chlorsulfuron showed relatively medium mobility demonstrating moderately less probabilities of leaching. The highest K_{oc} value for Soil 2 (1440.5) is also an indicant for additional adsorption and reduced mobility in the soil. This may be beneficial to predict whether and to what extent a certain soil may be deterrent for the ground water resources underneath it. This parameter can be calculated using the 3-phase and 4-phase equilibrium partitioning models. These models are effective in calculating a precise soil concentration that safeguards the ground water. According to studies the $K_{oc} < 50$ indicates mobility in soils to be the highest. While K_{oc} values from 50 to 150 projected mobility to be slightly high and from 150 to 500 depicted it to be of medium mobility [22].

Statistical Analysis

Table 4. Regression and Correlation analysis for sorption properties of selected soils

Sorption Coefficient	Property (x)	Correlation coefficient (r)	Probability level (p)	Intercept (a)	Slope (b)
K_d	pH	-0.936	0.04	82.503	-9.848
	OM	0.989	0.03	-20.733	12.444
	TOC	0.988	0.03	-20.762	21.48

Investigations were performed to find the correlation between $K_{d(ads)}$ and the physiochemical properties of soil (pH, OM and TOC) (Table 4). The data was analysed for the effect of physiochemical properties on K_d by linear regression analysis. The statistical analysis on $K_{d(ads)}$ revealed that pH is negatively correlated ($r=-0.936$, $p<0.05$) while OM and TOC are positively correlated with $K_{d(ads)}$ ($r=0.989$, $p<0.05$ and $r=0.989$, $p<0.05$ respectively). Thus, lowered pH values increase adsorption. Consequently, pH values are responsible for dissociation or protonation process of pesticide and soil. While increasing OM and TOC values result in enhanced adsorption. The results also specified that the Soil 2, having highest $K_{d(ads)}$ value ($23.0 \mu\text{g/ml}$), contains the highest percentage of soil OM and TOC proving the fact that soil OM and TOC is directly proportional with the rate of adsorption occurring in that particular soil.

Table 5. Regression and Correlation analysis for different soil textures

Sorption Coefficient	Property (x)	Correlation coefficient (r)	Probability level (p)	Intercept (a)	Slope (b)
K_d	Clay	0.897	0.01	10.739	0.354
	Sand	-0.990	0.09	50.331	-0.954
	Silt	-0.820	0.05	21.940	-0.160

Another regression correlation was performed among $K_{d(ads)}$ and different soil textures (Table 5). The results indicated positive correlation among K_d and clay content of soil ($r=0.897$, $p<0.05$). However sand and silt content in soil displayed negative correlation with K_d ($r=-0.990$, $p=0.09$ and $r=-0.820$, $p=0.05$). This is due to the fact clay content is pivotal textural factor for adsorption of Chlorsulfuron in soil. Owing to small particle size and negatively charged surface, clay has immense surface area for ion exchange making it a good cation adsorbent.

Table 6. Univariate ANOVA analysis of Soil samples and K_d values

Source of Variation	SS	df	MS	F	P-value	F crit
Between groups	54.18	1	54.18	1.68	0.32	18.51
Within groups	64.34	2	32.17	-	-	-

The means of soil samples and adsorption distribution coefficient K_d were analysed by one-way ANOVA, using BioStat 2009 Professional 5.7.8 statistics tool, on all four soil samples along with their K_d values. In the univariate ANOVA sum of squares (SS), mean square (MS), F statistics (F), P value and F critical values (F crit) were investigated within the same groups and between groups (Table 6). For this test we assume that all observations are originating from normal distributions and all the four groups of soils have equal variances. In this regard, our P value (0.32) is more than the alpha value (α) (0.05), so the null hypothesis (H_0) is not rejected in this case i.e, the assumption made earlier. It was also observed that the F critical value (F crit) was found to be 18.51. F crit is the value such that any number greater than the F crit value would cause us to reject our null hypothesis (H_0). In this experiment the F statistics value (1.68) falls much lower than the F crit value hence it does not lie in the rejection region.

From the residual plots we determine that the ordinary least square assumptions are being met. Satisfying these assumptions indicates the ordinary least squares regression will produce unbiased coefficient estimates with the minimum variance. Normal probability plots of residuals, residuals versus fits and residuals versus order of data were plotted in Minitab. Normal probability plot of residuals shows that our data is distributed normally.

CONCLUSIONS

Adsorption of Chlorsulfuron was seen to be increasing with augmented pesticides concentration. Soil physiochemical properties play great role in adsorption and desorption i.e. organic matter, pH and clay content. Statistical tool ANOVA, MS Office Excel Correlation and Regression analysis were utilized to further study the role of soils' physicochemical make up on Chlorsulfuron make up. Adsorption distribution coefficient K_d value was low demonstrating less interaction between Chlorsulfuron and soil particles. Soil 2 exhibited the highest value of K_d i.e. 23.0 $\mu\text{g}/\text{ml}$. For desorption $K_{d(\text{des})}$ showed higher values indicating its inverse relation with $K_{d(\text{ads})}$ and thus sample 2 showed lowest value of $K_{d(\text{des})}$ i.e. 7.83 $\mu\text{g}/\text{ml}$. K_{foc} values were large which means that the herbicide showed less mobility in soil with more clay content and these differences in sorption of Chlorsulfuron in different soils can be associated with physicochemical properties of soil mainly organic matter, pH and CEC. Linear and Freundlich correlation and regression analysis showed positively relationship between adsorption coefficients and organic matter, total organic content and clay while pH negatively impacted adsorption.

EXPERIMENTAL SECTION

99.9% pure analytical grade Acetone, Methanol, Anhydrous powder of Sodium Chloride and Calcium Chloride, Concentrated Hydrogen peroxide 35%, Concentrated Hydrochloric acid, Nitric acid, Ammonium acetate and Sodium Hydrogen Carbonate were obtained from Sigma–Aldrich (Steinheim, Germany). Analytical standard Chlorsulfuron was purchased from ACCU Standard USA. While the instruments used were; Weighting machine (AUX220, Shimadzu, U.S.A), Hot air drier (UN55plus, Memmert, Germany), Octagonal sieve shaker (Octagon200, Endecotts, UK), pH meter (pH 7110, WTW Ino Labs, Germany), EC meter (525-A, Crison, Spain), Furnace (JFF-2000, Ncycraft, U.S.A), Orbital and incubator shaker (2102, Irmeco GmbH, Germany), Centrifuge (26-E, Hettich, U.S.A), Hot plate (MSH-20D, Wisestir, Germany) and UV-Visible spectrophotometer (BMS-1602, Biotechnology Medical Services K. Group, U.S.A). Soil sampling was done by collection of 7 soil subsamples of 4kg from four geographically distinct areas of Bahawalpur (Punjab) Sample 1, Gilgit (Gilgit-Baltistan) Sample 2, Swabi (Khyber Pukhtoonkhwa) Sample 3, Sialkot (Punjab) Sample 4, Random sampling was carried out by selecting some specific points of each district followed by evaluation of physicochemical parameters [23].

Adsorption and desorption experiments was performed with 1 mM Chlorsulfuron solution with neutral pH at room temperature. Each experiment was performed with duplicated and the mean value was used. The solution was photometrically checked with UV-Vis Spectrophotometer. Further eight dilutions i.e. 0ppm, 0.25ppm, 0.5ppm, 0.75ppm, 1.0ppm, 2.5ppm, 5.0ppm and 7.5ppm were prepared and 0.1 mM NaCl was added as background electrolyte. Pesticide dilutions were prepared with 10ml pesticide in soils by keeping ratio 1:20 for soil/pesticide solution. The assemblage was shaken for 24hours and then centrifuged prior to UV-Vis Spectrophotometry [16]. Desorption studies were performed on the same pesticide-soil solution. The tubes were reweighed after supernatant decantation. 9 ml of freshly prepared 0.01M CaCl₂ solution was added followed by 24hours shaking and centrifugation prior to photometric analysis [16].

REFERENCES

1. K.S. Ahmad, N. Rashid, M. Zakria, *Journal of the Chemical Society of Pakistan*, **2015**, 37, 380.
2. M. Sarwar, *International Journal of Bioinformatics and Biomedical Engineering*, **2015**, 1, 130.

3. Y. Liu, X. Pan, J. Li, *Agronomy for Sustainable Development*, **2015**, 35, 83.
4. C. A. Damalas, *Journal of Food Safety*, **2016**, 43.
5. C. Wu, S. Zhang, G. Nie, Z. Zhang, J. Wang, *Journal of Environmental Science*, **2011**, 23, 1524.
6. V.H. Springer, A.G. Lista, *Talanta*, **2010**, 83, 126.
7. S. Kaczmerek, K. Matysiak, *Journal of Plant Research*, **2015**, 55, 8.
8. J. Mankowski, K. Pudelko, *Industrial Crops and Products*, **2015**, 70, 185.
9. U. Eugen, F. Lipşa, I.P. Chiriac, I.G. Coroi, *Lucrări Ştiinţifice*, **2010**, 53, 157.
10. C.A. Mallory-Smith, D.C. Thill, M.J. Dial, *Weed Technology*, **1990**, 4, 163.
11. M.A. Martinez-Ghersa, C.M. Ghersa, R.L. Benech-Arnold, R. Mac Donough, R.A. Sanches, *Plant Species Biology*, **2010**, 15, 127.
12. Heap, Proceedings of an international conference, Brighton, UK, **2015**.
13. Szmigielski, B. Geisel, E. Johnson, F. Holm, J. Schoenau, (2011). "Application of a laboratory bioassay for assessment of bioactivity of ALS-inhibiting herbicides in soil". INTECH Open Access Publisher, **2011**, chapter 7.
14. M.S. Başaran, A. T. Serim, *Selçuk Journal of Agriculture and Food Sciences*, **2010**, 24, 54.
15. A. Vicari, P. Catizone, R.L. Zimdahl, *Weed Research*, **1994**, 34, 147.
16. K.S. Ahmad, N. Rashid, S. Tazaiyen, M. Zakria, *Journal of the Chemical Society of Pakistan*, **2014**, 36, 1189.
17. B. Gevao, K.T. Semple, K.C. Jones, *Environmental Pollution*, **2000**, 108, 3.
18. K.S. Ahmad, N. Rashid, M.F. Nazar, S. Tazaiyen, *Journal of the Chemical Society of Pakistan*, **2013**, 34, 1017.
19. Y. Liu, Z. Xu, X. Wu, W. Gui, G. Zhu, *Journal of hazardous materials*, **2010**, 178, 462.
20. M. Kumar, L. Philip, *Chemosphere*, **2006**, 62, 1064.
21. C. Flores, V. Morgante, M. González, R. Navia, M. Seeger, *Chemosphere*, **2009**, 74, 1544.
22. K.A. Sudduth, S.T. Drummond, N.R. Kitchen, *Computers and Electronics in Agriculture*, **2001**, 31, 239.
23. M.Y. Corapciogluand, A.L. Baehr, *Water Resources Research*, **1987**, 23, 191.

IDENTIFICATION OF MASS TRANSFER PARAMETERS FOR ROCK SALT DISSOLUTION IN A PLUG FLOW SYSTEM

SZABOLCS FOGARASI^a, MELINDA NAGY^b, FLORICA IMRE-LUCACI^c,
ARPAD IMRE-LUCACI^{a*}

ABSTRACT. Considering the particularities of rock salt solution mining, the current paper aims to determine the mass transfer parameters for rock salt dissolution in a plug flow system. The influence of crucial operating parameters such as flow rate and channel depth on the mean driving force, volumetric mass transfer coefficient and extraction yield was evaluated. It was found that flow rate increase intensifies the dissolution process leading to a more rapid dissolution of the rock salt deposit. Similar effect was noticed in the case of flow channel depth increase which leads to higher mass transfer area, increasing the amount of dissolved salt from the rock salt deposit.

Keywords: *dissolution, mass transfer, salt mining, plug flow*

INTRODUCTION

Romania has one of the largest salt rock deposits in Europe reaching over 43 billion tones and in some situation containing layers of 2 km thick. The biggest mines are at Gura Slănic (14 mil. t), Ocnele Mari (12 mil. t), Cacica (10 mil. t), Ocna Mureș and Praid (9 mil. t) [1]. There are two main industrial scale techniques applied for rock salt extraction: traditional shaft

^a "Babes-Bolyai" University, Faculty of Chemistry and Chemical Engineering, Department of Chemical Engineering, 11 Arany Janos Str., RO-400028, Cluj-Napoca, Romania.

^b University of Agriculture Science and Veterinary Medicine, Department of Food Science and Technology, 3-5 Calea Mănăștur Str., RO-400375, Cluj-Napoca, Romania.

^c Physico-Chemical Analyses Center, Interdisciplinary Research Institute on Bio-Nano-Sciences, Babeș-Bolyai University, 42 Treboniu Laurian Str., RO-40271, Cluj-Napoca, Romania.

*Corresponding author: aimre@chem.ubbcluj.ro

mining or via solution mining [2]. An important advantage of solution mining is accounted to the direct production of saturated raw brine which can be used for chlorine and soda ash production as well as for food products and for a wide range of industrial applications [3]. For instance, at Ocnele Mari 1.5 million m³ of concentrated brine (308-310 g/L) was produced for a chemical plant, using partially saturated brine (100-110 g/L) which was introduced in ten operational dissolution wells and evacuated through two extracting wells [2]. The feasibility of solution mining is sustained by the fact that the operation at Ocnele Mari cashed 1.3 millions € which fully covered the cost of the drillings and pipe system necessary to transport the brine [2]. Also, salt solution mining is applied on large scale in the USA where just in New York state 241 wells produced more than 7 million m³ of brine in 2014 for evaporating and chemical manufacturing [4].

Although it is applied at industrial scale, solution mining deals with several technical issues like roof collapsing, cavity shape control and cavity coalesce, which need to be solved for an efficient and safe operation [5]. As a result, the development of efficient solution mining technologies requires the study and understanding of fundamental aspects of two phase solid-liquid mass transfer which is a key issue in the dissolution and extraction of salt from mineral deposits [6]. Many techniques are used in the literature for the evaluation of mass transfer parameters such as fix and fluidized bed dissolution [7], rotating disc method and plug flow systems [8-10]. In the majority of the situations the dissolution techniques are applied in isothermal and isobaric conditions, mainly at atmospheric pressure and ambient temperature and well defined hydrodynamical conditions [10].

Considering that fixed and fluidized bed reactors are widely used in the industry [11], offering a potential solution for process intensification, they present the most common approaches for the study of mass transfer in solid-liquid systems using columns with short or long bed of active particles [12, 13]. It could be also applied for the study of rock salt dissolution by using salt particles with well defined geometries or by implying active particles which consist of spherical or cylindrical cores coated with a thin layer of melted rock salt [14, 15].

However, based on the technical particularities of rock salt solution mining encountered at industrial level [1, 2], it would be more suitable and realistic to assess the dissolution process using a plug flow system besides other techniques. As a result, the current paper aims to study the rock salt dissolution process and determine the evolution of several mass transfer parameters in time, using different flow rates and cylindrical flow channels drilled in a block of rock salt deposit.

RESULTS AND DISCUSSIONS

The following main assumptions were considered in the evaluation of the mass transfer parameters for rock salt dissolution in the defined plug flow system:

- It was considered that during the dissolution process channel diameter varied uniformly along the channel depth, maintaining the initial cylindrical geometry.
- The insoluble impurities present in the rock salt deposit have the same influence on the dissolution process regardless the experimental conditions.
- In comparison to the channels, the cavities formed at the bottom of the channels have a neglectable impact on the mass transfer parameters.
- All the drilled channels have the same rugosity involving similar hydrodynamic conditions and the same ratio between the real and geometrical surface areas.

Based on the above assumptions, the volumetric mass transfer coefficients were determined from the experimental results using the following equation:

$$k_v = \frac{\Delta m}{\Delta t \cdot \Delta C_{med}} \quad (1)$$

where: k_v - mean volumetric mass transfer coefficient for period Δt , ($\text{kg}/(\text{kg}\cdot\text{m}^{-3}\cdot\text{s}^{-1})$); Δm - amount of dissolved rock salt over the period of time Δt , (kg); Δt - dissolution time period, (s) and ΔC_{med} - mean driving force, ($\text{kg}\cdot\text{m}^{-3}$).

The results indicate (Fig. 1) that the volumetric mass transfer coefficients are increasing in time regardless the applied flow rate or channel depth. This can be accounted to a more rapid increase of mass transfer surface area than the decrease of mass transfer coefficients due to the geometry variations in time.

It was also found, that the difference between the volumetric mass transfer coefficients obtained at the lowest and highest flow rates decrease from 70 % to 18 % with the increase of channel depth from 3 cm to 5 cm. However, it is obvious that this difference can be accounted to a more significant increase of volumetric mass transfer coefficients at the flow rate of 10 mL/min than at 30 mL/min, which suggests that the dissolution process is more strongly affected by channel depth variations at low flow rates.

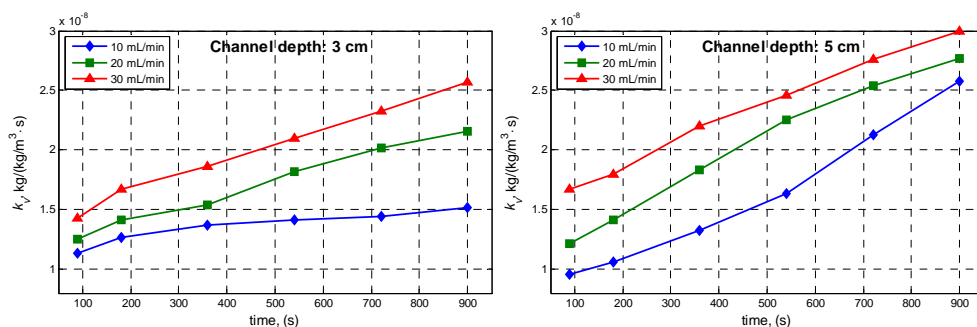


Figure 1. Volumetric mass transfer coefficient vs. time at different channel depths and flow rates.

According to other studies there are two methods for the calculation of the driving force: (i) as the difference between the saturation concentration and the concentration of salt at the exit of the channel or (ii) by the mean driving force defined by eq. (2). The driving force has comparable values for both methods when the salt concentration at the entrance is equal to zero. Still, the driving force for rock salt dissolution was determined by eq. (2), considering that even in this particular situation several studies recommend the use of the mean driving force.

$$\Delta C_{med} = \frac{(C^* - C_i) - (C^* - C_f)}{\ln \frac{C^* - C_i}{C^* - C_f}} \quad (2)$$

where: ΔC_{med} - mean driving force ($\text{kg}\cdot\text{m}^{-3}$); C^* - saturation concentration, ($310 \text{ kg}\cdot\text{m}^{-3}$); C_i - initial concentration, ($\text{kg}\cdot\text{m}^{-3}$) and C_f - final concentration, ($\text{kg}\cdot\text{m}^{-3}$).

Channel geometry variation also leads to the increase of the mass transfer surface area and residence time in the channel which together involve the formation of a more saturated solution in time. As a result, higher concentrations in the effluent involve the decrease of the mean driving force in time for all the experimental conditions.

However, Fig. 2 shows that this tendency is more important at low flow rates which involve higher residence times and higher salt concentrations than at higher flow rates. The results also indicate that the increase of channel depth from 3 cm to 5 cm also diminishes the mean driving force which decreased with 10 % at 10 mL/min and with only 2 % at 30 mL/min, being more stable in time at higher flow rates.

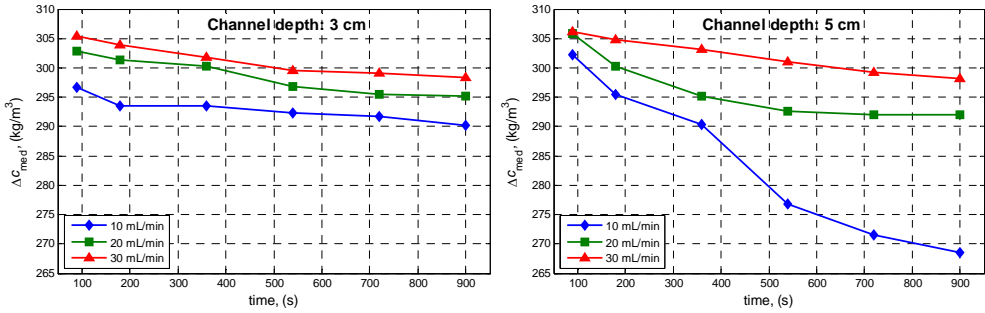


Figure 2. Mean driving force vs. time at different flow rates and initial channel depths.

Another important parameter, the extraction yield (η_i) was also evaluated being defined as the ratio between the amount of dissolved rock salt (Δm_i) and the amount of rock salt that can be theoretically dissolved (m_o) during the experiment if the obtained solutions would have been saturated.

$$\eta_i = 100 \cdot \left(\frac{\Delta m_i}{m_o} \right) \quad (3)$$

The extraction yield is a useful parameter because it indicates the operating conditions which allow the extraction of the highest amount of salt with the lowest amount of solvent. According to Fig. 3 the extraction yield increases with the increase of channel depth and with the decrease of flow rate. It can be observed that the geometry variations during the dissolution process also lead to the increase of the extraction yield with time, due to the formation of more saturated solutions. It was found that the extraction yields obtained at the lowest flow rate are 2-3 times higher than the ones obtained at the highest flow rate. Similarly to the volumetric mass transfer coefficient and mean driving force, the extraction yield is affected more strongly by channel depth increase at low flow rates than at higher ones.

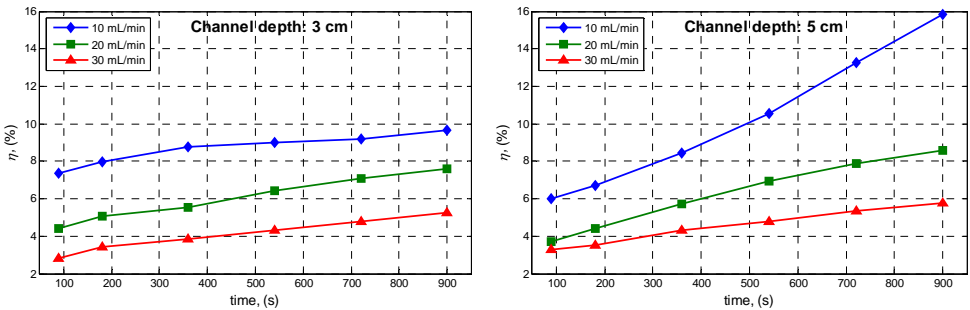


Figure 3. Extraction yield vs. time at different flow rates and initial channel depths.

CONCLUSIONS

The current study revealed that rock salt extraction for brine production can be applied efficiently via solution mining by using a continuous plug flow system. Based on the experimental results it can be concluded that process performance is more strongly affected by channel depth variations at low flow rates than at higher ones. As an overall conclusion, it can be stated that the dissolution of rock salt in the studied continuous plug flow system occurs the most rapidly at 30 mL/min and a channel depth of 5 cm while the most efficiently at 10 mL/min and a channel depth of 5 cm.

EXPERIMENTAL SECTION

The experimental setup used for the assessment of rock salt extraction performance via solution mining (Fig. 4) included a rock salt block, pump for solvent and solution circulation and reservoirs for solvent and obtained solution storage.

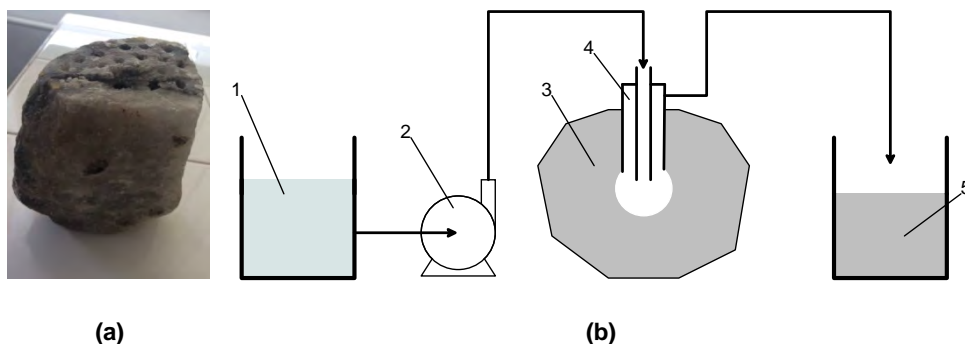


Figure 4. Rock salt block (a); Experimental setup (b).

1 - fresh water tank; 2 - pump; 3 - rock salt block; 4 - extraction head; 5 - brine tank.

The experimental tests were performed at room temperature and atmospheric pressure using channels with constant diameter of 3.3 mm. The dissolution process with duration of 15 min implied two channel depths of 3 and 5 cm and solvent flow rates ranging between 10 and 30 mL/min. In order to determine the mass transfer parameters, the dissolved salt concentration in the obtained brine was quantified for different periods of time at the exit of the channel and in the reservoir as well. Sample concentration, c , was determined based on the below calibration curve using refractive index, n , measurements (Fig. 5).

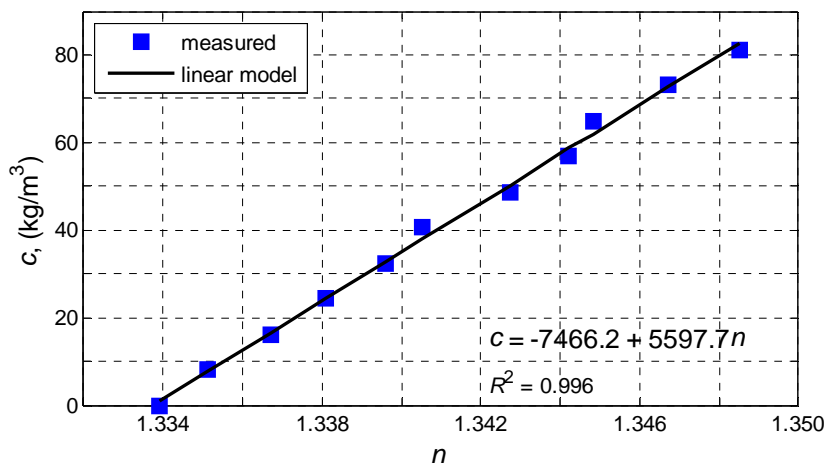


Figure 5. Calibration curve.

REFERENCES

1. G. Udubasa, S.S. Udubasa, *Romanian Journal of Mineralogy*, **2008**, 83, 27.
2. F. Zamfirescu, N. Giurgiu, V. Popescu, S. Copaescu, *Romanian Journal of Mineralogy*, **2008**, 83, 31.
3. S. Mihaș, D.P. Marian, E. Cozma, I. Onica, *International Multidisciplinary Scientific GeoConference Surveying Geology and Mining Ecology Management, SGEM*, **2015**, 3, 543.
4. J.D. Johnson, J.R. Graney, R.C. Capo, B.W. Stewart, *Appl Geochem*, **2015**, 60, 37.
5. T.E. Tomastik, *Carbonate Evaporite*, **1997**, 12, 2, 236.
6. S. Dragan, *Studia UBB Chemia*, **2016**, LXI, 3, Tom I, 227.
7. S. Fogarasi, F. Imre-Lucaci, S. Dragan, A. Imre-Lucaci, *Studia UBB Chemia*, **2016**, LXI, 3, Tom II, 495.
8. M.H. Abdel-Aziz, M. Bassyouni, I.A.S. Mansour, A. Nagi, *J Ind Eng Chem*, **2014**, 20, 5, 2650.
9. L. Zeng, Y. Zhang, Q. Liu, L. Yang, J. Xiao, X. Liu, Y. Yang, *Chem Eng J*, **2016**, 289, 452.
10. S. Petrescu, I. Fechete, C. Ciubotariu, *Chem Eng J*, **1998**, 69, 39.
11. I. Mohammed, T. Bauer, M. Schubert, R. Lange, *Chem Eng Sci*, **2014**, 108, 223.
12. S. Drăgan, *Studia UBB Chemia*, **2015**, 60, 3, 183.

13. S. Drăgan, *Studia UBB Chemia*, **2013**, 58, 4, 53.
14. R.V. Garić-Grulović, Ž.B. Grbavčić, N. Bošković-Vragolović, Z.L. Arsenijević, *Powder Technol*, **2009**, 189, 1, 130.
15. L.A. Calcada, L.A.A. Martins, C.M. Scheid, S.C. Magalhães, A.L. Martins, *J Petrol Sci Eng*, **2015**, 126, 97.

SYNTHESIS OF THREE NEW BIFUNCTIONAL GLUCOSE-THIOUREA ORGANOCATALYSTS AND THEIR APPLICATION IN ASYMMETRIC *MICHAEL* ADDITION

SÁNDOR NAGY^a, PETRA KOZMA^a, PÉTER KISSZÉKELYI^a,
DÓRA BEZZEGH^a, PÉTER HUSZTHY^a, JÓZSEF KUPAI^{a,*}

ABSTRACT. Three new glucose-based asymmetric bifunctional organocatalysts containing a 6-aminopyridyl or a 6-methylpyridyl or a cinchona unit were synthesized. Asymmetric *Michael* addition of pentane-2,4-dione to β -nitrostyrene was catalyzed successfully by these catalysts. In case of the cinchona based glucose-thiourea derivate the *S* enantiomer of the corresponding *Michael* adduct was formed with moderate enantiomeric excess in three different solvents.

Keywords: organocatalyst, carbohydrates, cinchona alkaloids, *Michael* addition, asymmetric syntheses

INTRODUCTION

Chiral catalysts containing both acidic and basic (nucleophilic) structural units are of growing importance in the development of asymmetric synthesis [1, 2].

Thiourea derivatives play important roles in catalyst design and modification. Numerous asymmetric reactions, such as aldol, *Mannich*, *Michael*, *Henry*, amination, *Biginelli*, cyanosilylation and *aza-Morita–Baylis–Hillman* reactions, have been accomplished by these catalysts [3]. Recently, bifunctional thiourea derivatives have been recognized as effective organocatalysts for asymmetric *Michael* addition reactions [4–6]. Therefore, the development of simple and efficient bifunctional thiourea catalysts has great interest. Carbohydrates are easily accessible chiral precursors of asymmetric catalysts [7]. Glucose is very attractive because of its availability and well-defined stereochemistry. Recently, cinchona derived thiourea catalysts have received special attention in the field of organocatalysis [4, 8–10]. The interaction between the catalyst and the reactants can be promoted by the protonated nitrogen of the chiral cinchona skeleton (**Figure 1**) [6].

^a Budapest University of Technology and Economics, Department of Organic Chemistry and Technology, 1111, Budapest, Szent Gellért tér 4., Hungary

*Corresponding author: jkupai@mail.bme.hu

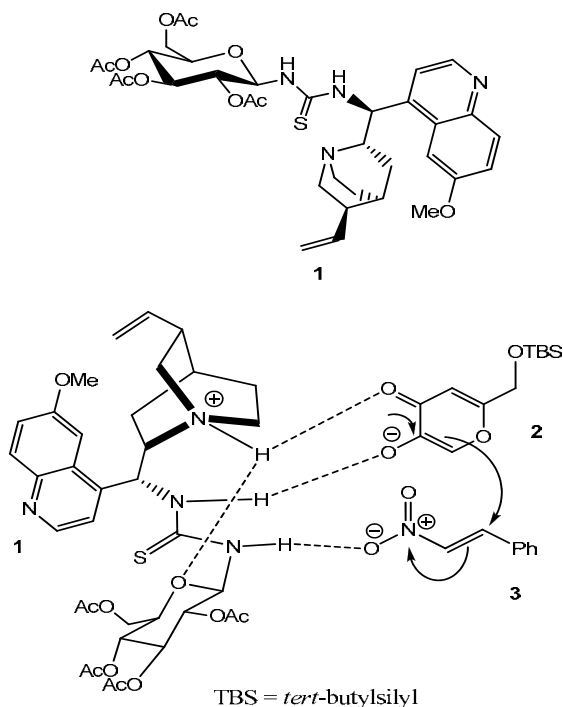


Figure 1. Mechanism of a glucose-based thiourea catalyst (**1**) promoting *Michael* addition of **2** enolate to β -nitrostyrene (**3**) [6].

The *Michael* addition reaction is one of the most elegant approaches for the construction of carbon-carbon bonds under mild condition in an atom economic fashion [12].

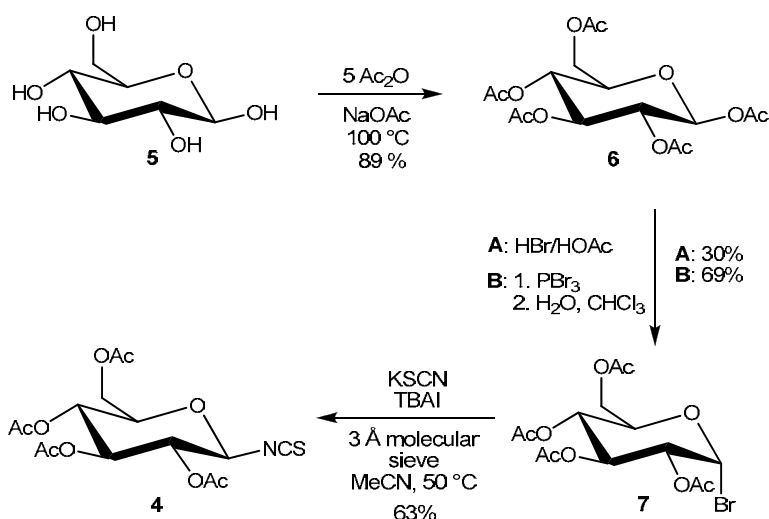
Inspired by thiourea based organocatalysis, our aim was the synthesis of novel glucose-cinchona hybrids for asymmetric *Michael* addition reactions. The addition of pentane-2,4-dione to β -nitrostyrene is important, because the product of this reaction is an intermediate in the synthesis of baclofen, a GABA receptor agonist drug.

RESULTS AND DISCUSSION

Synthesis

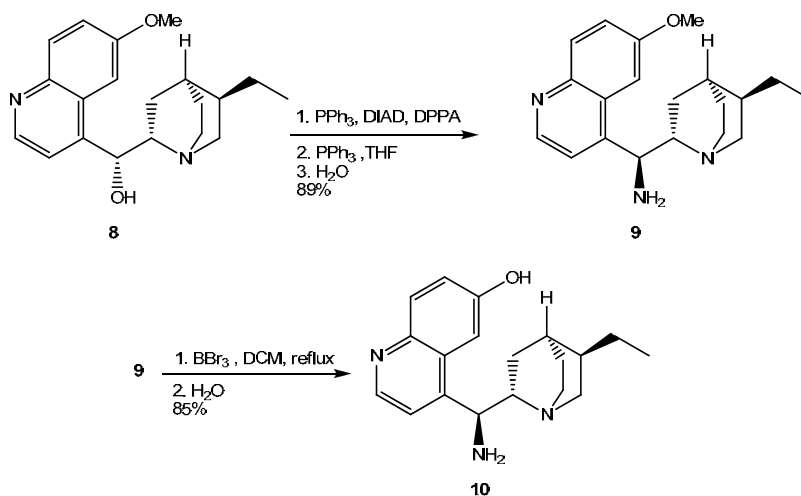
The common precursor of our new organocatalysts is the tetraacetyl glucose isothiocyanate **4** (**Scheme 1**), which was synthesized from commercially available D-glucose (**5**). It was *O*-acetylated with acetic anhydride in the presence of sodium acetate at 100 °C. The reaction gave pentaacetyl glucose (**6**) as a

main product with high yield [13]. The acetobromo glucose (**7**) was prepared in the reaction of glucose pentaacetate **6** with acetic acid solution of hydrogen bromide (Method A) or with phosphorous tribromide in chloroform with catalytic amount of water (Method B). We gained the bromo derivative **7** with higher yield in case of the latter method (69% instead of 30%) [14]. Then the glucose isothiocyanate **4** was prepared using a reported procedure [15]. Bromo sugar derivative **7** was reacted with potassium thiocyanate in the presence of tetrabutylammonium iodide (TBAI) as phase transfer catalyst at 50 °C using molecular sieve (3 Å). This reaction gave the sugar precursor **4** with a medium yield (63%).



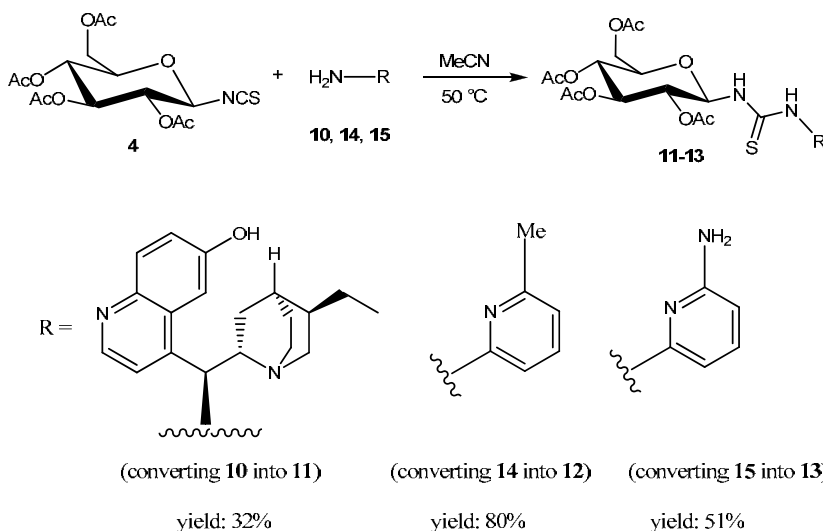
Scheme 1. Synthesis of glucose isothiocyanate derivative **4**.

The cinchona skeleton was built up starting from commercially available hydroquinine (**8**) (**Scheme 2**). First the hydroxyl group at C9 position of the cinchona was converted into amino group in a one-pot reaction using a reported procedure [8]. In a *Mitsunobu* reaction applying diisopropyl azodicarboxylate (DIAD) and diphenylphosphoryl azide (DPPA) the corresponding azide was formed [8], which was reduced to amine **9** by a *Staudinger* reaction using triphenylphosphine in tetrahydrofuran (THF). The demethylation of methoxy derivative **9** was performed using DCM solution of boron tribromide [16] affording cinchona precursor **10** with a high yield (85%).



Scheme 2. Synthesis of the cinchona precursor **10**.

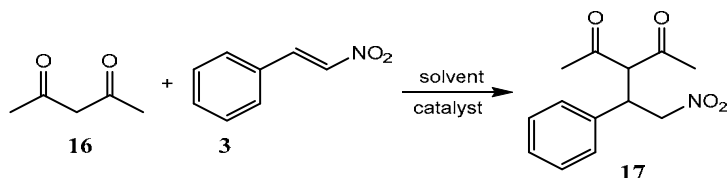
In order to prepare bifunctional organocatalysts we needed to react the glucose isocyanate precursor **4** with amines bearing a basic skeleton (like quinuclidine or pyridine) forming hydrogen bond donor thiourea derivatives. Three new potential enantioselective organocatalysts **11–13** were synthesized in the reaction of the sugar isothiocyanate **4** and three amines containing quinuclidine (**10**), or pyridine (**14** or **15**) moieties in acetonitrile at 50 °C (**Scheme 3**).



Scheme 3. Synthesis of new glucose-based bifunctional organocatalysts **11–13**.

Application of the new organocatalysts in asymmetric *Michael* addition

In recent studies [6, 17] carbohydrate thiourea derivatives showed good enantioselectivities in *Michael* reactions in acetonitrile and dichloromethane. In addition, according to our unpublished results, cinchona thioureas and squaramides obtain excellent chiral induction in *Michael* reactions in methyl *tert*-butyl ether (MTBE). Thus, new glucose-thiourea catalysts **11–13** were used in the *Michael* addition of pentane-2,4-dione (**16**) to β -nitrostyrene (**3**) (**Scheme 4**) in the above mentioned three solvents. In case of cinchona catalyst **11** the highest enantiomeric excess with a moderate yield was achieved in MTBE (**Table 1**). In dichloromethane and acetonitrile only lower yield and enantiomeric excess were obtained. In case of pyridine based catalysts **12** and **13** only racemic products were isolated, so the successful asymmetric induction needs not only the glucose but the cinchona unit as well.



Scheme 4. Asymmetric *Michael* addition catalyzed by the new organocatalysts.

Table 1. Results of the test reactions.

*: Determined from optical rotations by comparing to the literature value [18]

Catal.	11			12			13		
% (n/n)	1	1	1	1	1	1	1	1	1
Solvent	DCM	MTBE	MeCN	DCM	MTBE	MeCN	DCM	MTBE	MeCN
Yield	42	40	28	31	32	26	33	37	30
ee (%), (S)*	58.6	64.1	36.6	racemate			racemate		

Nowadays more and more attention is paid to protect our environment, so catalyst recovery can be a useful tool for reach this goal. Our recent article [19] presents a preliminary study of the potential of the so-called organic solvent nanofiltration (OSN) [20–22] in the purification and recovery of pyridino- and piperidino-crown ether based organocatalysts. According to these results, the sustainable technology of OSN has been proposed for catalyst **11** and solvent recovery based on which we will shortly report a new process for our organocatalysts in asymmetric *Michael* additions.

CONCLUSIONS

Three new enantiopure, glucose-based thiourea organocatalysts (**11–13**) were synthesized and the cinchona based one (**11**) was successfully applied in *Michael* addition of pentane-2,4-dione (**16**) to β -nitrostyrene (**3**) in three different solvents. Using the pyridine based organocatalysts (**12** and **13**) only racemic products were obtained with lower yields. Presumably the high basicity of the quinuclidine unit is needed for the higher yield, and the cinchona skeleton is also necessary for the successful asymmetric induction.

EXPERIMENTAL SECTION

General

Infrared spectra were recorded on a Bruker Alpha-T FT-IR spectrometer. Optical rotations were measured on a Perkin-Elmer 241 polarimeter. NMR spectra were recorded in CDCl₃ either on a Bruker DRX-500 Avance spectrometer (at 500 MHz for ¹H and at 125 MHz for ¹³C spectra) or on a Bruker 300 Avance spectrometer (at 300 MHz for ¹H and at 75 MHz for ¹³C spectra) and it is indicated in each individual case. Mass spectra were recorded on CAMAG TLC-MS Interface (HPLC pump: Shimadzu LC-20AD Prominence SQ MS: Shimadzu LCMS-2020 MS settings: Detector Voltage: 1.10 kV, m/z: 105-1000, Scan speed: 1075 u/sec, DL temperature: 250 °C, Nebulizing Gas Flow: 1.5 L/min, Drying Gas Flow: 15 L/min. eluent: acetonitrile: 0.1 v/v% formic acid 95:5, 1.500 mL/min). Elemental analyses were performed on a Vario EL III instrument (Elementanalyze Corp., Germany) in the Microanalytical Laboratory of the Department of Organic Chemistry, Institute for Chemistry, L. Eötvös University, Budapest, Hungary. Melting points were taken on a Boetius micro-melting point apparatus and they were uncorrected. Starting materials were purchased from Aldrich Chemical Company unless otherwise noted. Silica gel 60 F₂₅₄ (Merck) plates were used for TLC. Silica gel 60 (70-230 mesh, Merck) was used for column chromatography. Ratios of solvents for the eluents are given in volumes (mL/mL). Evaporations were carried out under reduced pressure unless otherwise stated.

(2S,3R,4S,5R,6R)-(+)-2-(Acetoxymethyl)-6-isothiocyanatotetrahydro-2H-pyran-3,4,5-triyl triacetate (4)

Potassium thiocyanate (3.35 g, 30 mmol) and tetrabutyl ammonium iodide (3.2 g, 8.6 mmol) were dissolved in anhydrous acetonitrile. 3 Å molecular sieve (12.74 g) was added and the mixture was stirred for 2.5 h at room temperature. A solution of acetobromo glucose (**7**) (3.54 g, 8.6 mmol) in acetonitrile (3.5 mL) was added to the reaction mixture and it was stirred for 7 h at 50 °C. The reaction was monitored by TLC (SiO₂ TLC; hexane:ethyl acetate = 1:1,

$R_f = 0.40$). The mixture was filtered and the solid material was washed with acetonitrile. The filtrate was evaporated. The residue was dissolved in dichloromethane (300 mL), and it was shaken with water (3×300 mL). The combined organic phase was dried over anhydrous $MgSO_4$ and evaporated. The crude product was purified by column chromatography on silica gel using hexane:ethyl acetate (1:1) mixture as an eluent to give white crystals (2.11 g, 63%).

M.p.: 112–114 °C (lit. mp: 112 °C [15]); $[\alpha]_D^{25} = +5.5$ (c 1.00 $CHCl_3$) (lit.: $[\alpha]_D^{25} = +5.0$ (c 1.00 $CHCl_3$) [15]). The obtained product had the same spectroscopic data than those of reported [15].

(2S,3R,4S,5R,6R)-(+)-6-(Acetoxymethyl)tetrahydro-2H-pyran-2,3,4,5-tetraol tetraacetate (6)

A mixture of anhydrous sodium acetate (16 g, 195 mmol) and anhydrous D-glucose (**5**) (20.0 g, 111 mmol) in acetic anhydride (100 ml, 1.06 mol) was heated at 100 °C for 2 h. The reaction was monitored by TLC (SiO_2 TLC; methanol:toluene = 1:4, $R_f = 0.55$). After the reaction was completed the mixture was poured into cold water and the white precipitate was filtered off and washed with water. The crude product was recrystallized from methanol-water to give white crystals (38.56 g, 89%).

M.p.: 130–133 °C (lit. mp: 131–132 °C, methanol-water [23]); $[\alpha]_D^{25} = +3.7$ (c 1.00 $CHCl_3$) (lit.: $[\alpha]_D^{25} = +4.0$ (c 1.00 $CHCl_3$) [23]). The obtained product had the same spectroscopic data than those of reported [23].

(2S,3R,4S,5R,6R)-(+)-2-(Acetoxymethyl)-6-bromotetrahydro-2H-pyran-3,4,5-triyl triacetate (7)

Method A: A solution of hydrogen bromide in acetic acid (35 mL, 35 w %) was added dropwise to pentaacetyl glucose (**6**) (7.93 g, 20 mmol) at 0 °C. The mixture was stirred at this temperature for 2 h and then at room temperature overnight. The reaction was monitored by TLC (SiO_2 TLC; hexane:ethyl acetate = 1:1, $R_f = 0.79$). After the reaction was completed the mixture was poured into cold water and the precipitated white crystals were filtered off. The latter crude product was dissolved in dichloromethane (100 mL), and washed with water (100 mL). The organic phase was separated, dried over anhydrous $MgSO_4$ and filtered. The filtrate was evaporated. Hexane (20 mL) was added to the residue and the precipitated white crystal was filtered off (2.47 g, 30%).

M.p.: 78–80 °C (lit. mp: 77–79 °C, ethyl acetate-petroleum ether [24]); $[\alpha]_D^{25} = +181$ (c 1.00 $CHCl_3$) (lit.: $[\alpha]_D^{25} = +182.0$ (c 1.00 $CHCl_3$) [24]).

The obtained product had the same spectroscopic data than those of reported [24].

Method B: Phosphorous tribromide (3.9 mL, 40 mmol) in dichloromethane (20 mL) was added dropwise to a solution of pentaacetyl glucose (**6**) in dichloromethane (80 mL). The reaction mixture was stirred for 30 min, then water (1.4 mL) was added and stirred for 2 h. The reaction was monitored by TLC (SiO₂ TLC; hexane:ethyl acetate = 1:1, R_f = 0.62). After the reaction was completed saturated sodium bicarbonate solution (110 mL) was added to the mixture and stirred for 20 min. The mixture was diluted with water (200 mL) and extracted with dichloromethane (3×200 mL). The combined organic phase was dried over anhydrous MgSO₄, filtered and evaporated. Hexane (20 mL) was added to the residue and the precipitated white solid was filtered off (5.67 g, 69%).

M.p.: 78–80 °C (lit. mp: 77–79 °C (ethyl acetate-petroleum ether) [24]); $[\alpha]_D^{25} = +181$ (c 1.00 CHCl₃) (lit.: $[\alpha]_D^{25} = +182.0$ (c 1.00 CHCl₃) [24]). The obtained product had the same spectroscopic data than those of reported [24].

(1S,2S,4S,5R)-(+)-5-Ethylquinuclidin-2-yl(6-methoxyquinoline-4-yl)methanamine (9)

Hydroquinine (**8**, 1.5 g, 4.6 mmol) and triphenylphosphine (1.47 g, 5.6 mmol) were dissolved in dry THF (16 mL) under nitrogen at 0 °C. Diisopropyl azodicarboxylate (DIAD) (1.2 mL, 5.6 mmol) was added and the mixture was stirred at 0 °C for 2 h. A solution of diphenylphosphoryl azide (DPPA) (1.2 mL, 5.6 mmol) in THF (5 mL) was added dropwise to this solution. The mixture was stirred at room temperature for 16 h, and then at 45 °C for 30 min. Triphenylphosphine (1.47 g, 5.6 mmol) was added and the mixture was stirred at room temperature for 2 h, until the gas evolution stopped. In order to form amine, water (1.5 mL) was added and then this mixture was stirred for 2 h. After evaporation of THF the aqueous residue was shaken with the mixture of DCM (20 mL) and 2M HCl (20 mL). The aqueous phase was extracted with DCM (2×20 mL), and the pH was adjusted to 10 with 10 % aqueous NaOH solution. Then it was extracted with DCM (3×15 mL). The combined organic phase was dried over anhydrous MgSO₄, and the solvent was evaporated. The crude product was dissolved in dry diethyl ether (20 mL) and 2 M HCl solution in diethyl ether (10 mL) was added. The precipitated solid was filtered off and washed with diethyl ether (5 mL) (trihydrochloric salt formed, 1.8 g) to give the crude product as pale yellow crystals. M.p.: 200 °C (decomposes) (lit. mp: 214–215 °C (decomposes) (ethyl acetate-methanol) [25]).

The trihydrochloric salt was dissolved in water (20 mL) and the pH was adjusted to 10 with 10 % aqueous NaOH solution to form the free base. This aqueous solution was extracted with DCM (3×20 mL). The combined organic phase was dried over anhydrous MgSO₄ and evaporated to give cinchona amine **9** (1.31 g, 89%) as a pale yellow oil.

$[\alpha]_D^{25} = +63.6$ (c 0.97 CHCl₃) (lit.: $[\alpha]_D^{25} = +71.8$ (c 0.97 CHCl₃) [8]). The obtained product had the same spectroscopic data than those of reported [8].

4-(-)-((1S)-Amino((2S,4S,5R)-5-ethylquinuclidin-2-yl)methyl)quinoline-6-ol (10)

Methoxamine (**9**, 0.96 g, 2.95 mmol) was dissolved in dry DCM (96 mL) under nitrogen. Boron tribromide (12 mL, 1 M DCM solution, 12 mmol) was added dropwise to it and the mixture was stirred for 4 h at 40 °C. The mixture was cooled to room temperature, then filtered, and the solvent was evaporated. The crude product was purified by preparative thin layer chromatography on silica gel using trimethylamine (45 V/V% in water): methanol: acetonitrile: (0.1:1:1) mixture as an eluent to give pale brown crystals (0.78 g, 85%).

M.p.: 135 °C (decomposes) $[\alpha]_D^{25} = -10.2$ ° (c 0.6 MeOH) The obtained product had the same spectroscopic data than those of reported [16].

General procedure for the formation of glucose-based thiourea organocatalysts (11–13)

Amine derivative (**10** or **14** or **15**, regarding the amounts see below for each components) was added (**Scheme 3**) to a solution of isothiocyanate **4** (regarding the amounts see below for each components) in acetonitrile (70 mL) under argon. The mixture was stirred for 7 h at 50 °C. The reaction was monitored by TLC (SiO₂ TLC; methanol:toluene:triethylamine = 1:3:0.1). After the reaction was completed the solvent was evaporated. The residue was dissolved in a mixture of DCM (80 mL) and water (80 mL). The organic phase was separated and dried over anhydrous MgSO₄, filtered and evaporated. The crude product was purified as described below for each compound to result in new thiourea derivatives.

(2R,3R,4S,5R,6R)-(+)-2-(Acetoxymethyl)-6-(3-((S)-((2S,4S,8R)-8-ethylquinuclidin-2-yl)(6-hydroxyquinolin-4-yl)methyl)thioureido)tetrahydro-2H-pyran-3,4,5-triyl triacetate (11)

The glucose-based thiourea organocatalyst **11** was prepared as described above in the General procedure starting from cinchona amine **10** (75.8 mg, 0.24 mmol) and isothiocyanate **4** (94.8 mg, 0.24 mmol). The crude product was purified by preparative thin layer chromatography on silica gel using methanol:toluene:triethylamine (1:3:0.1) mixture as an eluent to give **11** (55 mg, 32%) as white crystals.

R_f: 0.45 (SiO₂ TLC, methanol:toluene:triethylamine = 1:3:0.1); m.p.: 169–173 °C; $[\alpha]_D^{25} = +4.0$ (c 1.00 CHCl₃); IR (KBr) ν_{\max} 3415, 2960, 2918, 2850, 1741, 1621, 1540, 1490, 1472, 1464, 1399, 1362, 1262, 1214, 1196, 1083, 1030, 907, 855, 803, 777, 730, 720, 692, 661, 645, 581, 495 cm⁻¹; ¹H NMR

(500 MHz, CDCl₃) δ (ppm) 0.76–0.81 (m, 3H), 0.81–0.88 (m, 1H), 1.12–1.21 (m, 2H), 1.29–1.34 (m, 5H), 1.98–2.06 (m, 12H), 2.34–2.36 (m, 1H), 2.64–2.68 (m, 1H), 2.97–3.04 (m, 3H), 3.79–3.83 (m, 2H), 4.23–4.27 (m, 1H), 5.00–5.10 (m, 2H), 5.27–5.33 (m, 2H), 5.64–5.75 (m, 1H), 5.77 (br. s, 1H), 7.13–7.26 (m, 2H), 7.39–7.42 (m, 1H), 8.03 (d, 1H), 8.72 (d, 1H), 9.97 (br. s, 1H), 11.39 (d, 1H); ¹³C NMR (125 MHz, CDCl₃) δ (ppm) 12.10, 20.60, 20.70, 20.90, 21.20, 25.30, 26.10, 27.60, 28.20, 37.40, 41.30, 50.60, 57.80, 61.70, 62.00, 68.20, 68.70, 70.40, 73.50, 82.90, 105.10, 123.20, 123.30, 129.40, 131.40, 143.70, 146.50, 146.80, 156.50, 169.40, 169.80, 170.00, 170.90, 182.40. MS: 700.28 (M+1)⁺. Anal. Calcd. for C₃₄H₄₄N₄O₁₀S: C 58.27, H 6.33, N 7.99, S 4.57 %, found: C 58.24, H 6.39, N 7.98, S 4.55 %.

(2R,3R,4S,5R,6R)-(+)-2-(Acetoxymethyl)-6-(3-(6-methylpyridin-2-yl)thioureido)tetrahydro-2H-pyran-3,4,5-triyl triacetate (12)

Glucose-based thiourea organocatalyst **12** was prepared as described above in the General procedure starting from 2-amino-6-methylpyridine (**14**, 71 mg, 0.66 mmol) and isothiocyanate **4** (100 mg, 0.26 mmol). The crude product was purified by preparative thin layer chromatography on silica gel using hexane:ethyl acetate (1:1) mixture as an eluent to give **12** (102 mg, 80%) as a white oil.

R_f: 0.34 (SiO₂ TLC, hexane:ethyl acetate = 1:1); [α]_D²⁵ = +0.2 (c 1.00 CHCl₃); IR (KBr) ν_{\max} 3230, 3195, 3126, 304, 2948, 1757, 1732, 1618, 1557, 1539, 1451, 1367, 1296, 1245, 1222, 1210, 1177, 1161, 1129, 1117, 1073, 1055, 1037, 938, 913, 903, 845, 780, 748, 716, 667, 653, 628, 597, 572, 509, 473, 450 cm⁻¹; ¹H NMR (500 MHz, CDCl₃) δ (ppm) 1.95 (s, 3H), 2.00 (s, 3H), 2.03 (s, 3H), 2.06 (s, 3H), 2.50 (s, 3H), 3.89–3.94 (m, 1H), 4.06–4.08 (m, 1H), 4.11–4.15 (m, 1H), 5.13–5.16 (m, 1H), 5.19–5.23 (m, 1H), 5.35–5.39 (m, 1H), 5.86–5.92 (m, 1H), 6.67 (d, 1H), 6.82 (d, 1H), 7.52 (t, 1H), 9.39 (br. s, 1H), 12.74 (d, 1H); ¹³C NMR (75.5 MHz, CDCl₃) δ (ppm) 20.68, 20.71, 20.87, 21.13, 23.66, 61.94, 68.43, 68.61, 70.30, 73.62, 82.80, 109.11, 118.34, 139.20, 152.38, 156.14, 169.74, 169.74, 170.07, 170.80, 182.74. MS: 495.15 (M+1)⁺. Anal. Calcd. for C₂₁H₂₇N₃O₉S: C 50.70, H 5.47, N 8.45, S 6.44 %, found: C 50.67, H 5.49, N 8.44, S 6.44 %.

(2R,3R,4S,5R,6R)-(-)-2-(Acetoxymethyl)-6-(3-(6-aminopyridin-2-yl)thioureido)tetrahydro-2H-pyran-3,4,5-triyl triacetate (13)

Glucose-based thiourea organocatalyst **13** was prepared as described above in the General procedure starting from 2,6-diaminopyridine (**15**, 131 mg, 0.51 mmol) and isothiocyanate **4** (200 mg, 0.51 mmol). The crude product was purified by preparative thin layer chromatography on silica gel using hexane:ethyl acetate (1:1) mixture as an eluent to give **13** (131 mg, 51) as pale yellow oil.

R_f : 0.66 (SiO₂ TLC, hexane:ethyl acetate = 1:1); $[\alpha]_D^{25} = -18.0$ (c 1.00 CHCl₃); IR (KBr) ν_{\max} 3480, 3379, 3220, 3139, 2965, 1754, 1631, 1609, 1584, 1531, 1455, 1368, 1262, 1229, 1165, 1095, 1042, 921, 799, 725, 703, 661, 600, 475, 406 cm⁻¹; ¹H NMR (500 MHz, CDCl₃) δ (ppm) 1.92 (s, 3H), 1.94 (s, 3H), 1.96 (s, 3H), 1.98 (s, 3H), 3.96–3.99 (m, 1H), 4.02–4.04 (m, 1H), 4.18–4.21 (m, 1H), 4.99–5.03 (m, 1H), 5.38–5.43 (m, 2H), 5.85–5.88 (m, 1H), 6.10 (d, 1H), 6.19 (br. s, 2H), 6.24 (d, 1H), 7.35 (t, 1H), 10.52 (br. s, 1H), 12.49 (d, 1H); ¹³C NMR (75.5 MHz, CDCl₃) δ (ppm) 20.26, 20.33, 20.39, 20.53, 61.82, 68.12, 70.47, 72.16, 72.59, 81.53, 98.77, 101.74, 139.76, 151.83, 156.89, 169.38, 169.45, 169.52, 170.01, 181.48. MS: 498.14 (M+1)⁺. Anal. Calcd. for C₂₀H₂₆N₄O₉S: C 48.19, H 5.26, N 11.24, S 6.43 %, found: C 48.17, H 5.31, N 11.22, S 6.42 %.

General procedure for asymmetric *Michael* reaction

Organocatalysts **11–13** (0.03 mmol) and β -nitrostyrene (**3**, 894.9 mg, 6.0 mmol) were added to a solution of pentane-2,4-dione (**16**, 307 μ L, 300.4 mg, 3.0 mmol) in different solvents (see **Table 1**). The reaction mixture was stirred at room temperature while monitored by TLC (SiO₂ TLC; acetone:chloroform = 1:100, $R_f=0.63$). After the reaction was completed (about a day) the solvent was removed. The crude product was purified by preparative thin layer chromatography on silica gel using acetone:chloroform (1:100) mixture as an eluent to give *Michael* adduct **17** as white crystals (yields, e.e values can be seen in **Table 1**).

M.p.: 123–126 °C (lit. mp: 124–126 °C [19]). The obtained product had the same spectroscopic data than those of reported [19].

ACKNOWLEDGMENTS

The financial support of the Hungarian Scientific Research Fund/National Research, Development and Innovation Office, Hungary (OTKA/NKFIH Nos. K 112289 and PD 108462) is gratefully acknowledged.

REFERENCES

1. M. Christmann, Stefan Bräse, *Asymmetric Synthesis – The Essentials*, **2007**, 2nd Edition, chapter 1.
2. S.B. Tsogoeva, M.J. Hateley, D.A. Yalalov, K. Meindl, C. Weckbecker, K. Huthmacher, *Bioorganic and Medicinal Chemistry*, **2005**, 13, 5680.
3. M.S. Taylor, E.N. Jacobsen, *Angewandte Chemie International Edition*, **2006**, 45, 1520.

4. S.J. Connon, *Chemical Communications*, **2008**, 2499.
5. Y. Takemoto, *Chemical and Pharmaceutical Bulletin*, **2010**, *58*, 593.
6. B.V.S. Reddy, S.M. Reddy, M. Swain, S. Dudem, S.V. Kalivendi, C.S. Reddy, *Royal Society of Chemistry Advances*, **2014**, *4*, 9107.
7. M. Irmak, A. Groschner, M. M. K. Boysen, *Chemical Communications*, **2007**, 177.
8. B. Vakulya, S. Varga, A. Csámpai, T. Soós, *Organic Letters*, **2005**, *7*, 1967.
9. B. Vakulya, S. Varga, T. Soós, *Journal of Organic Chemistry*, **2008**, *73*, 3475.
10. S. Bota, I. Neda, L. Silaghi-Dumitrescu, *Studia UBB Chemia*, **2011**, *56*, 279.
11. C. Curti, G. Rassu, V. Zambrano, L. Pinna, G. Pelosi, A. Sartori, L. Battistini, F. Zanardi, G. Casiragi, *Angewandte Chemie International Edition*, **2012**, *51*, 6200.
12. P. Perlmutter, *Conjugate addition reactions in organic synthesis*, Pergamon: Oxford, UK, **1992**.
13. Zhang S.; Moussodia, R.O.; Sun, H.J.; Leowanawat, P.; Muncan, A.; Nusbaum, C.D.; Chelling, K.M.; Heiney, P.A.; Klein, M.L.; André, S.; Roy, R.; Gabius, H.J.; Percec, V. *Angewandte Chemie International Edition*, **2014**, *53*, 10899.
14. S.C. Timmons, D.L. Jakeman, *Organic Letters*, **2007**, *9*, 1227.
15. M.J. Camarasa, P. Fernández-Resa, M.T. García-López, F.G. De Las Heras, P.P. Méndez- Castrillón, A. San Felix, *Synthesis*, **1984**, 509.
16. C. Cassani, R. Martin-Rapun, E. Arceo, F. Bravo, P. Melchiorre, *Nature Protocols*, **2013**, *8*, 325.
17. B.V.S. Reddy, S.M. Reddy, M. Swain, *Royal Society of Chemistry Advances*, **2013**, *3*, 930.
18. D.A. Evans, S. Mito, D. Seidel, *Journal of the American Chemical Society*, **2007**, *129*, 11583.
19. J. Kupai, P. Kisszékelyi, E. Rojik, G. Dargó, L. Hegedűs, D. Bezzegh, P. Maszler, L. Szabó, T. Németh, Gy. T. Balogh, P. Huszthy, *Arkivoc*, **2016**, 130–151.
20. J.F. Kim, G. Szekely, M. Schaeperstoens, I.B. Valtcheva, M.F. Jimenez-Solomon, A. G. Livingston, *ACS Sustainable Chemistry & Engineering*, **2014**, *2*, 2371.
21. G. Szekely, M.F. Jimenez-Solomon, P. Marchetti, J.F. Kim, A.G. Livingston, *Green Chemistry*, **2014**, *16*, 4440.
22. M. Schaeperstoens, C. Didaskalou, J.F. Kim, A.G. Livingston, G. Szekely, *Journal of Membrane Science*, **2016**, *514*, 646.
23. D. Wahler, O. Boujard, F. Lefevre, J.-L. Reymond, *Tetrahedron*, **2004**, *60*, 703.
24. L.A. Yu-Ya, J.M. Chalker, B.G. Davis, *Journal of the American Chemical Society*, **2010**, *132*, 16805.
25. S.H. McCooey, S.J. Connon, *Organic Letters*, **2007**, *4*, 599.

UNMODIFIED AND GOLD-MODIFIED SEMICONDUCTOR CATALYSTS FOR SOLAR LIGHT ASSISTED PHOTODEGRADATION OF CRYSTAL VIOLET

ZSIGMOND PAPP^{a*}

ABSTRACT. Different unmodified and modified semiconductor photocatalysts were used for the complete decolorization of an unbuffered crystal violet solution. The decolorization efficiency of commercially available ZnO and TiO₂ (anatase nanopowder) was compared with those of newly prepared gold-modified ZnOs (Au/ZnOs). Two Au/ZnOs were prepared from pure ZnO powder through deposition of gold by direct current (DC) sputtering. The morphological characterization of the Au/ZnOs was done with the aid of scanning electron microscopy. ZnO-based catalysts show significantly higher decolorization power in comparison with TiO₂. Au/ZnOs show slightly higher activity than unmodified ZnO.

Keywords: semiconductor oxides, modification with gold, sputter coating, photodegradation, crystal violet

INTRODUCTION

Effluents of various industries usually contain high quantities of synthetic organic dyes. The discharge of these colored compounds in the environment causes considerable non-aesthetic pollution and serious health-risk factors. Since dyes usually show high stability under sunlight and resistance to microbial attack and temperature, the large majority of these compounds are not degradable in conventional wastewater treatment plants. The research of powerful and practical treatments to decolorize and degrade dyeing wastewaters to decrease their environmental impact has then attracted increasing interest over the past two decades. Physico-chemical, chemical and electrochemical methods, advanced oxidation processes (AOPs), microbiological treatments, and enzymatic decomposition are the most important among these technologies [1].

^a Faculty of Biofarming, John Naisbitt University, Maršala Tita 39, 24300 Bačka Topola, Serbia, e-mail: pappzsigmond@yahoo.com, zpap@naisbitt.edu.rs

AOPs, which involve the in-situ generation of highly potent chemical oxidants such as the hydroxyl radical, have emerged as an important avenue of technologies to accelerate the non-selective oxidation and thus the destruction of a wide range of non-degradable organic contaminants in wastewater which cannot be eliminated biologically [2, 3].

Recently, the application of metal oxide semiconductors in the AOPs has gained wide interest for the treatment of dye wastewater owing to its good degradation efficiency, low toxicity and physical and chemical properties [2]. On the other hand, photocatalytic efficiency of semiconductor particles is often limited by the quick recombination of the photogenerated charge carriers [4, 5]. One of the mostly used ways to overcome these limitations is deposition of noble metals on the semiconductor surface, which prevents the recombination of the electron-hole pairs and consequently increases its photocatalytic activity [6-8]. Noble metal-modified ZnOs are nowadays broadly applied in photocatalytic degradation of different dyes [9-30]. These catalysts are practically always synthesized in solution using a large variety of different synthetic procedures. Only few examples are presented about the use of sputtering technique for obtaining such catalysts for the degradation of organic dyes [18, 20]. To best of my knowledge there are no publications dealing with gold-modified ZnOs obtained by sputtering technique for the photocatalytic degradation of crystal violet dye (Fig. 1).

In this work two gold-modified ZnO photocatalysts (Au/ZnOs) were prepared by direct current (DC) sputtering and their decolorization efficiency was compared with those of commercially available ZnO and TiO₂ (anatase nanopowder). Scanning electron microscopy/energy dispersive spectrometry (SEM / EDS) was applied for morphological, structural and elemental characterization of the modified catalysts.

RESULTS AND DISCUSSION

The decolorization efficiency of unmodified ZnO and TiO₂ was compared to those of Au/ZnOs under direct and diffuse natural solar irradiation (in further text Au/ZnO/1 and Au/ZnO/2 denote Au/ZnO samples with lower and higher gold content, respectively; see Experimental section for details). The photolytic degradation was also monitored under the same conditions. Generally, the efficiency of ZnO-based catalysts was undoubtedly higher in comparison with TiO₂ under both irradiation types (Fig. 2A, B; bars 2-5). Although ZnO showed quite high activity, both newly synthesized gold-modified catalysts surpassed its efficiency (Fig. 2A, B; bars 2-4).

The relative difference between ZnO-based catalysts was more pronounced under direct irradiation (Fig. 2A; bars 2-4). While the relative difference between Au/ZnO/2 and ZnO was around 14% under direct irradiation (Fig. 2A; bars 2, 4), this difference was just around 5% in case of diffuse sunlight (Fig. 2B; bars 2, 4). Similar conclusion is valid for the comparison of TiO₂ and ZnO-based catalytic systems (both unmodified and modified). While the decolorization time is 9.5–11.1 times higher under direct irradiation (Fig. 2A; bars 2-5), it is just 6.1–6.4 times higher in case of diffuse sunlight (Fig. 2B; bars 2-5).

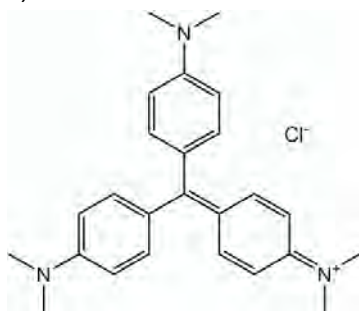


Figure 1. Structural formula of crystal violet.

The photolytic degradation was incomparably slower to catalytic ones in both cases (Fig. 2A, B; bars 1-5). The decolorization time under diffuse irradiation is significantly higher than under direct sunlight for all investigated systems (56.3x for photolysis, 23.1x for TiO₂, 36.1x for ZnO, 38.2x for Au/ZnO/1, 40.0x for Au/ZnO/2).

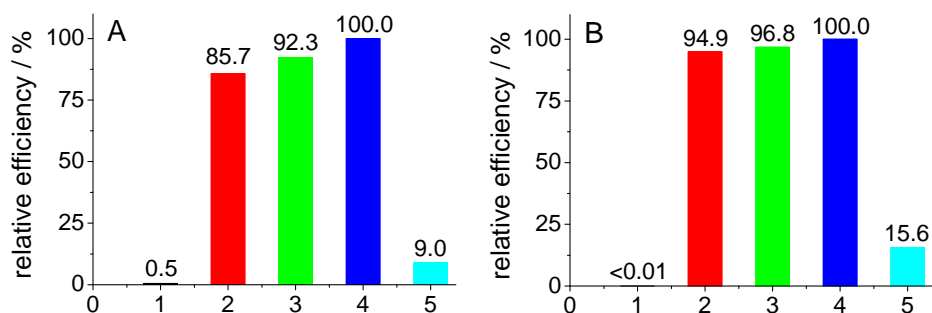


Figure 2. Comparison of the efficiency of different procedures of crystal violet photodegradation under direct (A) and diffuse solar irradiation (B): photolysis (1), ZnO (2), Au/ZnO/1 (3), Au/ZnO/2 (4), TiO₂ (5); C_{catalyst} (2-5) = 2.00 g dm⁻³.

The optimal catalyst concentration for the most efficient catalytic system (Au/ZnO/2) was determined in a separate experiment (Fig. 3). It was found that the decolorization time was the shortest at 2.00 g dm^{-3} concentration. Both lower and higher catalyst amounts resulted in slower decolorization. The reason of lowered efficiency above the optimum concentration could be explained by particle aggregation, decreased light penetration and increased light scattering.

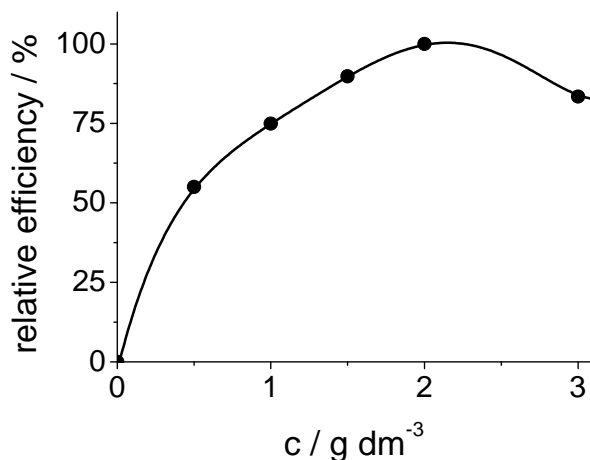


Figure 3. Effect of Au/ZnO/2 concentration on decolorization efficiency.

Under the optimal Au/ZnO/2 concentration (2.00 g dm^{-3}), full decolorization of crystal violet was achieved in less than 7 minutes under direct solar irradiation (Fig. 4). The decolorization kinetics was monitored spectrophotometrically. The signal decreased linearly with time at all investigated absorption maxima both in UV (302 and 249 nm) and visible range (590 nm), indicating zero-order kinetics. The reaction rate constant was 3.06×10^{-8} (590 nm), 2.97×10^{-8} (302 nm), and $3.08 \times 10^{-8} \text{ mol dm}^{-3} \text{ s}^{-1}$ (249 nm), showing very similar behavior at all maxima. It was also clear that adsorption of crystal violet occurred before the photodegradation process ($\sim 20\%$ in 15 minutes without irradiation; Fig. 4A, upper two spectra).

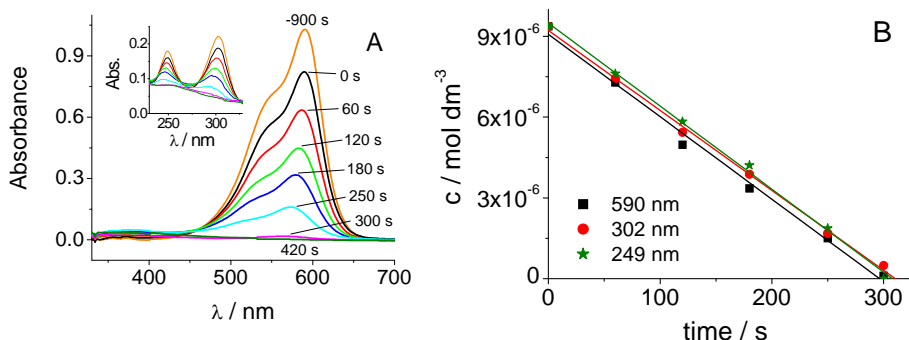


Figure 4. Spectrophotometric monitoring of crystal violet decolorization over Au/ZnO/2 (A) together with corresponding kinetic curves (B). Upper two spectra (A) correspond to the adsorption process in dark before the kinetic experiment.

Au/ZnO/2 catalyst was also subjected to a physicochemical investigation. Typical micrographs taken under different magnifications (Fig. 5A, B) show its morphological characteristics. Agglomerates consisted from smaller particles with the size mostly in 80–500 nm range are clearly visible. Separate gold particles with size comparable to the size of ZnO particles were not identified in the sample.

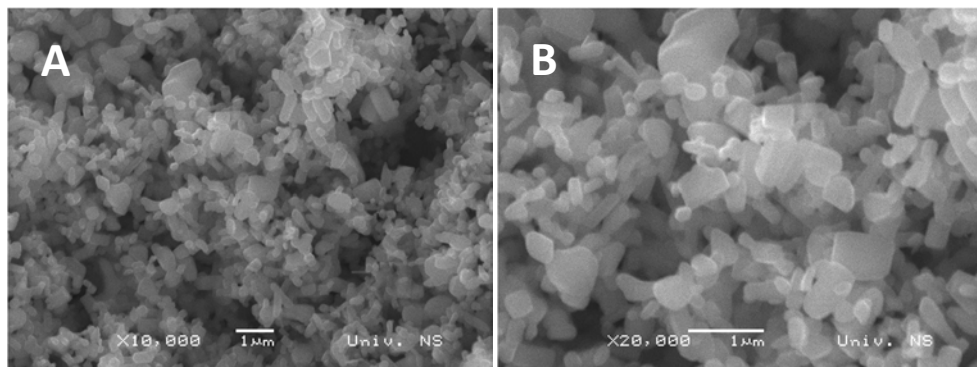


Figure 5. SEM micrographs of the Au/ZnO/2 sample under different magnifications ($\times 10,000$ (A), $\times 20,000$ (B)).

The EDS analysis of the catalyst showed the expected ratio of zinc and oxygen for pure ZnO, while the concentration of Au was under 0.35% (w/w). The presence of other elements was negligible.

CONCLUSIONS

New gold-modified zinc oxides (Au/ZnOs) have been prepared from pure ZnO by DC sputtering technique and successfully applied in solar photodegradation of crystal violet dye. These modified catalysts were compared with unmodified ZnO and TiO₂. ZnO-based catalysts were significantly more efficient in comparison with TiO₂ (anatase nanopowder). The presence of gold slightly enhanced the efficiency of pure ZnO. The differences in the catalytic activities of the investigated catalysts were more pronounced in the case of direct solar irradiation. As expected, the degradation was undoubtedly faster under direct than diffuse sunlight. The most efficient from the investigated catalysts (Au/ZnO/2) was morphologically characterized using SEM. The optimal concentration of Au/ZnO/2 was also determined (2.00 g dm⁻³). Degradation of crystal violet over this catalyst showed zero-order kinetics.

It must be stated that from the economic point of view (economicity vs. effectiveness), higher catalytic efficiency achieved with gold modification is not sufficiently justified, especially because of excellent activity of unmodified ZnO. In any case, this contribution broadens the field of preparation and application of noble metal-modified semiconductor catalysts for solar photodegradation of organic pollutants.

EXPERIMENTAL SECTION

Chemicals and solutions

Solution of crystal violet (Merck) was prepared by dissolving the dye in double distilled water ($c_0 = 1.18 \times 10^{-5}$ mol dm⁻³; $Abs_0 (590 \text{ nm}) = 1.02$). TiO₂ nanopowder (Sigma-Aldrich, anatase, <25 nm, 99.7% trace metals basis) and ZnO powder (Kemika, p.a., min. 99%) were used as received.

Preparation of Au/ZnOs

Both gold-modified ZnO catalysts were prepared from pure ZnO powder by DC sputtering using a BAL-TEC SCD-005 (Bal-Tec) sputter coater. 500 mg ZnO was measured in 5 cm diameter Petri-dish, dispersed in thin layer and sputtered with gold for 4×15 s (Au/ZnO/1) or 4×90 s (Au/ZnO/2). The watch-glass covered dishes were intensively shaken between consecutive sputtering steps. The sputtering parameters were as follows: working time, 4×15 s or 4×90 s; used current, 30 mA; working distance, 50 mm).

Surface characterization

Surface characterization of Au/ZnO/2 was done with the aid of JSM-6460LV electron microscope (Jeol, Japan) and INCAx-sight EDS detector (Oxford Instruments, United Kingdom).

Photodegradation

Identical borosilicate glass beakers (IsoLab, 013.01.101) containing 10.00 cm³ of crystal violet solution with or without catalyst were subjected to natural solar irradiation (direct and diffuse) in consecutive sunny summer days. All catalyst-containing solutions were mixed during the experiments to minimize sedimentation. All experiments were done in duplicate. When the time of degradation was higher than the daily available insolation time (direct or diffuse), the samples were put into the dark before the next insolation session (next day).

Visual decolorization monitoring

During the preliminary comparative experiments (optimization) the decolorization of the samples was monitored visually. The time for the total decolorization (t) was determined and mutually compared using a relative scale taking 100% for the most efficient system: *relative efficiency (%)* = $100 \times t_{\text{most eff.}} / t$. Kinetic investigation of the Au/ZnO/2 system was done by spectrophotometry according to procedure described below.

Spectrophotometry

Spectrophotometric investigation of the Au/ZnO/2 system was performed on a PG Instruments T80+ UV–visible double-beam spectrophotometer (PG Instruments, United Kingdom) using quartz cuvettes with 1.00 cm path length. The samples for the analysis were filtered through appropriate membrane filters. The degradation of crystal violet was monitored at its three absorption maxima both in UV and visible range (249, 302 and 590 nm). The initial absorbance was determined after the adsorption step (15 min in the dark).

ACKNOWLEDGMENTS

The financial support of the Ministry of Education, Science and Technological Development of the Republic of Serbia (Project No. ON172059) is gratefully acknowledged. Author would also like to thank Mr. Miloš Bokorov for his help in this research.

REFERENCES

1. C.A. Martínez-Huitle, E. Brillas, *Applied Catalysis B: Environmental*, **2009**, *87*, 105.
2. S.H.S. Chan, T.Y. Wu, J.C. Juan, C.Y. Teh, *Journal of Chemical Technology and Biotechnology*, **2011**, *86*, 1130.
3. S. Palit, *Nature Environment and Pollution Technology*, **2012**, *11*, 697.

4. P.V. Kamat, *Chemical Reviews*, **1993**, 93, 267.
5. G. Rothenberger, J. Moser, M. Grätzel, N. Serpone, D.K. Sharma, *Journal of the American Chemical Society*, **1985**, 107, 8054.
6. P.V. Kamat, *Journal of Physical Chemistry B*, **2002**, 106, 7729.
7. P.V. Kamat, *Pure and Applied Chemistry*, **2002**, 74, 1693.
8. K. Rajeshwar, N.R. de Tacconi, C.R. Chenthamarakshan, *Chemistry of Materials*, **2001**, 13, 2765.
9. A.A. Ashkarran, *Applied Physics A*, **2012**, 107, 401.
10. P.-K. Chen, G.-J. Lee, S. Anandan, J.J. Wu, *Materials Science and Engineering: B*, **2012**, 177, 190.
11. C. Chen, Y. Lu, H. He, K. Wu, Z. Ye, *Applied Physics A*, **2013**, 110, 47.
12. J.W. Chiou, S.C. Ray, H.M. Tsai, C.W. Pao, F.Z. Chien, W.F. Pong, C.H. Tseng, J.J. Wu, M.-H. Tsai, C.-H. Chen, H.J. Lin, J.F. Lee, J.-H. Guo, *Journal of Physical Chemistry C*, **2011**, 115, 2650.
13. R. Georgekutty, M.K. Seery, S.C. Pillai, *Journal of Physical Chemistry C*, **2008**, 112, 13563.
14. C.A.K. Gouvêa, F. Wypych, S.G. Morales, N. Durán, P. Peralta-Zamora, *Chemosphere*, **2000**, 40, 427.
15. J. Kim, K. Yong, *Journal of Nanoparticle Research*, **2012**, 14, art. No. 1033.
16. Y. Lai, M. Meng, Y. Yu, *Applied Catalysis B: Environmental*, **2010**, 100, 491.
17. P. Li, Z. Wei, T. Wu, Q. Peng, Y. Li, *Journal of the American Chemical Society*, **2011**, 133, 5660.
18. G. Sinha, L.E. Depero, I. Alessandri, *ACS Applied Materials & Interfaces*, **2011**, 3, 2557.
19. L. Sun, D. Shao, Z. Song, C. Shan, Z. Zhang, B. Li, D. Shen, *Journal of Colloid and Interface Science*, **2011**, 363, 175.
20. T. Tan, Y. Li, Y. Liu, B. Wang, X. Song, E. Li, H. Wang, H. Yan, *Materials Chemistry and Physics*, **2008**, 111, 305.
21. K. Thongsuriwong, P. Amornpitoksuk, S. Suwanboon, *Journal of Sol-Gel Science and Technology*, **2012**, 62, 304.
22. J. Wang, X.M. Fan, Z.W. Zhou, K. Tian, *Materials Science and Engineering: B*, **2011**, 176, 978.
23. J. Wang, Q. Hu, Z. Li, J. Guo, Y. Li, *Materials Letters*, **2012**, 79, 277.
24. T.-J. Whang, M.-T. Hsieh, H.-H. Chen, *Applied Surface Science*, **2012**, 258, 2796.
25. J.-J. Wu, C.-H. Tseng, *Applied Catalysis B: Environmental*, **2006**, 66, 51.
26. F. Xiao, F. Wang, X. Fu, Y. Zheng, *Journal of Materials Chemistry*, **2012**, 22, 2868.
27. J. Xie, Q. Wu, *Materials Letters*, **2010**, 64, 389.
28. D. Zhang, F. Zeng, *Research on Chemical Intermediates*, **2010**, 36, 1055.
29. Y. Chen, D. Zeng, K. Zhang, A. Lu, L. Wang, D.-L. Peng, *Nanoscale*, **2014**, 6, 874.
30. Q. Huang, S. Liu, W. Wei, Q. Yan, C. Wu, *RCS Advances*, **2015**, 5, 27075.

PREPARATION, CHARACTERIZATION, AND EVALUATION OF THE PHOTOCATALYTIC EFFECT OF α -Fe₂O₃/SAPO-34 IN THE ELIMINATION PROCESS OF THE ANTI-CANCER DRUG DOXORUBICIN FROM AQUEOUS SOLUTION

MOHAMMAD HOSEIN BIGTAN^a AND KAZEM MAHANPOOR^{a*}

ABSTRACT. In this investigation, α -Fe₂O₃/SAPO-34 nano-structure were synthesized and characterized by XRD, SEM and FT-IR techniques. Morphologically, the shape of α -Fe₂O₃/SAPO-34 nanoparticles is close to spherical nanoparticles with an average particle size of 93 nm determined by Debye-Scherrer equation. The photocatalytic activity of α -Fe₂O₃/SAPO-34 nano-structure was investigated through the degradation of doxorubicin, an anti-cancer drug using a batch reactor under UV-C irradiation and H₂O₂ as oxidant. The effect of various factors including drug concentration, catalyst dosage, pH and H₂O₂ concentration on the degradation yield were investigated. The results showed that optimum conditions were: Initial concentration of DOX = 20 ppm, pH = 8, amount of α -Fe₂O₃/SAPO-34 = 150 mg/L, and H₂O₂ concentration 4 mol/L.

Keywords: Doxorubicin, Photocatalytic degradation, α -Fe₂O₃/SAPO-34, Nanocatalyst

INTRODUCTION

Adriamycin is a trade name for Doxorubicin (DOX) which is an anthracycline antitumor antibiotic. DOX has been synthesized via biotechnological methods [1]. DOX is applied in the treatment of various cancers such as bladder, stomach, breast, ovaries, lung, thyroid, multiple myeloma, soft tissue sarcoma, leukemia, Hodgkin's lymphoma and other kinds of cancers [2]. In the pharmaceutical industry, this drug can be excreted into the environment through production excretion, formulation sites, as well as un-metabolised substances or their metabolites in urine or stool of the direct consumers of the

^a Department of Chemistry, Arak Branch, Islamic Azad University, Arak, Iran;
Tel. +98-86-33422226; Fax. +98-86-33470017.

* Corresponding author: k.mahanpoor@gmail.com, k-mahanpoor@iau-arak.ac.ir

drug [3]. So due to the high toxicity of this drug, it should be completely degraded before entering the environment. To remove the anti-cancer drugs, several methods have been reported such as using a membrane, activated carbon adsorption, electrolysis, sonolysis and ozonation [4–7]. Since conventional treatments are often inadequate and inefficient to remove DOX and other pharmaceuticals from wastewater [8], further investigations on alternative treatment options are intensively pursued. Advanced oxidation processes (AOPs) as an appropriate alternative can act about biological wastewater treatments, as a pre-treatment, enhancing the biodegradability by partial oxidation or can be used as a post-treatment to degrade persistent compounds [9]. Among the AOP's, heterogeneous photocatalytic oxidation has shown high efficiency in the treatment of industrial wastewaters, ground waters and contaminated air [10].

In this study, α - Fe_2O_3 nanostructure was supported on porous SAPO-34 to increase its photocatalytic activity. Photocatalytic properties of α - Fe_2O_3 /SAPO-34 on removing the anti-cancer drug, DOX were evaluated, and operational parameters were considered and optimized.

RESULTS AND DISCUSSION

As it could be seen in Figure 1, the XRD patterns of SAPO-34 (catalyst support) and α - Fe_2O_3 /SAPO-34 were showed the interaction between α - Fe_2O_3 and SAPO-34. As observed in the XRD pattern of α - Fe_2O_3 /SAPO-34, the SAPO-34 frame structure has not being destroyed after α - Fe_2O_3 loading. An average particle size of 93 nm for α - Fe_2O_3 /SAPO-34 particles was obtained by employing the Debye-Scherrer equation.

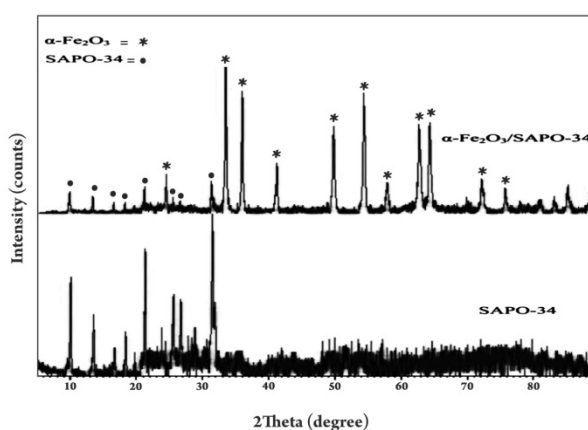


Figure 1. XRD powder patterns of α - Fe_2O_3 /SAPO-34 and SAPO-34 as a catalyst support

As it is evident in Figure 2, the size of iron oxide nanoparticles supporting on SAPO-34 is not quite the same, and their distribution is not uniform. Non-Uniformity of the catalyst surface confirms that the photocatalytic activity of these nanoparticles is increased. Morphologically, the shape of $\alpha\text{-Fe}_2\text{O}_3/\text{SAPO-34}$ nanoparticles is close to spherical nanoparticles.

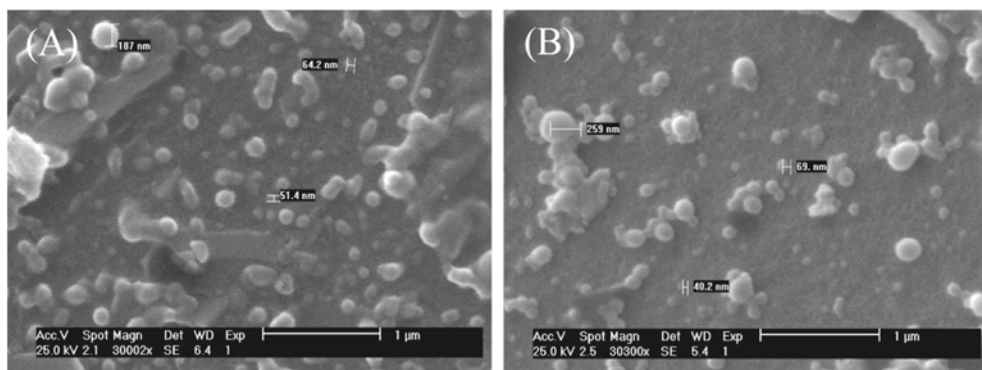


Figure 2. SEM images of $\alpha\text{-Fe}_2\text{O}_3/\text{SAPO-34}$ nanoparticles (A) and SAPO-34 (B)

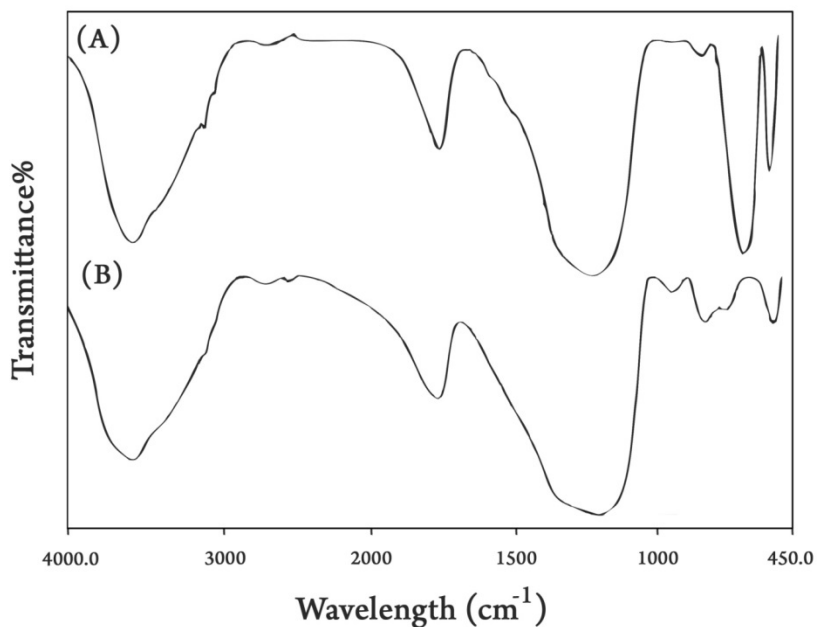


Figure 3. FTIR spectra of $\alpha\text{-Fe}_2\text{O}_3/\text{SAPO-34}$ (A), catalyst support of SAPO-34(B)

Figure 3 illustrates the FTIR spectra of the synthesized catalysts. In the primary spectra of SAPO-34 catalyst support (Figure 3A), the bending around 520 cm^{-1} is the signature of SiO_4 that attributes to Si which incorporated to the tetragonal structure of SAPO-34. The peaks at wave numbers about 780 , 1100 and 1650 cm^{-1} belong to the asymmetric stretch of O–P–O, symmetric stretch of O–P–O and physically adsorbed water, respectively. The peak at 3440 cm^{-1} ascribed to the structural OH [11]. This peak includes P–OH, Si–OH, Al–OH and Si–OH–Al bonds which are active sites in the cages of SAPO-34. In the FTIR spectra of the nano photocatalyst $\alpha\text{-Fe}_2\text{O}_3/\text{SAPO-34}$ (Figure 3B), the peaks at about 3430 and 1640 cm^{-1} are assigned to stretching and bending modes of OH. The peak at about 720 cm^{-1} ascribed to the Fe–O bond [12]. Other Spectral changes between 450 and 700 cm^{-1} imply the formation of new bonds between $\alpha\text{-Fe}_2\text{O}_3$ and SAPO-34.

Photocatalytic degradation investigation of DOX

Hematite is an *n*-type semiconductor with the band gap of 2.2 eV , the conduction band edge at $+0.28\text{ V}$ and the valance band edge at $+2.4\text{ eV}$ [13]. This photocatalytic process is based on the adsorption and desorption of molecules on the catalyst surface. The UV light irradiation to the porous $\alpha\text{-Fe}_2\text{O}_3/\text{SAPO-34}$ causes the valence band (VB) electrons to eject into the conduction band (CB), so holes are generated in the valence band. The photogenerated holes undergo a reaction with adsorbed water on the surface of the catalyst to produce the highly reactive hydroxyl radical ($\cdot\text{OH}$). On the other hand, a superoxide anion radical ($\text{O}_2^{\cdot-}$) is produced since O_2 is an electron acceptor. Moreover, $\text{O}_2^{\cdot-}$ acts as an oxidizing agent or an additional source of $\cdot\text{OH}$. The high oxidative potential of these reactive radicals degrades DOX drug into non-toxic organic compounds. So stabilization of $\alpha\text{-Fe}_2\text{O}_3$ on SAPO-34 catalyst support leads to increase the photocatalytic activity. The increase of photocatalytic activity is due to the suitable position of SAPO-34 for adsorption of DOX in the vicinity of $\alpha\text{-Fe}_2\text{O}_3$ which is the producer of reactive hydroxyl radical ($\cdot\text{OH}$).

The effect of initial DOX concentration on photodegradation efficiency is shown in Figure 4. It was observed that the photodegradation conversion of DOX decreases when the initial concentration of DOX is increased. The probable reason is that when the initial concentration of DOX is increased, more and more DOX molecules are adsorbed on the surface of $\alpha\text{-Fe}_2\text{O}_3/\text{SAPO-34}$. A significant amount of adsorbed DOX is thought to have an inhibitive effect on the reaction of DOX molecules with photogenerated holes or hydroxyl radicals, because of the lack of direct contact between them. Once the concentration of DOX is increased, it also causes the DOX molecules to absorb light, and the photons never reach the photocatalyst surface. Thus the photodegradation efficiency decreases.

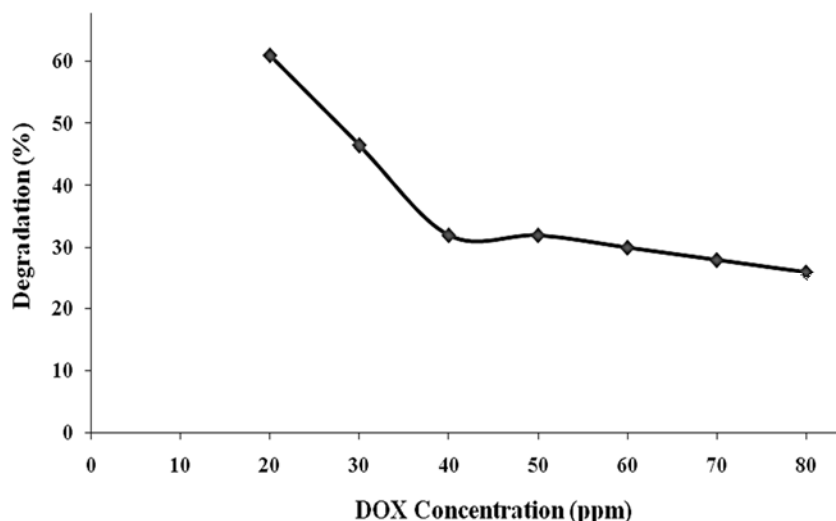


Figure 4. Effect of initial DOX concentration on photo degradation efficiency ($\alpha\text{-Fe}_2\text{O}_3/\text{SAPO-34}$ = 400 mg/L, initial pH = 5; irradiation time = 120 min)

Figure 5 shows the amount of $\alpha\text{-Fe}_2\text{O}_3/\text{SAPO-34}$ nano photocatalyst on DOX degradation in a constant initial concentration (20 ppm), pH = 5, and the irradiation time of 120 min. By increasing the amount of the catalyst up to 150 mg, degradation increases. The further increase of the catalyst leads to a decrease in degradation. Based on the observations, the optimized value of the catalyst loading is about 15 mg under the given experimental condition. The pollutant degradation improvement because of photocatalytic loading is because of the access to the total surface area and active sites of the catalyst. The observed decrease in degradation efficiency, by using an excess amount of the catalyst, is a result of the created opacity in high concentrations of the photocatalyst.

As it can be seen in Figure 6, in alkaline media, the possibility of $\cdot\text{OH}$ radicals generation increases as the result of the reaction between hydroxyl ions (OH^-) and produced holes in the valence band. Generating higher amounts of $\cdot\text{OH}$ radicals, leads to more radical attacks to DOX molecules, so the process efficiency increases. Furthermore, due to the structure of DOX molecule, the presence of the OH groups attached to the benzene ring and hydroxyl groups with acidic hydrogen (because of the high polarity of OH) can lose hydrogen in an alkali media followed by the formation of negatively charged oxygen in the molecule. Since the catalyst surface is acidic, the adsorption capability of DOX onto catalyst increases and so $\cdot\text{OH}$ radicals attack the adsorbed DOX molecules more and the process efficiency increases.

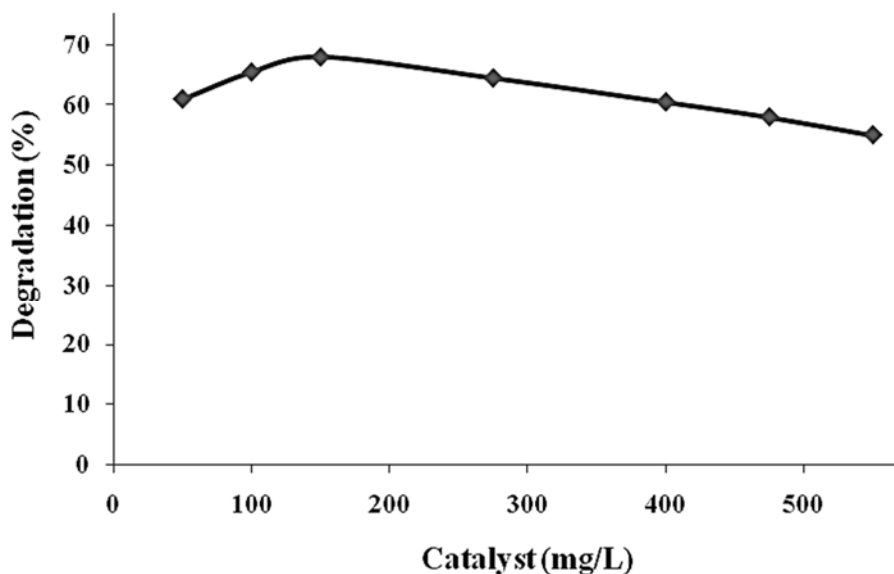


Figure 5. The effect of the amount of $\alpha\text{-Fe}_2\text{O}_3/\text{SAPO-34}$ on photodegradation efficiency of DOX (Initial concentration of DOX = 20 ppm, pH= 5; irradiation time = 120 min)

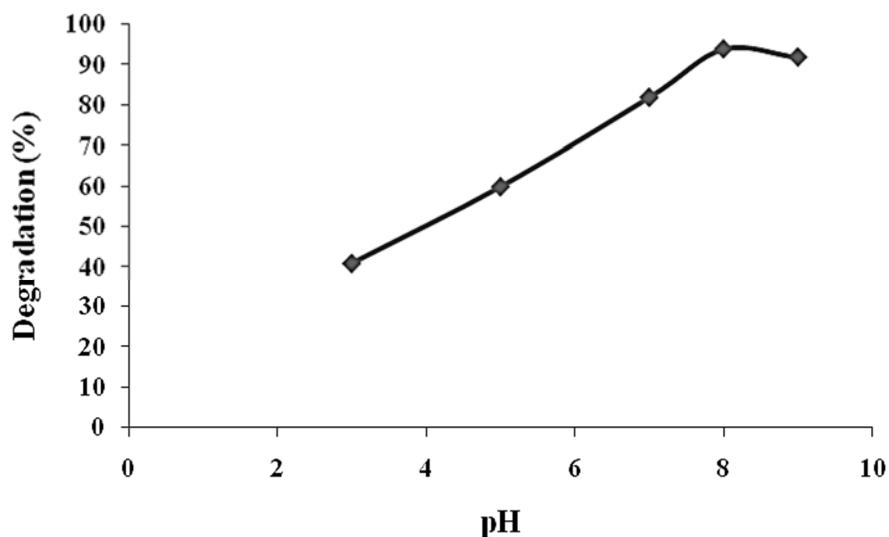


Figure 6. Effect of pH value on photodegradation efficiency of DOX at the irradiation time of 120 min (Initial concentration of DOX = 20 ppm, $\alpha\text{-Fe}_2\text{O}_3/\text{SAPO-34}$ = 150 mg/L)

H₂O₂ is an electron scavenger which accepts photogenerated electrons from the conduction band and prevents the electron-hole recombination to generate hydroxyl radicals ([•]OH) [14]. The photo-catalytic degradation of DOX was performed at different concentrations of hydrogen peroxide and in the presence of an optimized amount of other laboratory factors. The results are shown in Figure 7. By increasing H₂O₂ concentration up to 4 mol/L, the complete degradation of DOX occurs in a short time (30 min). Degradation efficiency enhancement by increasing the amount of H₂O₂ could be attributed to increasing the concentration of reactive hydroxyl radicals (1). Moreover, by light radiation, the hydrogen peroxide molecule undergoes a cleavage to produce O₂ gas (2). According to the photocatalytic mechanism, the O₂ gas reacts with conduction band electrons through several steps and generates [•]OH radicals (3-5).

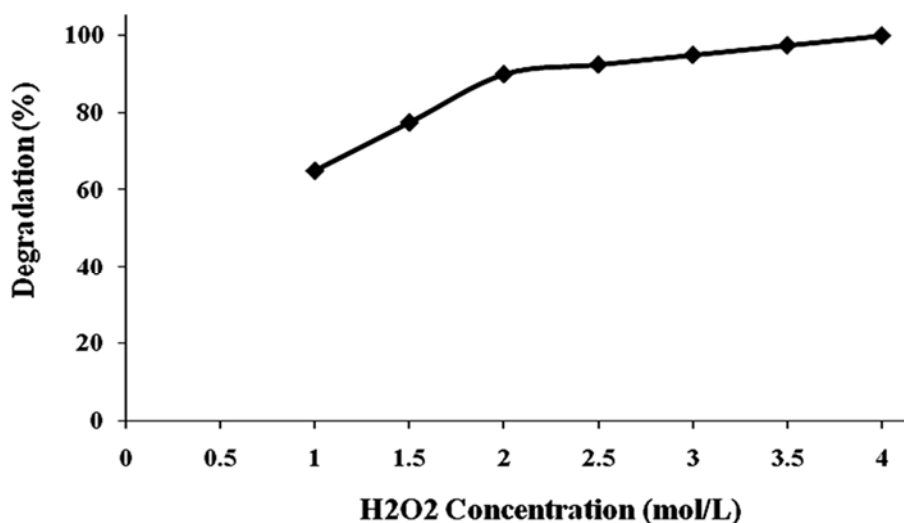
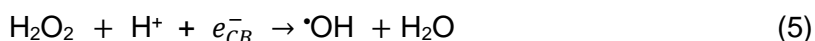


Figure 7. Effect of H₂O₂ concentration on DOX degradation after 30 min in UV/ α -Fe₂O₃/SAPO-34 process (Initial concentration of DOX = 20 ppm, pH = 8, amount of α -Fe₂O₃/SAPO-34 = 150 mg/L)

CONCLUSIONS

The α -Fe₂O₃/SAPO-34 nanostructure was prepared by encapsulation of α -Fe₂O₃ with SAPO-34 and was characterized by XRD, SEM and FT-IR techniques. Next, the photocatalytic degradation removal of DOX through advanced oxidation processes (AOP) has been studied under basic conditions using UV/ α -Fe₂O₃/SAPO-34/H₂O₂ system. The results obtained showed that the photocatalytic degradation of DOX decreases with an increase in the concentration of DOX. The effect of initial DOX concentration, catalyst dosage, pH and H₂O₂ concentration on the photocatalytic of DOX were investigated. Finally, the optimum condition were determined as Initial concentration of DOX = 20 ppm, pH = 8, amount of α -Fe₂O₃/SAPO-34 = 150 mg/L, and H₂O₂ concentration 4 mol/L. Using α -Fe₂O₃/SAPO-34 nano photocatalyst at different alkaline pHs can be a logical economic and scientific solution for the treatment of wastewaters containing this anticancer drug. This work suggested that the α -Fe₂O₃/SAPO-34 nanostructures could be regarded as a prominent catalyst for the degradation of drugs under mild conditions. It is hoped that the present survey opens a new window of magnetically catalysts to be used as a photocatalyst in the field of drug degradation.

EXPERIMENTAL SECTION

Iron(III) chloride hexahydrate was purchased from Daejung Company (Korea). Fumed silica was purchased from Sigma-Aldrich (USA). Aluminum isopropoxide and cyclohexylamine were purchased from Titrachem Company (Iran). Hydrogen peroxide (30%) was purchased from Chem Lab Company (Belgium). Other reagents such as Urea, orthophosphoric acid, ethanol (96%), sodium hydroxide and sulfuric acid (95-97%) were purchased from Merck (Germany). DOX was purchased from RPG Life Sciences Limited (Mumbai, India). The absorbance measurements were taken on a Perkin Elmer Lambda 25 UV/Vis spectrophotometer using silica cells with a path length of 10 mm. The surface morphology of the catalyst was analyzed using scanning electron microscopy (SEM) on a Philips XL 30 microscope. X-ray powder diffraction patterns were recorded using a Cu radiation (λ = 1.5406) source on a Philips PW 1800 X-ray diffractometer. Fourier transform infrared spectroscopy (FT-IR) was carried out on a Perkin Elmer Spectrum 400 spectrophotometer using a KBr pallet for sample preparation. The solutions pH values were measured on a Metrohm 780 pH meter.

Preparation of α -Fe₂O₃ nano-particles

α -Fe₂O₃ nanoparticles were synthesized according to the procedure reported by Chaudhari *et-al.* [15] as follow: a solution of ferric chloride hexahydrate (0.25 mol in 1L of water) was mixed with a solution of urea (1 M) and the mixture was magnetically stirred for 30 min and subsequently refluxed for 12 hours. The precipitate was filtered, washed with 100 mL of aqueous ethanol, dried at 80 °C for 2 hours and calcinated at 300 °C for 1 hour to obtain the hematite as yellowish brown powder.

Preparation of SAPO-34

a mixture of Aluminum isopropoxide (6.8 g) and Orthophosphoric acid (3.3 g) was dissolved in deionised water (14 g) and vigorously stirred for 1 hour. Subsequently, an aqueous solution of Cyclohexylamine (9.9% w/w) was added to the mixture and stirred for another 1 hour. The resultant mixture was combined with fumed Silica (0.96 g) and the solution was allowed to be stirred for 2 hours, until a gel was formed. Next, the synthesized gel was transferred into a 60 mL stainless steel autoclave and kept at 200 °C for 24 hours. The obtained product was filtered and washed with water, dried at room temperature and calcinated at 550 °C for 20 hours [16].

Preparation of α -Fe₂O₃/SAPO-34 nano photocatalyst

To a mixture of SAPO-34 and α -Fe₂O₃ with the weight ratio of 3:1, ethanol was added dropwise to obtain a mud-like shape. The obtained mixture was dried at 80 °C for 2 hours and calcinated at 300 °C for 1 hour to get the yellowish brown powder. [18].

The photocatalytic activity of α -Fe₂O₃/SAPO-34

Typical procedure: A batch reactor amended with three Philips lamps (15 W, UV- C) was used to investigate the photocatalytic activity of α -Fe₂O₃/SAPO-34. 20 mL of each DOX solution (20 ppm) was inserted into 100 mL glass beaker. Catalyst with the concentration of 150 mg/L was added to the beaker. The pH of the solution was adjusted to 8 using NaOH solution. The mixture was stirred at dark for 15 min to establish adsorption-desorption equilibrium. The solution was then exposed to the batch reactor for variable time intervals (10 min). At each time interval, about 3.0 mL of the suspension was collected after centrifugation to remove the photocatalyst particles and was quickly subjected to concentration measurement using a UV-1780 UV-vis spectrophotometer (Shimadzu, Japan) at room temperature.

The efficiency of degradation was calculated using the formula: $\text{Degradation}\% = (A_0 - A_t)/A_0$, where A_0 is the initial absorption of the sample and A_t is the absorption through the t sampling time.

ACKNOWLEDGMENTS

The authors are thankful to Islamic Azad University, Arak Branch for the preparation of experimental setup.

REFERENCES

1. A. Grimm, K. Madduri, A. Ali, C.R. Hutchinson, *Gene*, **1994**, 151, 1.
2. A. Brayfield, ed. "Doxorubicin". Martindale: The Complete Drug Reference. Pharmaceutical Press, **2013**.
3. S.N. Mahnik, K. Lenz, N. Weissenbacher, R.M. Mader, M. Fuerhacker, *Chemosphere*, **2007**, 66, 30.
4. Z. Chen, G. Park, P. Herckes, P. Westerhoff, *J. Adv. Oxid. Technol.*, **2008**, 11, 254.
5. J. Hirose, F. Kondo, T. Nakano, T. Kobayashi, N. Hiro, Y. Ando, H. Takenaka, K. Sano, *Chemosphere*, **2005**, 60, 1018.
6. C.A. Somensi, E.L. Simionatto, J.B. Dalmarco, P. Gaspareto, C.M. Radetski, *J. Environ. Sci. Health A.*, **2012**, 47, 1543.
7. X.H. Wang, A.Y.C. Lin, *Environ. Pollut.*, **2014**, 186, 203.
8. N. De la Cruz, J. Giménez, S. Esplugas, D. Grandjean, L.F. De Alencastro, C. Pulgarín, *Water Res.*, **2012**, 46, 1947.
9. A. Chatzitakis, C. Berberidou, I. Paspaltsis, G. Kyriakou, T. Sklaviadis, I. Poullos, *Water Res.*, **2008**, 42, 386.
10. E. Aghaei, M. Haghghi, *Powder Technol.*, **2015**, 269, 358.
11. M. Nikazar, K. Gholivand, K. Mahanpoor, *Kinet. Catal.*, **2007**, 48, 214.
12. J.M. Wu, T.W. Zhang, *J. Photochem. Photobiol. A.*, **2004**, 162, 171.
13. E. Pipelzadeh, A.A. Babaluo, M. Haghghi, A. Tavakoli, M. Valizadeh Derakhshan, A. Karimzadeh Behnami, *Chem. Eng. J.*, **2009**, 155, 660.
14. Y.X. Yang, M.L. Liu, H. Zhu, Y.R. Chen, G.J. Mu, X.N. Liu, Y.Q. Jia, *J. Magn. Mater.*, **2008**, 320, L132.
15. N.K. Chaudhari, H.C. Kim, D. Son, J.-S. Yu, *Cryst. Eng. Comm.*, **2009**, 11, 2264.
16. E. Aghaei, M. Haghghi, *Powder Technol.*, **2015**, 269, 358.

SEASONAL EVOLUTION AND DEPTH VARIABILITY OF HEAVY METAL CONCENTRATIONS IN THE WATER OF FIRIZA-STRÎMTORI LAKE, NW OF ROMANIA

THOMAS DIPPONG^a, CRISTINA MIHALI^a, FIRUTA GOGA^{b*},
ELENA CICAL^a

ABSTRACT. The paper follows the spatial variability and seasonal evolution of the heavy metal content of the Firiza-Strîmtori Reservoir that is the main source of drinking water for Baia Mare city located in the northwestern part of Romania. Water samples were collected from 10 sampling points located along the median line of the lake at different depths (at surface, at 5 m, 10 m, 15 m and 20 m). The experiments were carried out in the winter, spring, summer and autumn of 2015. We determined the concentration – depth profiles, both for the heavy metals iron (Fe), manganese (Mn), zinc (Zn), copper (Cu), cadmium (Cd), lead (Pb) and also for sodium (Na), potassium (K), calcium (Ca) and magnesium (Mg). We determined the concentrations of heavy metals by atomic absorption spectrometry. We found that concentrations of heavy metals increase with depth. Generally, the concentrations of heavy metals are within the legal limits for the water used as drinking water sources. Mathematical models with high correlation coefficients were obtained in the case of heavy metal concentrations depending on depth and also for the seasonality of heavy metals upload.

Keywords: *heavy metals, water quality, water reservoir, seasonality, mathematical models,*

INTRODUCTION

Heavy metal pollution in aquatic environments is a growing problem worldwide and currently it has reached an alarming rate, especially for drinking water sources such as rivers and water reservoirs [1-2].

^a *Technical University of Cluj-Napoca, North University Center at Baia Mare, Faculty of Science, 76 Victoriei Street, 430122, Baia Mare, Romania*

^b *Babeş-Bolyai University, Faculty of Chemistry and Chemical Engineering, 11 Arany Janos str., RO-400028, Cluj-Napoca, Romania*

* *Corresponding author: firutagoga@yahoo.com*

There are various sources of heavy metals in aquatic environment such as natural sources through geological weathering of the rocks and anthropic sources such as mining effluents, industrial effluents, domestic effluents, agricultural nonpoint source pollution, transport or recreational activities (boating, fishing, camping). Heavy metals occur in small amounts naturally and may enter into the aquatic system through leaching of rocks especially by rainwater, atmospheric deposition of airborne dust or industrial emissions, forest fires and vegetation [1, 3-5].

In a water reservoir, heavy metals can be distributed in the water column or can be adsorbed on the surface of suspended particles that are finally deposited as sediments on the bottom. These processes lead to the accumulation of higher levels of heavy metals in sediments [4-5]. However, the dissolved species of heavy metals continuously undergo a chemical exchange with the suspended fraction and bottom sediments [6-7]. The sediments can be a source of heavy metals through resuspension, especially when events such as storms or heavy rainfall occur [8]. Studies showed that aquatic sediments absorb water contaminants to levels significantly higher than the water column concentrations and so they act as endogenic sources of contaminations [9-11].

Heavy metals in aquatic environments can be harmful both to the environment (aquatic organisms including fish) and to human beings [12-13]. Some heavy metals such as Pb and Cd are toxic to living organisms, but others are naturally found in the human body at low concentrations and are essential for human health, such as Fe, Zn, Cu. Fe, for example, prevents anaemia, and Zn is a cofactor in over 100 enzyme reactions [7]. In the aquatic environment, metals undergo chemical and biogeochemical processes that control their solubility, mobility, bioavailability and toxicity [14]. It is important to know the distribution of contaminants in lake water because it provides information about their origin, transformation and migration that are useful in water reservoir management [9, 15-16].

Water reservoirs provide important services to human communities such as supplying raw water, controlling floods and generating electricity [2]. However, with time, water quality tends to decrease due to sediment accumulation, low flow, accumulation of pollutants in sediments and their release in the water column by diffusive processes or by sediment disturbances [2, 15].

In temperate regions, water quality in a reservoir is not constant across the seasons, but is influenced by rainfall and solar heating, resulting in seasonal variations in water quality and also by the input and output of water [16]. The water content in heavy metals depends on the water depth. In warm seasons, water is stratified due to the incomplete or lower recirculation between the superficial layer of water, the epilimnion, and the deeper layer

hypolimnion [17]. Thus, the deeper layer is excluded from gas exchange with the atmosphere, leading to anoxic conditions at the bottom of the reservoir. In these anaerobic conditions, reduced chemical species, especially Fe and Mn are released from the sediments and enter the hypolimnion [2,17].

The Strîmtori-Firiza Reservoir is the main water supply for Baia Mare town [18-21] being also used for electricity generation, recreational activities, and flood prevention. The reservoir was built between 1961-1964 on the Firiza River and was inaugurated in 1964. It is located at about 10 km north of Baia Mare municipality and has a total capacity of 16.3 million cubic meters of water with an usable capacity of 13.9 million cubic meters and a maximum depth of 51.5 m [19]. The Firiza Lake is located upstream of the pollution sources, at a higher altitude than the town [21]. The reservoir is surrounded by forested hills with limited human activity. A road passes on the right bank of the reservoir.

The present study aimed to assess the spatial, seasonal variation and also the influence of depth on the degree of heavy metal upload (Fe, Mn, Zn, Cu, Cd and Pb) of the water columns in the Firiza-Strîmtori Reservoir. In this purpose, water samples were taken in 10 points of the median part of Firiza-Strîmtori Reservoir at the surface, and at the depth of 5, 10, 15 and 20 m under the water surface. In addition, the concentrations of the major metals (Na, K, Ca and Mg) in water were analysed to examine possible correlations between data. The originality of the study consists in the complex study that processes a large data base about major and trace metal content in the water column, the variation of metal content with depth, the way in which the seasonality influences the profile of heavy metal concentration with depth.

The results were processed to assess the influences of depth and seasons on the metals content of the water in Firiza-Strîmtori Reservoir. The functions that quantify the dependence of heavy metal content on depth were studied aiming to find the best mathematical models.

Until now there are no studies about the influence of the water column depth on heavy metal content of water in this area.

RESULTS AND DISCUSSION

Annual variation of metals

The spatial and temporal variations of the concentration of the major metallic ions and also of the heavy metals in the water samples of Firiza-Strîmtori Reservoir were assessed using 10 sampling points along the median part of the reservoir. 4 sets of samples were taken in the four seasons for 5 depths: 0 m (at the surface of the water), 5, 10, 15 and 20 m. The average values

and standard deviations of concentrations of the major cations of metals in Firiza-Strimtori Reservoir such as Na, K, Ca and Mg as well as the heavy metals concentration (Fe, Mn, Zn, Cu, Cd and Pb) are shown in Table 1.

We see an increase in metal concentrations with depth for each of the analysed metal. As a general trend, the metal concentrations increase with the depth of sampling. The highest absolute increase in concentration values for the maximum depth of 20 m was found for Ca with 0.94 mg/L considering the difference between the average Ca concentration at surface and the average Ca concentration at 20 m, followed by Na, Mg, Fe, Mn, Zn, Cu, Pb and Cd.

Table 1. The yearly average values of the metal concentrations in the water samples of Firiza-Strimtori Lake, mg/L (for 10 sampling points and 4 times of sampling)

Depth Metals	TV*	0 m	5 m	10 m	15 m	20 m
Na	-	1.42±0.01	1.48±0.01	1.55±0.02	1.61±0.02	1.68±0.03
K	-	1.01±0.02	1.06±0.02	1.11±0.02	1.15±0.015	1.20±0.013
Ca	100	5.37±0.06	5.62±0.06	5.85±0.10	6.09±0.09	6.31±0.06
Mg	50	1.46±0.008	1.52±0.01	1.58±0.02	1.64±0.02	1.71±0.021
Fe	0.2	0.249±0.001	0.285±0.004	0.320±0.005	0.359±0.005	0.399±0.003
Mn	0.05	0.082±0.0014	0.106±0.003	0.131±0.002	0.162±0.003	0.191±0.004
Zn	5	0.018±0.002	0.038±0.002	0.064±0.003	0.085±0.004	0.107±0.003
Cu	0.1	$(19±0.76)·10^{-4}$	$(20±0.62)·10^{-4}$	$(22±0.73)·10^{-4}$	$(24±0.66)·10^{-4}$	$(26±0.62)·10^{-4}$
Cd	0.005	$(32±1.7)·10^{-6}$	$(55±2)·10^{-6}$	$(77±3)·10^{-6}$	$(99±4)·10^{-6}$	$(122±4)·10^{-6}$
Pb	0.01	$(14±0.51)·10^{-4}$	$(15±0.57)·10^{-4}$	$(17±0.71)·10^{-4}$	$(19±0.91)·10^{-4}$	$(21±0.12)·10^{-4}$

*Threshold value for drinking water according to Romanian legislation

Considering the ratio between the metal average concentration at surface (0 m) and at 20 m depth, the highest value was found for Zn (about 6) followed by Cd (3.9), Mn(2.3), Fe (1.6), Pb and Cu around 1.4 while for Mg, Ca Na and K, the ratio was very close around 1.18. The levels of distribution for the studied metals are presented in Fig. 1.

Heavy metal concentrations do not exceed the contamination threshold value for drinking water except for Fe and Mn. The water of Firiza-Strimtori Reservoir has a good quality and can be used as raw material for preparing drinking water in the treatment plant where it is subjected to treatment processes, finally obtaining values under the maximum concentration allowed for all metals.

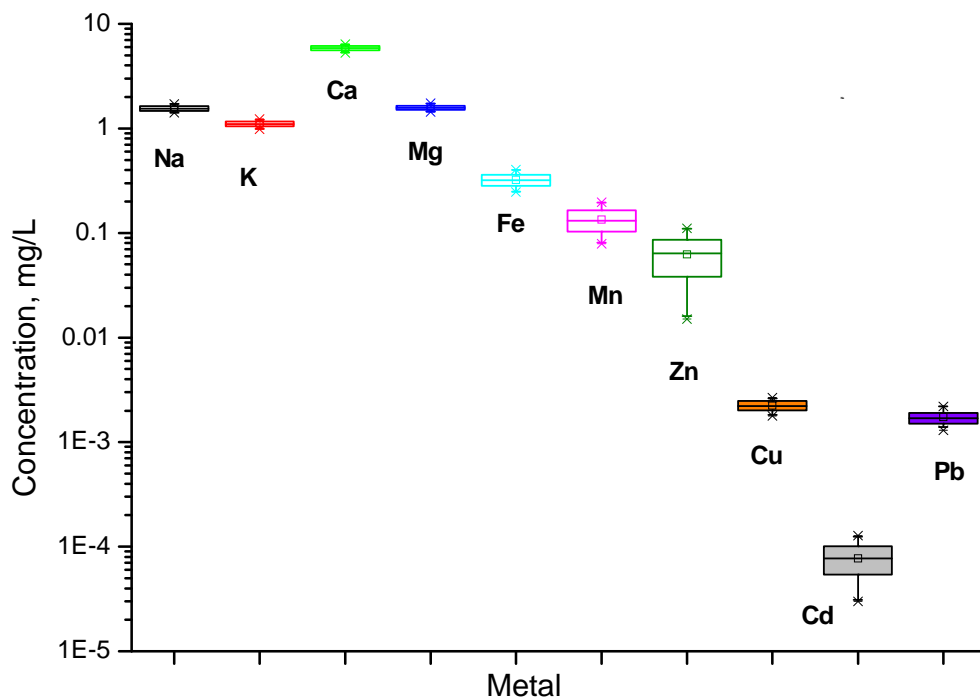


Figure 1. The distribution of the concentration of major metals and heavy metals in the Strimtori-Firiza Reservoir for the 10 sampling points and 5 levels of depth

By correlating the average values of metals concentration presented in Table 1 and the levels of concentrations depicted in Figure 1 as Box plot it can be concluded that the concentration of the studied metals decreases in the following sequence: $Ca > Na > Mg > K > Fe > Mn > Zn > Cu > Pb > Cd$. For all the studied metals, an increasing with depth was observed, probably due to the release of the metal ions into the water column as an endogenic source of contamination based on the alteration in the oxidation-reduction status of sediments. In Firiza-Strimtori Reservoir, the heavy metal sources were the weathering of volcanic rocks that are found in the area and also the industrial atmospheric deposition over the reservoir during decades when a copper smelter and a lead smelter have worked in Baia Mare. Since 2008 and 2010 respectively, these smelters have been closed, but the atmospheric powders deposited as sediments to the bottom of the reservoir can be released from the sediments being an endogenic source of pollution.

The last years have shown a trend of enhancement in pollution by heavy metals present in the sediments of surface water [8,14]. In this context, the distribution pattern of contaminants across the water column could provide some useful information on the environmental characteristics of heavy metals such as their transformation and migration [9].

Seasonal variation of metals

Figures 2 and 3 show the variation of the concentrations of metals with depth across the four seasons for each of the 10 sampling points. Thus, a family of curves was obtained showing the degree of reproducibility and of homogeneity of the water within the reservoir for each analysed metal. Also, the differences between the 4 seasons regarding the metal concentration in water columns could be observed. The variation of the metal concentrations with depth indicated an increase of the concentration with said depth [22-24].

Na concentrations in the reservoir water decreased in autumn and winter compared to those registered in spring and summer. This trend could be explained by the dilution effect in the cold seasons, richer in precipitation. A similar pattern was found in the case of K, with the exception of a partial overlap of the functions that described potassium concentrations depending on depth, $c_K = f(\text{depth})$.

Ca content in water was highest in winter, decreased in summer, decreasing even more in spring. The lowest concentrations of Ca were registered in autumn. Mg shows similar trend with a certain particularity: the lowest values were found in spring. Ca and Mg concentrations in water are influenced by the carbon dioxide content of water that increases in the cold seasons due to a higher solubility. Also, in the warm seasons, due to the photosynthesis process as well as to the decomposition of the organic matter, the water content in carbon dioxide was enriched.

Fe concentration trends were similar to those of Mn in Firiza-Strîmtori Reservoir: the highest values were registered in spring, followed by those found in winter. The lowest values of Fe and Mn concentrations were found in autumn and summer. In the warm season a stratification of the reservoir occurs and thus anoxic conditions are found. Part of the heavy metals precipitate in the reductive medium as metal sulphides [22-23].

The concentrations of heavy metals are shown in Fig. 3. In the case of Zn there is not a clear difference between the pattern of Zn depending on the depth for the four set of data sampled in different seasons. However, a downward trend of the concentrations found in warm seasons (summer and spring) compared to the colder ones (winter and autumn) can be observed.

SEASONAL EVOLUTION AND DEPTH VARIABILITY OF HEAVY METAL CONCENTRATIONS ...

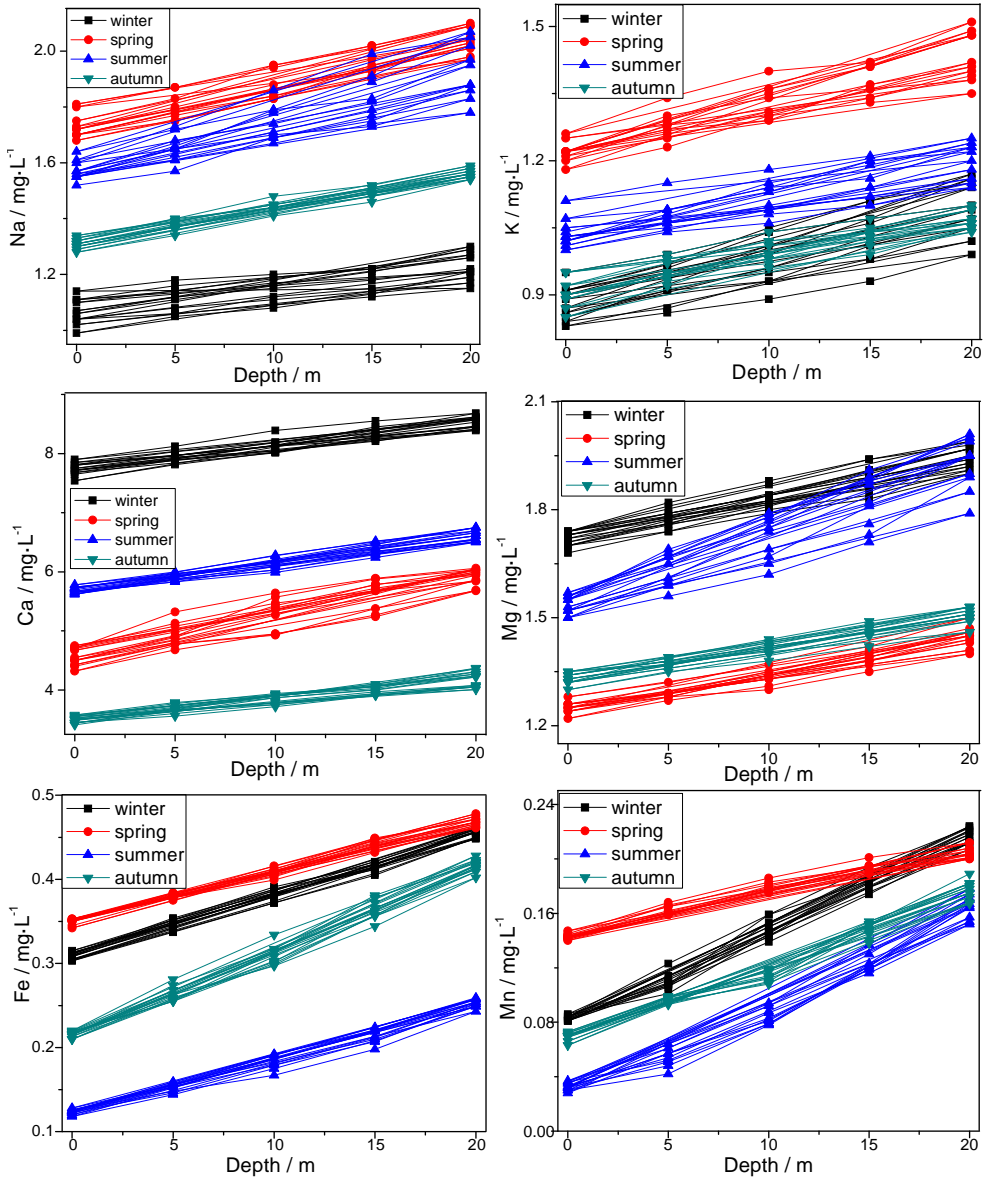


Figure 2. The variation of Na, K, Ca, Mg, Fe and Mn depending on season and depth

Higher concentrations were found for Zn in the summer especially at the depth of 10, 15 and 20 m, showing a stratification of the reservoir water that is specific to the warm season.

In the case of Cu, the highest concentrations were registered in winter followed by those found in summer and autumn. The lowest concentrations were found in spring, probably due to the dilution effect of precipitations and runoff in the reservoir.

Cd showed the highest concentrations in summer and spring. A lowering trend was observed in winter and autumn.

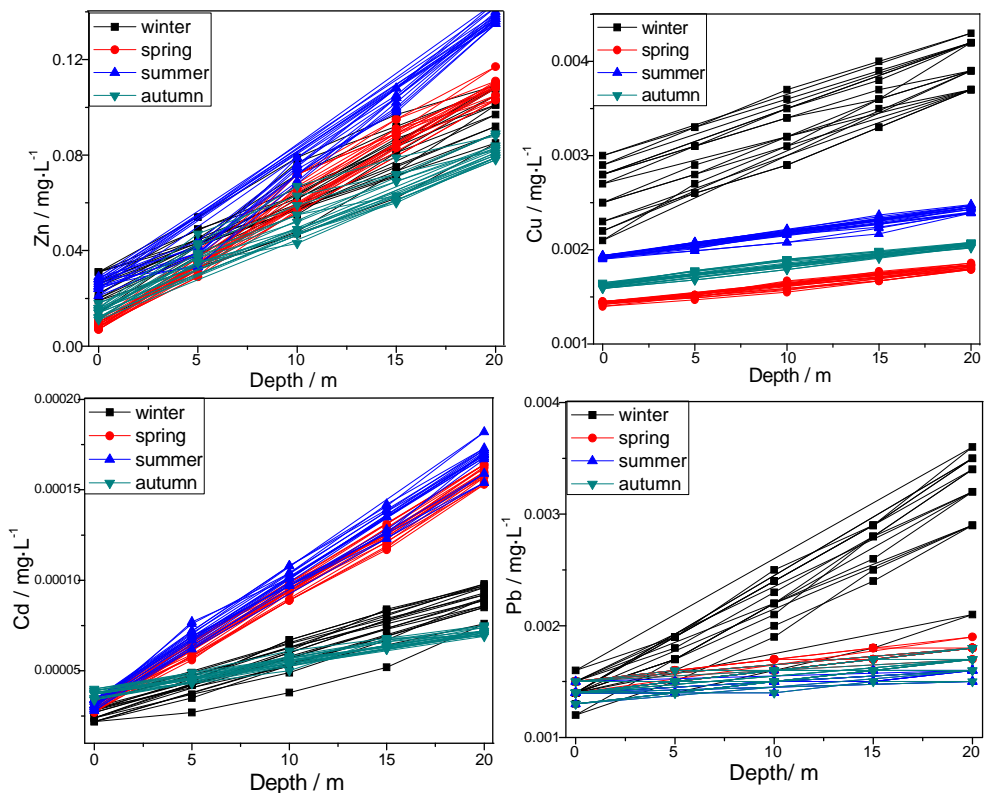


Figure 3. The variation of Zn, Cu, Cd, si Pb depending on season and depth in the 10 sampling points of the Strîmtori-Firiza Reservoir

The Pb concentrations showed a low variability and they were higher in winter.

The concentrations of Zn as the other analyzed heavy metals increased with depth.

The differences between the concentrations of Fe, Mn, Cu, Cd and Pb at water surface and those found in the deeper layers are caused by the differences in pH and redox conditions [23].

In figure 4, the distribution of levels of heavy metals for the four seasons is shown. The highest concentrations of Ca were registered in winter. The seasonal variation of Pb, Cd, Cu, Mn and Zn concentrations could be explained by the different trends of the suspended particulate matter in different seasons. The suspended particulate matter is the main agent that promotes the vertical transport of the heavy metals. In the warm seasons, summer and spring, the stratification of water column occurs while in winter and autumn the vertical mixing of the water layers prevails [23].

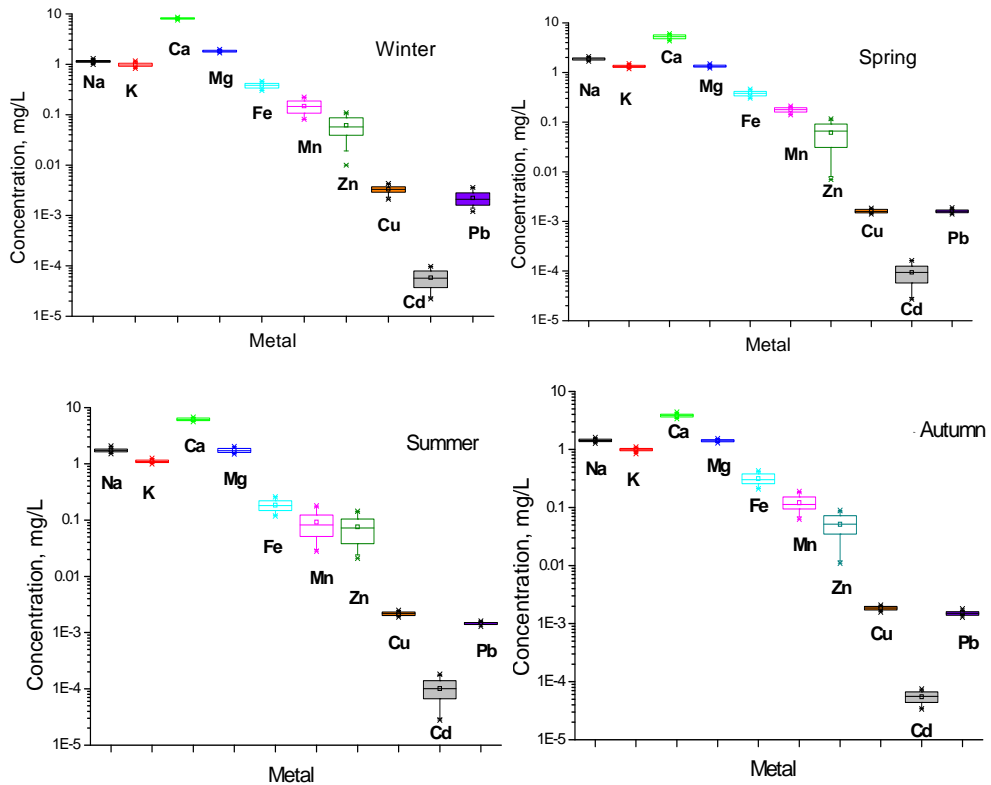


Figure 4. The levels of concentration of the major metals and heavy metals depending on the seasons

Comparative study of iron concentration in raw and filtrated water

In Fig. 5 the variations of the Fe concentrations with the depth in the four seasons for the filtered water and for the raw (unfiltered) water that contains the Fe ions in the dissolved forms and also the colloidal forms of Fe are plotted. The highest values of Fe contents in the raw (unfiltered) water samples were found in winter while in the filtered water, the highest concentrations were found in summer and the lowest ones were found in spring, both for the unfiltered and for filtered water as it is shown in Fig. 5.

The study was performed only for Fe content. Among heavy metals, Fe was present in the highest concentrations and the tendency of Fe to pass in colloidal forms due to the hidrolisis and oxidation processes is well known.

The presence of iron in higher concentration in raw and filtered water is explained by the colloidal iron [20]. Most metallic elements such as Pb, Cd, Cu and Zn are toxic for aquatic biota [20].

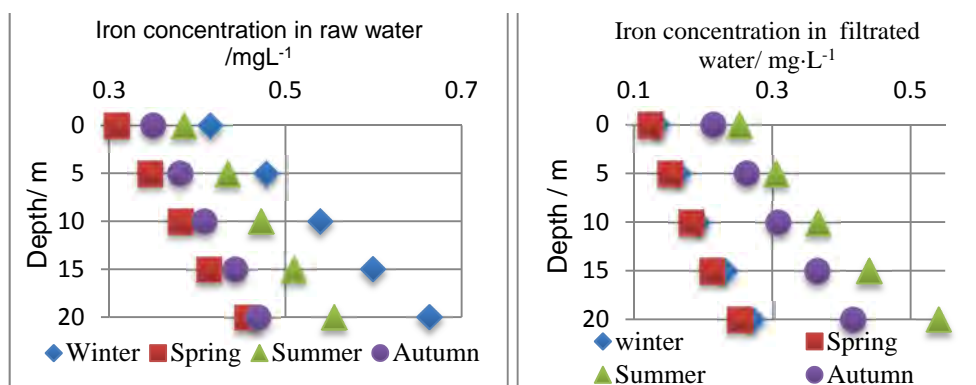


Figure 5. The comparison between the concentrations of iron (Fe) in the raw water (left) and in the filtered water (right)

Mathematical modeling

The mathematical model aimed to find the dependence of the studied heavy metal concentrations with depth. Nonlinear regression method was applied in order to obtain the function with the best-fitted values of the metal concentrations. Based on the mathematical models that fit the experimental data the study attempted to predict the future trends of the analyzed metal concentrations in reservoir water.

The mathematical models that better described the variation of the metals' concentrations with depth and the seasonality as a function of metals' concentration in different seasons consist of a set of non-linear functions obtained by regression with Table Curve Windows program.

Some of the heavy metals' concentrations are strongly correlated. The highest correlations were found for Mn and Fe, Zn and Cd and also for the major elements Mg and Ca.

The variation of heavy metal content with depth was subjected to mathematical analysis of data trying to find the function describing the increase of metals with depth. Only in the case of Zn a function with a good correlation coefficient was found.

The mathematical model that describes the variation of Zn concentration with depth is a polynomial function given by the equation (1) with the model accuracy indicator, $R^2=0.858$ ($F=294$)

$$y = 0.018 - 0.0056x + 0.0086x^{1.5} - 0.0024x^2 + 0.000214x^{2.5} \quad (1)$$

The accordance between the results generated by the mathematical models and the experimental data showed that a multivariable model can be utilized in the estimation of the correlations among the different metals' concentration is presented in table 2. In this purpose a model was utilized based on a function $f(x, y, z)$ generated by the TableCurve3D program. The shapes of the function are shown in Fig. 6.

Table 2. Mathematical models obtained by correlation of different heavy metals concentration

Variation	Mathematical model	Model accuracy indicator	
		R ²	F
Mn = f(Fe)	$y = 0.9 - 68x + 2111x^2 - 32409x^3 + 282469x^4 - 1422373x^5 + 3862949x^6 - 4378076x^7$	0.810	116
Cd = f (Zn)	$y = 0.000006 - 0.0061x + 0.47x^2 - 18.78x^3 + 419x^4 - 5654x^5 + 44909x^6 + 191037x^7 + 333034x^8$	0.821	110
Mg = f(Ca)	$y = 41011 - 74696x + 60518x^2 - 28726x^3 + 8848x^4 - 1848x^5 + 265x^6 - 25x^7$	0.902	174
Pb = f(Ca,Mg)	$z = -0.18 - 0.24x \ln x + 0.16x^2 - 0.05x^3 \ln x + 0.002x^3$	0.802	151
Cd = f(Mn,Fe)	$z = -0.0019 - 0.0011x + 0.28y - 0.013y^2 + 0.015y^3$	0.772	167
Cd = f(Zn, Cu)	$z = 0.000033 + 0.0027x - 0.67x^2 + 0.67x^3 - 2.38y^2 - 0.016y - 0.072y^2$	0.881	237
Pb = f(Cu, Cd)	$z = 0.0021 + 0.031x + 0.89y - 1.88x^2 - 2.24y^2 - 0.088xy$	0.810	157

Both metals, Mn and Fe, are found in more oxidation states, they vary with the depth in a similar manner and are susceptible to oxidation or reduction. At higher depths due to the lack of oxygen, these metals are found in the reduced oxidation states [2,25]. Cd and Zn are known to be geochemically similar and similar also in their behavior in the environment [25].

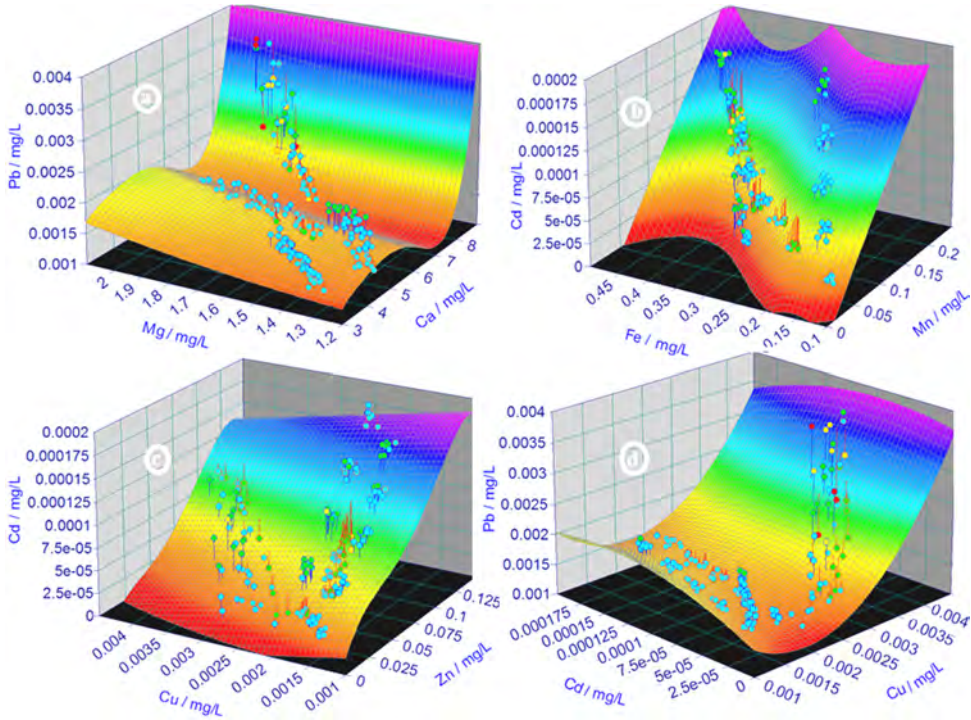


Figure 6. Mathematical models for the correlation of following group of metals:
 $(C_{Mg}, C_{Pb})=f(C_{Ca})$; $(C_{Fe}, C_{Cd})=f(C_{Mn})$; $(C_{Cu}, C_{Cd})=f(C_{Zn})$; $(C_{Cd}, C_{Pb})=f(C_{Cu})$

Also, the mathematical models of the metal concentrations depending on the season were established. Thus, in the case of metal concentration in water of Firiza-Strîmtori reservoir function of seasonality a 3D mathematical model, described in table 3 and figure 7, was obtained.

Table 3. Mathematical models obtained by correlation of the heavy metals concentration in different seasons

Variation	Mathematical model	Model accuracy indicator	
		R ²	F
$C_{Usummer}= f(C_{Uspring}, C_{Uautumn})$	$z = 57 - 28\ln x + 3(\ln x)^2 - 0.36(\ln x)^3 - 0.09(\ln x)^4 - 0.005(\ln x)^5 + 0.01y^{-1}$	0.962	94
$Zn_{spring}= f(Zn_{summer}, Zn_{winter})$	$z = 0.034 - 1.09x + 41x^2 - 485x^3 - 2028x^4 - 0.124y + 12.3y^2 - 37.3y^3$	0.981	333
$Cd_{summer} =f(Cd_{autumn}, Cd_{spring})$	$z = 0.001 + 191.5x^2 + 208.5y^2\ln y + 0.043y^{0.5} + 0.0128(\ln y)^{-1}$	0.971	343
$Fe_{spring}=f(Fe_{summer} , Fe_{winter})$	$\ln z = -1.27 + 3.15x^{2.5} - 0.12y^{-2}$	0.980	1181

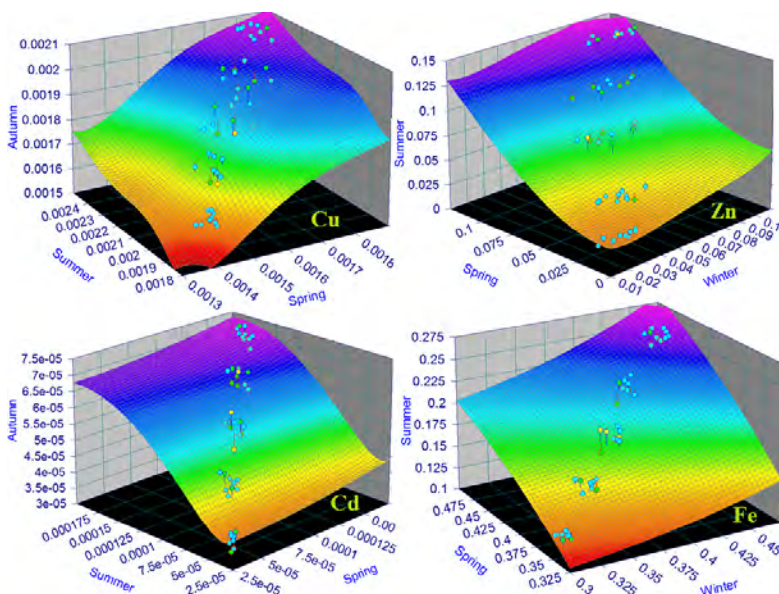


Figure 7. Mathematical models of correlation between the concentrations of Cu, Zn, Cd and Fe across the seasons

There concentrations of the heavy metals in different seasons showed good correlations with correlation coefficients higher than 0.96 showing a relative constancy of water composition across the seasons. The function shows a similar seasonality as in the case of Cu probably due to similar sources of these heavy metals: endogen sources, the resuspension of sediments and exogen ones as fertilizers and pesticides) [25]. For all the developed models, the increase of the upload of metals with depth due to the accumulation trend of heavy metals to the bottom of Firiza-Strímtori Reservoir is obvious.

EXPERIMENTAL SECTION

Sampling

Water samples were collected from 10 sampling points along the lake Strímtori-Firiza (Fig. 8) in four sampling campaigns during the year 2015: February 10th, April 20th, August 10th and October 14th in order to obtain specific data for the seasonality. In each sampling point, the water samples were collected from 5 depth: 0, 5, 10, 15 and 20 m. With this purpose, the water samples were taken using a boat equipped with a telescopic sampler of 20 m length. The collected samples were prepared in order to the determination the heavy metal content. In this respect, a mineralization of water samples with aqua regia (HNO₃ 67%:HCl 37% = 3:1) was realized.

Analysis of metals

The Na, K, Ca and Mg were analysed by atomic emission spectrometry while the heavy metals analysis (Fe, Mn, Zn, Cu, Pb, Cr, Cd) according to SR ISO8467/2001, was done by flame absorption atomic spectrometry and by graphite furnace atomic absorption spectrometry using a Perkin Elmer spectrophotometer. Flame Atomic Absorption Spectrometry and Flame Atomic Emission Spectrometry are techniques recommended for detecting metals in environmental samples [25-26]. For the heavy metals present in samples at low levels such as Cd, Cu and Pb, Graphite Furnace Atomic Absorption Spectrometry was used. This technique is a more efficient atomizer than a flame and it can directly accept very small absolute quantities of sample. Samples are placed directly into the graphite furnace, then, they are heated in several steps to dry the sample, ash organic matter, and vaporize the analyte atoms.

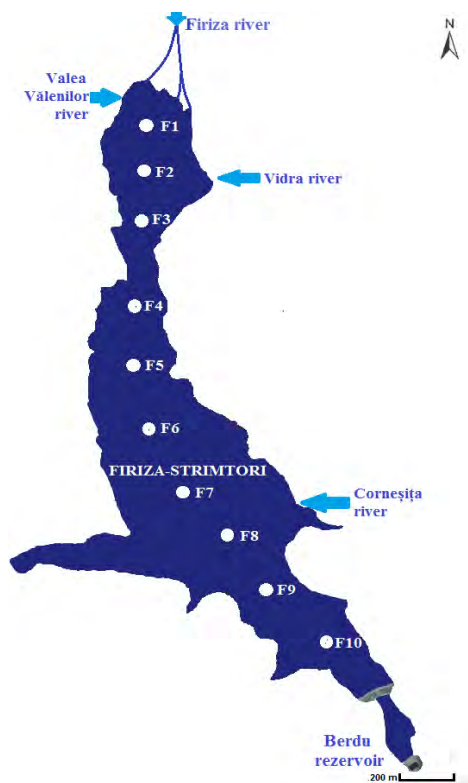


Figure 8. The map of Strîmtori-Firiza Reservoir showing the 10 sampling points (located along its median part)

Models development

The four sets of data sampled in the four seasons, each at them containing 10 sampling points with 5 depth were statistically analysed and shown using Box plot graphics. Models of correlations between the metal concentrations and depth were developed using regression analysis with TableCurve Windows program. We chose the models with the best-fit values of variables quantified by model accuracy indicator, R. The analysed variables were metals' concentrations and depth. The 3D correlations were established between the metal concentrations. The influence of seasons on heavy metal upload was established by developing 3D models with the best model accuracy.

CONCLUSIONS

A complex study on the spatial and seasonal variability of major metals (Na, K, Ca, Mg) and also of heavy metals (Fe, Mn, Cu, Zn, Cd and Pb) was accomplished for the water of Firiza-Strîmtori Reservoir that is the main source of drinking water for the municipality of Baia Mare. The influence of depth on the concentration of metals was studied and models of the concentration's variation with depth were developed. An increase of metals' concentrations with depth for all metals but in different extent was found. In spring the highest values were found for Na, K, Fe and Mn, while in winter higher values for Ca, Mg, Cu and Pb were found. The lowest concentrations of Na and K were found in winter while in summer the lowest uploads of Fe and Mn were determined. Mg and Cu concentrations were lowest in spring while in autumn lowest concentrations for Ca, Zn, Cd and Pb were found. Models that quantify the influence of depth on metals' concentrations were proposed. The correlation between the groups of metals such as (Ca, Mg, Pb), (Mn, Fe, Cd), (Zn, Cu, Cd), (Cu, Cd, Pb) were established as 3D models. The influence of the season on metals' concentration was studied for Cu, Zn, Cd and Fe.

REFERENCES

1. D.O. Ogoyi, C.J. Mwita, E.K. Nguu, P.M. Shiundu, *The Open Environmental Engineering Journal*, **2011**, 4, 156-161.
2. T. Hunag, X. Li, H. Rijnaarts, T. Grotenhuis, W. Ma, X. Sun, J. Xu, *Science of the Total Environment*, **2014**, 485-486, 820-827.
3. E. Nixdorf, B. Boehrer, *Hydrology and Earth System Sciences*, **2015**, 19, 4505–4515.
4. S. Chowdhury, M.A. Jafar Mazumder, O. Al-Attas, T. Husain, *Science of the Total Environment*, **2016**, 569–570, 476–488.
5. H. Bing, J. Zhou, Y. Wu, X. Wang, H. Sun, R. Li, *Environmental Pollution*, **2016**, 485-496.
6. L. Zhang, Q. Liao, S. Shao, N. Zhang, Q. Shen, C. Liu, *International Journal of Environmental Research and Public Health*, **2015**, 12, 14115-14131.
7. I. Nhapi, U.G. Wali, D. Usanzineza, J.J. Kashaigili, N. Banadda, R. Kimwaga, *The Open Environmental Engineering Journal*, **2012**, 5, 96-102.
8. M. Wojtkowska, J. Bogacki, A. Witeska, *Science of the Total Environment*, **2016**, 551–552, 387–392.
9. Y. Wang, Jiwei Hu, K. Xiong, X. Huang, S. Duan, *Procedia Environmental Sciences*, **2012**, 16, 51 – 58.

10. P. Palma, L. Ledo, S. Soares, I.R. Barbosa, P. Alvarenga, P., *Science of the Total Environment*, **2014**, 470–471, 780–790.
11. Q. Gao, Y. Li, Q. Cheng, M. Yu, B. Hu, Z. Wang, Z. Yu, *Water Research*, **2016**, 92, 262-274.
12. C.Y. Chen, R.S. Stemberger, B. Klaue, J.D. Blum, P.C. Pickhardt, C.L. Folt, *Limnology and Oceanography*, **2000**, 45(7), 1525–1536.
13. M.M. Arafa, A.T. Ali, *Egyptain Journal of Comparative Pathology and Clinical Path*, **2008**, 21(3), 191 – 201.
14. A. Kuriata-Potasznik, S. Szymczyk, A. Skwierawski, K. Glinska-Lewczuk, I. Cymes, *Water*, **2014**, 358 (8), doi:10.3390/w8080358.
15. G. Wang, A.Yinglan, H. Jiang, Q. Fu, B. Zheng, *Journal of Hydrology*, **2015**, 520, 37–51.
16. A. Serafim, M. Morais, P. Guilherme, P. Sarmiento, M. Ruivo, A. Magrico, *Limnetica*, **2006**, 25, 771-786.
17. X. Li, T. Huang, W. Ma, X. Sun, H. Zhang, *Science of the Total Environment*, **2015**, 521–522, 27–36.
18. S. Filip, `Depresiunea și Munceii Băii Mari – studiu de geomorfologie environmentală`, Presa Universitară Clujeană, Cluj-Napoca, **2008**, p. 186.
19. Cical, E., `Contribuții privind îmbunătățirea tehnologiei de potabilizare a apei provenită din lacurile de acumulare`, Editura Politehnica, Timișoara, **2010**, 63-65.
20. E. Cical, C. Mihali, M. Mecea, A. Dumuța, T. Dippong, *Studia UBB Chemia*, **2016**, LXI(2), 225-238.
21. O-C. Modoi, C. Roba, Z. Török, A. Ozunu, *Environmental Engineering and Management Journal*, **2014**, 13(9), 2325-2336.
22. D. Chapman, `Water quality assessments: A guide to the use o biota, sediments and water in environmental monitoring`, 2nd ed., Chapman & Hall, London, **1996**, 108-168.
23. C. Rădulescu, C. Stih, I.D. Dulama, E.D. Chelarescu, P. Bretcan, D. Tanislav, *Romanian Journal of Physics*, **2015**, 60(1–2), 246–256.
24. C. Rădulescu, I.D. Dulama, C. Stih, I. Ionita, A. Chilian, C. Necula, E.D. Chelarescu, *Romanian Journal of Physics*, **2014**, 59(9–10), 1057–1066.
25. J.A. Plant, N. Voulvoulis, K. Vala, `Pollutants, Human Health and the Environment: A Risk Based Approach`, Wiley-Blackwell, John&Sons, Ltd. Publication, Oxford, **2012**, 90-98.
26. E. Darvasi, N. Muntean, C. Szentkirályi, *Studia UBB Chemia*, **2016**, LXI(3), 311-320.

BENFOTHIAMINE ADMINISTRATION IN PATIENTS WITH DILATED CARDIOMYOPATHY AND ADVANCED HEART FAILURE WITH CHRONIC DIURETIC TREATMENT

DANA-ADRIANA ILUȚIU-VARVARA^a, DAN RĂDULESCU^{b*},
VALER DONCA^b

ABSTRACT. It is well known that long term administration of high dose loop diuretics in patients with heart failure, may in some cases aggravate the cardiac failure symptoms. Part of this effect may be due to thiamine depletion secondary to diuretics use. The aim of our present study was to assess whether administration of benfothiamine in patients with advanced congestive cardiac failure treated on long term with high dose loop diuretics, can prevent the alteration of heart failure.

Keywords: *benfothiamine, cardiovascular diseases, cardiomyopathy, diuretic treatment, heart failure, thiamine.*

INTRODUCTION

Thiamine (Fig. 1) is a water soluble vitamin. The best-characterized form is thiamine pyrophosphate (TPP), a coenzyme in the catabolism of sugars and amino acids. Thiamine is present in meat and cereals. Thiamine pyrophosphate is a key enzyme in carbohydrates metabolism. It results from thiamine and ATP in kidneys, liver, blood cells. In thiamine depletion states, the hexose monophosphate and citric acid cycles are affected. These states are secondary either to poor nutrition (rice), or to chronic alcohol intake, hyperthyroidism, diarrhea, diuretics. Thiamine is present in tissues, at least in 3 forms (mono-, di and triphosphate). In humans, thiamines exist especially

^a *Universitatea Tehnică din Cluj-Napoca, Facultatea de Instalații, Str. Memorandumului, Nr. 28, RO-400114 Cluj-Napoca, Romania*

^b *Universitatea de Medicină și Farmacie Iuliu Hațieganu, Facultatea de Medicină, Str. Emil Isac, Nr. 13, RO-400023 Cluj-Napoca, Romania*

* *Corresponding author: dan_rad31@yahoo.com*

as thiamine diphosphate, more than two thirds being present in erythrocytes. A low erythrocyte transketolase activity is a marker of thiamine deficiency. In general, we appreciate the serum diphosphate activity, by measuring the thiamine pyrophosphate effect (over 15% in thiamine deficiency). Some researchers measure the erythrocyte thiamine diphosphate, while others measure thiamine levels by using high performance liquid chromatography [1, 2, 3].

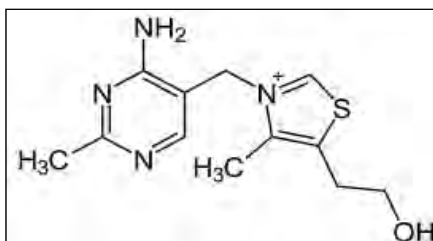


Figure 1. Chemical structure of thiamine

Thiamine (Fig. 2), as well as its phosphate derivatives, can also be detected directly in whole blood, tissues, foods, animal feed, and pharmaceutical preparations following the conversion of thiamine to fluorescent thiochrome derivatives (Thiochrome Assay) and separation by high-performance liquid chromatography (HPLC) [4].

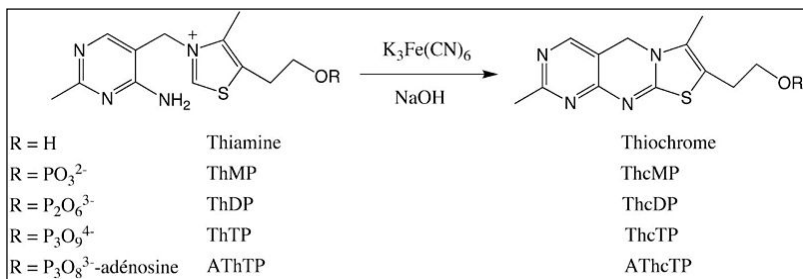


Figure 2. Detection of Thiamine through Thiochrome Assay [4, 5]

Severe thiamine depletion generates cardiac failure (wet beriberi), but recent studies documented left ventricular insufficiency even after moderate thiamine depletion, in patients receiving loop diuretics [5].

In a study on 23 cardiac failure patients treated with furosemide over a period of 3 to 14 months, was observed a serum thiamine depletion (by measuring thiamine pyrophosphate effect), secondary to high urinary thiamine excretion. After oral thiamine supplementation in these patients, was reported an increase in left ventricular ejection fraction, in NYHA exercise capacity, in systolic and diastolic pressures, in these patients. In another study, in 30 patients with heart failure treated longer periods with furosemide, Shimon et al. documented a 22% rise in left ventricular ejection fraction after thiamine administration. Plasma thiamine which was low after diuretic therapy, increased after thiamine administered intravenous. After intravenous thiamine, thiamine pyrophosphate levels decreased in the thiamine supplementation arm in comparison to the placebo one [6].

For thiamine supplementation to be efficient, high levels of this water soluble vitamin in tissues are required. Fujiwara et al., [7] discovered in vegetables a class of lipid soluble thiamines (allithiamines), of which benfotiamine has the highest bioavailability. After oral administration benfotiamine generates considerably higher thiamine concentrations (at least five times greater) in tissues, than the water soluble thiamine. Benfotiamine has an open thiazole ring, which closes once benfotiamine is absorbed passively through intestinal mucosa, generating active thiamine. Benfotiamine is available in a proportion of at least 25%, for 8 days in tissues, much longer than water soluble thiamine [8, 9]. It is very efficient in the treatment of macrovascular and microvascular endothelial dysfunction and oxidative stress, in patients with diabetes mellitus and secondary complications [10, 11, 12].

The first lipophilic thiamine derivative was isolated from garlic (*Allium sativum*) extracts in the early 1950s [7]. It is an allyl disulfide derivative called allithiamine (Fig. 3). Since then, several analogs of this molecule were synthesized with the hope that they would be better absorbed and have a higher bioavailability than thiamine hydrochloride or mononitrate [13,14].

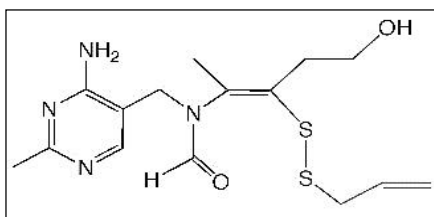


Figure 3. Chemical structure of allithiamine (thiamine allyl disulfide)

Benfotiamine (Fig. 4) is a third derivative with better bioavailability than thiamine. In contrast to the above-mentioned derivatives it is not a disulfide but an S-acyl derivative.

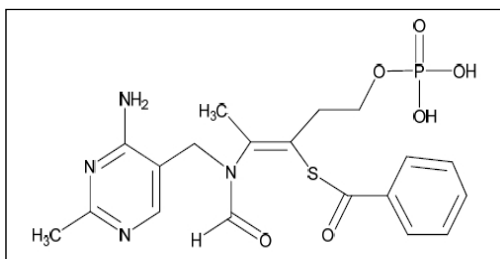


Figure 4. Chemical structure of benfothiamine (S – benzoylthiamine O – monophosphate)

Benfothiamine can also be detected directly in whole blood, tissues, foods, animal feed, and pharmaceutical preparations after derivatization, through chemical oxidation with ferricyanide at pH 13 to form fluorescent thiochrome. Fluorimetric detection is carried out in conjunction with dispersive liquid – liquid microextraction (DLLME) coupled to liquid chromatography (LC) [15].

The purpose of our paper was to assess whether administration of benfothiamine in patients with advanced congestive cardiac failure treated on long term with high dose loop diuretics, can prevent the aggravation of heart failure.

RESULTS AND DISCUSSION

In Table 1 are presented the parameters of both groups at the beginning of the study. As can be seen the parameters are very close between groups.

Table 1. Patients data at the start of treatment

Data	Study group (thiamine)	Control group
Number of patients	20	20
Age (year)	64 ±	66 ±
NYHA class	3.1 ± 0.7	3.3 ± 0.8
Diuretic (furosemid mg/day)	100 ± 20	100 ± 40
Systolic BP (mmHg)	100 ± 14	104 ± 16
EF (%)	24 ± 8	26 ± 10
Cardiac output (l/min)	3.2 ± 0.6	3.4 ± 0.8
Diuresis (l/day)	1.44 ± 0.4	1.64 ± 0.6
NTproBNP (pg/ml)	3860 ± 838	4020 ± 926

In Table 2 are the same parameters at three months, at the end of study.

Table 2. Patients data after three months of treatment

Data	Study group (thiamine)	Control group
Number of patients	10	10
Age (year)	64 ±	66 ±
NYHA class	2.6 ± 0.6	3.4 ± 0.6
Diuretic (furosemid mg/day)	80 ± 30	80 ± 40
Systolic BP (mmHg)	99 ± 12	102 ± 14
EF (%)	28 ± 9	25 ± 8
Cardiac output (l/min)	3.3 ± 0.7	3.5 ± 0.9
Diuresis (l/day)	2.20 ± 0.7	1.70 ± 0.5
NTproBNP (pg/ml)	1020 ± 222	2800 ± 428

As can be seen, we documented, in the study group, after three months of thiamine supplementation, amelioration of the NYHA class with a higher left ventricular ejection fraction, a higher diuresis. At three months we found significantly lower levels of NT proBNP (brain natriuretic peptide) in the study group, compared to the control group. There were no significant differences concerning systolic blood pressure and cardiac output variation, between the two groups at the end of study.

After 3 months of benfotiamine administration, we documented in the study group an amelioration of the NYHA class with a higher left ventricular ejection fraction, a higher diuresis and especially lower levels of NT proBNP, compared with the control group. There were no significant differences concerning systolic blood pressure and cardiac output variation, between the two groups. We noticed no adverse effects of benfotiamine administration (hypotension, gastrointestinal disturbances, as some others reported).

Different studies on streptozocin-induced type 2 diabetes in murine models have shown that benfotiamine prevented ventricular diastolic dysfunction and heart failure through Akt/Pim-1 mediated survival pathway. By preventing cardiomyocyte apoptosis, myocardial fibrosis and microvascular rarefaction in diabetic experimental hearts, benfotiamine improved their ventricular performance [16]. Other studies documented an improvement of left ventricular systolic performance in clinical and experimental models of heart failure after benfotiamine administration, whereas the drug had no effect in healthy hearts [16,17]. Benfotiamine, a transketolase activator, directing glucose to the pentose phosphate pathway, improves experimentally, the functional recovery of infarcted murine hearts, by activation of pro-survival G6PD/Akt signalling pathway and modulation of neurohormonal response [18].

The liposoluble benfotiamine is superior to thiamine as it inhibits formation of advanced glycation end products not only in diabetic but also in aging organisms. As it is well known, glycation produces renal, nerve and retinal damage and also cardiovascular disease. As a consequence, benfotiamine may prevent or even treat neuropathies, blindness, renal failure, cardiomyopathy, arterial peripheral vascular disease. Treatment with thiamine did not significantly affect the formation of advanced glycation end products and as a consequence thiamine cannot prevent the mentioned diseases [19,20]. Deficiency of thiamine, like in beriberi, produces an increased angiogenesis. Benfotiamine increases significantly the angiogenesis. As opposed to thiamine which cannot help in Alzheimer disease, benfotiamine improves the condition of Alzheimer patients and also reduces amyloid formation [18].

As it is well known, thiamine deficiency is associated with oxidative stress. Oxidative stress affects the blood-brain barrier, mitochondrial integrity, nucleic acid and neural stem cell function, induces neuroinflammation and apoptosis. Secondary to producing reactive oxygen species and diminishing the generation of antioxidants, hyperglycemia causes oxidative stress. Benfotiamine diminishes superoxide and hydroxyl radical levels in diabetic and aging hearts by regenerating the antioxidant NADPH, secondary to the activation of the pentose phosphate shunt. By preventing advanced glycation end products accumulation, benfotiamine prevents myocardial interstitial fibrosis [21,22,23].

There were some limits of our study: the number of patients was not very large; as the patients had advanced heart failure, we could not practice exercise test, in order to better quantify the left ventricular failure, than by simple clinical NYHA class.

CONCLUSIONS

After 3 months of benfotiamine supplementation, we documented an improved clinical status, left ventricular ejection fraction, cardiac output in patients with advanced heart failure treated with high dose furosemid. Also serum NT proBNP decreased considerably in this group of patients.

EXPERIMENTAL SECTION

The study group comprised 20 patients with dilated cardiomyopathy (DCM) and advanced heart failure, on standard therapy and high dose furosemid under oral thiamine supplementation 200mg/day, monitored for three months. The control group comprised gender and aged matched similar patients with DCM and severe heart failure, treated with standard therapy

and high dose furosemid, but without oral thiamine. Both groups were treated with furosemid 80 mg and over daily, orally, also in the last three months and continued it during at least three months, till the end of study. All 40 patients were suffering from primitive or ischemic DCM. Patients with recent myocardial infarction, atrial fibrillation, valvulopathies, patients with left ventricular ejection fraction over 40%, were excluded. We also excluded patients on other diuretics than furosemid and patients thiamin deficient of other causes (neoplasia, alcoholism, malnutrition, infections, thyroid, liver or renal diseases, diabetes mellitus).

Cardiac function was assessed clinically during the three months study:

- ✓ NYHA functional class;
- ✓ blood pressure;
- ✓ heart rate;
- ✓ daily diuresis;
- ✓ body weight.

For ultrasound examination an Aloka echocardiograph with a 3.5 MHz transducer and Doppler mode was used, the examination being performed in conformity with the guidelines of the American Society of Echocardiography. The left ventricular systolic performance was assessed by measuring the global EF, monthly, based on apical 4 chambers view according to ASE. Cardiac output was measured using Doppler at left ventricular outflow tract.

Serum brain natriuretic peptide NT proBNP was determined by immunoassay in each patient at the beginning and at the end of the study (normal value 20-40 pg/ml).

We used an unpaired test for normally distributed variables (respectively the Wilcoxon two sample tests for skewed distributions) for comparison between 2 groups. We reported normally distributed variables as mean \pm SD, and the skewed distributed as median and range. We used Pearson's coefficient test to assess correlations between variables and considered $p < 0.05$ significant.

REFERENCES

1. D. Loew, *International Journal of Clinical Pharmacology and Therapeutics*, **1996**, 34, 47.
2. Howard Smithline, M. Donnino, D.J. Greenblatt, *BMC Clinical Pharmacology*, **2012**, 12, 4.
3. K.T. Weber, *Journal of the American College of Cardiology*, **2004**, 44, 1308.

4. J. Lu, E.L. Frank, *Clinical Chemistry*, **2008**, *54*, 901.
5. D. Leslie, M. Gheorghide, *American Heart Journal*, **1996**, *131*, 1.
6. Shimon, S. Almog, Z. Vered, H. Seligmann, M. Shefi, E. Peleg, *American Journal of Medicine*, **1995**, *98*, 485.
7. M. Fujiwara, H. Watanabe, K. Matsui, *Journal of Biochemistry*, **1954**, *41*, 29.
8. P. Balakumar, A. Rohilla, P. Krishan, P. Solairaj, A. Thangathirupathi, *Pharmacological Research*, **2010**, *61*, 482.
9. M.L. Volvert, S. Seyen, M. Piette, B. Evrard, M. Gangolf, J.C. Plumier, L. Bettendorff, *BMC Clinical Pharmacology*, **2008**, *8*, 10.
10. Stirban, M. Negrean, B. Stratmann, *Diabetes Care*, **2006**, *29*, 2064.
11. Stirban, M. Negrean, B. Stratmann, *Diabetes Care*, **2007**, *30*, 10.
12. D.A. Fraser, N.P. Hessvik, N. Nikolić, V. Aas, K.F. Hanssen, S.K. Bøhn, G.H. Thoresen, A.C. Rustan, *Genes & Nutrition*, **2012**, *7*, 459.
13. Greb, R. Bitsch, *International Journal of Clinical Pharmacology and Therapeutics*, **1998**, *36*, 216.
14. D. Lonsdale, *Evidence Based Complementary and Alternative Medicine*, **2006**, *3*, 49.
15. P. Vinas, M. Bravo-Bravo, I. Lopez-Garcia, M. Hernandez-Cordoba, *Analytical Methods*, **2012**, *4*, 2759.
16. R.G. Katare, A. Caporali, A. Oikawa, M. Meloni, C. Emanurli, P. Madeddu, *Circulation Heart Failure*, **2010**, *3*, 294.
17. J. DiNicolantonio, C.J. Lavie, A.K. Niazi, J.H. O'Keefe, T. Hu, *Ochsner Journal*, **2013**, *13*, 495.
18. R. Katare, A. Caporali, C Emanuelli, P. Madeddu, *Journal of Molecular and Cellular Cardiology*, **2010**, *49*, 625.
19. H. Stracke, H.P. Hammes, D. Werkmann, K. Mavrakis, I. Bitsch, M. Netzel, *Experimental and Clinical Endocrinology & Diabetes*, **2001**, *109*, 330.
20. M.L. Volvert, S. Seven, M. Piette, B. Evrard, M. Gangolf, J.C. Plumier, *BMC Pharmacology*, **2008**, *12*, 8.
21. S. Hazell, S. Faim, G. Wertheimer, V. R. Silva, C. S. Marques, *Neurochemistry International*, **2013**, *62*, 796.
22. Stirban, M. Negrean, B. Stratmann, T. Gawlowski, T. Horstmann, C. Gotting, *Diabetes Care*, **2006**, *29*, 2064.
23. Nenna, F. Nappi, S.S. Avtaar Singh, F.W. Sutherland, F. Di Domenico, M. Chello, C. Spadaccio, *Research in Cardiovascular Medicine*, **2015**, *23*, 2.

INVESTIGATION OF THE EFFECT OF A HYBRID DRYING METHOD ON THE COLOR QUALITY OF NECTARINE SLICES AND ENERGY CONSUMPTION

FATMAGÜL MUTLU DEMIREL^a, OSMAN ISMAIL^{b,*}

ABSTRACT. The main objective of a product quality study for drying agricultural products without causing distortion is to reduce the product moisture value to a final moisture value while expending the least energy and time. In the first stage of this study, nectarine slices were dried in a microwave and cabinet dryer under different drying conditions. Experiments in the microwave dryer were done at four different power levels: 90, 180, 360, and 600 W. Hot air drying was done at two temperatures, 50 and 70 °C, with a constant air velocity (2.0 m/s). In the second stage, after those experiments, the hybrid drying method were constructed based on the color parameter, and moisture ratio. In the hybrid drying method, hot air drying was carried out with microwave pretreatment. The most effective hybrid drying method in terms of optimal drying time, energy consumption, and color parameters was found to be at 180 W microwave power and 70 °C.

Keywords: *Nectarine, hybrid drying, color, energy consumption*

INTRODUCTION

Nectarine (*Prunus persica var. nectar maxim*) is a summer-borne fruit of the Rosaceae family. The nectarine is not a different species from the peach but rather a sub-variety of the peach with recessive genes, and because it lacks fuzz or short hairs it is sometimes referred to as a "shaved peach" or "fuzz-less peach" [1]. The Food and Agriculture Organization of the United

^a T.R. Ministry of Culture and Tourism, Directorate of Central and Laboratory for Restoration and Conservation, İstanbul, Turkey

^b Yildiz Technical University, Davutpasa Campus, Faculty of Chemical and Metallurgical Engineering, Department of Chemical Engineering, 34210 Esenler, İstanbul, Turkey

* Corresponding Author: ismail@yildiz.edu.tr

Nations (*FAOSTAT*) statistical data showed that the yield of peaches and nectarines world-wide is about 21 million tons. Turkey produced 575,730 tons in 2012 [2].

The ripened nectarine is perishable and deteriorates rapidly after harvesting, hence the need to apply an appropriate postharvest technology to prolong the shelf life of the fruit; drying is among the most frequently used methods for that purpose [3-5]. Drying is a mass transfer process consisting of the removal of water or another solvent by evaporation from a solid, semi-solid or liquid. Drying is one of the most commonly used processes to improve food stability, because it decreases the water activity of the material considerably, reduces microbiological activity, and minimizes physical and chemical changes during storage [3, 6].

Fruits and vegetables have a high initial moisture content and suffer alterations of their original form during the drying process through significant shrinkage. Hot air drying has many disadvantages such as lower energy efficiency and long drying times, but despite that it has been used widely [7, 8]. Because of the low thermal conductivity of foods, heat transfer to the inner sections during conventional heating is limited. To reduce the processing time, hence to accelerate the drying process, some obstacles must be overcome. Fast and effective thermal processing has resulted in the increasing use of microwaves for food drying. This technique has been extensively employed both in the food and the chemical engineering industries [9]. The internal temperature reached by food dried by microwave drying is higher than the surface temperature, and a more dynamic moisture transfer is accomplished compared with that by convection drying [10]. Because of its quick drying ability, high energy efficiency, and fewer drying area concerns, microwave drying is an acceptable alternative method to convection drying [11]. Microwave drying of biological products, such as fruits and vegetables with high moisture content, is very advantageous [12, 13]. Several studies have been carried out to compare the advantages of microwave and convection drying of agricultural materials, for example, for okra [14], mango ginger [15], grape [16], and garlic [17].

Drying causes changes in food properties including discoloration, aroma loss, nutritive value, and changes in physical appearance and shape. A higher drying temperature reduces the drying time but may result in poor product quality, heat damage to the surface, and higher energy consumption. In contrast, drying conditions at a lower temperature may improve the product quality but decrease the drying rate thus lengthening the drying time [18]. Therefore, any small improvement in energy efficiency in the food drying process will lead to a sustainable development from the global energy perspective [19].

Hybrid drying combines the advantages of microwave and hot air. The hybrid process can be operated at low temperatures with high energy efficiency and with better retention of the original color of food and heat-sensitive nutrients. Although some investigations have focused on the drying characteristic of peaches, there is no information on the drying of nectarines a sub variety of the peach. The purpose of the present work is to investigate the effect of microwave, hot air, and hybrid (microwave pretreatment plus hot-air) drying methods on the drying time, color quality of nectarine slices, and the concomitant energy demand. Another objective of studying the hybrid drying method is to investigate its differences by comparison with other drying methods.

RESULT AND DISCUSSION

Drying Curves

The drying curves (time versus moisture content) of the nectarine slices dried at different microwave power levels are presented in Figure 1.

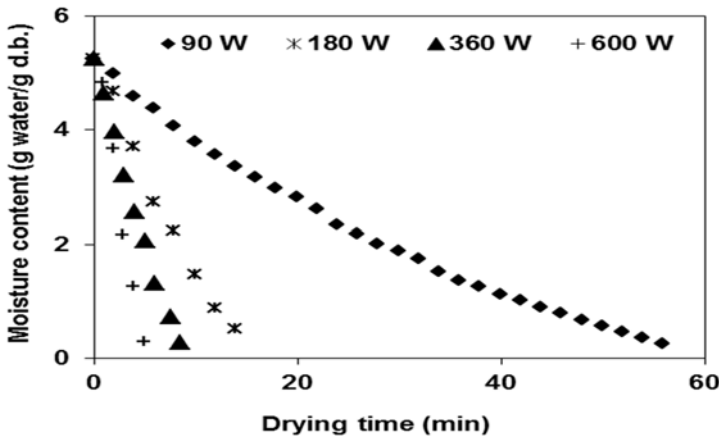


Figure1. Drying curves of nectarine slices at different microwave power levels

The moisture content of nectarine slice samples was calculated by a simplified version of Eq. (1).

$$M_{initial} = \frac{W_w - W_d}{W_d} \tag{1}$$

Drying curves were used to determine the effect of microwave power levels on the drying time: microwave power level is a very important factor in the drying procedure. Water molecules at increased microwave output power with a given frequency are subjected to a greater number of electromagnetic waves. Thus, more heat is produced in the nectarine slices, thus accelerating evaporation of water molecules. The moisture ratio decreased exponentially with time in nectarine slice samples, in agreement with the results reported under different conditions in which peach samples were dried [10, 20]. In the microwave, final moisture content was attained at about 56 min of 90 W output power, and this value was calculated as approximately 15, 8, and 5 min for 180, 360, and 600 W output power, respectively.

The characteristic drying curves showing the changes in moisture ratio of the nectarine slices with time at drying temperatures of 50 and 70 °C are given in Figure 2.

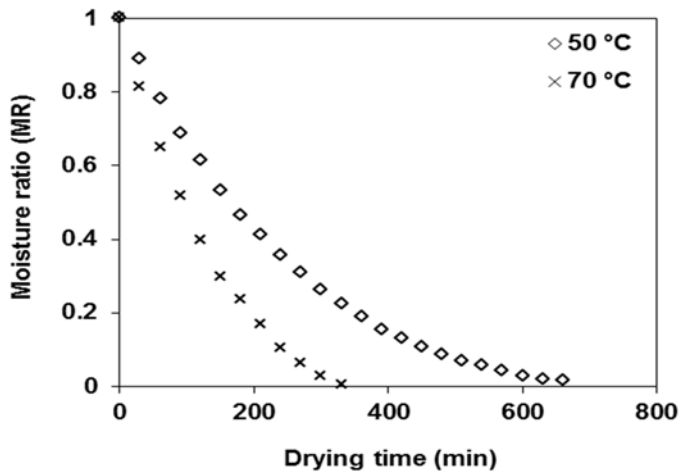


Figure 2. Experimental moisture ratio of nectarine slices versus drying time

The moisture ratio of nectarine slice samples was calculated using a simplified version of Eq. (2).

$$MR = \frac{M_t - M_e}{M_o - M_e} \quad (2)$$

It is clear that the drying air temperature had a significant effect on the drying time. As shown in Figure 2, the higher air temperature of 70 °C results in a higher drying rate compared with that at 50 °C, as expected. Therefore, at higher temperatures mass transfer is more rapid and water loss is more

excessive. Decreasing drying time with an increase in the drying air temperature has been reported for many agricultural products such as orange slices [21] and okra slices [22]. It is apparent that moisture ratio decreases continuously with drying time. From Figure 2, it is observed that the drying time required for reducing the moisture content of nectarine slices was 660 and 330 min, at the air temperatures of 50 and 70 °C, respectively. The drying air temperature of 70 °C resulted in a shorter drying time than that in 50 °C by approximately 330 min for nectarine slice samples.

The selection of hybrid drying method

Hybrid drying is applied combining hot air drying with a microwave pretreatment. The samples were initially dried by microwave for 2–30 min until the water content dropped to 65%–70% of the initial value, and then hot-air dried to the final water content. An orthogonal design was used to produce the optimal parameters. The synthetic evaluation index values are given in Table 1.

Table 1. Synthetic evaluation index (SEI) for each drying microwave power levels and hot-air temperatures

Microwave (W)	T (°C)	t (min)	Synthetic evaluation index (SEI)
90	50	335	0.74±0.03
90	70	205	0.78±0.07
180	50	282	0.78±0.08
180	70	160	0.80±0.05
360	50	276	0.48±0.10
360	70	154	0.59±0.08
600	50	272	0.41±0.13
600	70	151	0.36±0.11

The drying method that yielded the highest synthetic evaluation index value was the lowest level of combination drying, i.e. MW=180 W, T=70 °C; therefore, hybrid drying at this level produces an acceptable final product in terms of color, moisture content and moisture ratio, with relatively rapid dehydration properties and within a relatively short processing time.

Selected hybrid drying

Two different combination levels were applied in combination drying: using a microwave power level of 180 W and air temperatures of 50 and 70 °C. The moisture–time graphic obtained by fixing the temperatures at 50 and 70 °C

and combining them with microwave power level of 180 W is shown in Figure 3. The drying process is characterized by a progressive decreasing in the moisture content with time.

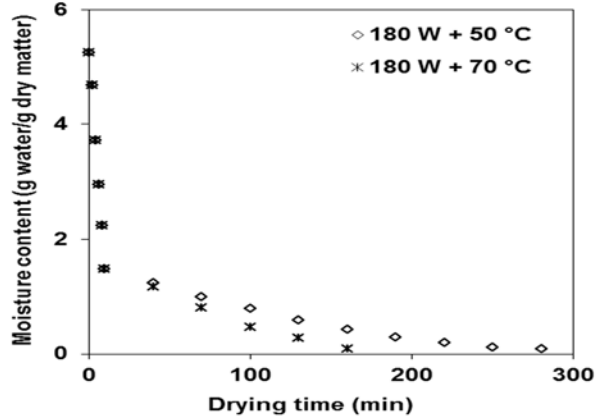


Figure 3. Variation of moisture content with drying time

In both hybrid drying methods, 70% of the total moisture content of the samples was removed by microwave drying. The remaining moisture was dried up to 0.085 ± 0.01 (g water/g dry matter) as final moisture content via hot air at 50 and 70 °C. In the microwave and hot air combined drying process, the drying time was determined to be 10 min at 180 W power and 270 and 150 minutes for temperatures at 50 and 70 °C, respectively. As seen in Figure 3, the drying period was shortened by increasing the drying temperature at a constant microwave power level. The decrease in the drying period can be attributed to increased internal vapor pressure at the high power level and high temperature. Combined drying processes at 70 °C were completed within the shortest time in each of the constant power levels, whereas those at 50 °C needed the longest time for completion. Accordingly, the shortest drying time in combination trials was obtained through the drying process consisting of the combination of 180 W microwave power and 70 °C temperature for 160 min, whereas the longest drying process resulted from the combination of 180 W and 50 °C in which the temperature was kept at a minimum for 280 min. As expected, a strong effect of microwave power level and temperature on moisture content was observed, as reported in the literature [16, 23, 24].

Color Analysis

The samples surface color was measured with a Minolta Chroma Meter CR-400 (Konica Minolta Sensing Inc., Japan) at three different edge spots on the surface of each sample before and after the drying treatment. The mean

values of the measured data are described as the color values in this study. The color values were expressed as “*L*” (whiteness/darkness), “*a*” redness/greenness), and “*b*” (yellowness/blueness).

The color difference (ΔE) was determined using the following Equation 3 [25]. L_0 , a_0 and b_0 are the parameter values before drying the fresh nectarine samples.

$$\Delta E = \sqrt{\left((L_0 - L)^2 + (a_0 - a)^2 + (b_0 - b)^2 \right)} \quad (3)$$

The fresh nectarine slices had values 62.19, 10.31, and 19.72 for “*L*”, “*a*”, and “*b*”, respectively. Table 2 show the color data in terms of Hunter “*L*”, “*a*” and “*b*” values of dried nectarine slices obtained by different drying methods under different conditions. Also, before and after the drying process, ΔE and (a/b) values of nectarine slices were calculated; these results are given in the Table 2.

Table 2. Color parameter values of dried nectarine slices

Drying methods	Drying conditions	Color Parameters			ΔE	(a/b)
		<i>L</i>	<i>a</i>	<i>b</i>		
Microwave	90 W	53.85	11.10	19.47	8.38	0.57
	180 W	52.92	12.89	20.91	9.69	0.61
	360 W	49.85	13.57	19.69	12.76	0.70
	600 W	40.68	11.90	9.97	23.66	1.19
Hot-air	50 °C	71.33	16.27	33.58	17.64	0.36
	70 °C	74.56	10.32	36.80	21.08	0.28
Hybrid	90 W + 50 °C	65.61	15.03	31.99	13.58	0.46
	90 W + 70 °C	69.85	14.22	34.35	16.97	0.41
	180 W + 50 °C	69.91	11.39	30.64	13.41	0.35
	180 W + 70 °C	73.01	11.19	34.33	18.20	0.32
	360 W + 50 °C	54.15	15.14	28.43	12.79	0.53
	360 W + 70 °C	56.03	14.67	28.23	11.34	0.52

The temperature and drying time are the main factors affecting the color change of material during drying process [26]. Table 2 shows that “*L*”, “*a*” and “*b*” values increased as the drying air temperature increased from 50 °C to 70 °C. To the contrary, the lightness values (8.34, 9.27, 12.34, and 21.51 at 90, 180, 360, and 600 W, respectively) decreased as microwave power level increased, and slice colors darkened. In some cases, blackness occurred. The amounts of sugar, acids (pH), and amino acids, as well as time of processing, have been reported to affect the color of processed products by causing

formation of brown pigments [27]. After hybrid drying of the nectarine slices, an increase in the lightness (an “*a*” increase in the “*L*” value) was observed (Table 2): “*a*” and “*b*” increased in all the dried samples when compared with fresh nectarine slices. Visually, the redness and yellowness increased. The total color difference (ΔE), as calculated by Equation (3), allows a simple way of identifying the possible changes occurring when comparing one set of coordinates with the reference set, which in the present case was the fresh state. Table 2 shows the values of color difference for the nectarine slices under various drying conditions. The lowest changes occurred at the lowest temperature and microwave power level. The color difference parameter had a value of 17.64 for the nectarine slices dried at the lower temperature (50 °C) and increased to 21.08 at the highest temperature (70 °C). The color difference value of the nectarine slices samples dried with the hybrid method at (180 W + 50 °C) and (180 W + 70 °C) was 13.41 and 18.20, respectively. The higher “*L*” and lower “*a/b*” values are preferred in dried food products [28]. From these results, drying at 70 °C was found to be the optimal temperature for nectarine slices. Also, hot air drying with microwave pretreatment had an important effect on the color of nectarine slices.

Energy Consumption

The energy consumption values obtained in the drying trials carried out using the three different drying methods are given in the Figure 4.

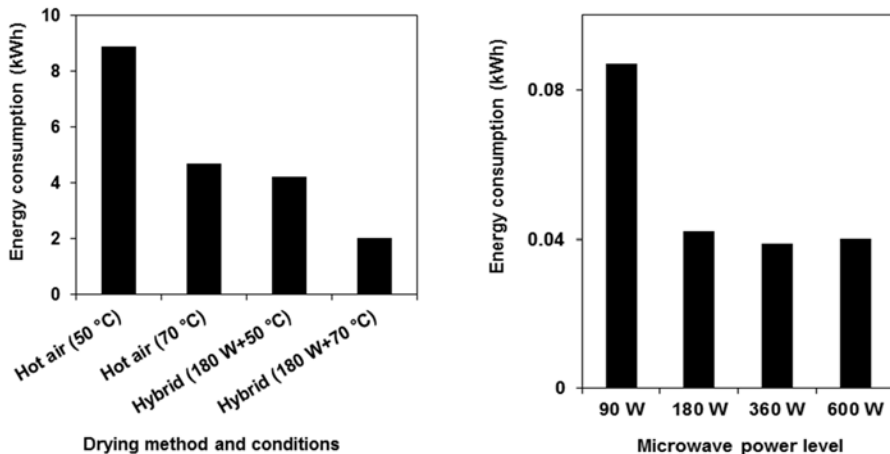


Figure 4. Energy consumption versus different drying methods of nectarine slices during the drying process

When three different drying methods were compared with the associated energy consumption values, the lowest energy consumption occurred in the microwave drying method, followed by the hybrid and the hot air drying methods. The energy consumption decreases with the increasing air temperature and power level. Among all the drying methods, the optimal energy consumption was obtained through microwave drying at 180 W power: energy consumption at this level was 0.042 kWh. Among all the drying methods the highest value of energy consumption was obtained in the hot-air drying process at 50 °C and 8.91 kWh. Energy consumption was 0.039–0.087, 2.03–4.25, and 4.72–8.91 kWh for microwave, hybrid, and hot air drying, respectively.

CONCLUSIONS

In this study, nectarine slices were dried by three different methods, and the following conclusions were reached. First, nectarine slices dried in a microwave dryer at 90, 180, 360, and 600 W microwave power levels could not obtain the desired color parameters. In microwave drying, the color quality decreases as the microwave power level increases. Second, for nectarine slices dried in a cabin dryer at 50 and 70 °C with hot air was effective for the desired color values. The color quality increases as the air temperature increases. Finally, to obtain the positive effects of these two drying methods, the color quality was used as a basis for a hybrid drying method. A combination of microwave and convective drying at microwave power of 180 W and air temperature of 70 °C resulted in a dehydrated product with optimal quality within the range of experimental conditions studied. The hybrid drying method yielded good results in terms of drying time, energy consumption, and color.

EXPERIMENTAL SECTION

Materials

Fresh nectarines (*Prunus persica* var. *nectarina* maxim) were purchased from a local market in İstanbul, Turkey and kept at 4 °C prior to experiments. The initial moisture content of the fresh nectarines was determined using the Association of Official Analytical Chemists method [29]. The average initial moisture content of the nectarines was 84% (w.b.).

Drying Procedures

Before each drying process, the nectarine samples were washed and cut into 1 ± 0.2 cm thick slices.

The microwave drying experiments were carried out in a Robert Bosch Hausgerate GmbH (Germany) model microwave oven, which has a maximum output of 800 W working at 2450 MHz. The adjustment of microwave output power and processing time was done with the digital control facility located on the microwave oven. Drying experiments were carried out using sliced nectarines with a weight of about of 30 ± 2 g arranged as thin layer on the rotatable plate fitted inside the microwave oven cabin. The rotating plate provides for equal distribution of microwave radiation energy throughout the sample. Drying was performed at a single power level. In the microwave drying method, four power levels of 90, 180, 360, and 600 Watts were used. Moisture loss was measured during 60 s intervals with a digital balance (Precisa, model XB220A, Precisa Instruments AG, Dietikon, Switzerland) with an accuracy of 0.001 g. Microwave drying continued until the moisture was reduced to about 0.18 g water/g (on a dry basis) of the initial moisture content.

Drying experiments were performed in a cabinet-type dryer (API & PASILAC Limited of Carlisle, Cambria, UK). In each experiment, 100 ± 2 g of nectarine slices was used. Drying experiments of nectarine slices were conducted at two temperatures, 50 and 70 °C, at a constant air velocity (2.0 m/s). Moisture loss in the nectarine slices was measured with a balance and recorded at 30 min intervals. Drying was considered complete when the moisture content of the samples was approximately 0.085 g water/g dry matter (dry basis) at air temperatures of 50 and 70 °C, respectively.

Drying conditions were determined after pre-experiments; 30 g of nectarine slice samples was used for drying. Eight levels of combined drying (comprising the two convective and four microwave settings described previously) were investigated (50 and 70 °C) \times (90, 180, 360, and 600 W). Drying was considered complete when the moisture content of the samples was approximately 0.085 ± 0.01 g water/g dry matter (dry basis).

Synthetic evaluation index

The synthetic evaluation index (*SEI*) was used in the hybrid drying method and adopted to reflect the contributions of moisture ratio and dried product quality. The quality parameters measured in the study were ranked in order of significance as follows: color, moisture content, moisture ratio, and assigned weights ($\lambda_1, \lambda_2, \lambda_3$) of 0.3, 0.2, 0.1, respectively. The *SEI* [25] was then calculated for each of the experimental conditions by the following Equation 4.

$$SEI = \sum_{i=1}^3 \lambda_i Y_i$$

$$Y_1 = 1 - \frac{\Delta E - \Delta E_{\min}}{\Delta E_{\max} - \Delta E_{\min}}; Y_2 = \frac{X_d - X_o}{T_{AD} + T_{MWD}}; Y_3 = \frac{MR - MR_{\min}}{MR_{\max} - MR_{\min}} \quad (4)$$

where MR is the moisture ratio, X_d and X_0 are the water contents of the dehydrated sample and the fresh sample on dry basis. T_{AD} and T_{MWD} are the drying times of air drying process and microwave drying process, respectively.

Energy Consumption

The energy consumption value required for drying nectarine slices in the microwave was calculated with Equation 5 [30].

$$E_t = P * t \quad (5)$$

where E_t is the energy consumption (kWh), P is the microwave output power (kW), t is the drying time (h).

In hot air drying, the drying process energy consumption was measured for the drying and blowing air by electric heater and fan. The energy consumption value was calculated with Equation 6 [31]:

$$E_t = \rho_a \cdot A \cdot v \cdot c_p \cdot \Delta T \cdot D_t \quad (6)$$

where ρ_a is the air density (kg/m^3), A is the tray area (m^2), v is the air velocity (m/sec), c_p is the specific heat ($\text{kJ/kg } ^\circ\text{C}$), ΔT is a temperature difference between the air inlet and outlet of the dryer ($^\circ\text{C}$), and D_t is the total drying time of each sample (h).

REFERENCES

1. M. Rieger, Peach: <http://www.uga.edu/fruit/peach.html> **2007**.
2. FAO, FaoStat: Agriculture data, <http://faostat3.fao.org/download/Q/QC/E>. Accessed November 23, **2014**.
3. M.K. Krokida, D. Marinos-Kouris, *Journal of Food Engineering*, **2003**, 57, 1.
4. M. A. Karim, M. N. A. Hawlader, *International Journal of Heat and Mass Transfer*, **2005**, 48, 4914.
5. B. Alaei, R. Amiri Chayjan, *Acta Scientiarum Polonorum*, **2015**, 14, 15.
6. A. Midilli, H. Kucuk, Z. Yapar, *Drying Technology*, **2002**, 20, 1503.
7. H. Feng, J. Tang, R.P. Cavaliere, *Transactions of the ASAE*, **2002**, 45, 129.
8. Z. Pan, R. Khir, L.D. Godfrey, R. Lewis, J.R. Thompson, A. Salim, *Journal of Food Engineering*, **2008**, 84, 469.
9. J. Bondaruk, M. Markowski, W. Blaszczyk, *Journal of Food Engineering*, **2007**, 81, 306.
10. J. Wang, K. Sheng, *LWT-Food Science and Technology*, **2006**, 39, 247.
11. A. Harish, M. Rashmi, T.P. Krishna Murthy, B.M. Blessy, S. Ananda, *International Food Research Journal*, **2014**, 21, 1081.
12. A.K. Datta, S.S.R. Geedipalli, M.F. Almeida, *Food Technology*, **2005**, 59, 36.

13. D. Arslan, M.M. Özcan, *LWT- Food Science and Technology*, **2010**, 43, 1121.
14. L.V. Mana, T. Orikasab, Y. Muramatsuc, A. Tagawaa, *Journal of Food Processing & Technology* **2012**, 3, 1.
15. T.P. Krishna Murthy, B. Manohar, *International Journal of Food Science & Technology*, **2012**, 47, 1229.
16. I. Alibas, *International Journal of Food Science & Technology*, **2014**, 10, 69.
17. A. Calín-Sánchez, A. Figiel, A. Wojdylo, M. Szaryez, A.A. Carbonell-Barrachina, *Food and Bioprocess Technology*, **2014**, 7, 398.
18. C. Kumar, M.A. Karim, U.H.J. Mohammad, *Journal of Food Engineering*, **2014**, 121, 48.
19. T. Kudra, *Drying Technology*, **2004**, 22, 917.
20. A. Zhu, X. Shen, *International Journal of Heat and Mass Transfer*, **2014**, 72, 345.
21. S. Rafiee, M. Sharifi, A. Keyhani, M. Omid, A. Jafari, S.S. Mohtasebi, H. Mobli, *International Journal of Food Properties*, **2010**, 13, 32.
22. P.K. Wankhade, R.S. Sapkal, V.S. Sapkal, *Procedia Engineering*, **2013**, 51, 371.
23. O. Eştürk, Y. Soysal, *Journal of Agricultural Science*, **2010**, 16, 26.
24. S. Minaei, A. Motevali, G. Najafi, S.R. Mousavi Seyedi, *Australian Journal of Crop Science*, **2011**, 6, 584.
25. A. Jiao, X. Xu, Z. Jin, *Food and Bioproducts Processing*, 2014, 92, 259.
26. P. Somkiat, P. Paveena, S. Somchart, *Drying Technology*, **2004**, 22, 2095.
27. W.A. Gould, The AVI Publishing Company, Inc., Westport, CT, USA, **1983**, chapter 8.
28. O. İsmail, A.K. Figen, S. Pişkin, *Heat Mass Transfer*, **2015**, 51, 807.
29. AOAC, Official Methods of Analysis of AOAC International, 16th edn., AOAC International, Virginia, **1995**.
30. A. Motevali, S. Minaei, M.H. Khoshtagaza, *Energy Conversion and Management*, **2011**, 52, 1192.
31. M. Aghbashlo, M.H. Kianmehr, H. Samimi-Akhijahani, *Energy Conversion and Management*, **2008**, 49, 2865.

INVESTIGATION OF TITANIUM-DIOXIDE COATINGS ON MEMBRANE FILTRATION PROPERTIES

ILDIKÓ KOVÁCS^a, SÁNDOR BESZÉDES^a, SZABOLCS KERTÉSZ^a,
GÁBOR VERÉB^a, CECILIA HODÚR^a, IBOLYA ZITA PAPP^b,
ÁKOS KUKOVECZ^{b,c}, ZSUZSANNA LÁSZLÓ^{a*}

ABSTRACT. In this study, synthesized TiO₂ nanorods and commercial Aeroxide P25 TiO₂ nanoparticles were deposited on polyethersulfone (PES) membrane surfaces to compare their photocatalytic activity and effects on membrane surface and filtration properties. The catalysts were deposited on the membrane surface by physical deposition. The effect of the TiO₂ amount on the stability of the catalyst layer and its effect on membrane resistance in presence and absence of UV irradiation were investigated. 1.2 mg/cm² catalyst coverage proved to be a minimal appropriate coverage to prevent membrane damage during UV irradiation. The catalysts formed hydrophilic layers on the surface, and in case of both catalyst the surface free energy increased compared to the neat membrane. The photocatalytic activity and retention of the modified membranes were tested spectrophotometrically by using Acid Red1, azo dye.

Keywords: membrane filtration, TiO₂ coated membranes, photocatalysis, azo dye, Acid Red 1

INTRODUCTION

Polyethersulfone (PES) is a widely-used material in asymmetric membrane manufacturing, because of its good performances [1]; it has high mechanical strength, thermal stability, environmental endurance, and

^a Department of Process Engineering, Faculty of Engineering, University of Szeged, H-6725 Szeged, Moszkvai krt. 9., Hungary

^b Department of Applied and Environmental Chemistry, University of Szeged, H-6720 Szeged, Rerrich Béla tér 1., Hungary

^c MTA-SZTE "Lendület" Porous Nanocomposites Research Group, H-6720 Szeged, Rerrich Béla tér 1., Hungary

* Corresponding author: zsizsu@mk.u-szeged.hu

processing [2, 3]. However, it has low permeability and high fouling tendency due to its inadequate hydrophilic property [1–3]. This limits its application as a membrane material. To overcome these flaws, it is possible to modify PES membranes to improve their hydrophilicity [2], since back-flushing and chemical cleaning are not providing a permanent solution against membrane fouling and require serious optimization [4].

Some authors specifically investigated approaches to modify PES membrane with TiO_2 to increase its hydrophilicity and to decrease its tendency to fouling. TiO_2 is favoured over other semiconductors due to its good physical and chemical properties, availability, photocatalytic activity, desirable hydrophilic and potential antifouling properties [5–7].

PES composite membrane modified by self-assembly of TiO_2 nanoparticles showed good separation qualities and higher water flux compared to the unmodified membrane, improved thermal stability, and increased hydrophilicity [2, 8]. Three different modified PES membranes were compared by Rahimpour and co-workers [1]: TiO_2 -entrapped membranes, UV-irradiated TiO_2 -entrapped membranes, and UV-irradiated TiO_2 -deposited membranes. It was found that by adding TiO_2 to the casting solution changes the morphology of the membrane, by making a more hydrophilic and porous structure that has photocatalytic activity. However, the TiO_2 -deposited membranes had superior characteristics in terms of fouling mitigation.

The membrane fouling properties are determined by the interactions between foulants and the membrane surface. These interactions are weak secondary forces such as van der Waals, hydrogen and electrostatic forces. The strength of these forces depends on the characteristics of the membrane such as wettability or surface free energy. Generally, it can be stated that higher hydrophilicity and lower surface free energy leads to lower fouling property [6, 9, 10].

In this work PES microfiltration membranes were coated with commercial Aeroxide P25 TiO_2 and synthesised TiO_2 nanorods. The aim of the work was to examine and compare the two layers made of catalysts of different geometry and different hydrophilicity. Contact angle measurements were carried out to determine the effect of the catalyst layer on the membrane surfaces wettability and surface free energy. Acid Red 1 (AR1, Azophloxine) dye was used as a model pollutant to determine the photocatalytic activity of the TiO_2 P25 and TiO_2 NR layers. AR1 is a reactive azo dye belonging to the largest class of dyes commonly employed in textile industry [11].

RESULTS AND DISCUSSION

Characterization of the used photocatalyst

For the membrane coating a commercial and a self-prepared titanium dioxide photocatalyst was applied. The synthesised TiO_2 “nanorods” (TiO_2 NR, Figure 1) can be characterized with $\sim 50\text{--}70$ nm length, $\sim 20\text{--}30$ nm width and a $\sim 54\text{ m}^2\text{g}^{-1}$ specific surface area (determined by nitrogen adsorption at 77 K, using BET method). Based on the XRD diffractogram of TiO_2 NR (Figure 2) it consists of 100% anatase phase. Commercial Aeroxide P25 titanium dioxide (produced by Evonik Industries) was also used for our experiments, which have spherical shape with a primer particle size of ~ 25 nm [12]; however, it should be noted that in a suspension it forms aggregates nearly $1\mu\text{m}$ in diameter [13]. This titania is a mixture of anatase (90%) and rutile (10 %) phase, and it has similar specific surface area ($49\text{ m}^2\text{g}^{-1}$) like our self-prepared TiO_2 NR.

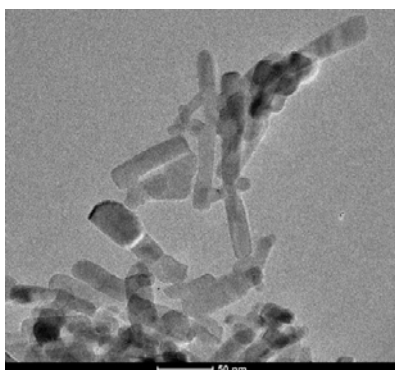


Figure 1. TEM image of titania nanorods (TiO_2 NR)

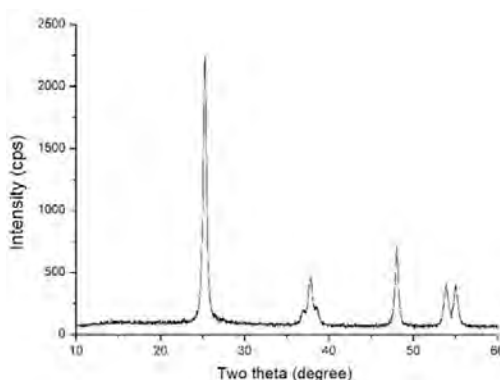


Figure 2. XRD of titania nanorods (TiO_2 NR)

Neat and TiO₂ Coated Membrane Surface Property

To investigate the effect of the catalyst layer on the membrane surface, TiO₂ suspension was filtered through the membrane in a dead-end stirring cell to provide a specific cake layer. The SEM images of top surface of 0.6 g cm⁻² TiO₂ P25 coated and the 0.6 g cm⁻² TiO₂ NR coated membranes are shown in Figure 3. In case of both catalysts the aggregates are larger than the membrane pores, thus depositing on the surface, this amount of the catalysts does not provide a full coverage of the membrane and are not distributed uniformly. TiO₂ P25 forms a thick layer of uniform aggregates on the membrane surface. TiO₂ NR deposits on the surface forming different sized aggregates. To achieve better coverage of the membrane to protect from UV damage the amount of the catalyst was doubled, and its effect was investigated in further experiments.

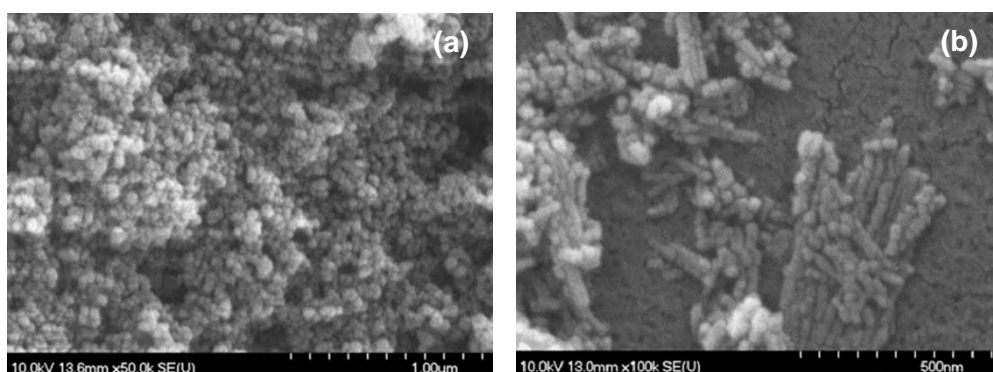


Figure 3. SEM images of top layers of (a) 0.6 g cm⁻² TiO₂ P25 coated, and (b) 0.6 g cm⁻² TiO₂ NR coated membranes

To characterize the wettability of the modified membrane surfaces, contact angles (with distilled water and glycerol) were measured and the surface free energy values were calculated. Figure 4 shows the contact angles of water and glycerol and the surface free energies. The contact angles of the TiO₂ P25 coated membrane show that the catalyst forms a hydrophilic layer on the surface. The hydrophilicity of TiO₂ NR coated membranes also increased compared to the neat membranes. Reportedly, the reactivity of TiO₂ surface and its affinity toward water is dependent on TiO₂ crystal phase [14].

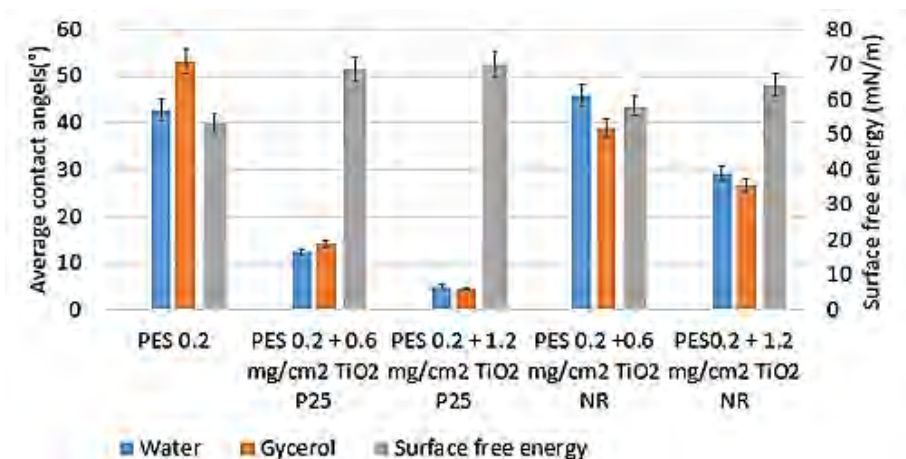


Figure 4. Contact angles of water and glycerol and surface free energies of neat and TiO₂ coated membranes

Investigation of the membrane stability under UV irradiation

To investigate the effect of UV irradiation on the membrane stability, the membrane flux changes were measured and the membrane resistances were calculated before and after UV irradiation of the neat and coated membranes. It was found that the neat PES 0.2 membrane resistance (calculated by Equation (2)) decreased 30% after 1 hour UV ($\lambda = 254$ nm) irradiation (Figure 5) due to its sensitivity to UV. According to the literature, similar decrease in membrane resistance was achieved after 24 hours of UV-A light irradiation of an ultrafiltration PES membrane [15, 16]. This was attributed to the fact that PES contains sulphur that is highly susceptible to UV light. In the next series of experiments the effect of the amount of the catalyst on membrane stability under UV irradiation was examined. By coating the membrane with higher amounts of catalyst layer the decrease of membrane resistances were less extensive after 1 hour UV irradiation, since the catalyst layer absorbs the UV light. The 1.2 mg/cm² catalyst layers in case of both types of TiO₂ provided a sufficient coverage to be used for investigating the photocatalytic activity of the catalyst layer without extensive damage of the membrane during the irradiation.

To investigate the stability of the catalyst layer on the membrane surface, all coated membranes were left overnight in the stirring cell. 100mL distilled water with 300rpm for 24 hours was stirred over them to check if the layer would wash off during operation. It was found that the turbidity of the distilled water did not change; the catalyst did not resuspend thus the TiO₂ coating did not wash off.

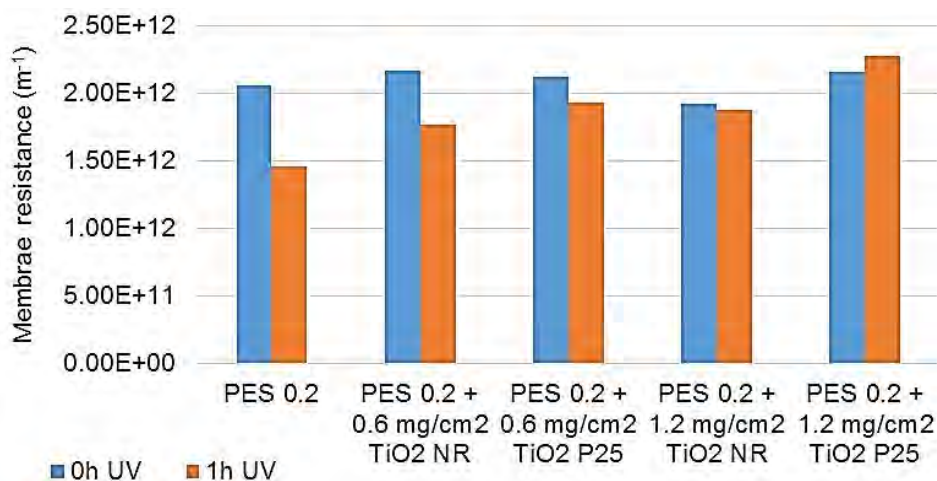


Figure 5. Changes of resistances of neat and TiO₂ coated PES 0.2 membranes before and after UV irradiation

Photocatalytic activity of the catalyst coated membranes

The photocatalytic efficiencies of the catalyst layers were characterized by the decolourization of Acid Red 1 dye solution. In the first series of experiments the effect of UV irradiation on the decolourization of Acid Red1 was examined. During these experiments 100mL of 15mg/L Acid Red 1 solution was UV irradiated for an hour, and it was found that the irradiation alone did not result in colour intensity change of the solution. The photocatalytic activity of the coatings was examined in two different experimental arrangements. First, a 1 hour UV irradiation was used as a pre-treatment in the presence of the coated membrane, which was followed by the filtration. Secondly, the photocatalysis was performed during the filtration.

First, the retention of the neat membrane was measured and calculated by filtering the dye solution through it, using Equation (3). The TiO₂ coated membranes had different retention values compared to the neat membrane (Figure 6). The TiO₂ P25 coating resulted in a 26% increase of the retention, which can be explained with the dense structure of the TiO₂ layer [17], the layer behaves as an additional filtration layer which can adsorb the positively charged dye ions, due to its hydrophilic character. The TiO₂ NR coating resulted in a 62% retention decline compared to the neat membrane. The TiO₂ NR coating prevents the dye molecules from adsorbing on the membrane surface, due to its lower surface free energy compared to TiO₂ P25, which means that this surface is less prone to fouling.

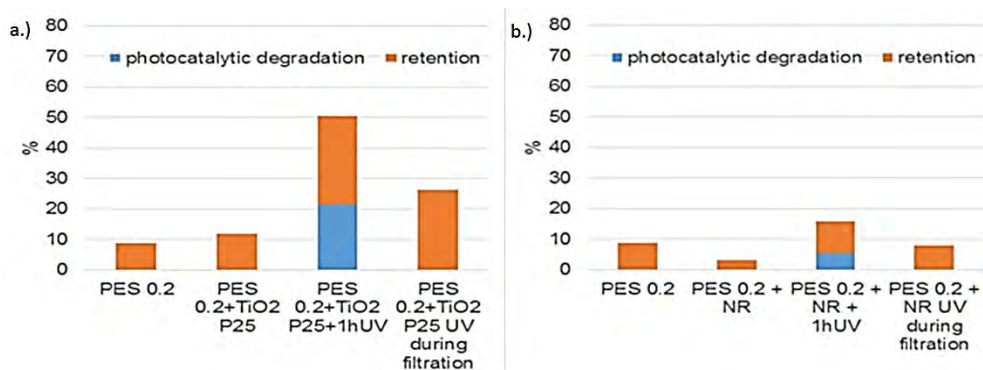


Figure 6. Neat and TiO₂ P25 (a.) and TiO₂ NR (b.) coated membrane dye retention

It was found that as a pre-treatment, irradiating the solution in the presence of the TiO₂ P25 coated membrane for an hour resulted in a 22% decolourization of the dye; this was only 8% in case of the TiO₂ NR coating. These results prove that the catalyst layers have photocatalytic activity, which means that the reactive species generated by heterogeneous photocatalysis react with the dye molecules. These results show that the efficiency of the photocatalytic degradation depends on the adsorption ability of the organic molecules on the catalyst surface: since the dye is less prone to adsorb on the surface of the TiO₂ NR coated membrane the efficiency of photocatalytic reaction is lower.

Filtering of the pre-treated solution through the TiO₂ P25 coated membrane resulted in a nearly 50% dye retention. In case of the TiO₂ NP coated membrane the membrane retention was significantly higher than the neat membrane retention, but significantly lower compared to the TiO₂ P25 coated membrane. In the case of continuous irradiation during filtration through the TiO₂ P25 and TiO₂ NP coated membranes the retention was lower compared to the pre-treatment that was followed by the filtration due to shorter exposure to the UV irradiation. In case of the pre-treatment the irradiation time was 1 hour while the simultaneous irradiation and filtration lasted for only 6 minutes.

CONCLUSIONS

Polyethersulfone microfiltration membranes were coated with commercial TiO₂ P25 and synthesized TiO₂ NR. The minimal appropriate catalyst coverage of the membrane surface was determined to be 1.2 mg/cm², to create a stable coating which adsorbs the UV making the membrane withstand the irradiation.

The coated membrane surfaces become more hydrophilic compared to the neat membrane, and the catalyst layer resulted in a higher surface free energy. The results showed that the surface hydrophilicity and the surface free energy determined the adsorption ability of the dye particles; the more hydrophilic TiO₂ P25 coating adsorbed higher amount of dye. Based on the results the surface free energy is in relation with the photocatalytic activity of the catalyst coating; the TiO₂ NR coated membranes have lower surface free energy, which means that it is less prone to adsorb dye particles, and this type of modified membrane showed lower photocatalytic activity, even though the specific surface area was similar in both cases.

EXPERIMENTAL SECTION

TiO₂ (anatase) (BA01-01), TiO₂ P25 (AEROXIDE) and Acid red1 were supplied by UNIVAR, EVONIC Industries and Synthesia respectively. The concentration of AR1 solution used in membrane filtration measurements was 15 mg/L.

The preparation of TiO₂ nanorods were as follows: in 1 L of a 10 M NaOH solution 250 g TiO₂ (anatase) was suspended, then for 24 hours the suspension was stirred in a rotating autoclave at 3 rpm and 155°C. Then the resulting product was washed and protonated with 0.1 M HCl, after maintaining a pH value between 3 and 4 for 30 minutes the product was washed with 0.01 M HCl for 3 days than with distilled water to remove the remaining chloride ions. The resulting TiO₂ nanotubes were dried at 80°C for a day. The TiO₂ nanotubes (NT) were then heat treated at 600°C for 6 hours. As a resulting product TiO₂ nanorods (TiO₂ NR) arose.

Polyethersulfone membranes (PES-MF (NEW LOGIC Research INC, USA) with a 0.2 µm were coated with commercial TiO₂ P25 and synthesized TiO₂ NR. The membranes were coated by filtering through the membrane 50 mL and 100 mL 0.4 g/L catalyst suspension in a dead end cell, at 0.1 MPa without stirring, that resulted in 0.6 and 1.2 mg/cm² TiO₂ coating respectively. The filtration was carried out with a Millipore batch filtration unit (XFUF04701, Solvent-resistant Stirred Ultrafiltration Cell, Millipore, USA). For the photocatalytic tests were carried out by the presence of the catalyst coating and UV irradiation, the stirring cell cap was modified and a UV light source was fitted in it (Fig. 7). This way a photocatalytic membrane reactor was set up. The UV light source was a low pressure mercury-vapour-lamp (GERMIPAK LightTech, Hungary, 40W, λ=254nm). The filtrations of the dye solution were carried out at 0.1 MPa transmembrane pressure, without stirring at 20°C. In case of every filtration 100 mL water or dye solution was filtered to volume reduction ratio 5 (VVR=5). VRR [-], was defined as:

$$VRR = \frac{V_F}{V_F - V_P} \quad (1)$$

where V_F and V_P is the volume of the feed and permeate [m^3] respectively at any time.

The membrane resistance (R_M) was calculated as [18]:

$$R_M = \frac{\Delta p}{J_w \eta_w} [m^{-1}] \quad (2)$$

where Δp is the transmembrane pressure (Pa), J_w is the water flux of the clean membrane and η_w is the viscosity of the water (Pas).

The retention values were calculated by the following equation:

$$R = \left(1 - \frac{c}{c_0}\right) 100\% \quad (3)$$

where c is the concentration of the permeate phase, and c_0 is the concentration of the feed, both calculated from the absorbance of the solutions.

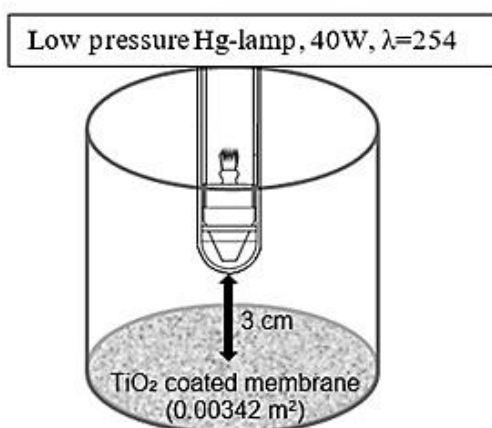


Figure 7. Schematic of the photocatalytic membrane reactor

UV irradiation of certain samples was done in the dead end cell before the filtration as a pre-treatment for 60 minutes and during the filtrations for as long as the filtration lasted.

Transmission electron microscopy (TEM; Philips CM10) images were recorded to determine the morphology and size of the TiO₂ NT and TiO₂ NR. The nitrogen adsorption isotherms were recorded at 77 K using a QuantaChrome Nova 2000 surface area analyzer. Before the nitrogen adsorption, the samples were outgassed at 423 K for 1 h to remove any adsorbed contaminants. The specific surface areas were calculated from multipoint BET method.

During XRD measurements, titania nanorods were registered in the $2\Theta = 10\text{--}60^\circ$ range on a Rigaku Miniflex II instrument, using Cu $K\alpha$ ($\lambda = 1.5418 \text{ \AA}$) radiation.

The concentration of the dye was measured by spectrophotometer (Nanocolor® UV/Vis, Macherey-Nagel GmbH, Germany) at $\lambda=532 \text{ nm}$.

Membrane hydrophobicity was quantified by measuring the contact angle that was formed between the (neat and coated) membrane surface and distilled water. 10 μL water was carefully dropped on the top of the membrane surface and immediately measured, within 30 seconds. Contact angles were measured using the sessile drop method (Dataphysics Contact Angle System OCA15Pro, Germany). The measurements were repeated five times and the average value was calculated and is presented in this work. The surface free energies of membranes were calculated by the Owens, Wrrndet, Rabel, and Kaelble (OWRK) method, using the OCA15 software package (Dataphysics).

ACKNOWLEDGMENTS

The János Bolyai Research Scholarship of the Hungarian Academy of Sciences supported this project. The authors are also grateful for the financial support provided by the project Hungarian Science and Research Foundation (NKFI contract number K112096).

REFERENCES

1. A. Rahimpour, S. S. Madaeni, A.H. Taheri, Y. Moghaddam, *Journal of Membrane Science*, **2008**, 313, 158.
2. M.L. Luo, J.Q. Zhao, W. Tang, C.S. Pu, *Applied Surface Science*, **2005**, 249, 76.
3. Y. Mansourpanah, S.S. Madaeni, A. Rahimpour, A. Farhadian, A.H. Taheri, *Journal of Membrane Science*, **2009**, 330, 297.
4. A.H. Moghaddam, J. Shayegan, J. Sargolzaei, *Journal of the Taiwan Institute of Chemical Engineers*, **2016**, 62, 150.
5. V. Vatanpour, S.S. Maadaeni, R.A. Khataee, E. Salehi, S. Zinadini, A.H. Monfared, *Desalination*, **2012**, 292, 19.
6. A. Razmjou, J. Mansouri, V. Chen, *Journal of Membrane Science*, **2011**, 378 (1-2), 73.
7. S. Leong, A. Razmjou, K. Wang, K. Hapgood, X. Zhang, H. Wang, *Journal of Membrane Science*, **2014**, 472, 167.
8. J.F. Li, Z.L. Xu, H. Yang, L.Y. Yu, M. Liu, *Applied Surface Science*, **2009**, 255, 4725.

9. K.H. Choo, C. H. Lee, *Journal of Colloidal and Interface Science*, **2000**, 226, 367.
10. G. Belfort, R.H. Davis, A. Zydney, *Journal of Membrane Science*, **1994**, 96, 1.
11. Cs. Földváry, L. Wojnárovits, *Radiation Physics and Chemistry*, **2007**, 76, 1485.
12. G. Veréb, Z. Ambrus, Zs. Pap, Á. Kmetykó, A. Dombi, V. Danciu, A. Cheesman, K. Mogyorósi, *Applied Catalysis A: General*, **2012**, 417–418, 26.
13. K. Mogyorósi, N. Balázs, D.F. Srankó, E. Tombácz, I. Dékány, A. Oszkó, P. Sipos, A. Dombi, *Applied Catalysis B: Environmental*, **2010**, 96, 577.
14. Z.X. Low, Z. Wang, S. Leong, A. Razmjou, L.F. Dumée, X. Zhang, H. Wang, *Industrial & Engineering Chemistry Research*, **2015**, 54, 11188.
15. S.S. Chin, K. Chiang, A.G. Fane, *Journal of Membrane Science*, **2016**, 275, 202.
16. N.S. Allen, M. Edge, “Fundamentals of Polymer Degradation and Stabilization”, Elsevier Applied Science, London, **1992**, chapter 1.
17. H. Bai, Z. Liu, D.D. Sun, *Chemical Communications*, **2010**, 46, 6542.
18. S. Kertész, Z. László, E. Forgács, G. Szabó, C. Hodúr, *Desalination and Water Treatment*, **2012**, 35, 195.

INFLUENCE OF THE Ni/Mg RATIO ON THE COLOUR OF SPINEL PIGMENTS PREPARED BY A MODIFIED SOL – GEL METHOD

FIRUTA GOGA^a, ROXANA DUDRIC^b, LILIANA BIZO^a,
ALEXANDRA AVRAM^a, ALEXANDRU HORATIU MARINCAS^a,
CSABA VARHELY JR.^a, THOMAS DIPPONG^{c,*}

ABSTRACT. This paper focuses on the synthesis and analysis of some spinel-structured, ceramic pigment nanopowders ($Mg_{(1-x)}Ni_xAl_2O_4$) using a modified sol – gel method. This study emphasizes the influence of the Ni/Mg ratio and that of the thermal treatment on the properties of the obtained powders. The behavior of the dried gels during calcination was studied by differential thermal analysis. The formation of the spinel structure after calcination was analyzed using x-ray diffraction. The colour of the powders was characterized by UV – VIS spectroscopy, determining the absorption spectra. In addition, the trichromatic coordinates were determined, and the corresponding pigment positions were fixed on the chromaticity diagram.

Keywords: *ceramic pigment nanopowders, nickel spinels, sol – gel method, sucrose, pectine.*

INTRODUCTION

Thermoresistant pigments, also known as ceramic pigments, have been specially designed for coloring enamels and glazes under severe conditions of elevated temperature and chemical attack. [1]. Spinel materials are a class

^a Babeş-Bolyai University, Faculty of Chemistry and Chemical Engineering, 11 Arany Janos Street., RO-400028, Cluj-Napoca, Romania

^b Babeş-Bolyai University, Faculty of Physics, 1 M. Kogalniceanu Street, RO-400084, Cluj-Napoca, Romania

^c Technical University of Cluj-Napoca, Faculty of Science, Department of Chemistry and Biology, 76 Victoriei Street, 430122, Baia Mare, Romania

* Corresponding author: dippong.thomas@yahoo.ro

of minerals with the formula AB_2O_4 , having a highly thermal and chemical resistant structure that corresponds to the high requirements needed by ceramic pigments. Spinel structures are efficient hosts for a wide range of colored cations.

Spinel crystals in a cubic system [2]. The unit cell of a spinel structure is comprised of 8 molecules of AB_2O_4 , in which the anions form a compact cubic lattice, with 64 tetrahedral and 32 octahedral sites, partially occupied by A^{2+} and B^{3+} cations. There are two ideal versions to this structure – the normal and the inverse spinel. The unit cell of the normal type spinel, has 8 tetrahedral sites occupied by A^{2+} cations, and 16 octahedral sites occupied by B^{3+} cations. In the case of the inverse spinel, the 8 tetrahedral sites are occupied by B^{3+} cations, and the A^{2+} and the rest of the B^{3+} cations, occupy the 16 octahedral sites [1]. The formation of a normal or inverse lattice is due to certain factors that influence the cation distribution among the tetrahedral and octahedral sites, factors like the ionic radius and the electronic configuration. The ions with a larger positive charge have an affinity for octahedral sites where they are surrounded by 6 O^{2-} , and the ions with a smaller positive charge prefer tetrahedral sites, where they are surrounded by 4 O^{2-} . The A cations are bivalent: Mg^{2+} , Zn^{2+} , Fe^{2+} , Co^{2+} , Ni^{2+} , Mn^{2+} and the B cations are trivalent: Co^{3+} , Al^{3+} , Cr^{3+} , Fe^{3+} [3].

The blue colour of ceramic products is based especially on the colour of the tetracoordinated Co^{2+} cation, present in a wide range of minerals, such as Co_2SiO_4 (olivine), $(Co,Zn)_2SiO_4$ (willemite) and $CoAl_2O_4$ (cobalt spinel).

The blue tones obtained with cobalt are very intense. Recently, cyan spinel with a Ni^{2+} chromophore have been obtained. For milder tones, mixed spinel systems, $(CoZn)Al_2O_4$, $(NiZn)Al_2O_4$, $(MgNi)Al_2O_4$, based on the formation of spinel solid-state solutions, were studied. [4]

In terms of crystalline structure, magnesium aluminate is the original (normal) spinel, $MgAl_2O_4$ in which Mg^{2+} ions fill the tetrahedral sites and Al^{3+} ions occupy the octahedral positions in the cubic closed packing of O^{2-} anions. On the other hand, the cation arrangement in nickel aluminate is typical for a partially inverse spinel, $(Ni_{1-z}Al_z)[Ni_zAl_{2-z}]O_4$, in which Ni^{2+} and Al^{3+} ions are randomly located in both tetrahedral and octahedral positions, respectively. At ambient temperature and pressure, the inversion parameter z of $NiAl_2O_4$ is around 0.8 (z stands for the site occupancy factor of Al^{3+} on tetrahedral sites) and it decreases as the temperature increases [5].

Despite the well-known structure and applications of $MgAl_2O_4$ and $NiAl_2O_4$, little attention has been paid to the investigation of $MgAl_2O_4$ – $NiAl_2O_4$ solid solutions in terms of synthesis and characterization. Several authors have investigated the distribution of Ni^{2+} ions among octahedral and tetrahedral sites

in NiAl_2O_4 – MgAl_2O_4 spinel solid solutions. Most of the NiAl_2O_4 – MgAl_2O_4 solid solutions were prepared by solid state method which requires elevated temperature and long soaking time. For instance, the formation of $\text{Mg}_{(1-x)}\text{Ni}_x\text{Al}_2\text{O}_4$ solid solutions starting from the corresponding metal oxides demands a heat treatment of at least 2 h at 1200 °C [5].

Ceramic pigments have been synthesized by several solution techniques, such as, sol–gel, co-precipitation, hydrothermal, alkoxide hydrolysis, the Pechini method and the low combustion method [3-5]. The properties of the final powder depend on the preparation method and the calcination temperature and time. A modification of the physical properties of the solid solution can be associated with dopant cations and with change defects in the compound's structure. [6,7]

The sol-gel method is a very efficient one, with great results in the synthesis of nanomaterials, not needing high synthesis temperatures and leading to homogenous powders with uniform particle sizes. These results are due to a very good homogenization of the precursor solution with the chelation agents, leading to the formation of particle aggregates, sols that subsequently transform into a porous, tridimensional network [8-10].

In the present paper, for the synthesis of the single phase, crystalline, cyan, $\text{Mg}_{(1-x)}\text{Ni}_x\text{Al}_2\text{O}_4$ ($0 \leq x \leq 1$) spinel refractory ceramic pigment, a modified sol – gel method was applied, using metal nitrates as well as sucrose and pectin as nontoxic organic precursors.

RESULTS AND DISCUSSIONS

Differential thermal analysis

The $\text{Mg}_{(1-x)}\text{Ni}_x\text{Al}_2\text{O}_4$ ($x=0.4$) gel thermogram is presented in fig. 1. Up until 200°C, an endothermic process with mass loss of 17% takes place. This loss represents the elimination of residual water from the gel pores. The complete oxidation of the organic components takes place between 200-600°C, manifesting in two exothermic processes, with a mass loss of 60.55% and 11.67%, respectively. Between 600-1000°C, there are no decomposition processes, the mass variation being reduces by approximately 2%, from 10.88% la 8.85%. The DTA curve shows the presence of an exothermic process, between 750-1000°C, that can be attributed to the formation of the solid-state spinel solutions.

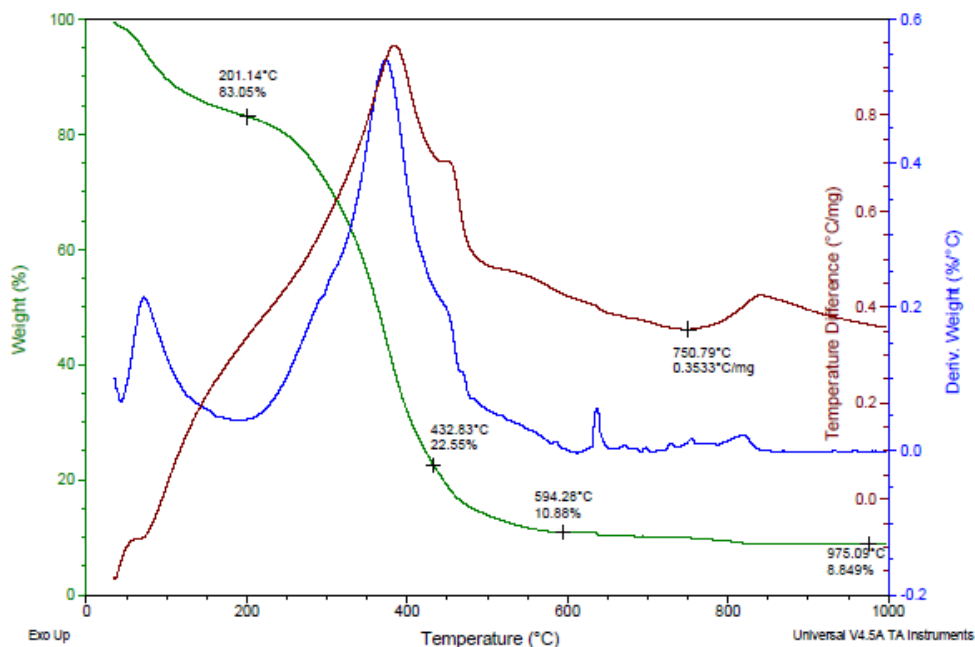


Figure 1. The TG – DTA – DTG diagram for the $\text{Mg}(1-x)\text{Ni}_x\text{Al}_2\text{O}_4$ gel ($x=0,4$)

X – ray diffraction analysis

The diffraction spectra for $\text{Mg}_{(1-x)}\text{Ni}_x\text{Al}_2\text{O}_4$, ($0 \leq x \leq 1$) powders obtained by calcination at 1000°C are presented in fig. 2. The spectra indicates the formation of the spinel structure for all the powders containing variable amounts of the two oxides, namely MgO and NiO. For samples with $x=0.4$ and $x=0.8$, a slight separation of NiO, of about 2-3%, is observed.

The reticular parameters of the crystalline spinel structures, for $0 \leq x \leq 1$, and the crystallite dimensions are presented in table 1. The crystallite dimensions were determined using the Debye-Scherrer formula, with a diffraction maximum at approximately 45° . The obtained values are between 21-29 nm and are not influenced by the Ni/Mg ratio. The nanometric scale of the powders represents an important factor in the case of pigments, the coloration capacity being dependent on the specific surface of the particles.

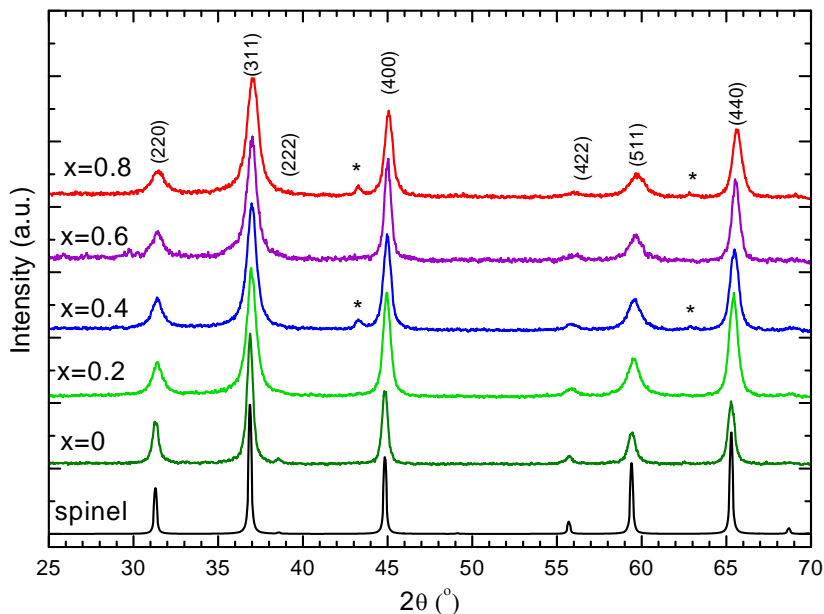


Figure 2. The diffraction spectra of Mg_(1-x)Ni_xAl₂O₄ calcined for 30 minute at 1000 °C

Table1. XRD values for the structural lattice parameter and the crystalline particles diameter, correlated to the Ni/Mg ratio

X	a (Å)	D (nm)
X=0	8.083	29±1
X=0.2	8.075	21.5±1
X=0.4	8.065	21±1
X=0.6	8.048	25±1
X=0.8	8.041	22±1
X=1	8.044	23±1

Characterization of the obtained pigments

Fig.3 shows the absorption spectra of the solid solutions, Mg_{1-x}Ni_xAl₂O₄ (0≤x≤1) obtained by calcination at 1000°C.

The absorption spectra of the powders calcined at 1000°C for 30 minutes present absorption bands with maximums at 370-430nm, 600 - 640nm, 710-760nm. Literature assigns these absorption patterns as follows: the width with maximums between 370 – 430 nm is attributed to a charge transfer of

the Ni^{2+} cation [11], that with amximums between 600 – 640 nm is characteristic to the tetracoordinated Ni^{2+} , and the 710 – 760 width is characteristic to the octahedrally coordinated Ni^{2+} [1,11-14].

The spectra with the highest absorbance is that of the NiAl_2O_4 ($x=1$) powder. The 710 – 760 nm absorbance width is very weak, barely perceptible and only decreases with the decrease of x , indicating a lack of octahedrally coordinated Ni^{2+} .

The absorption spectra for the $\text{Mg}_{1-x}\text{Ni}_x\text{Al}_2\text{O}_4$ ($0 \leq x \leq 1$) solid solutions are similar to that of NiAl_2O_4 ($x=1$),but have weaker absorption intensities, the intensity decreasing with the decrease of the Ni/Mg ratio. The MgAl_2O_4 ($x=0$) spectrum does not present absorption in the visible domain.

For the characterization of the pigment colours, the trichromatic coordinates were determined and they were represented on the chromaticity diagram, fig.4. The obtained colours pertain to the blue-green domain, characteristic to the cyan colour given by NiO , with aproximately the same values as the dominant wavelength. The intensities are however different, the ones pertaining to a smaller Ni/Mg ratio being closer to the center of the diagram, a domain characteristic of the white colour.

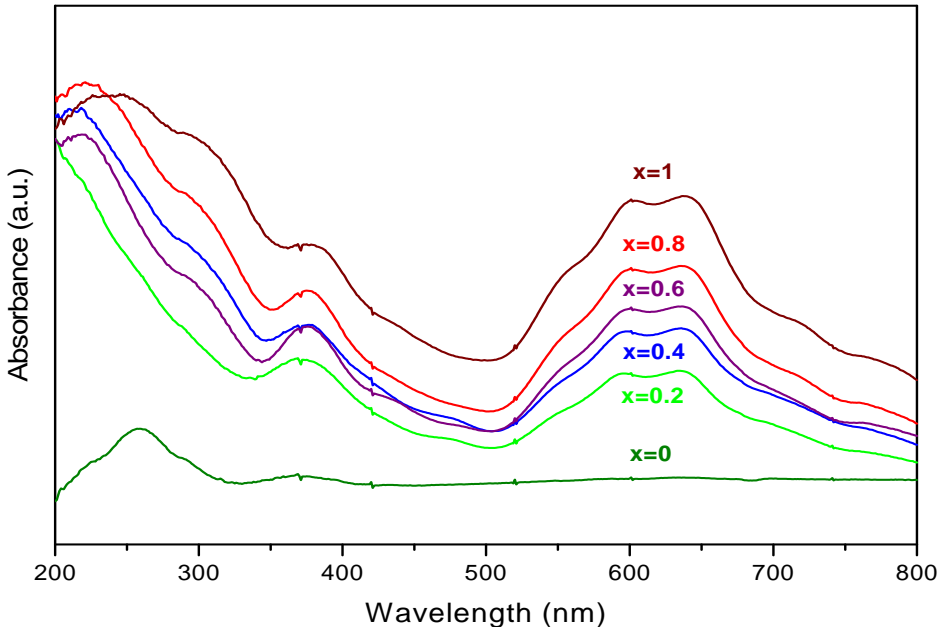


Figure 3. The absorption spectra of powders $\text{Mg}_{(1-x)}\text{Ni}_x\text{Al}_2\text{O}_4$, ($0 \leq x \leq 1$) obtained by calcination for 30 min at 1000 °C

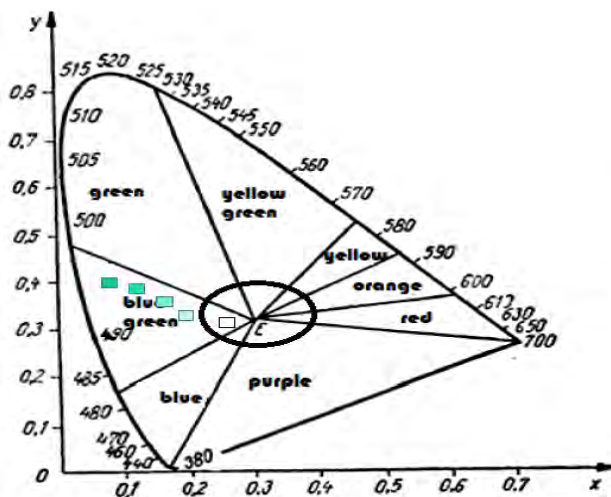


Figure 4. The Chromaticity diagram. The locus of the pigments $Mg_{(1-x)}Ni_xAl_2O_4$ solid solutions

CONCLUSIONS

As a result of the experiments, certain conclusions can be drawn:

The modified sol – gel method, based on sucrose and pectin as organic precursors, leads to the formation of powders with crystallite dimensions under 30 nm, when applied to $NiAl_2O_4$ and $Mg_{(1-x)}Ni_xAl_2O_4$ solid solutions.

The XRD diffraction spectra of the $NiAl_2O_4$ powders, calcined at temperatures in the 600-1000°C range, indicate the formation of a spinel structure at 800°C. A consolidated crystalline structure is obtained at 1000°C. $Mg_{1-x}Ni_xAl_2O_4$, ($0 \leq x \leq 1$) type solid solutions, calcined at 1000°C, indicate a well consolidated crystalline spinel structure. Crystallite dimensions, determined based on diffraction spectra, are situated between 21-29 nm, and are not influenced by the Ni/Mg ratio.

The colour of the powder is the characteristic cyan for $NiAl_2O_4$, becoming less deep for smaller Ni/Mg ratios. The UV – VIS absorption spectra shown specific maximums in conformity to the literature data. The colour of the powders is dependent on the calcination temperature. The colour for $NiAl_2O_4$ varies from a yellowish green, obtained at 600°C to a bluish green at 700 - 800°C and finally cyan, for the sample calcined at 1000°C.

The absorption spectra for the $Mg_{1-x}Ni_xAl_2O_4$ ($0 \leq x \leq 1$) solid solution, is similar to the $NiAl_2O_4$ ($x=0$) spectrum, but have weaker absorption intensities, the intensity decreasing with the decrease of the Ni/Mg ratio. The $MgAl_2O_4$ ($x=0$) spectrum has no absorption in the visible domain.

EXPERIMENTAL SECTION

$Mg_{(1-x)}Ni_xAl_2O_4$ synthesis has been conducted similarly to that of $NiAl_2O_4$ in [2].

The sol – gel process is based on the formation of a solution that contains the salts or metal alkoxides, followed by the conversion of the gel, by hydrolysis and condensation, into the oxide gel lattice. The control parameters temperature, pH, concentration, water/ alcohol ratio. The gel formation mechanism as well as the roles of the pectin and sucrose are discussed more in detail in referances [2, 8-10].

For obtaining $Mg_{(1-x)}Ni_xAl_2O_4$ spinels, $Ni(NO_3)_2 \cdot 6H_2O$, $Mg(NO_3)_2 \cdot 6H_2O$ and $Al(NO_3)_3 \cdot 9H_2O$ were used. The salts were dissolved in ultrapure water, to obtain concentrated solutions. The solutions were stirred in with the added sucrose for 1 hour (with a 2:1 molar ratio for sucrose:oxides), at about 40 – 45°C and with a pH corrected to 1 – 1.5. The consolidation of the tridimensional gel is realized by keeping the mixture in a resting state for 24 to 60 hours. The elimination of water present in the gel pores lead to the formation of a porous structure. The calcination of the said dried gels was done in an electric furnace, in porcelain crucibles. The furnace temperature had an increase rate of 300°C/h, with an isothermal plateau of 30 minutes, 1000 °C.

The behavior of the gels during heating was studied with a Differential Thermal Analysis, done with a TA Instruments SQD 600 analyzer, on a interval of 30 – 1000 °C, and a heating rate of 10°C/min, in alumina crucibles and a dynamic air atmosphere.

Previous results obtained in [2], dealing with the study of temperature influence on $NiAl_2O_4$ spinel structure formation, were further utilized in determining the proper thermal treatment. The gels were calcined at temperatures in the range of 600 – 1000°C, and kept for 30 minutes at maximum temperature. The diffraction spectra on the powders obtained at lower temperatures, 600 - 700°C, show reflexes consistent with those of spinel structures, but are broader, implying a weak crystallization. A well consolidated crystalline structure can be seen in the diffraction spectrum for the 1000°C powder.

These results are in accordance with [11], indicating difficulties in the formation of NiAl₂O₄ at temperatures lower than 1000 °C.

The structural characterization has been carried out at room temperature by powder X-ray diffraction using a Bruker D8 Advance AXS diffractometer with Cu K α radiation in the 2 θ region 25°-70°. The crystallite-sizes were calculated using the Debye – Scherrer formula [1]:

$$D = \frac{k\lambda}{\beta \cos\theta} \quad [1],$$

where β is the peak full width at half maximum (in radians) at the observed peak angle θ , k is the crystallite shape factor (was considered 0.94) and λ is the X-ray wavelength.

The characterization of the pigment colour was realized by measuring the absorption in UV - VIS and by determining the trichromatic coordinates (X, Y, Z), with an MOM colorimeter. The UV-visible absorption spectra were recorded with a Jasco V-650 spectrophotometer (Japan) equipped with an ISV-722 Integrating Sphere, in the range 200-800 nm with a scan rate of 400 nm/min.

REFERENCES

1. L.K.C. de Souza, J.R. Zamian, G.N. da Rocha Filho, L.E.B. Soledade, I. M.G. dos Santos, A.G. Souza, Th. Scheller, *Dyes and Pigments*, **2009**, 81, 187.
2. F. Goga, R. Dudric, L. Bizo, A. Avram, T. Dippong, G. Katona, G. Borodi, A. Anton, *Studia UBB Chemia*, **2016**, 62(3), 263.
3. I.S. Ahmed, H.A. Dessouki, A.A. Ali, *Polyhedron*, **2011**, 30, 584.
4. M. Gaudonn, L.C. Robertson, E. Lataste, M. Duttine, M. Ménétrier, A. Demourgues, *Ceramics International*, **2014**, 40, 5201.
5. H.E.H. Sadek, R.M. Khattab, A.A. Gaber, M.F. Zawrah, *Spectrochimica Acta Part A: Molecular and Biomolecular Spectroscopy*, **2014**, 125, 353.
6. E. Popovici, E. Dvininov, *Nanostructured materials - nanoparticles*, Ed. Demiurg lasi, **2009**, ISBN 978-973-152-001-8
7. I. Lazau, C. Pacurariu, Z. Ecedi, R. Ianos, *Unconventional Methods Used for Oxide Compounds Synthesis*, Ed. Politehnica, Timisoara, **2008**.
8. C. Suci, A.C. Hoffman, A. Vik, F. Goga, *Studia UBB Chemia*, **2007**, 52(2,) 3.
9. C. Suci, A. Vik, F. Goga, E. Dorolti, R. Teteanu, A.C. Hoffman, *Studia UBB Chemia*, **2009**, 54(4), 262.
10. C. Suci, A.C. Hoffman, A. Vik, F. Goga, *Chemical Engineering Journal*, **2008**, 138, 608.

11. I. Lazau, C. Corcoveanu, C. Pacurariu, R.I. Lazau, *Romanian Journal of Materials*, **2013**, (43), 425.
12. A.B.P. Lever, *Inorganic Electronic Spectroscopy*, Elsevier Pub. Comp. Amsterdam, London, New York, **1968**.
13. G. Lorenzi, G. Baldi, F.D. Benedetto, V. Faso, *Journal of European Ceramic Society*, **2006**, 26, 317.
14. F. Iova, A. Trutia, *Optical Materials*, **2000**, 13, 455.